KM3NeT

Technical Design Report for a Deep-Sea Research Infrastructure in the Mediterranean Sea Incorporating a Very Large Volume Neutrino Telescope

KM3NeT

Metamorphosis

Created somewhere in the Universe
Thousands of galaxies I did traverse
To fly through earth and into sea
Where I changed identity
I struggle on with added girth
Shedding light on the process of my birth

Paulus P. Pluska

KM3NeT

Technical Design Report for a Deep-Sea Research Infrastructure in the Mediterranean Sea Incorporating a Very Large Volume Neutrino Telescope

P. Bagley, J. Craig, A. Holford, A. Jamieson, T. Niedzielski, I.G. Priede
University of Aberdeen, United Kingdom

M. de Bell, J. Koopstra, G. Lim, E. de Wolf
University of Amsterdam, the Netherlands

B. Baret, C. Donzaud, A. Kouchner, V. Van Elewyck
APC–AstroParticule et Cosmologie–UMR 7164 (CNRS, Université Paris 7, CEA, Observatoire de Paris), Paris, France

E.G. Anassontzis, L.K. Resvanis
University of Athens, Greece

S. Anvar, F. Chateau, Th. Chaleil, G. Decock, E. Delagnes, F. Druillole, D. Durand, V. Gautard, J. Giraud, I. Grenier, F. Guilloux, M. Karolak, P. Kestener, P. Lamare, H. Le Provost, P. Lotrus, S. Loucatos, F. Louis, G. Maurin, E. Monmarthe, L. Moscoso, Ch. Naumann, J.-P. Schuller, F. Schussler, Th. Stolarczyk, B. Vallage, G. Vannoni, P. Vernin, E. Zonca
CEA, IRFU, Centre de Saclay, 91191 Gif-sur-Yvette, France

C. Rabouille
CEA-CNRS-UVSQ , LSCE/IPSL, 91198 Gif-sur-Yvette, France

D. Bacciola, M. Borghini, M. Fassin, G.P. Gasparini, K. Schroeder, S. Sparnocchia, P. Traverso
CNR-ISMAR, La Spezia, Trieste, Genova, Italy

M. Ageron, J-J. Aubert, V. Bertin, S. Beurthey, M. Billault, A. Brown, J. Brunner, J. Busto, L. Caillat, A. Calzas, J. Carr, A. Cosquer, P. Coyle, C. Curtil, D. Dornic, J.-P. Ernenwein, S. Escoffier, F. Gensolen, C. Gojak, G. Hallewell, P. Keller, P. Lagier, P. Payre, J. Roux
CPPM, Aix-Marseille Université, CNRS/IN2P3, Marseille, France

J.A. Aguilar, J. Bernabeu-Verdú, J.P. Gómez, J.J. Hernández-Rey, S. Mangano, D. Real, F. Salesa, S. Toscano, F. Urbano, J.D.Zornoza
CSIC, Valencia, Spain

C. Nicolaou, P. Razis
University of Cyprus

F. Aharonian, S. Delaney, L. Drury, S. Gabici, A. Hooper, D. Malishev, A. Taylor
Dublin Institute For Advanced Studies, Ireland

G. Anton, R. Auer, T. Eberl, A. Enzenhöfer, F. Fehr, F. Folger, U. Fritsch, K. Geyer, K. Graf, B. Herold, J. Hößl, M. Kadler, O. Kalekin, A. Kappes, U.F. Katz, R. Klein, C. Kopper, I. Kreykenbohm, S. Kuch, R. Lahmann, H. Motz, M. Neff, C. Richardt, R. Richter, K. Roensch, F. Schöck, T. Seitz, R. Shanidze, A. Spies, S. Wagner, J. Wilms
University of Erlangen, Germany

A. Albert, F. Cohen, C. Racca, D. Stubert-Drouhin
Groupe de Recherche en Physique des Hautes Energies (GRPHE)/EA3438/Université de Haute Alsace, Colmar, France

M. Alexandri, G. Chronis, H. Kontoyiannis, V. Lykousis, S. Stavrakakis
Hellenic Centre for Marine Research (HCMR), Greece

G. Bourlis, P. E. Christopoulou, I. Gialas, N. Gizani, A. Leisos, C. Papageorgiou, A. Tsirigotis, S. Tzamarias
Hellenic Open University, Patras, Greece

E. Barbarito, A. Ceres, M. Circella, M. Mongelli, M. Romita
INFN Sezione Bari and University of Bari, Italy

M. Bazzotti, S. Biagi, G. Carminati, S. Cecchini, T. Chiarusi, G. Giacomelli, A. Margiotta, M. Spurio
INFN Sezione Bologna and University of Bologna, Italy

S. Aiello, L. Caponetto, A. Grimaldi, E. Leonora, D. Lo Presti, N. Randazzo, S Reito, G.V. Russo, D. Sciliberto, V. Sipala, S. Urso
INFN Sezione di Catania and University of Catania, Italy

M. Anghinolfi, A. Bersani, M.Battaglieri, M. Brunoldi, R. Cereseto, R.DeVita, H. Costantini, K. Fratini, S. Minutoli, P. Musico, M. Osipenko, D. Piombo, G. Ricco, M. Ripani, M. Taiuti, D. Torazza
INFN Sezione Genova and University of Genova, Italy

I. Amore, G. Cacopardo, R. Cocimano, R. Coniglione, M. Costa, A. D'Amico, C. Distefano, V. Giordano, M. Imbesi, D. Lattuada, E. Migneco, M. Musumeci, A. Orlando, R. Papaleo, V. Pappalardo, P. Piattelli, G. Raia, G. Riccobene, A. Rovelli, P. Sapienza, M. Sedita, A. Trovato, S. Viola
INFN Laboratori Nazionali del Sud, Catania, Italy

R. Habel, A. Martini, L. Trasatti
INFN Laboratori Nazionali di Frascati, Italy

G. Barbarino, G. De Rosa , S. Russo
INFN Sezione Napoli and University of Napoli, Italy

E. Castorina, V. Flaminio, R. Garaguso, D. Grasso, A. Marinelli, M. Morganti, C. Sollima
INFN Sezione Pisa and University of Pisa, Italy

F. Ameli, M. Bonori, A. Capone, G. De Bonis, F. Lucarelli, R. Masullo, F. Simeone, M. Vecchi
INFN Sezione Roma and University of Roma 1, Italy

B. Bigourdan, P. Bouquet, D. Choqueuse, G. Damy, J. Drogou, Z. Guédé, J. Marvaldi, J. Rolin, P. Valdy
IFREMER, France

G. Etiope, P. Favali, C. La Fratta, G. Marinaro
Istituto Nazionale di Vulcanologia, Italy

G, Guillard T. Pradier
University of Strasbourg and Institut Pluridisciplinaire Hubert Curien/IN2P3/CNRS, Strasbourg, France

D. Felea, O. Maris, G. Pavalas, V. Popa, A. Radu, M. Rujoiu, D. Tonoiu
Institute of Space Sciences, Machurele-Bucharest, Romania

N. Bellou, F. Colijn, P. Koske, T. Staller
University of Kiel, Germany

N. Kalantar-Nayestanaki, O. Kavatsyuk, H. Löhner
KVI and University of Groningen, the Netherlands

S. Bradbury, J. Rose, R.J. White
University of Leeds, United Kingdom

F. Jouvenot, C. Touramanis
University of Liverpool, United Kingdom

D. Lenis, E.C. Marcoulaki, C. Markou, I.A. Papazoglou, P.A. Rapidis, I. Siotis, E. Tzamariudaki
National Center of Scientific Research "Demokritos", Athens, Greece

A. Assis Jesus, E. Berbee, A. Berkien, R. de Boer, H. Boer Rookhuizen, M. Bouwhuis, C. Chen, P. Decowski, D. Gajanana, A. Heijboer, E. Heine, M. van der Hoek, J. Hogenbirk, P. Jansweijer, M. de Jong, H. Kok, A. Korporaal, S. Mos, G. Mul, D. Palioselitis, H. Peek, E. Presani, C. Reed, D. Samtleben, J.-W. Schmelling, J.Steijger, P. Timmer, P. Werneke, G. Wijnker
NIKHEF, Amsterdam, the Netherlands

R. Bakker, R. Groenewegen, H. van Haren, T. Hillebrand, J. van Heerwaarden, M. Laan, M. Smit
Koninklijk Nederlands Instituut voor Onderzoek der Zee (NIOZ), Texel, the Netherlands

T. Athanasopoulos, A. Ball, A. Belias, A. Fotiou, Y. Kiskiras, A. Kostoglou, S. Koutsoukos, M. Maniatis, E. Markopoulos, A. Psallidas, L.K. Resvanis, G. Stavropoulos, V. Tsagli, G. Vermisoglou, V. Zhukov
NOA / NESTOR, Pylos, Greece

J. Perkin, L. Thompson
University of Sheffield, United Kingdom

F. Gasparoni, F.Bruni
Tecnomare, Venice, Italy

E. Kendziorra, A. Santangelo
University of Tübingen, Germany

P. Kooijman
University of Utrecht and University of Amsterdam, the Netherlands

C. Bigongiari, U. Emanuele, H. Yepes, J. Zúñiga
University of Valencia, Spain

J. Alba, M. Ardid, M. Bou-Cabo, F. Camarena, V. Espinosa, G. Larosa, J. Martínez-Mora, J. Ramis, J. Redondo, V. Sánchez-Morcillo
Universidad Politécnica Valencia / IGIC, Spain

Contents

Executive summary

KM3NeT is a deep-sea multidisciplinary observatory in the Mediterranean Sea that will provide innovative science opportunities spanning Astroparticle Physics and Earth and Sea Science. This is possible through the synergy created by the use of a common infrastructure allowing for long term continuous operation of a neutrino telescope and marine instrumentation. The present KM3NeT Design Study concludes with this Technical Design Report which develops the ideas put forward in the Conceptual Design Report published in April 2008 [1].

Neutrino astronomy opens a unique new window for the observation of the Universe. At the present time, the most sensitive neutrino telescope in the world is the IceCube detector at the South Pole which in its final configuration will instrument a cubic kilometre of polar ice. Building on the experience gained with the ANTARES neutrino telescope and other projects in the Mediterranean Sea, the construction of the KM3NeT infrastructure is projected with a sensitivity exceeding that of IceCube by a substantial factor. KM3NeT will be an essential node in the global network of multimessenger instruments in astronomy.

The principal goal of KM3NeT is the observation of cosmic point-like sources of neutrinos, in particular in a region of the sky complementary to the field of view of IceCube. This science objective has been the driving consideration in the optimization of the detector design. The resulting sensitivity is compared to that of IceCube in the figure below, showing that KM3NeT extends substantially the visible region of the sky and even improves the discovery potential in the same field of view. This gain is due to the far larger instrumented volume possible with the project budget, together with the significantly better angular resolution achievable in water compared to ice.

The hostile environment of the deep sea together with the envisaged operation over at least 10 years, impose severe constraints on the telescope design. The design presented conforms to all these requirements within a budget of 250 M€ and surpasses the original objective of the Design Study substantially. A strategy to pursue technical alternatives for critical aspects, in particular the mechanical structure of the detection units, has been adopted. All solutions have a similar cost for equal performance but remain to be fully evaluated for viability. The feasibility of construction has been addressed together with environmental aspects and decommissioning issues.

Unprecedented prospects for real-time data collection from the deep sea are provided with the observatory instruments. Science fields such as climatology, geosciences, marine biology and oceanography will profit enormously from these data. Representatives from these communities are involved in the design stage to ensure compatibility with their needs.

Different potential sites have been identified and investigated in detail. The site decision will be taken in the framework of the ongoing KM3NeT Preparatory Phase project.

Final technical and site decisions will be made at the end of 2011 and a technical proposal will be presented in early 2012. Final prototyping and construction could begin in 2013. Data taking will already start during the construction period of about five years with first science data anticipated in 2014.

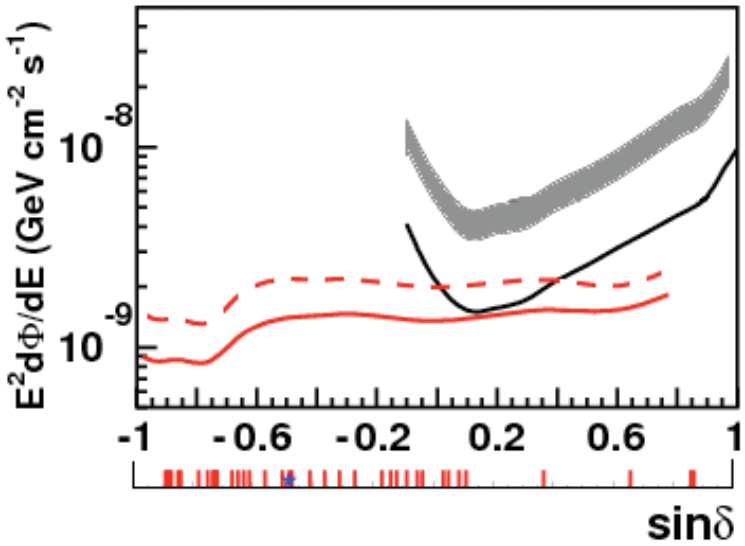

A: Sensitivity of the full KM3NeT detector (see Table 9.1 for details) to neutrino point sources with an E^{-2} spectrum for one year of observation, as a function of the source declination. The red lines indicate the flux sensitivity (90% CL;full line) and the discovery flux(5σ, 50% probability; dashed line). Both are estimated with the binned analysis method. The black line is the IceCube flux sensitivity for one year, estimated with the unbinned method [2] (full line). IceCube's discovery flux (5σ, 50% probability) is also indicated (shaded band, spanning a factor 2.5 to 3.5 above the flux sensitivity). The red ticks at the bottom of the horizontal axis show the positions of Galactic gamma ray sources [3]; the position of the Galactic Centre is indicated by a blue star.

1. Introduction

This document describes the technical design of a future deep-sea research infrastructure in the Mediterranean Sea hosting a multi-cubic-kilometre neutrino telescope and scientific nodes for longterm, continuous measurements in earth and marine scientific research.

The science case for the neutrino telescope is overwhelming: Neutrinos are unique messengers from the most violent, highest-energy processes in our Galaxy and far beyond. Their measurement will allow for new insights into the mechanisms and processes that govern the non-thermal Universe and will complement high-energy gamma ray astronomy and cosmic ray studies. The multi-messenger picture emerging from these modalities of observation is one of the most exciting future prospects of astronomy and astrophysics.

Neutrino astronomy is experimentally highly demanding, in particular since it requires vast volumes of target material, most easily implemented in naturally abundant, transparent media, such as water or ice. It therefore took more than 20 years for the field to mature from first-generation pilot projects to large-scale neutrino observatories. Currently, the world's largest neutrino telescope, IceCube, is under construction at the South Pole and will encompass one cubic kilometre of glacial ice in its final configuration. KM3NeT will be significantly larger, exceeding IceCube in its sensitivity and complementing its field of view. In particular, KM3NeT will have the Galactic Centre and a large part of the Galactic plane in its field of view most of the time. It thus offers a prime observation opportunity for various types of Galactic candidate sources of neutrinos.

The construction of a deep-sea neutrino telescope is technically highly challenging: the components must withstand the enormous pressure and chemically aggressive sea water whilst being reliable enough to minimize complex maintenance operations. The deployment operations must be safe, robust and precise. The design described here builds on the extensive experience gained in the Mediterranean pilot projects ANTARES, NEMO and NESTOR, as well as on deep-sea know-how from other fields of science and industry. A major step forward was the ultimate proof of feasibility for a deep-sea neutrino telescope provided by the successful installation and operation of the ANTARES experiment.

In the past four years, an in-depth design study[1] for KM3NeT has been performed, where existing technologies and design solutions have been developed further and new approaches evaluated, tested and verified. Optimising the design for cost effectiveness, feasibility of construction and reliability of operation narrowed down the design options to a scenario with a limited number of alternative solutions. Final decisions will require further studies including prototyping efforts and field tests.

The deep-sea infrastructure of the neutrino telescope also offers unique possibilities for a wide spectrum of other research activities, such as in environmental sciences, geology and geophysics, marine biology and oceanography. Furthermore, it could be used to provide information for future hazard warning systems. The KM3NeT installation will be an important node in a global network of deep-sea observatories, operated by the projects ESONET, EMSO, GMES in Europe, Neptune Canada, DONET Japan and the US OOI.

[1] *Funded through EU FP6, contract number 011937.*

In recognition of its unique, multidisciplinary scientific potential and its advanced technical status, KM3NeT was selected as one of 35 European priority research infrastructures by the ESFRI[2] panel in 2006; this status was confirmed in the 2008 review process. As a consequence, KM3NeT is receiving further EU support in a Preparatory Phase project (2008-12)[3] with the objectives of addressing the legal, funding and strategic issues and pursuing technical preparatory work. This project will provide the organisational framework for the remaining path toward a dedicated proposal, along a timeline that foresees final decisions on the site and the remaining technical options by 2011.

This document presents the technical design of the KM3NeT research infrastructure to the scientific community, to stakeholders and decision makers, and to potential future partners in a world-wide context. The ESFRI roadmap featured an overall budget estimate of 220 to 250 M€ The design study has shown that the major physics objectives can be met within this budgetary constraint. The technical design is modular and so allows for staged implementation with continuously increasing science capabilities.

1.1 Science Case - Neutrino Astronomy

Multi-messenger astronomy extends our knowledge of the Universe, beyond that which can be gained from astronomy using electromagnetic radiation. Detailed reviews of neutrino astronomy have been presented in numerous articles [4,5,6,7]. The KM3NeT conceptual design report [1] presents the science case in some detail.

Neutrinos are electrically neutral and thus travel in straight lines from their origin to Earth. They interact weakly and thus can escape dense regions where they are generated. They are inevitably produced in any environment containing protons or nuclei at the typical energies observed in cosmic rays. Neutrinos are ideal for observing the highest-,energy phenomena in the Universe and, in particular, pinpointing the hitherto unknown sources of cosmic rays.

The KM3NeT telescope will detect neutrinos by measuring the Cherenkov light emitted by charged secondary particles produced in neutrino interactions with the sea water or the rock beneath. Since neutrinos interact so weakly, a huge volume of water must be observed to collect a sufficient number of such events. The direction of the incoming neutrino can be reconstructed with the telescope and its energy estimated. Accumulations of neutrino events pointing to particular celestial directions will establish the coordinates and characteristics of cosmic accelerators or other astrophysical neutrino sources.

In order to reliably distinguish the neutrino events from cosmic-ray induced particles from the upper hemisphere, neutrino telescopes look downwards, using the Earth as a shield against any such background. The KM3NeT field of view therefore complements that of IceCube and covers the Southern sky, in particular the Galactic centre and a large part of the Galactic plane.

At energies of several hundred TeV the Earth starts to become opaque to neutrinos. Since at such energies the atmospheric muon background is small, cosmic neutrinos from directions above the horizon can be identified.

Various astrophysical sources are expected to produce high-energy neutrinos that may be detected with KM3NeT. The information that can be gained by detecting just a handful of events emanating from a cosmic source cannot be underestimated.

[2] *European Strategy Forum on Research Infrastructures.*

[3] *Grant agreement number 212525.*

The existence of these neutrino sources will be proved and more importantly knowledge of their behaviour, which cannot be acquired by other means, will be gained.

Potential neutrino sources are:

- Galactic objects such as shell-type supernova remnants, pulsar wind nebulae, micro-quasars or unidentified TeV gamma ray sources. The energy spectra from these objects are expected to be steeply falling and can extend up to 100 TeV.
- Extragalactic point sources, such as Active Galactic Nuclei (AGNs) or Gamma Ray Bursts (GRBs). These objects have electro magnetic emissions that can have significant variations in time. In these cases, time correlations of neutrino events with flare or burst observations may significantly reduce the background. The energy spectra are expected to be harder than those of the galactic sources. This will also help to identify the signals.
- Since neutrinos can escape dense environments from where no photons can emerge it is possible that unexpected neutrino sources will be discovered.
- A high-energy diffuse flux is expected from distant, individually indistinguishable sources and neutrinos produced in collisions of cosmic rays with interstellar matter or radiation fields.
- There are strong indications for the existence of Dark Matter even though little is known of its nature. A possibility is that it consists of weakly interacting massive particles (WIMPs). In this case, neutrinos may be produced through WIMP annihilations in regions of large WIMP density, such as in gravitational centres like the Earth, Sun or Galactic Centre. The energy of the emerging neutrinos is low but can extend up to a maximum of the WIMP mass, typically assumed to be less than a few TeV.

The design presented in this document has been optimised in sensitivity to point sources with an energy spectrum, behaving as E^{-2}. Simulation studies show, however, that the optimization is different for each potential neutrino source.
The corresponding neutrino energy spectra require different compromises between proximity of light sensors (to collect sufficient light from a single event) and size of instrumented volume (to observe a target mass as large as possible). The design allows for a flexible choice of the detector "footprint" that can thus be adapted both to new scientific findings and to refined simulation results.

1.2 Science Case Marine science

In general research in the deep sea is currently limited by power and communication constraints. Most observations are made by autonomous measuring systems, deployed for up to a year and requiring recovery in order to retrieve the data.
Data storage and battery capacity have limited data sampling rates in such systems to sampling periods of 10 minutes or more and there are inevitable breaks in data collection.

A cabled deep sea observatory will remove these constraints by providing a continuous and steady power supply enabling real time data acquisition. This will allow for the use of intelligent systems that can react dynamically to events and adapt sampling rates to changing conditions, or activate the monitoring of additional parameters and thus obtain a more realistic view of the deep sea environment.

The KM3NeT infrastructure enables the collection of data at sampling rates vastly larger than the ones presently available and for an overall duration of at least ten years. Furthermore, beyond the detailed data collected by the instrumentation of the separate earth and sea sciences nodes, relevant data will also be collected by sensors that are part of the neutrino telescope array itself.
This latter data stream, albeit not of as detailed nature as the former, will for the first time allow the real time monitoring of a large volume of water with samples taken at locations separated by distances of the order of a few kilometres.

As a result it will be possible for the first time to investigate phenomena such as internal waves and short time-scale oscillations in the water column.

This will extend our knowledge of some of the physical processes of the ocean and their effects on the distribution of suspended geological, chemical and biological materials. A novel approach will be to use data from the telescope's optical sensors and correlate them with data from conventional oceanographic instruments.

Real time tracking of bio-acoustic emissions or vertical migrations of organisms will also be possible. For example it will be feasible to connect elements of the new Ocean Tracking Network [8] that will be capable of tracking fishes and marine mammals equipped with implanted transmitters.

The system will also provide continuous observations to investigate the behaviour of transitory hazardous events such as earthquakes and slope failures that may have catastrophic consequences (e.g. tsunamis). It will have the potential to contribute elements for the regional tsunami early warning system under ICG/NEAM with better performance than data buoys currently being deployed.

The Earth-Sea science component of KM3NeT will be multidisciplinary, with stations monitoring the rocks, sediments, bottom water, biology and events in the water column. It will form the basis of the Mediterranean section of the EU plan for long-term monitoring of the ocean margin environment around Europe. It is part of the Global Monitoring for Environment and Security (GMES) system and will complement oceanographic networks such as GOOS (Global Ocean Observing System), EuroGOOS, and DEOS (Dynamics of Earth and Ocean Systems). Furthermore close cooperation will be pursued with EMSO (European Multidisciplinary Seafloor Observatory).

Interest in marine observations has been highlighted in a recent workshop on an integrated system of Mediterranean marine observatories sponsored by the Mediterranean Science Commission (CIESM) [9,10]. It was stated that the Mediterranean is in effect a miniature ocean and is therefore an ideal model to study oceanic processes and land-ocean-atmospheric interaction. Geological records show that its ecosystem amplifies climatologic variations and this makes it an ideal test bed for climate studies.

Sustainable development will depend more and more on an intelligent management of the marine environment in order to protect marine ecosystems and minimize the impact of climate change whilst maintaining the economic benefit to the region. As a result the formulation of policies must be based on informed decisions which in turn will depend on real time data and numerical modelling. Multi-purpose observatories represent the way forward and combining their observations with economical, environmental and social parameters will provide the required integrated management approach [11].

1.3 Global Context

The process of building neutrino telescopes has gone through a long and sometimes painful learning curve over the last three decades. Initial pioneering work for the DUMAND project (deep sea, near Hawaii) was followed by successful installations in Lake Baikal (fresh water, Siberia) and the ice of the South Pole (AMANDA). These projects demonstrated the feasibility of neutrino telescopes, but their results also indicated that km^3-sized detectors are needed to exploit the full scientific potential.

Consequently, the IceCube experiment – to instrument one km^3 of ice – is now under construction at the South Pole.

In order to cover the full sky and to observe the Galactic plane, a second instrument of at least a similar size is needed in the Northern hemisphere. The Mediterranean projects, in particular the successful operation of the ANTARES experiment, have meanwhile demonstrated that deep-sea neutrino detection is technically feasible and scientifically advantageous. The time has now come to build on the experience gained and to follow the recommendations of the HENAP4 panel from 2002 and construct a multi-km^3-sized detector, KM3NeT, in the Mediterranean Sea.

Substantial progress towards a reliable, cost-effective and high-performance technical design of the KM3NeT telescope has been made over the last years in the framework of the EU-funded Design Study. This and its unique scientific potential have led to the inclusion of KM3NeT into the priority list of ESFRI and to strong supporting recommendations in the European Roadmaps of Astroparticle Physics and of Astronomy. Since 2008, a Preparatory Phase project funded by the EU through FP7 allows KM3NeT to address the legal, governance, financial and strategic issues to be solved before construction can go ahead.

KM3NeT and IceCube will be major instruments for neutrino astronomy in the coming decade and already the operation of both detectors in the context of a *Global Neutrino Observatory* is already being discussed. For such plans to materialise, a sufficient overlap in operation time is required implying a timely start of the KM3NeT construction.

Neutrino astronomy is tightly related to other activities in astroparticle physics through common scientific quests and observations of astrophysical objects and processes of mutual interest. One example is neutrino emission in conjunction with high-energy photon production or with cosmic-ray acceleration processes (requiring multi-messenger observations, i.e. in conjunction with TeV gamma ray or cosmic ray observatories). Another example is the case of neutrinos produced in the annihilation of Dark Matter particles (making a connection to accelerator-based particle physics, direct cryogenic Dark Matter searches, and also to ground-based and satellite-borne gamma ray observatories). Progress in astroparticle physics will require a global network of major installations, one of which will be KM3NeT.

Various projects are currently pursued at a global scale that will be nodes in this network – amongst them the Cherenkov Telescope Array (CTA, gamma rays), the Pierre Auger Observatory (cosmic rays), gravitational wave observatories and deep-underground experiments for Dark Matter detection. Europe has the lead for several of these research infrastructures, including KM3NeT and CTA. Due to the global context in which they are embedded, it can be expected that these projects will attract partners from outside Europe once they are on the road to construction. In the case of KM3NeT, such partnerships are actively sought.

Similarly, the KM3NeT Research Infrastructure will also provide opportunities for deep-sea measurements for earth and sea sciences. Also in this context, the project is embedded in a series of global research and monitoring networks. Particular emphasis will be placed on the synergy with the EMSO research infrastructure.

[4] *High-Energy Neutrino Astronomy Panel of the Particle and Nuclear Astrophysics and Gravitation International Committee (PaNAGIC), which is part of the International Union of Pure and Applied Physics (IUPAP).*

2. Infrastructure Description

The deep sea infrastructure described in this document consists of a neutrino telescope and a network of nodes for marine and earth science investigations. The neutrino telescope occupies an area of several square kilometres of the seabed and the marine and earth science nodes are located far enough to avoid interference with the neutrino telescope but close enough to make use of a common deep sea cable network.

2.1 Neutrino Telescope

The telescope is designed for the detection of high-energy neutrinos of cosmic origin, having energies of a few hundred GeV and above,. Neutrinos are indirectly observed by detecting the reaction products of their interactions with matter (in and around the detector's volume). Since these interactions proceed via the weak interaction they are rare and therefore to enhance their detection a huge target should be used.

Detection principles

A cost effective way to obtain a huge target mass is to use a large volume of seawater as the detection medium, the target being the material of the detector itself and the sea and rock surrounding it. In the neutrino interactions with the matter in and around the detector particles are produced many of which are charged and travel faster than light in water. Such particles can be detected through the Cherenkov light they produce.

An underwater neutrino detector is best suited for detecting charged current interactions of muonneutrinos that produce high-energy muons. In contrast to most particles the muon loses very little energy as it travels through matter. This means that it travels large distances and can be produced far away from the detector and still be detected. This enlarges the target volume for interactions in which these muons are produced. For these interactions the effective interaction target volume becomes equal to the cross sectional area of the detector multiplied by the range of the muon. The range of the muon increases with energy and as a consequence the effective interaction volume grows with energy and becomes significantly larger than the instrumented volume of the detector.

For interactions where no muons are produced the particles produced only travel short distances and thus can only be detected if they occur inside or at least very near the instrumented volume of the detector. For this reason most of the detected neutrinos are muon-neutrinos.

Detected muons carry a large fraction of the neutrino's energy and as a result have a direction that is almost identical to that of the neutrino. The telescope is designed to determine the direction of the muon and by extension the direction of the original neutrino.

The telescope can generically be described as a three dimensional matrix of sensors that are sensitive to the emitted Cherenkov light in the visible range. Because the attenuation length of light in the deep sea is of the order of 50-60 m, at wavelengths around 470 nm, the sensor matrix can be sparse and spread out over a large volume.

The measured arrival time of the Cherenkov light at each of the sensors, combined with their known spatial position, are used to reconstruct the trajectory of the particle producing the Cherenkov light. In addition the amount of detected light can provide information on the energy of the particle.

Detector elements

The light sensors are photomultiplier tubes contained in glass spheres that are designed to resist the hydrostatic pressure of the deep sea environment. We refer to these instrumented spheres as *optical modules*.

These optical modules are kept suspended in the sea by vertical structures, which are anchored to the seafloor by a dead-weight and kept close to vertical by added buoyancy at their top. We refer to these structures together with their optical modules as *detection units*.

The power required for the photomultipliers and electronics located underwater is fed via a single cable from shore to a *primary junction box.* From there it is distributed via a seafloor cable network that branches via *secondary junction boxes* to the detection units. Inside the detection units the power is distributed further to the optical modules via a *vertical backbone cable*.

The data from the photomultipliers (time and amplitude) is digitised and transported to shore via a fibre optic network that is incorporated in the aforementioned cable network.

A *calibration system* is implemented to determine the positions of the optical modules and to provide timing synchronisation of the photomultiplier signals.
A shore station receives the data and is used to control the operation of the detector. It also houses computing facilities to filter and store the data from the telescope, before transferring them to remote nodes for analysis. The connection to the local power grid is also housed here.

Design Choices

Two extreme cases serve to illustrate a basic design choice for the detector. In one case a sparse arrangement of optical modules leads ultimately to an inefficient design since the light collection efficiency decreases as the distance between optical modules increases. In the other extreme, a very dense arrangement leads to a cost ineffective detector of small volume, since the same number of optical modules could be used to instrument a much larger device.

A key parameter in the design of such a detector is therefore the sensitive (photocathode) area of the photomultipliers per unit volume. The way in which the photocathode area is distributed in a cost effective manner over the volume of the detector, has been a major issue of the design study.

Two distinct approaches have been followed. One approach utilizes detection units placed at large distances. The optical modules are distributed in clusters *(storeys)* along the vertical extent of the detection unit. To maximize the number of independent measurements the optical modules at each storey are separated by several metres horizontally. The alternative approach attempts to minimize the cost of each unit allowing for a larger number of units to be placed at smaller distances. In this approach the clustering on the storey is achieved with small photomultipliers within a single optical module.

The design alternatives will be described in Chapter 3. The designs that follow the first approach, have a horizontal distance between detection units of 150 to 180 m and vertical distance between storeys of 40 m, leading to an instrumented volume of one cubic kilometre for every 50 detection units. Preliminary cost estimates indicate that a detector with 320 such units could be constructed for the envisaged budget. For the design following the second approach the distance between units is 130 m and the vertical separation between storeys is 30 m. This yields an instrumented volume of one cubic kilometre for every 100 units.

The cost estimates indicate that for this design a detector containing about 4 units could be constructed.
Detectors of such a size will require a certain amount of modularisation. For instance the power required and the data rate produced by such a telescope will require more than one cable running to the shore. Each such cable will require its own primary junction box and seafloor cable network.

A detector building block, see Figure 2-1 that can comfortably be constructed using a single cable network is at most half the size described above. The designs presented and used in the detector performance simulations feature a building block of half the ultimate size. The final performance is scaled accordingly.

2.2 Marine and Earth Sciences

The primary objective of the earth and sea science contribution to the KM3NeT programme is to establish a network of detection nodes. This network will incorporate a number of secondary junction boxes strategically positioned around the footprint of the neutrino telescope and connected to a primary junction box. Each secondary junction box will have a suite of sensors connected to it and will deliver continuous real-time data to shore, providing constant long-time monitoring.

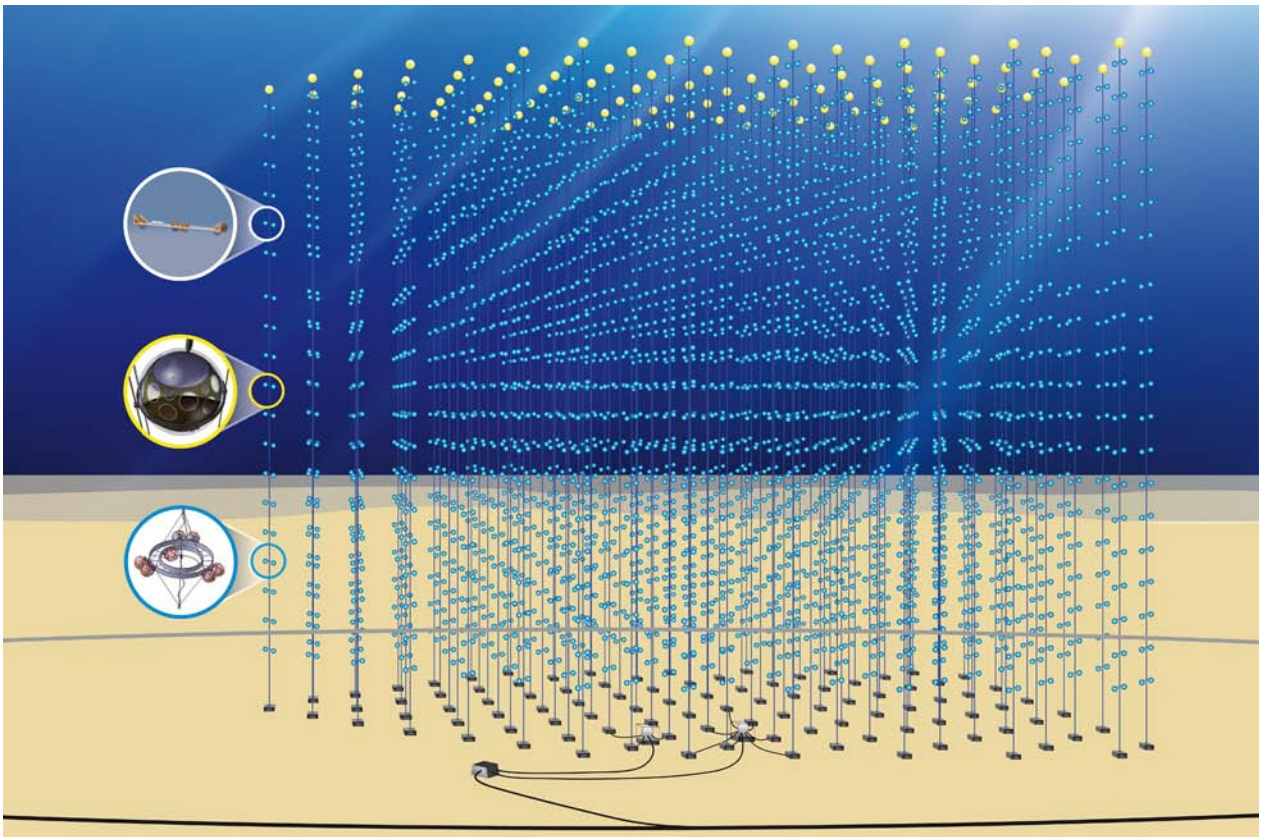

Figure 2-1: Artist's impression of the neutrino telescope.

The number of secondary junction boxes installed will depend on the site, the neutrino telescope footprint and the instrumentation resources required by the science community.
The earth and sea science community will use the same shore infrastructure and electro-optical cable for data transfer and power distribution as the neutrino telescope.

The specification of the secondary junction box will need to be customised in order to accommodate the specific power and data transfer requirements of the sea and earth science sensors.

The instrumentation will consist of sensors such as video cameras, acoustic devices, conductivitytemperature-depth probes, Doppler current profilers and chemical analysers. In addition seismic activity will be monitored. A customised interface will be required in the secondary junction boxes to manage the operation of and data acquisition from these devices.

2.3 Site Description

Three projects were undertaken in the Mediterranean Sea as forerunners of KM3NeT. These were the French based ANTARES, the Italian based NEMO and the Greek based NESTOR projects. As a result the sites chosen in the pilot projects have had extensive programmes of measurements into their environmental conditions. The measurements done at these sites were taken over periods that vary in length from a few days to several years of continuous or periodic data. These will be summarized in Chapter 5. The sites have shown to be valid candidate sites for hosting the KM3NeT infrastructure. Their locations are shown in Figure 2-2 and the geographical characteristics of the three sites are summarized below.

Toulon Site (ANTARES)

The Toulon site is located in the Ligurian Sea at 42°48′ N 06°10′ E. The distance to the coast at La Seyne-sur-Mer, the landfall of the ANTARES deep-sea cable, is 40 kilometres. The depth of the seafloor at the site is 2475 m. The coast around Toulon has several major harbours. For ANTARES the deployments took place from the FOSELEV marine yard at La Seyne-sur-Mer. The area is served by the airports of Nice, Toulon and Marseille. By road the town of La Seyne-sur-Mer is reached via the A50 motorway.

Capo Passero Site (NEMO)

The Capo Passero site is located in the West Ionian Sea at 36°16′ N 16°06′ E. The distance to the coast at Portopalo di Capo Passero on the south west tip of Sicily is 100 kilometres. The depth of the seafloor at the site is 3500 m. The nearest major port is Catania, from where the NEMO sea operations departed. Other ports are those of Siracusa, Augusta and Pozzallo. Portopalo also offers a harbour. The shore site is served by the Catania airport which is about 110 km from Capo Passero. By road Catania is reached by the E45 motorway and from there Capo Passero is reached via the A18/E45 and SP19 roads. To reach Sicily from mainland Europe a ferry crossing to Palermo, Messina or Catania is required.

Pylos Site (NESTOR)

The sea around Pylos in the East Ionian Sea offers a variety of possible deployment sites at various depths.

A plateau at a depth of 4550 m is located at 36° 33′ N 21°30′ E. The distance to the port of Methoni is 30 km.

Alternative sites near Pylos are located at: 36° 50′ N 21°32′ E, 15 km from the shore at Pylos at a depth of 3000 m; at 36° 33′ N 21°12′ E, 50 km from the port of Methoni at a depth of 5200 m; and at 36° 38′ N 21°36′ E, 20 km from Methoni at a depth of 3750 m. The nearest major port is that of Kalamata. Smaller ports are available at Methoni and Pylos itself. The site is served by the airport of Kalamata at a distance of 45 km. By road Kalamata is reached from Athens by the E65 motorway and from Patras by the E55. From there Pylos is reached via local roads.

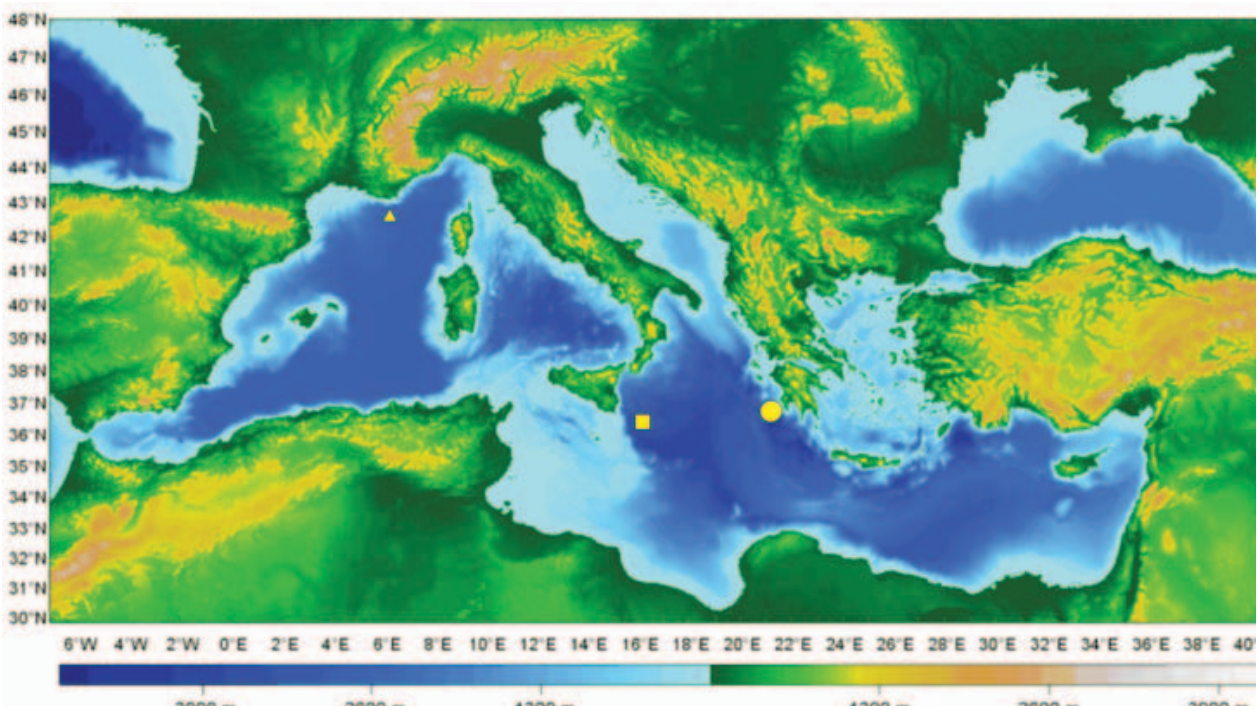

Figure 2-2: Bathymetry of the Mediterranean sea with the site locations marked; Triangle marks the Toulon site, the square the Capo Passero site and the circle contains the four possible sites near Pylos.

3. Technical Design of Neutrino Telescope

In this chapter the technical implementation of the generic structure of a neutrino telescope discussed in chapter 2 is presented. The neutrino telescope will consist of a three-dimensional array of photo-sensors (photomultipliers) supported by vertical structures anchored on the seafloor and connected to a seabed cable network for power distribution and data transmission.

To obtain the large photocathode area required for the planned sensitivity in a cost-effective way, it is optimal to arrange photomultipliers in local clusters. This objective can be achieved by using either local groups of optical modules containing one or two large photomultipliers each or groupings of smaller photomultipliers within a single multi-PMT optical module. These designs are currently being pursued, with a common solution for the front-end electronics that can be housed inside an optical module.

Optimisation based on cost, physics sensitivity and reliability has led to the consideration of modular mechanical structures that facilitate production, transport and deployment procedures. For deployment it is planned to transport detection units in a compact package which is easy to handle and which will allow the detection unit to unfurl once it is placed on the seafloor. Such deployment techniques have not been used extensively in the past and need to be subjected to further field trials. If the unfurling technique should prove to be unviable the deployment of the extended structures from the sea surface, similar to the method used in ANTARES, will have to be considered.

Simulations indicate that horizontal distances of a few meters in local optical module groups increase the reconstruction quality and thus the sensitivity. Therefore, a specific design being proposed and shown in Figure 3-1(a) incorporates extended mechanical structures in the form of 6-meter long horizontal bars to support optical modules. One detection unit consists of 20 such horizontal bars (storeys), with a vertical separation of 40 m between storeys.

These novel mechanical structures require extensive field tests that are beyond the scope of the design study phase. Other solutions, pursued in parallel, are string-like mechanical structures with storeys consisting of a single multi-PMT optical module (see Figure 3-1(b)) or with storeys with optical modules arranged in a triangular formation (Figure 3-1(c)).

The connection to shore for transferring electrical power, control, and data is achieved through an electro-optical submarine cable network using commercially available components where appropriate. Sea bottom connections between the detection units and the cable network are carried out through the use of deep-sea remotely operated vehicles (ROVs).

The overall power consumption of the telescope is approximately 125 kW and the expected data rate will be roughly 25GBytes/s. This large data stream to shore is carried on a point-to-point fibre optic network which transfers all the optical module data to the shore. A backup solution to the data transmission scheme within a detection unit is a fibre-optic daisy-chain concept.

A shore station will house the power supplies, the lasers that will drive the fibre optic network, and will also host the data acquisition system that will implement data filtering, recording and distribution.

It is planned that the studies of various components will conclude during 2011, to allow for a timely process of decision taking.

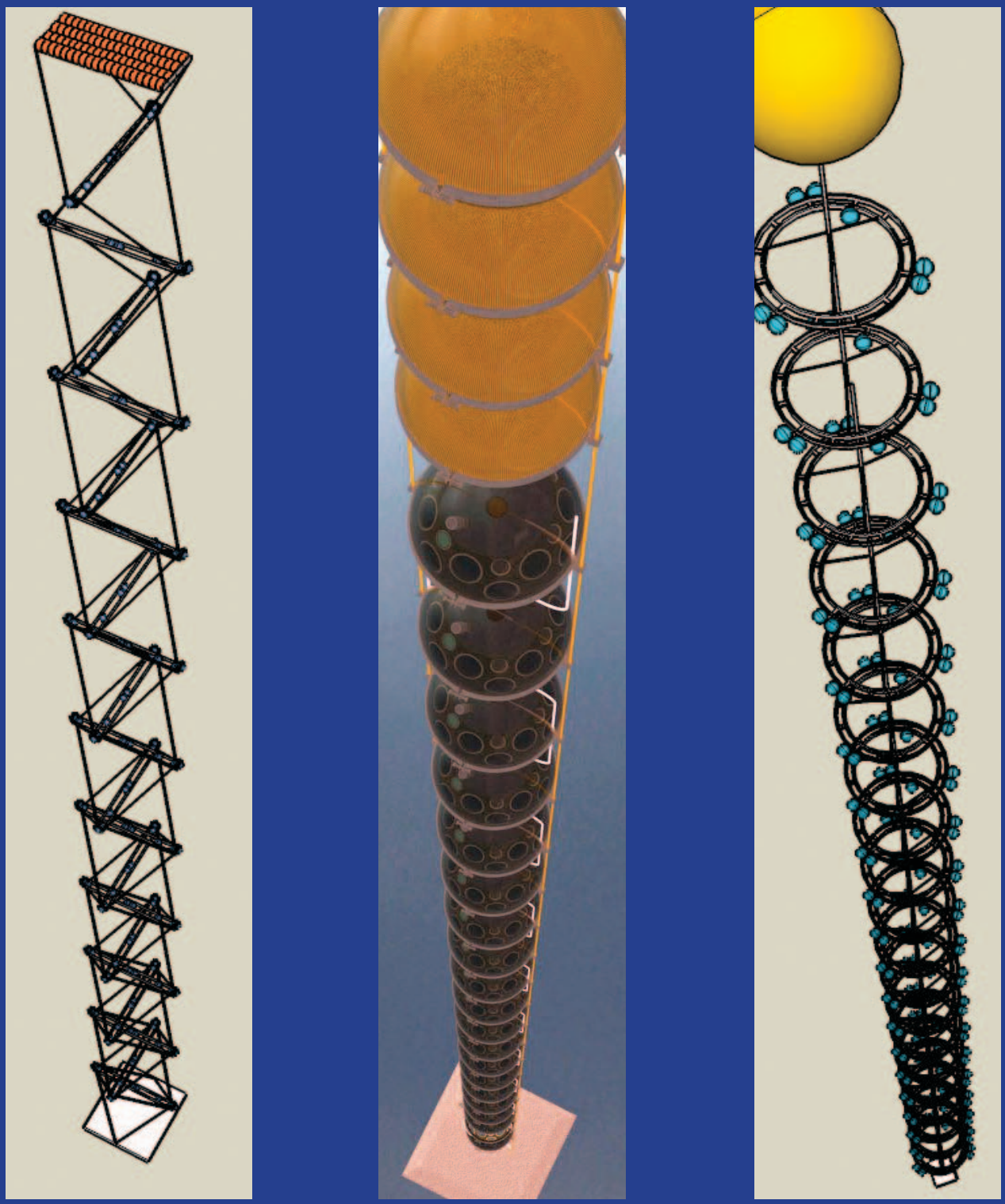

Figure 3-1: The three design options for the detection unit mechanical structures. The vertical separation of storeys is not to scale. The bar (a) has a horizontal extension of 6 m and incorporates 6 optical modules and an electronics container. The string (b) has a storey comprised of a single multi-PMT optical module. The triangle (c) has 6 optical modules arranged in pairs, placed at a distance of 1.1 m from the centre.

3.1 Optical Modules and Electronics Containers

Three types of optical modules will be presented in this section: spherical optical module with a large photomultiplier, capsule optical module with two large photomultipliers and multi-PMT spherical optical module, with 31 small photomultipliers.

3.1.1 Common features

The proposed optical module designs have several common features described below.

Optical Module Glass Vessel

The optical module glass vessel houses the photomultiplier and associated equipment, protecting them against the hydrostatic pressure and sea water. Commercially available transparent vessels considered are borosilicate glass spheres with diameters of 13 and 17 inches. They are delivered as two half spheres with a precisely ground interface that allows for a watertight joint between the two. There are two major producers of this kind of spheres, Nautilus GmbH, Germany and Teledyne Benthos, USA. Both companies have indicated that delivery at the rate of several thousand spheres per year is feasible.

Glass properties		
Refractive index	1.47	
Transmission	>95% (14 mm, λ>350 nm)	
Density at 20°C	2.23 g cm^{-3}	
Thermal conductivity	1.2 W $m^{-1}K^{-1}$	
Characteristics of spheres		
	13 inch	17 inch
Depth rating (m)	10000	6700
Overall diameter (mm)	330	432
Wall thickness (mm)	11	14
Mass (kg)	7.89	17.2
Buoyancy (empty) (N)	114	260
Diameter shrinkage per 1000m depth (mm)	0.30	0.41

Table 3.1: Properties of the glass vessels used for the optical modules.

As each penetration through the glass increases the leak risk, the number as well as the diameter of such penetrations is minimized; in particular there will be no evacuation valve. Around any penetration the surface of the sphere has to be flattened in order to locate the unique O-ring.

The handling of the glass spheres must avoid mechanical stress which can, over the lifetime of the sphere, induce cracks leading to leaks. In Table 3.1 the properties of the optical module vessels are summarised.

The water and air tightness at the level of the junction between the two halves is ensured by the aforementioned precision grinding and in addition by putty and tape on the outside of the joint.

The two halves are kept together by establishing a partial vacuum inside the sphere. A passive pressure sensor inside the vessel allows for leak diagnostics.

Experience of using these spheres with ANTARES shows that they are reliable, as of the roughly 1000 spheres deployed less than 2.5% leaked. Studies are underway to further reduce this rate.

Electronics cooling

A passive cooling system will be used, when necessary, to keep the temperature of the electronic components low. This is important as each 8 to 10 degrees rise in temperature typically decreases the lifetime of electronic components by a factor of two.

The main cooling mechanism used is heat conduction, via an aluminium or copper structure, to the surrounding seawater at 14 °C. The face of the metal structure is shaped such as to have a large surface in close contact (through a gel) with the inner surface of the glass container. This part and the gel must accommodate the shrinking of the glass vessel under pressure. Preliminary tests indicate that such a system can maintain temperatures below 30 °C for an overall power dissipation inside the glass vessel of up to 20 W.

High Voltage Base

The high voltage is generated from 3.3 V DC by a low power Cockcroft-Walton multiplier. The photomultiplier requires the most current at the last dynode, before the anode. This dynode is attached to the lowest stage of the CW chain, which can supply the highest current. The design of the supply has been optimized for low power consumption. A power dissipation of less than 4.5 mW has been achieved. Each photomultiplier will have its own base tuned to its own high voltage. Experience from the ANTARES experiment has shown that the gain of photomultipliers drifts with time. This effect could be attributed to ageing effects related to the integrated charge. In order to avoid such effects the high voltage bases are equipped with a preamplifier, allowing for photomultiplier operation at lower gain. This preamplifier consumes about 25 mW.

Optical Coupling

The photomultiplier will be glued in the sphere using a two-component transparent silicon rubber similar to the Silgel 612 from Wacker Chemie AG used in the ANTARES optical modules. The main requirements concern the refractive index (1.40) which has to be close to those of the glass envelope (1.47) and the window of the photomultiplier (1.51-1.54). The attenuation length is greater than 40 cm for wavelengths above 350 nm. In addition, this rubber is sufficiently elastic to absorb shocks and vibrations induced by transportation and deployment and to accommodate the shrinkage of the glass vessel under pressure.

3.1.2 Spherical OM with Large PMT

Large PMTs have been used in all existing neutrino telescopes, because they meet the main requirements:

- Large photocathode area
- Large angular coverage
- Good timing response.

Precursor experiments like DUMAND, BAIKAL and NESTOR used 15 inch PMTs housed in 17 inch glass spheres. The AMANDA experiment used 8 inch PMTs housed in 13 inch spheres, and the IceCube experiment houses 10 inch PMTs in 13 inch glass spheres.

Both the ANTARES and NEMO collaborations made the choice of 10 inch PMTs housed in 17 inch glass spheres. These solutions have proved to work. The natural conservative choice based on past experience is therefore to use optical modules of a similar design.

Considering present commercial availability and developments towards higher quantum efficiencies, a compact design incorporating an 8 inch photomultiplier in a 13 inch glass sphere has been selected (See Figure 3-2).

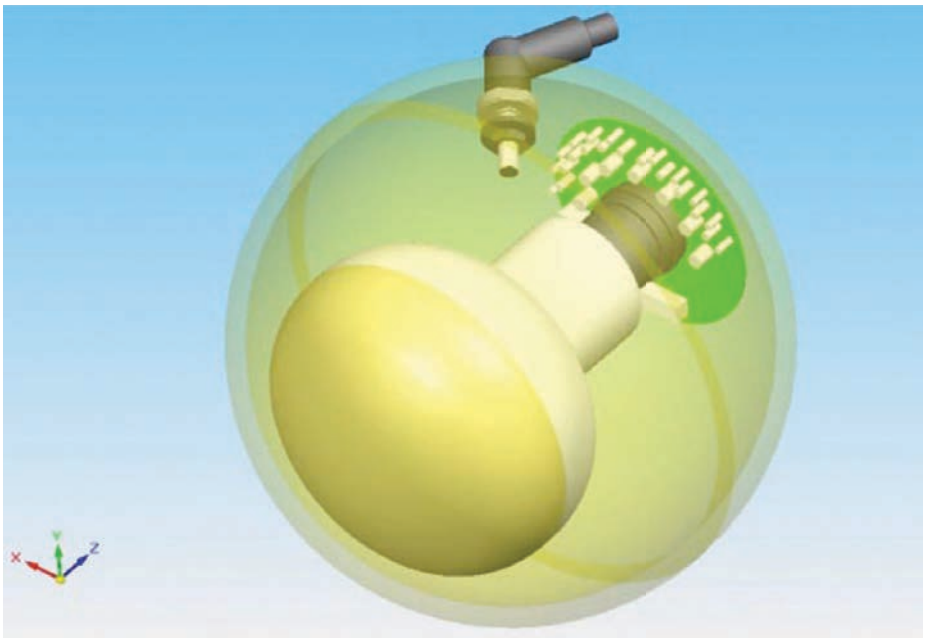

Figure 3-2: 8 inch PMT in a 13 inch sphere

Optical Module Components

The product breakdown of the large PMT optical module is given in Table 3.2. The PMT will be an 8 inch tube with the recently developed "Super Bialkali" photocathode giving improved peak quantum efficiency of about 30%, e.g. the Hamamatsu R5912 (see Figure 3-3) or the 9354 tube from ET Enterprises. The PMT gain will be below $1x10^7$ in order to limit ageing effects. The resulting single-photoelectron signal of 8 mV on 50 Ω will be amplified on the high voltage base.

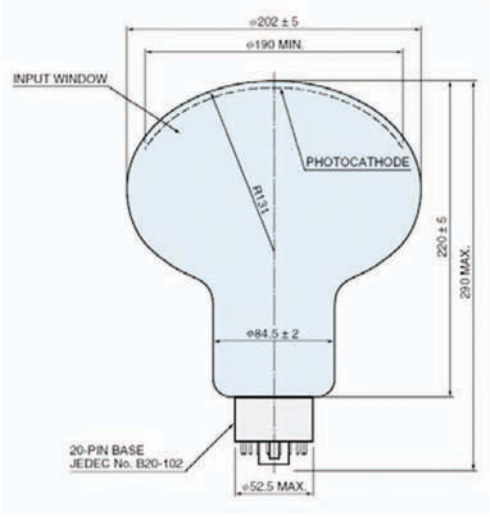

Figure 3-3: Dimensions of the 8 inch PMT in mm. Taken from http://www.hamamatsu.com.

Product breakdown for large PMT optical module		
Component	Description	Quantity
Glass sphere	Glass container to withstand the hydrostatic pressure. Made of two identical sealed halves. Diameter 13 inch.	1
Photomultiplier tube	A photo-electric sensor with high quantum efficiency. Size 8 inch.	1
High voltage base	Electronic circuit that provides high voltage to photomultiplier and amplifies the photomultiplier signal.	1
Outer connector	A penetrator through the glass with a cable and dry mateable connector at the far end.	1
Optical gel	The optical and mechanical interface between the PMT and the glass sphere.	
Pressure sensor	A pressure gauge mounted inside for test purposes.	1
Magneticshielding	A mu-metal cage, able to screen most of the Earth´s field, mounted around the PMT	1

Table 3.2: Product breakdown for large PMT optical module.

The Earth´s magnetic field is known to degrade the performance of large PMTs. First measurements with the 8 inch Hamamatsu without any screening resulted in an efficiency reduction up to 15%, depending on the orientation of the PMT in the ambient field. A magnetic shield made of thin mumetal wires will therefore encapsulate the PMT. The shadowing effect due to this cage is at the level of 3%.

A single 12 mm diameter hole is needed for a 4 contacts penetrator linking the OM to an electronics container at a distance of up to 4 m. Two conductors provide 3.3 V DC power and carry a control signal for the high voltage settings (e.g. RS232 protocol). The other conductors carry the amplified analogue PMT signals.

Electronics Container

In order to reduce the number of connections within a storey, a 13 inch glass sphere located in the central part of the storey, will contain all the required electronics and calibration devices (see Table 3.3).

The compass tiltmeter, optical nanobeacons and acoustic sensors will be implemented on a circular printed circuit board located at 45° of latitude on the glass sphere. Several parallel disks can be used, which will ease the routing on the printed circuit board for the FPGA, foreseen as the readout controller.

The spherical cap is in copper and covers latitudes from 45° to 90°. It is in contact with an aluminium disk collecting the power dissipated by the electronic board and the power system. The contact between the cap and the glass is made by a thermal conductive compound.
The cavity between copper and aluminium is used to accommodate the power system, in order to shield its electromagnetic emission.

The connections of the breakout unit and the electronic container as well as the ones between this container and the OMs are performed at integration time, before the deployment.

Product breakdown for the electronic container		
Component	Description	Quantity
Glass sphere	Glass container to withstand the hydrostatic pressure. Made of two identical sealed halves. Diameter 13 inch.	1
Power conversion board	Board providing internal DC low voltage using DC-DC converters	1
Front-end electronics board	Board containing 3 ASIC chips measuring time over threshold for several thresholds	6
Readout controller board	Board containing FPGA readout controller	1
OM connector	Electrical only, dry mateable connector or penetrator splitting for 3 OMs (e.g. SEACON MCBH-5/15-FS SPLIT)	2
Backbone connector	Dry mateable bulkhead connector (same as Multi-PMT design)	1
Instrument controller board	Board to control instrumentation and set voltages for high voltage base	1
Instruments	A3-axis compass, tiltmeter/accelerometer optical beacon	1 set
Cooling system	Copper cooling to transfer heat from electronics to outer surface	1
Pressure sensor	Passive pressure sensor for testing purposes	1

Table 3.3: Product breakdown for the electronic container

3.1.3 Capsule OM with two large PMTs

An ongoing development aims at integrating two 8 inch PMTs and their associated electronics into a single glass container. The objective is to reduce cost and improve reliability by reducing the number of penetrations.

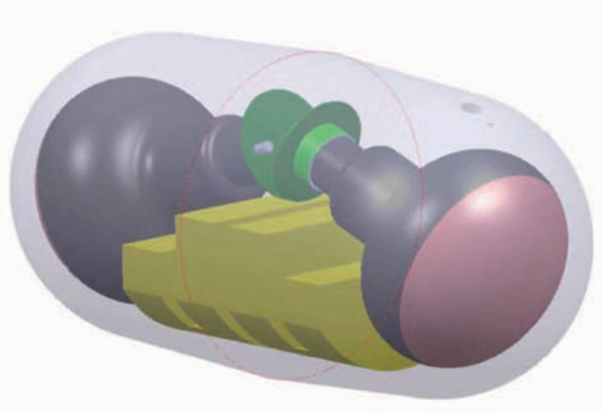

Figure 3-4: A 3D view of the capsule. The high-voltage bases are shown in green. The space for electronics is indicated in yellow.

The glass container (capsule) is made of two identical parts connected at their bases. Each half capsule has the shape of a cylinder of 11 inch diameter capped by a hemisphere. The layout of the capsule OM is shown in Figure 3-4. The PMTs are oriented at an angle of 30° with respect to the cylinder axis.

Each half-capsule contains the 8 inch photomultiplier in a magnetic shield and glued to the glass by optical gel. It also houses two electronics boards, one for the local power converter and the other for data acquisition and transmission. One of the two half-capsules will have the hole to receive a penetrator for the external connections. Finite element analysis shows that with a wall thickness of 16 mm no stresses exceed those observed in a normal 17 inch sphere. The electronics in the capsule will be cooled by heat conduction through an aluminium or copper structure glued to a large area of the glass cylinder by a thermally conductive paste.

3.1.4 MultiPMT OM

The multi-PMT optical module consists of 31 photomultipliers of 3 inch diameter housed in a 17 inch sphere. This approach gives several advantages which are summarized as follows:

- The total photocathode surface is 1260 cm^2, significantly exceeding that of three 8 inch photomultipliers.
- These photomultipliers are insensitive to the Earth's magnetic field and do not require mu-metal shielding.
- The segmentation of the detection area in the OM will aid in distinguishing single-photon from multi-photon hits. With the multi-PMT OM two-photon hits can be unambiguously recognized if the two photons hit separate tubes, which occurs in 85% of cases for photons arriving from the same direction.
- The loss of a single photomultiplier will degrade the performance of the OM minimally. Failure rates of small photomultipliers have been determined to be of the order of 10^{-4} per year.
- The photomultipliers run at a gain of 10^6 and their individual photocathode area is small, therefore the integrated anode charge is small.

The product breakdown of the Multi-PMT optical module is given in Table 3.4.

Product breakdown for the Multi-PMT optical module		
Component	Description	Quantity
Glass sphere	Transparent glass sphere built to withstand the ambient hydrostatic pressure and contain the photomultiplier tubes, frontend and readout electronics. Made of two identical halves. Diameter 17 inch.	1
Photomultiplier tube	The photomultiplier is a photon sensor with single photon sensitivity. It views the ambient water through the glass of the Pressure sphere. Type 3 inch.	31
High voltage base	Electronic circuit attached to each photomultiplier that provides the necessary high voltage. It also provides an extra amplification of the photomultiplier signal.	31
Signal collection board	A printed circuit board that collects signals from the photomultipliers for transfer to the sphere logic board.	2
Storey logic board	A printed circuit board that contains the local frontend circuitry for the signal preparation and the electronic and photonic components for the data transfer to shore. Also control systemfor instrumentation and high voltages.	1
Converter board	A printed circuit board that houses all DC-voltage generation circuitry.	1
Heat conductor	A mushroom shaped aluminium structure that transfers the heat generated by the storey electronics via the glass sphere to the seawater.	1
Outer connector	A dry mateable bulkhead connector that penetrates the glass sphere and allows for two power conductors and one fibre to be connected to the high pressure oil filled storey cable.	1
Cooling system	Copper cooling to transfer heat from electronics to outer surface	1
Pressure sensor	Passive pressure sensor for testing purposes	1
Instruments	A 3-axis compass, tiltmeter/accelerometer optical beacon	1 set

Table 3.4: Product breakdown for the Multi-PMT optical module.

Photomultiplier choice

The photomultiplier chosen for the multi-PMT optical module has a tube diameter of 76 mm and a length of less than 122 mm. The photocathode has a concave shape in order to achieve appropriate timing resolution. The photomultiplier has a 10-stage dynode structure with a minimum gain of 10^6. The front face of the photomultiplier tube is convex with a radius matching the inner radius of the glass sphere. In Figure 3-5 the dimensions of the photomultiplier tube are shown.

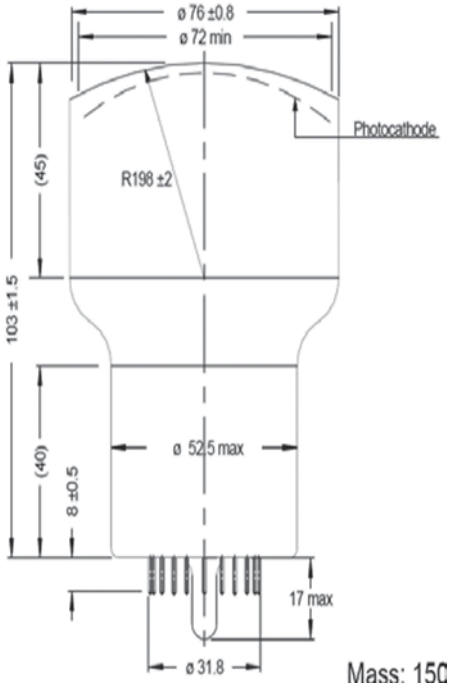

Figure 3-5: Dimensions of the PMT (in mm).

Testing has been performed on the Photonis XP53X2B tube. After the discontinuation of PMT production at Photonis, negotiations have started with both Hamamatsu and ET Enterprises in order to find a replacement tube. Hamamatsu now has available an appropriate model, R6233MOD. Table 3.5 presents the specifications for the PMT.

Similar negotiations are ongoing with ET Enterprises. They will also investigate the possible advantages of a Cesium-Rubidium photocathode that has a quantum efficiency superior to the the conventional Cesium-Potasium bialkali photocathode in the 450-500 nm range.

Both companies have indicated that a production rate of 50,000 photomultipliers per year is feasible.

Cathode	
Radiant blue sensitivity at 404 nm	>130 mA W^{-1}
QE at 404 nm	(CsK) > 32%
Inhomogenity of cathode response	< 10%
Supply voltage	< 1400 V
Gain	$5x10^6$
External electrostatic coating to the cathode	
Anode characteristics	
Dark count	< 3 kHz at 15 °C > 0.3 pe threshold
Transit time spread	< 2 ns (σ)
Peak to valley ratio	> 3
Environment	
Storage	0 – 60 °C
Operation	10 – 25 °C

Expansion Cone

The photomultiplier will be surrounded by an expansion cone. This cone provides a means of reflecting photons that would normally miss the photocathode, therefore effectively increasing its size. Recent measurements performed with a 5mm Perspex ring with a 45° aluminized bevelled edge indicate an increase of the effective photocathode radius by about 5 mm, see Figure 3-6. Ray tracing studies (see Figure 3-7) have shown that further improvement up to a 25% increase in the overall sensitivity is possible.

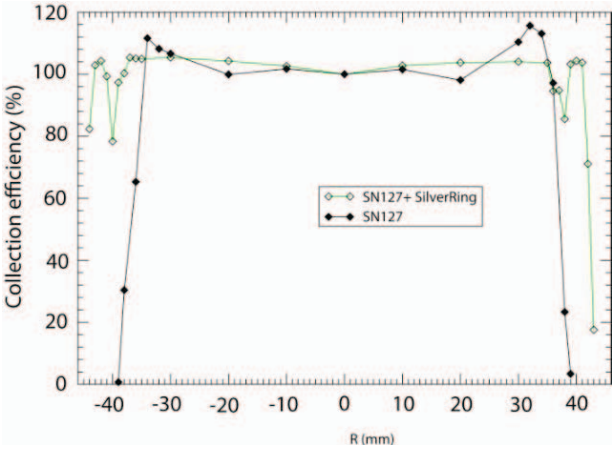

Figure 3-6: Collection efficiency with respect to centre with (green) and without (black) reflectivering.

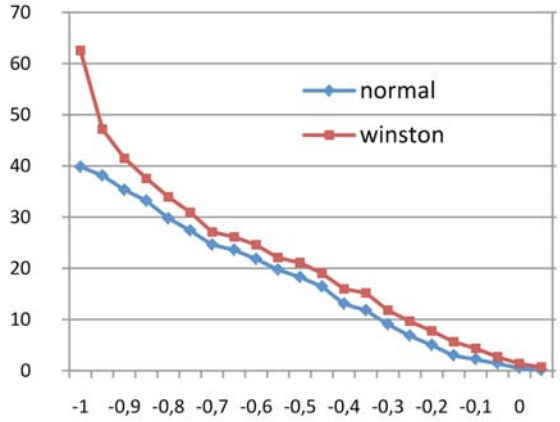

Figure 3-7: Effective photocathode area as a function of the cosine of the angle between incidence and photomultiplier axis.

Layout of photomultipliers

Figure 3-8 shows the geometrical layout of the photomultipliers in the optical module. Table 3.6 gives the directions in which the photomultipliers point. The centre of the front face of the photomultiplier is placed 4mm from the inner surface of the glass sphere.

The photomultipliers are supported by a foam structure. Optical gel fills the cavity between the foam support and the glass, in order to assure optical contact. The foam support and the gel are sufficiently flexible to allow for the deformation of the glass sphere under the hydrostatic pressure.

Layout of Electronics Boards

The geometrical layout of the electronics components and cooling system is shown in Figure 3-9. The optical module contains one board per hemisphere collecting the photomultiplier signals and transferring them to the storey logic board. The control of the high voltage also occurs via these collection boards. They are connected to the stem of the aluminium cooling unit (Figure 3-8). The orientation of the boards is vertical for ease of connection and to avoid blocking of the heat convection important for the cooling of the high voltage bases.

theta	phi					
50	30	90	150	210	270	330
65	0	60	120	180	240	300
115	30	90	150	210	270	330
130	0	60	120	180	240	300
147	30	90	150	210	270	330
180	0					

Table 3.6: Orientation of the photomultipliers within the optical module. The positive z-axis points upward.

The storey logic board is circular in shape and houses all frontend electronics and the electro-optical interface to the fibre optic readout. There is a possibility to extend the storey logic board with trapezium shaped auxiliary boards, for example for calibration components. Space has been reserved on the storey logic board for the communication components and fibre storage. It is mounted in close proximity to the cap of the cooling mushroom.

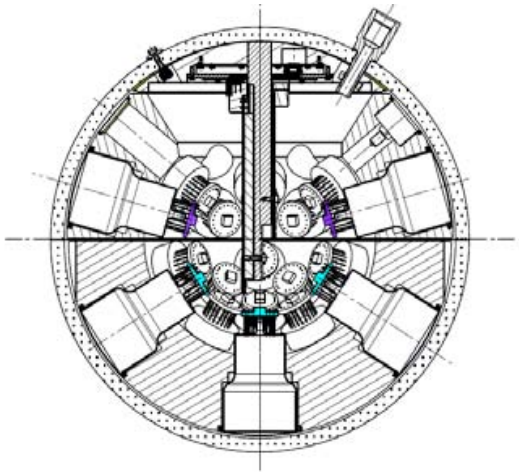

Figure 3-8: The multi-PMT Optical Module.

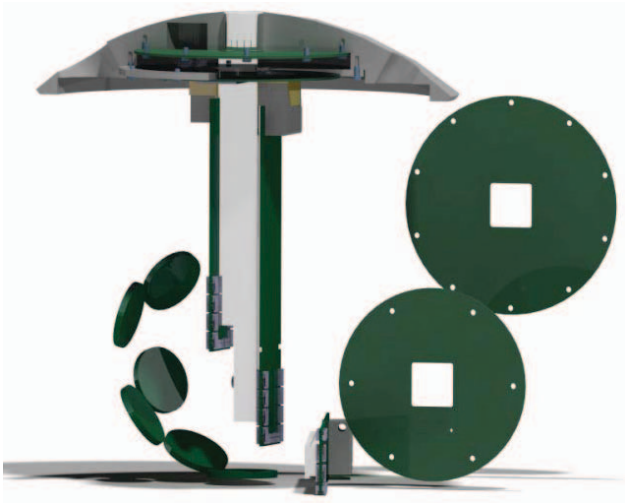

Figure 3-9: Layout of the electronic boards.

The voltage entering from the backbone cable is 10V and further conversion to the required voltages is performed on the converter board. Through the use of a resonant converter design with synchronous rectifying a high power conversion efficiency of >90% is achieved. This helps to keep the dissipation in the conversion circuitry low.

Layout of Calibration Devices

The multi-PMT optical module contains three calibration devices. These are:

• The nanobeacon incorporated on an extension board. A multimode fibre runs from the LED

Layout of Calibration Devices

The multi-PMT optical module contains three calibration devices. These are:

- The nanobeacon incorporated on an extension board. A multimode fibre runs from the LED to the glass and is oriented so as to illuminate the optical module vertically above;
- The compass-tiltmeter incorporated on the storey logic board;
- The acoustic piezo sensor glued to the inner surface of the glass sphere and its electronics incorporated on an extension board.

PMT HV	4.5×10^{-3} W	3.3 V
PMT detection	2.5×10^{-2} W	3.3 V
PMT signal rate	1.6×10^{-14} W	
PMT total power	0.030 W	3.3 V
31 PMTs	0.93 W	3.3 V
OM IC boards	0.40 W	3.3 V
OM sphere logic	3.2 W	0.9, 1.5, 3.3, 5 V
OM conversion	1.5 W	10 V_{in}
Acoustic sensor	0.2 W	5 V
LED beacon	0.2 W	5, 24 V
Compass	0.05 W	3.3 V
Total	6.48 W	

Table 3.7: Expected power dissipation and voltage levels.

Cooling System

Table 3.7 contains the expected power dissipation of the various components in the optical module. Figure 3-10 cooling indicates the positions inside the sphere where heat is generated.
The present estimate is a total power dissipation of 6.5 W inside the sphere. The cooling has therefore been designed to deal with a heat load of 10 W.

The cooling system consisting of a mushroom-shaped aluminium heat conductor transports the heat from the interior of the sphere via the glass to the surrounding seawater. The type of aluminium chosen for its high heat transfer coefficient of 200-220 W/m/K is AlMgSiO7(EN AW-6005 or 6060).

The aluminium conductor makes contact and is held to the glass sphere with gel. The planes of aluminium have a so-called Manhattan profile, following the contours of the components on the printed circuit boards to achieve the maximum heat transfer. The heat produced by the high voltage bases is transferred to the cooler by convection through the space in the centre. The dissipation of the base is kept as low as possible, as the convection is less efficient and is hampered by the presence of many cables in the convection space. Tests have shown that with this cooling system the maximum temperature difference with respect to the sea water is 14 $^{\circ}$C at a dissipation of 10 W.

OM Entry and Exit Cabling

Power will be provided by two copper conductors, and all data transmission and slow control communication requires a single optical fibre. The storey cable between the break-out in the backbone cable and the optical module consists of a 13 mm (0.5 inch) polyethylene oil-filled hose with a length between 50 and 100 cm. At the glass sphere there will be a dry-mateable bulkhead connector with a titanium shell. An appropriate connector has been designed by SEACON® which is a modification of one of their mini-series connectors. It requires a 13 mm diameter hole through the glass sphere.

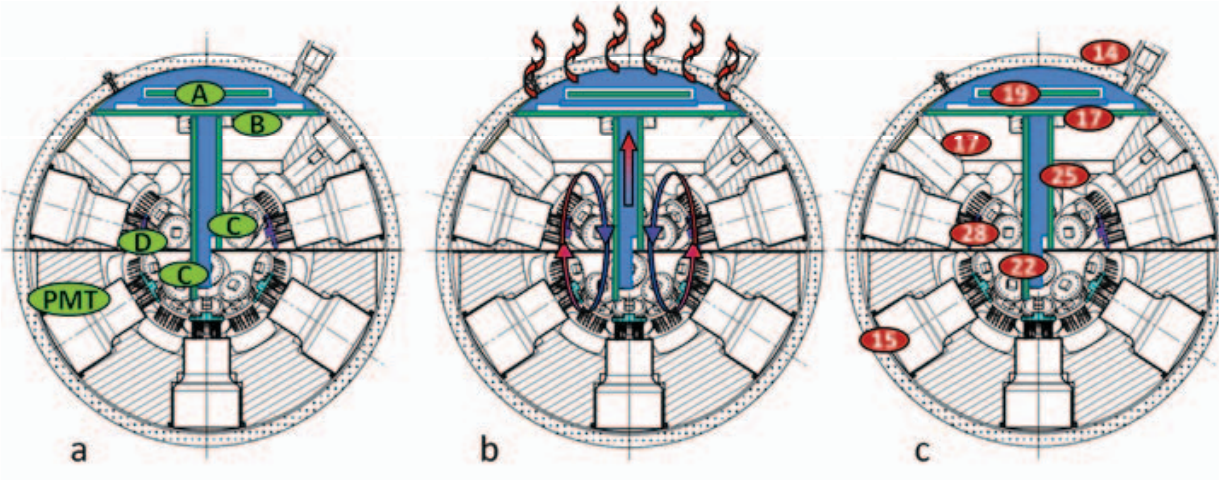

Figure 3-10: Cooling system. a) Boards dissipating energy. A: conversion board, B: storey electronics, C: Octopus, D: PMT base. b) Heat transfer mechanisms. Convection between PMT base and cooler, all other transfer by conducting. c) Temperature calculations and measurements show moderate values.

3.2 Data Readout and Transmission

This section discusses concepts in acquisition, processing, distribution and storage of data from the KM3NeT deep-sea infrastructure. The main purpose of the readout system is the conversion of the analogue outputs of the PMTs into formatted data for offline analysis. The deep sea infrastructure will also contain a large number of instruments for various scientific research activities. The operation of these instruments will be incorporated in the general readout system of the infrastructure.
The preferred solution for the readout system is one where all (digitised) data are sent to shore, to be processed in real-time.

For the envisaged photo-cathode area the total data rate amounts to about 0.2 Tb/s, assuming 64 bits per recorded photon. This data rate to shore can be accommodated on a number of optical fibres using dense wavelength division multiplexing (DWDM) techniques. The total data rate exceeds that of any data storage capacity by several orders of magnitude. Hence, the raw data have to be filtered. The rare neutrino (muon) signal can be discriminated from the random background utilising the time-position correlations produced by the traversing particle. The main challenge is the real-time filtering of the neutrino signal from the continuous random background. The data filtering has a significant impact on the performance of the neutrino telescope.
To first approximation, a detectable muon signal is defined by a minimal number of time-position correlated PMT hits (a hit is defined as a signal above a certain threshold, typically 0.3 p.e.). This is referred to as a "trigger".

The trigger algorithm efficiency is typically defined with respect to the number of events that produce a minimum number of detected Cherenkov photons anywhere in the detector. The trigger should be optimised in terms of purity and efficiency. "Triggers" are assembled from groups of chronologically and spatially correlated PMT signals.

The time resolution of individual PMT hits is required to be of the order of 2ns (rms) while the positions of the PMTs are required to be known to a precision of around 40cm. The timing is usually done by means of a designated clock system. The required timing accuracy should be achieved throughout a very large volume. Since the detector is subject to varying sea currents, the positions of the PMTs must be monitored continuously. This will be done via an acoustic triangulation system (section Positioning).

The overall readout system includes the submarine infrastructure, a shore station and various computing centres around Europe, together with external systems such as the gamma ray coordination network (GCN). The architecture of the submarine infrastructure is mainly constrained by the seabed, the distance to the shore station and the depth of the site.

The optical power budget depends on the length of the main cable and the number of branches. A shortage of optical power can be compensated by telecom-standard optical amplifiers.

The shore station houses the main power supply, the data processing facility and a control room. The total data rate from the submarine infrastructure should be reduced by a factor 10,000 to less than 10 Mb/s, to be able to transfer the data to the various computing centres in real-time and to store on a permanent medium. Therefore, a high-bandwidth link of 1 Gb/s to the various European computing centres is required. This internet link allows for remote operation of the infrastructure.

3.2.1 Data encoding, frontend electronics

SCOTT (Sampler of Comparators Outputs with Time Tagging) is the dedicated application specific integrated circuit (ASIC), designed for processing the electrical signal from PMTs. It has been designed to address the use of classical and multi-PMT optical modules.

Requirements

The general requirements for the front end electronics are (taken from Table 4.1 of the Conceptual Design Report):

- Time resolution (for a single photon, including transition time spread of the PMT and electronics) < 2 ns (RMS).
- Charge dynamic range ≈ 100 p.e. within a time window of 25 ns.
- Two-hit time separation < 25 ns.
- Experience gained from the Antares experiment lead to the following additional constraints:
- Common data processing for single and multiple photon hits.
- Average input photons flux capability of 250 kHz without dead time.
- Power consumption < 500 mW.

In addition, the ASIC should accommodate both optical module concepts under study for the final detector. The readout of the ASIC is done with a system-on-chip which allows for a second level of data processing –such as digital packets compression– and provides the interface to the data transmission electronics.

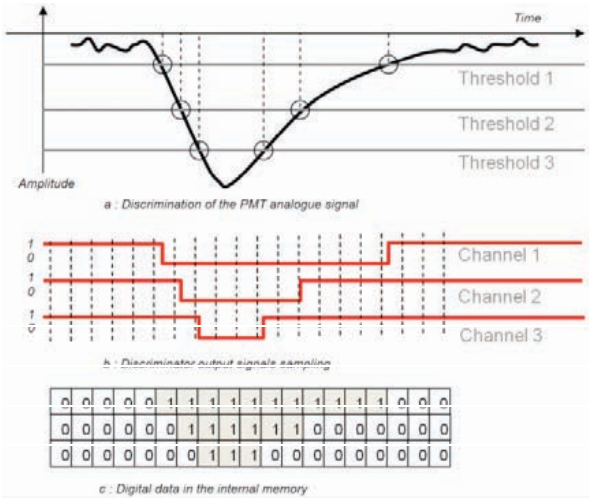

Figure 3-11: Example of signal reconstruction from crossing threshold points.

Electronic Front End principle

The front end electronics is based on the use of the time over threshold (TOT) as main signal processing[12,13]. The electrical signal from any PMT is compared with several thresholds (Figure 3-11). The answers of the comparisons are stored in memory with a fixed time interval between samples. The use of the amplitude information from thresholds and the time from sampled data allow for reconstruction of the original signal.

Architecture

The ASIC incorporates three main functionalities (Figure 3-12):

- The analogue processing is comprised of fast comparators and programmable digital to analogue converters (DAC) with 10 bit resolution.
- The digital sampling memory is composed of a delay-locked loop (DLL) to guarantee the accuracy of the sampling time, and two banks of memory.
- A first in first out (FIFO) digital memory is used to de-randomize the signal flux and to store data in a buffer for subsequent readout by the system-on-chip.
- Several other blocks are included to optimize the functionality of the ASIC such as a 16 bit counter to guarantee the synchronization with the data acquisition system, an internal "zero suppress" and a slow control driver for programming of registers.

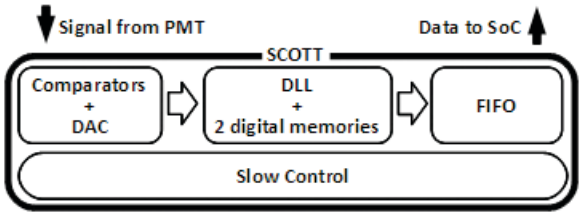

Figure 3-12: SCOTT data processing architecture.

Adapting to the two optical module concepts

The ASIC can process the analogue signal for a set of PMTs –with the required accuracy– independent of their size. In the case of a set of 3-inch PMTs, each channel of the ASIC is connected to a single PMT as illustrated in Figure 3-13, whereas in the case of a set of 8 inch PMTs, several channels are connected to the same PMT output in order to improve the charge reconstruction accuracy (Figure 3-14).

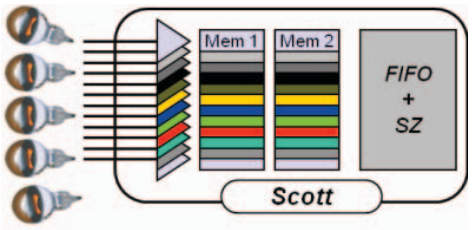

Figure 3-13: Schematic diagram of the SCOTT connected to several 3 inches PMTs.

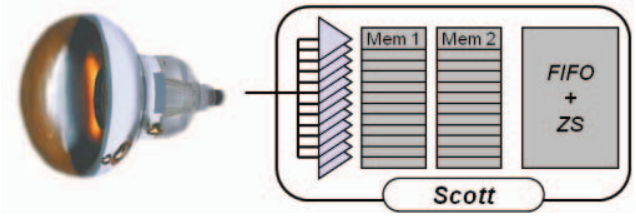

Figure 3-14: Schematic diagram of the SCOTT connected to a single 8 inches PMT.

The actual position of the ASIC within the system is dependent on the final optical module solution: in the case of the multi-PMT optical module, the ASIC should be placed as close as possible to the PMT outputs i.e. in the glass sphere containing the PMTs. For the optical modules with large PMTs, the ASIC is in a separate container connected to the optical modules with a cable a few metres long.

It should be noted that for a multi-PMT optical module, photon counting can also be achieved by simply counting the number of (simultaneous) hits on different PMTs. For small numbers of photons, this yields a 100% purity of the counting. For large numbers of photons, the length of the TOT signal can be used. This typically yields a logarithmic accuracy of the count. In this scenario, an early signal discrimination on a small ASIC chip on the base of each PMT could produce a TOT digital signal which is then time stamped on a SCOTT-like ASIC or directly within an FPGA.

SCOTT readout

The data in the SCOTT ASIC is read out by specific firmware before it is sent to shore. Although the output FIFO of the ASIC allows for some de-randomization, long data bursts of the order of several hundreds of milliseconds –typically due to bioluminescence– must be stored in local memory before being sent to shore.

3.2.2 Data transport

The detection unit consists of a number of storeys vertically distributed over a height of several hundreds of meters. The precise structure of the detection unit is explained in detail in section 3.3. Due to the distance from the shore, the data transmission relies on fibre optics.

The basic idea for detection unit data transmission is to have independent storeys which are connected to shore through a point-to-point link. To minimize the number of fibres per detection unit, the DWDM technique will be widely used throughout the optical network. This technology enables more channels to be transmitted on the same medium assigning each channel its own wavelength. Thus, each storey corresponds to a single "colour" and the colours from many storeys are multiplexed using passive optical devices. The use of passive devices increases the system reliability and decreases cost and power consumption.

The storey electronics can be viewed as a hub which gathers all the information produced at this level of the detection unit and transmits them to shore through the assigned DWDM channel; in the opposite direction, the information received from shore (mainly slow control commands) are used to manage the storey functions.

Since event reconstruction is based on the PMT hit time, a common timing reference must be available to front end boards, to allow for detector wide synchronization. The time offset between each acquisition channel and the fixed reference must be known in order to compare hit times. In order to facilitate the clock distribution a synchronous protocol will be used: the clock is embedded in the slow control data by an on-shore transmitter in a unique bit stream. The receiver, at the storey, is able to recover the clock and to extract the data. In this way, all the receivers will be synchronised by design to the on-shore time reference, which is derived from a GPS station.

The data flux is deeply asymmetric: very high from the apparatus to the shore and negligible in the opposite direction. PMT acquisition is the main contribution to the storey data rate , which accounts for a flux of the order of 200 Mb/s. In fact, the hydrophones needed by acoustic positioning, account for about 10 Mb/s and the remaining of instrumentation produces a few hundred of kb/s.

To manage the many peripheral interfaces on one side and the high speed data transmission on the other, the most suitable electronic device is an FPGA. The abundance of I/O channels and the availability of many I/O standards allows for easy interfacing with the various devices. The presence of on-board transceivers reduces cost, power and board integration time. The embedded processors available on-chip can be equipped with real-time operating systems in order to facilitate system development.
The most challenging aspect of the data transmission is the high speed interface: the preferred solution consists of exploiting the FPGA internal transceivers. The speed can be changed, even dynamically, from few hundreds of Mb/s up to tens of Gb/s. The electrical to optical conversion is implemented by a Reflective Electro Absorption Modulator (REAM). The key features of this component are the flexibility of the transmission speed, which can be selected from DC to 10 Gb/s, and the absence of an active transmitter which increases the overall reliability. Since the REAM is a sort of a mirror which can be turned on and off by an electrical modulating signal, it reflects the incoming wavelength: hence, just one wavelength per storey is needed for both directions. In contrast, common DWDM laser transmission requires one colour per direction.

The storey electronics receives a bit stream which carries both clock and data. The clock is used to maintain the synchronization of the storey electronics, while the data contain slow control information. The recovered clock is fed to the front end electronics which can stamp the PMT hit with the common reference. The high speed transmission is timed using this clock as well: the frequency for the required serializer can be synthesized by means of a PLL. The flexibility in speed selection provided by both the FPGA transceivers and the REAM aids system optimization. The maximum speed of the system is chosen as low as possible, compatible with the required data bandwidth, in order to reduce power consumption, increase optical power budget, decrease cost and ease printed circuit board (PCB) design.

The data in the detection unit backbone are transported via a single cable which contains one optical fibre for each storey. The number of fibres can be reduced by a factor of 2 when the (de-)multiplexer is located approximately half way along the length of the detection unit. The power conductors reside inside the same cable. At each storey level a break out extracts the required fibre and power wires. The multiplexing and de-multiplexing of optical signals is made inside the master module of the detection unit. Further multiplexing of signals from different detection units is performed in the secondary junction boxes, as explained in section 3.4.

Data Transmission System

The readout system is based on point-to-point data transfer between the undersea optical modules and the on-shore data acquisition system using current telecom DWDM technology. This approach gives several advantages which can be summarized as follows:

- It provides a dedicated data-format-transparent wide-bandwidth (10 Gb/s) communications channel between each optical module (or each set of optical modules) and the shore.
- The point-to-point high bandwidth channels support real-time readout with high timing resolution (< 1 ns).
- The reliability of the opto-electronic conversion is high, since all of the communications lasers are located on the shore. The optical modules only contain very high reliability photo diodes and electro-absorption modulators. The failure rate of these transducers is of the order of 1 FIT (1 failure in 109 hours).
- The design employs current telecoms technology, supports a staged deployment, and allows future upgrades as new technology becomes available.
- The system supports the store and forward readout approach as described above. The same system also supports a real-time readout approach. With a data rate of 10 Gb/s per channel, it is possible to sample continuously 33 independent signal channels with a timing accuracy of 0.87 ns (=3 ns/√12). This fits well within the quoted specifications. The time stamping of these signals can then be performed on shore. This minimises the number of off-shore electronic components and improves reliability and reduces power consumption. This flexibility allows engineering tradeoffs to be made between the transmission bandwidth used and the amount of processing hardware and software required in the off-shore modules.

Dimensioning

The optical readout solution is based on a type of telecommunications DWDM-PON (dense wavelength division multiplexed-passive optical network) employing a combination of space, wavelength and time-division multiplexing. This type of network is very similar to those considered today for long-reach (100 km) telecommunications access networks. The readout system has been dimensioned to support up to 6400 storeys arranged with 20 storeys on each detection unit. The best DWDM-PON solution for this size network employs 80 wavelength channels on 80 fibres (space dimension), each wavelength carrying the time-multiplexed data from the PMTs in each node. The number of wavelengths was chosen to be 80 because this is a standard multiplex for DWDM systems and it allows the signals from 4 detection units to be combined onto one return fibre. The 20 wavelengths for each detection unit are [de-]multiplexed in a central place approximately half way along its length, thus requiring 11 optical fibres in the vertical cable (11 bi-directional up; 9 bidirectional down; and 2 unidirectional to and from shore). A total of 80 readout fibres fit within a 96 fibre submarine cable with ample spare capacity. Four additional fibres are required for the downstream distribution of the DWDM optical carriers (seeds) and the clock and data signals employed for synchronisation and communications with the optical modules. The remaining fibres are for the use of the earth and sea sciences.

Readout System Description

In Figure 3-15, a simplified schematic of the DWDM-PON based readout architecture is shown. Light from a centralised array of 80 individual wavelength optical sources (seed light sources), located on the shore, is combined into a dense wavelength division multiplex with a channel spacing of 50 GHz (0.4 nm). The DWDM channel wavelengths are chosen to be consistent with international standards. The DWDM is copied to two booster amplifiers and transmitted over a main and standby path to the undersea station. On arrival at the undersea station the main, or the standby, copy of the DWDM is amplified and copied to

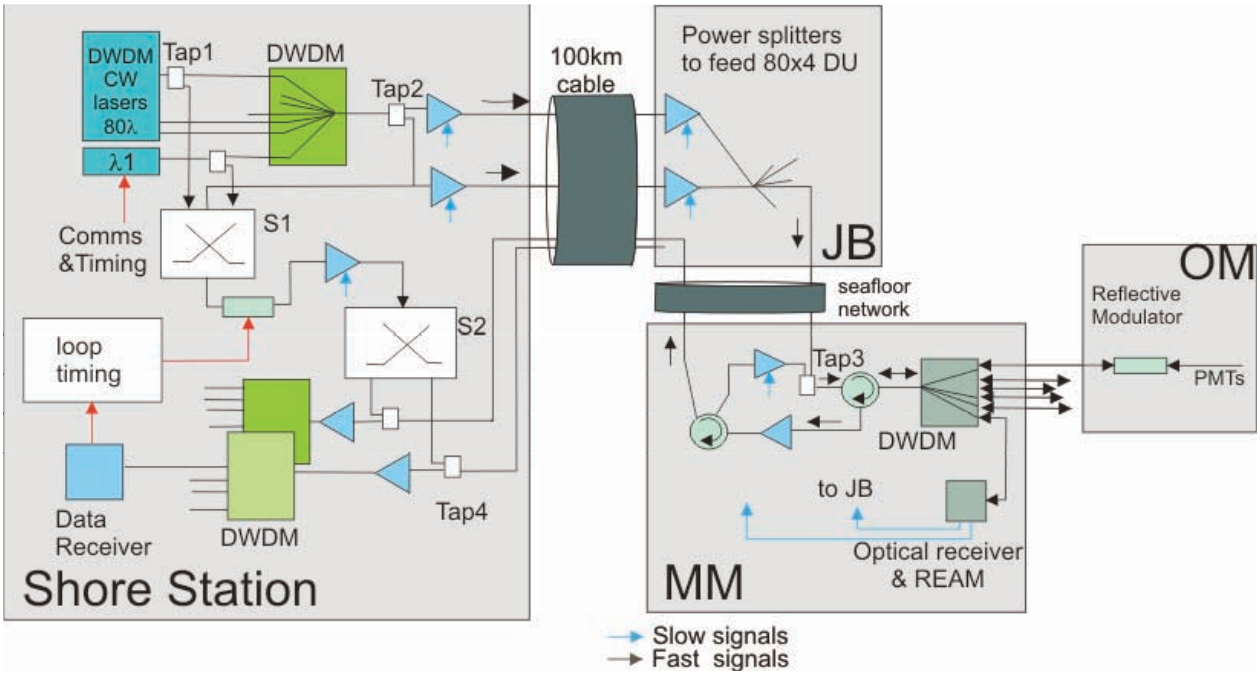

Figure 3-15: Schematic view of the opto-electronic readout architecture.

each of the 80 groups of 4 detection units. (Details of various amplification options are given later.) Each detection unit of 20 storeys contains one master module located approximately half way along its length. The master module contains a 20-channel DWDM AWG (arrayed waveguide grating) filter in order to route one wavelength channel to each of the storeys. The connections between the storeys and the master module are all single fibre. This minimises the weight and the cross-sectional area of the vertical cable, thus reducing drag. The maximum length of single fibre between the master module and storeys is less than 500 m. Over this distance, the impairments caused by coherent Rayleigh backscatter noise are negligible (< 1 dB). (The maximum distance for single fibre bi-directional operation between the reflection modulator and the DWDM filter is 2 km.) The master module also houses other passive optical components for use in clock and data distribution.

Figure 3-15 shows how one or a group of wavelengths can be selected from the shore-station DWDM array by switch S1 for use in loop timing or calibration measurements. The selected wavelength(s) are modulated (e.g., gated on / off for pulse-echo measurements) and transmitted over selected return fibres via switch S2. The resulting echo signals are detected and the propagation delay between the storeys and the shore can be calculated.

The signals from the frontend electronics are used to reflection modulate the seed light by means of REAMs. The reflection modulated signals are then re-multiplexed into a 20-channel DWDM by the AWG in the master module.
The 20-channel DWDMs on the return fibres from four detection units are combined with a 4-band coarse wavelength division multiplexer to create an 80-channel DWDM before being amplified for transmission back to shore. On shore, the 80-channel DWDM is amplified and de-multiplexed by an 80-channel AWG and fed to a photo-receiver array. One 10 Gb/s photo-receiver is associated with each storey.

Timing Calibration

Timing calibration is a critical requirement for a real-time readout system. The propagation delay from each storey to the shore will be different due to their unique distances from the shore and due to the fibre's wavelength specific group delay. This application will employ a low, non-zero, dispersion shifted fibre such as Corning Vascade® LEAF®. This type of submarine fibre has been specially de signed for use in long-haul transmission of DWDM signals. The 4 ps/nm/km dispersion leads to timing skew over 100 km due to wavelength of about 14 ns for an 80-channel multiplex with 50 GHz channel spacing. This timing skew is deterministic at a fixed temperature. Based on published figures, the bulk delay variation with temperature over 100 km is just under 10 ns per degree Centigrade. This affects all wavelengths equally. The timing skew variation due to temperature for LEAF® is not specified by the supplier, however, it is expected to be similar to standard fibre which implies a channel to channel variation of less than 10 ps per degree Celsius over 100 km for the 50 GHz spacing. These results show that the relative timings for all optical modules should remain almost constant for the temperature changes expected in this application and that we could track the absolute delay of all optical modules by monitoring the round trip delay of just one or two of them.

The fibre propagation delay is measured from the shore using an optical 'pulse echo' (or pseudo random binary sequence) technique. Since all optical and time multiplexing delays are deterministic (and may be tracked) the whole system could work synchronously which avoids the need for a master clock at the undersea station. Nevertheless, for added robustness, the proposed scheme will employ asynchronous readout. One or more wavelengths in the DWDM may be used for loop-timing purposes and for communications with the undersea station. Figure 3-16 summarises the delay calibration arrangement. (Note that the detection unit is drawn horizontally.)

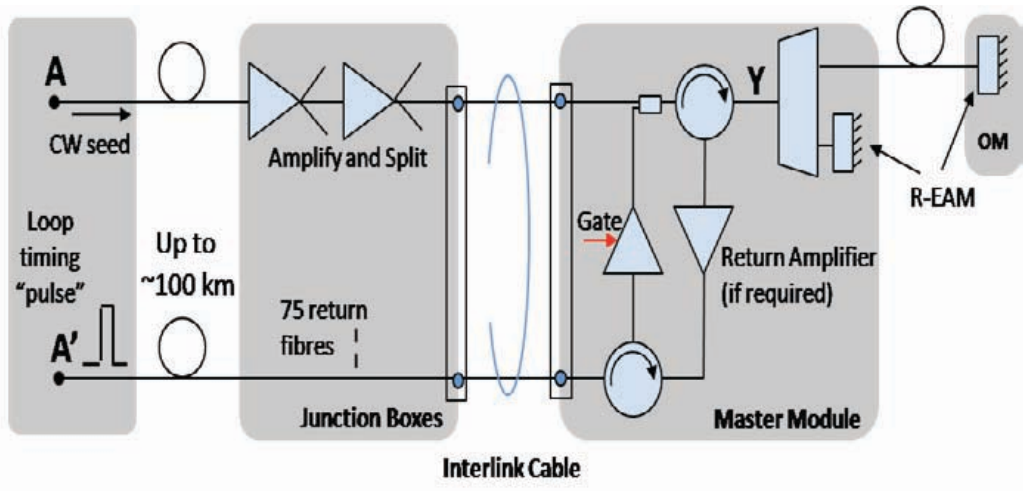

Figure 3-16: Schematic view of the delay calibration.

The optical path between points X and Y is either matched in terms of delay, or pre-measured before installation, so that the return delay from each optical module can be accurately determined. The propagation delay for each of the optical modules associated with each return fibre is measured during the commissioning phase, and at later dates if deemed necessary. These measurements are performed on each optical module in turn or on all 80 optical modules at the same time. The latter option could speed up the calibration procedure since most measurements would only need to record relative delay. The gated amplifier between the two circulators is only active during the loop calibration procedure in order to avoid amplification of Rayleigh backscatter during normal data transmission back to shore.

The round trip propagation delay between ports A and A' is measured and continuously monitored during operation. This allows the forward propagation delay to be calculated. Thus, as the forward and return fibres are in the same cable, temperature effects can be tracked simply by monitoring the round trip delay.

Timing Calibration Procedure

In order to perform an optical 'pulse echo' delay calibration procedure on an operational telescope it will be necessary to disconnect the seed light to the optical modules being measured. This is to prevent interference between the readout and pulse echo signals. There are a number of ways of doing this. The approach shown in Figure 3-15, is to turn off selected downstream booster amplifiers in the undersea station. This will allow different sections of the telescope to be disconnected, in turn, from the seed light, for calibration. The number of storeys affected will depend on the amplifier and power splitter structure (in the range 10% to 25% of channels). The time required to perform a pulseecho calibration will depend on the procedure adopted and on how many optical modules are measured in parallel. The round trip propagation delay over 100 km of fibre is 1ms, so if the results of 1000 measurements are averaged, then the minimum calibration time would be 1 second, assuming all optical modules are measured at the same time. The maximum calibration time, if each storey is calibrated in turn, would be 1 hour 40 minutes. In practice, a modest parallel approach will be employed.

The frequency of timing calibration procedures will depend on environmental factors such as deep water temperature and pressure cycles which may be seasonal. The timing calibration procedure and frequency will be evaluated by tests in a representative deep water environment.

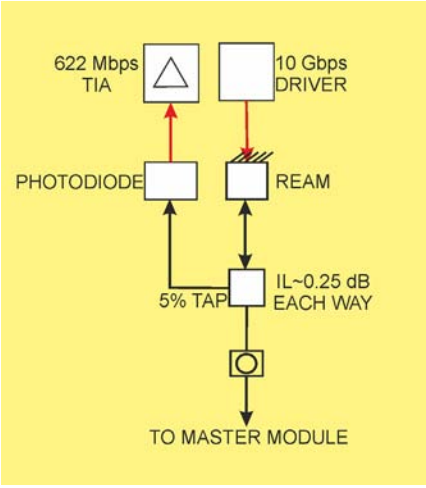

Figure 3-17: Optical module fibre interface.

Clock and Data Distribution

Figure 3-17 shows the additional passive components required inside each storey to support downstream clock and data distribution. It uses a passive power divider which allows the clock and data signals to share the same or similar wavelengths to the continuous wave seed. This approach relies on the ability of the optical receiver to discriminate between the seed and clock and data channels. The optical insertion loss has been specified to be 0.25 dB.
The downstream clock and data signals operate at the STM-4 standard line-rate of 622 Mb/s. This signal is routed by the power tap, to the detector photodiode which in turn is connected to a transimpedance amplifier (TIA).
The signal is broadcast to all storeys. The data capacity of a 622 Mb/s system is then approximately 500 channels at 1 Mb/s, or 6400 channels at 78 kb/s.

The passive power tap approach to distributing clock and data, shown in Figure 3-17, was originally devised for a dual-input AWG filter in the master module, however, such filters are not standard components off the shelf (see later section on DWDM filter technology). The power tap approach requires the photo-receiver to discriminate between the clock and data signal and the readout seed and timing calibrations signals. The readout seed signal is more easily dealt with as this is unmodulated, but in practice, it is unlikely that the receiver can be active during the timing calibration procedure.

Optical Amplification

Submarine quality 980 nm pumps are now available with power greater than 600 mW and failure rates of less than 25 FIT. A system with 16 pumps at 600 mW corresponds to 9.6 W of available power. The total required signal amplification power per bank of 20 fibres is 1.6 W. This will require approximately half of the available pump power. So, it is possible to run each pump at half power, to improve reliability still further. The complete down-stream booster amplifier array would require 64 pumps in total. The overall amplifier availability remains high if any single pump fails. The total electrical power required would be less than 100 W, assuming good heat-sinking to sea temperature.

DWDM Filter Technology

A key requirement is that the readout should use standard components off the shelf (COTS) wherever possible. This has a significant impact on the practicable choice of filter technology for the DWDMs. Standard telecommunications filters are available for optical channel spacing of typically 50 GHz, 100 GHz or 200 GHz and are usually limited to about 80-channels, although an 88-channel unit has recently appeared on the market. The narrower channel spacing filters (< 100 GHz) tend to use active temperature control (heaters) to lock them to the ITU grid, whilst the larger channel spacing filters are usually available in a-thermal packages. In principle, the 50 GHz 20-channel filters could be supplied in customised a-thermal packages, however, the near constant operating temperature of the master module means that temperature control may not be necessary. Based on the above assessment and an optical signal to noise ratio (OSNR) analysis, the DWDM filters employed in the master modules are based on 20- channel Gaussian AWGs. Custom a-thermal units are being investigated.

Parameter	value	notes
P AWG o/p	-10.5	Equivalent to continuous wave signal
Fibre losses	-0.5	
Connector losses	-1.0	
OM Tap	-13.5	5% tap + 0.5 dB
Pr clock/data	-25.5	dBm
Pr Cw	-25.5	dBm
Total P	-25.5	dBm
Ip	5.6	μA used to estimate MAX3658 added input referred noise
ER	3.0	linear -defined as P(1)/P(0)
Penalty	2.0	linear -defined as (ER+1)/(ER-1)
Penalty dB	3.0	dB
Added noise penalty	2.0	dB estimate based on graph of input referred noise MAX3658
Total penalty	5.0	dB
Net Rx sensitivity	-28.0	dBm based on MAX3658 (-33dBm)
Margin	2.5	dB

Table 3.8: Optical power budget for the passive power divider approach to clock and data distribution. This power budget is for a specific choice of splitting and without amplification (see text).

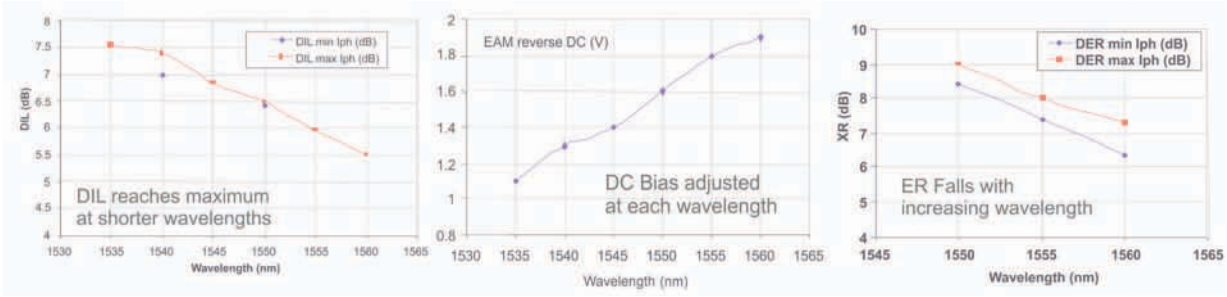

Figure 3-18: 10 Gb/s systems measurements over 80 km of standard fibre: Left, Dynamic Insertion Loss; Centre, Reverse bias; Right, Extinction Ratio.

REAM Selection

The measured system parameters of the REAM, optimised for operation at 1550 nm, are shown in Figure 3-18. The key parameters are the wavelength dependence of the REAM's dynamic insertion loss, on-off extinction ratio, and bias voltage. The curve on the left in Figure 3-18 shows the measured dynamic insertion loss as a function of wavelength. It decreases from a maximum of 7.5 dB at the short wavelength end of the spectrum to about 5.5 dB at the longest wavelength.

The optimum REAM bias voltage and data drive amplitude increases with wavelength, whilst the on-off extinction ratio falls with increasing wavelength (See also Figure 3-18).

An 80-channel 50 GHz DWDM requires a slightly larger wavelength range (1530 nm to 1565 nm). This extended wavelength range means that higher bias and drive voltages would be required in order to compensate for the standard devices lower extinction ratio at longer wavelengths.

The dynamic insertion loss has the greatest impact on system performance in the DWDM-PON architecture and should therefore be kept as low as possible. In order to reduce the dynamic insertion loss and the bias voltage range two versions of the REAM are employed: one optimised for short and the other optimised for long wavelengths. In addition to improving the optical system performance, colour banding will also simplify the REAM driver arrangements. At lower modulation bandwidths (up to 1 Gb/s) REAM colour banding may not be necessary. Optical Signal to Noise Ratio.

The OSNR calculations for the readout architectures shown in Figure 3-15 have been made. The noise figure for the optical amplifiers has been set to a conservative value of 6 dB and all of the loss values are assumed to be worst case values, so confidence in the real system attaining the calculated performance is very high.

The output OSNR is found to be just over 21 dB. An OSNR of 16 dB provides a theoretical bit error rate performance of 10^{-9}. There is thus ample margin for the low level of transmission impairments (< 2 dB) expected in this system. Raman fibre amplification is precluded at distances greater than 20km. The OSNR calculations for the pulse-echo ranging system yield similar results Optical Power Budget.

The optical power budget calculations are summarised in Table 3.8.

A commercial trans-impedance receiver, the Maxim MAX3658, is used as it has been designed for poor extinction ratio signals that introduce a power penalty. In this case the power penalty is < 5 dB, giving a worst-case operating margin of 2.4 dB.

This is based on the current design of the network, using a 5% power tap in the OM and the specifications of the MAX 3658 Trans Impedance Amplifier. Options to increase this optical margin are:

- Optimization of the extinction ratio, e.g. by using another ratio between CW and Clock/Data signal
- The use of a power splitter with e.g. 10% split ratio (this increases the optical power on the PIN detector in the OM but preserves the extinction ratio)
- Addition of optical amplification in specific sections of the architecture.

Technical aspects of these options will be studied during the detailed design activities for the KM3NeT architecture and final calculations of the optical parameters.

Backup System for Data Transmission

The architecture of the backup detection unit backbone consists of a "daisy chain" unidirectional optical path, as shown in Figure 3-19. Control information arrives from shore to the detection unit on a fibre going directly to the highest node of the chain. The serial stream is transmitted with a synchronous protocol that embeds clock, slow control and data. Each node extracts the clock from the stream and regenerates it locally in order to minimize the timing jitter. Each node of the chain handles the data-load of all the connected nodes. It receives the stream from the previous node extracts its own data and transmit all data including its own to the next one.

Since each node communicates only with adjacent nodes, the backbone can be implemented with single tracts of fibre driven with "Black and White" (B&W) transceivers, which are lower cost items than DWDM lasers. The distance between storeys is 40 m and signals are regenerated at each storey, therefore the optical power budget is not an issue, allowing for the use of cheap and standard connectors and cables.

A potential drawback is that, if a single node fails in the chain, the data transmission is interrupted causing the loss of the whole detection unit. In order to overcome this single-point-failure an optical switch is used to bypass the faulty node. This mechanism is such that even in the case of failure of all but one node, this node is still able to communicate with the secondary junction box. The switches are activated through a slow control system that transmits via the power line. The possibility of bypassing many consecutive faulty nodes with semi-passive optical devices is important in terms of reliability.

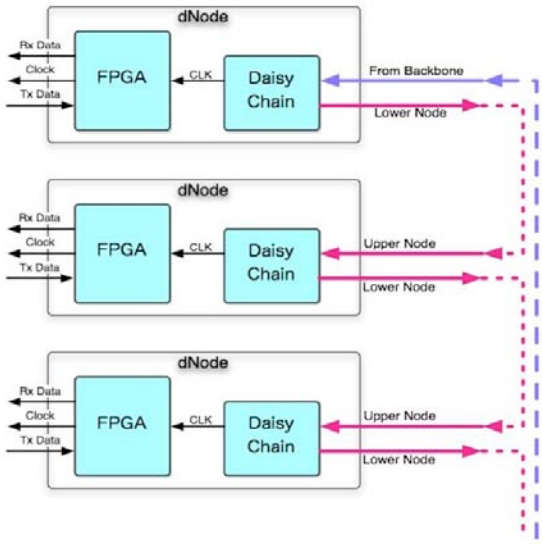

Figure 3-19: Schematic view of the optical daisy chain architecture.

In order to further increase the backbone reliability and the overall data bandwidth, the detection unit is served by two separated backbones, one for even and the other for odd storeys. The data rate of each single backbone is 2.5 Gb/s. With the total rate of 5 Gb/s the readout requirements of the detection unit are met. This architecture has as many data streams as backbones and each backbone can be assigned a colour for data transfer to shore.

3.2.3 Network Functionalities

The design of the on-shore DAQ system proposed here is independent of the actual implementation of the deep-sea readout system [14]. The design is guided by the following requirements:

- accommodate the bandwidths of any of the optical module designs;
- flexibility for implementation of any event selection algorithm;
- scalability with the use of off the shelf components.

Data Acquisition (Aggregation)

The data from each storey is routed on shore to its individual receiving port. Multiple receiving ports form the input to a concentrator, a unit that aggregates the data of a subset of the telescope in a single contiguous memory. This concentrator has several output ports. In addition to aggregation, a concentrator unit is able to perform data integrity checks and decodes and formats the data. As the data in the concentrator corresponds to a small part of the detector a filtering process can run at this stage providing a first level of data reduction. The number of storeys a concentrator unit can handle is determined foremost by the number of receiving ports, which in turn is matched to the size and speed of the internal memory, the processing power and the number and speed of its output ports. The concentration ratio, i.e. the ratio of the number of input to output ports, also depends on these factors, but will likely be in the order of 20 such that the data of all optical modules of an entire Detection Unit can be handled in one concentrator.

Data Routing (Coalescence)

The data are routed from the concentrators via the buffer system to the processing farm and from there to the data base and archiving systems. The routing takes place through a dedicated switch fabric. Data links from each concentrator are routed into the buffer system, available to any processing unit within the computing cluster. The total number of output ports on the concentrator units matches the total number of inputs to the buffer system. In case of mapping all optical modules per detection unit to a single concentrator, the number of links to the buffer system is of order $k \times N_{DU}$, where k is the number of output ports of a concentrator and N_{DU} is the number of detection units.

The buffer system acts as an intermediate stage prior to routing any data to the processing farm. The buffer system decouples the input data flow to the concentrators from any network congestion and latencies in the switch fabric. A processing unit can request data from the buffer system trough a separate dedicated switch fabric.

Data Processing (Event Building)

The data is gathered as a snapshot or timeslice. Each of these is processed in an individual processor within a large computer cluster. A snapshot covers a time span of 10-100 ms. A central control process allocates a time slice to a given processing unit. This unit in turn requests data from the buffer system and aggregates the data from the whole telescope for this time slice in its own memory. Thereby, a single processing unit acts on a snapshot of the whole telescope and is able to build events based on triggering and selection algorithms for the whole telescope. The algorithm used to process a time slice can be modified by receipt of an external alert from other earth- or space-based observatories.

Data Storage

The on-shore DAQ system has three types of storage.

- Transient storage that is inherent when buffering the data at various stages. This is performed during filtering, prior to routing the data and during processing.
- Temporary storage that is used locally to store in the shore station while it awaits transfer to final permanent storage facility.
- Permanent storage for data and data base storage.

(a) Transient Storage

Transient storage, associated with memory (RAM), occurs in the buffer system and in each of the processing units. The storage capacity envisaged for the buffer system will be large enough to accommodate the data from the whole telescope in several hundred time slices. Similarly the memory of each processing unit will be large enough to store the data for a few time slices. The storage system can also be dynamically configured to handle special operations such as calibration without stalling the data acquisition.

(b) Temporary Storage (Archival on site)

Storage on non volatile media, or the first archival of data happens at the shore station with subsequent transport of the data from the shore station to the permanent data storage facilities. Archiving of event data and the data base is part of the critical data path and the temporary storage system on-site is able to keep days worth of data before transfer to permanent storage is necessary.

(c) Permanent Storage (Final archiving)

The output from each processing unit is the raw data of a time slice that passed event selection criteria together with a set of event description data, called meta-data. The event meta-data for time slices which did not pass any selection may also be kept. For a fraction of these time slices the whole raw data may be archived to study biases and inefficiencies in the processing. The data base is also stored at the permanent data storage facilities. The database will be updated for each configuration change and after production of new calibration data.

We envisage the use of Grid concepts, as used by experiments at CERN, with a form of decentralisation for sharing computing resources in different tiers with Europe-wide (worldwide) distribution. All data from the shore station have to be copied to other remote facilities. A guiding principle is to ensure two copies of all data to be secure against accidental loss. A remote facility will provide permanent storage with access to primary processed versions of the data and the capability for reprocessing.

Control and Monitoring

Data taking will be managed by a single unit called the run control server unit. Monitoring the progress of data taking and processing, the state of the telescope (slow controls) and the state of each individual DAQ unit will be provided by a dedicated monitoring unit. Whereas only one run control instance will be in charge during data taking, the monitor unit will be able to serve multiple concurrent instances for collaborators to follow the telescopes operations.

3.2.4 DAQ Model

The DAQ model covers the distributed operation sequencing logic of the telescope's data acquisition. It is typically represented as a finite state machine, each state corresponding to a well-known, detector-wide situation in which the allocation of all resources (memory buffers, processes, network connections, etc.) is exactly determined; in this picture, the state transitions are associated with the set of operations that allocate or release these resources.

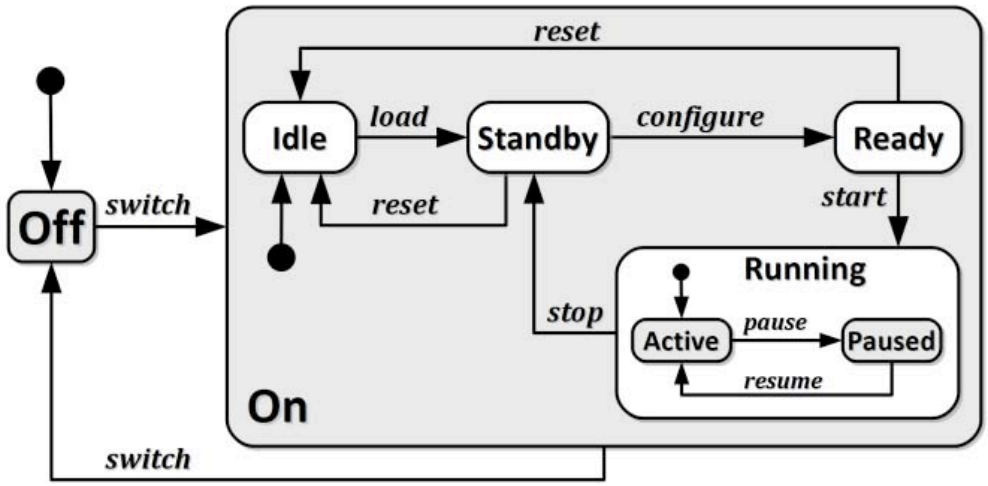

Figure 3-20: DAQ model hierarchical state machine.

The global system can be seen as a collection of hierarchically organized subsystems that are dynamically instantiated (or destroyed) during state transitions. Consequently, subsystems will behave only according to a subset of the global DAQ state machine, which calls for a hierarchical representation of the DAQ Model.
Typically, the operating sequence of the detector will include a configuration selection sequence, followed by the actual configuration of the distributed hardware and software modules, followed by the run start. This and the hierarchical organization of the subsystems yields a state machine shown in Figure 3-20.

The state machine transitions will be triggered by the specified events (switch, load, etc.) issued by the "run control" process. All control processes of the different detector modules will have to implement this state machine and respond to the events issued by the central run control.
This behaviour will be implemented through a "distributed state machine software framework" that will ensure state synchronization between the controllers of all detector modules and will be developed using a distributed, multi-language CORBA-like middleware such as ZeroC Ice with a hierarchical state machine specification framework such as CHSM.
In order to archive data efficiently, the run control programme will start a new data taking run regularly (typically every 2-5 hours).
The configuration and control of the telescope will be managed via a user interface that allows the user to specify hardware nodes, devices and registers using a static configuration. A central server allows for interfacing in several programming languages. Each component in the system can be controlled and configured using a graphical user interfaces (GUIs) that can be developed using highlevel programming languages. The configuration data are stored a priori in and retrieved from the central database.

3.2.5 DAQ software and firmware

The DAQ firmware includes all reprogrammable electronics implemented on FPGAs throughout the detector. The DAQ software includes all programs running on standard workstations (onshore) and embedded platforms (offshore), including microcontrollers. The DAQ firmware and software cover functions relating to detector and instrumentation control, configuration and readout, data transmission and routing, data filtering and storage, configuration management. Table 3.9 shows where firmware and software implementations are indispensable, possible (depending on technological choice) or not needed.

Implementation choice

A number of architectural and technological choices will have important consequences for the implementation in software and firmware. This choice depends on whether the readout and control and configuration intelligence is implemented entirely in firmware or with some additional software over a system-on-chip platform. A system-on-chip solution allows for a flexible offshore subsystem and eases the development process especially for the integration of modules developed by different laboratories.

Implemented functions	Offshore		Onshore	
	Firmware	Software	Firmware	Software
Control/configuration of frond end chips	●	●	×	●
Primary readout of front-end chips	●	×	×	×
Control/configuration of PMT and instrumentation	●	●	×	●
Primary readout of instrumentation	●	●	×	×
Data transmission (over network)	●	●	●	●
Data routing	●	●	●	●
Data filtering	×	●	×	●
Data storage	×	●	×	●
●=indispensable ● =possible ×=not needed				

Table 3.9: Firmware and software implementations of main DAQ functions.

Firmware or software data routing

The detector is partitioned into subsets representing logical units of data flow to be processed onshore by a corresponding data routing processor (e.g. one detector unit processed by one routing processor on shore). Each of these routing processors will handle multi-gigabits per second data flow to be routed through standard Ethernet switching to the filtering farm units. This high-performance processing can be implemented either in firmware of software. The software solution has the advantage of higher flexibility and easier development but its feasibility depends on the possibilities of multi-gigabits per second Ethernet I/O on standard workstations, either using specialized components of the shelf boards or multiple Gigabit Ethernet boards. A firmware implementation has the advantage of higher performance and can probably allow for more compact lower consumption electronics.

3.2.6 Persistency and database

Three types of data will have to be stored on persistent media:

- PMT acquisition data
- Control and configuration data
- Instrumentation acquisition data

Storing them in the form of flat files or through the use of a database server depends on the amount of data and the type of processing required. The persistency model must also take into account the detector production process, including production test bench data and integration processes taking place over multiple sites in parallel.

PMT acquisition data

This kind of data constitutes the main bulk of all the data produced by the experiment. It is organized in "runs", each run being associated with the run conditions in which the data have been acquired. Past experience has shown that such large amounts of data are handled with better performance over "flat" files, possibly using specialized high performance file I/O software frameworks such as ROOT I/O. For this kind of data, only the corresponding metadata should be stored in the experiment database, using potentially complex relations between the different elements of data description.

Control and configuration data

Configuration data is typically stored on a relational database because of the complex inter-data relationships. This kind of data describes the hardware setup and the values of all the parameters with which this setup has been configured before producing its acquisition data. The hardware setup can be the actual detector or any test bench or other hardware subsystem being integrated on a production site. The control and configuration data must be time tagged and associated with the corresponding acquisition data in a non modifiable way. At the same time, it has to be structured in a way that makes it intelligible to those who operate the detector and those who analyse data. It has to be accessible in parallel from multiple production and science analysis sites. These requirements lead to the persistency model described in Figure 3-21. A consequence of this model is that all access to the database goes through a "configuration server" taking charge of:

- Metadata management
- Configuration history
- Run conditions management
- Multiple programming languages access
- Caching
- Database access performance

Software activities during the design study have produced the CConfig framework which implements all these characteristics. Configurations are defined as sets of tree structures, automatically mapped over Oracle or MySQL database tables and automatically support configuration history. The configuration server API is accessible in C++, Java, Python, C#, Ruby, PHP and Objective-C.

Instrumentation acquisition data

The main example of this kind of data is acoustic positioning data. These data can represent an important amount of data and are therefore stored in flat files for raw data and database storage for metadata. The data from low data volume instruments are stored directly in the database.

In thiscase, it is preferable to go through the proxy server. They can even be stored as CConfig structures, in which case they can be handled directly by the "Configuration server."

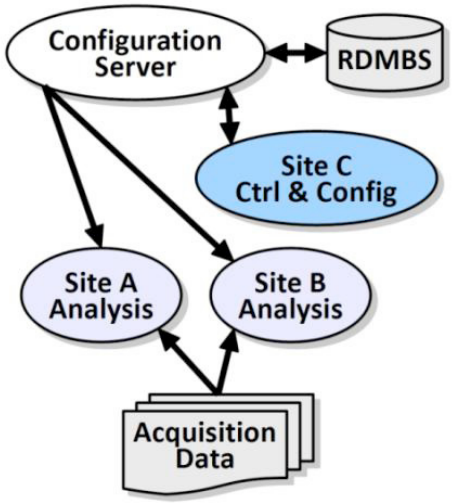

Figure 3-21: Persistency model.

3.3 Detection unit structure

As discussed in section 2.1 there are three options for the detection unit structure. All common considerations are presented first, followed by the specifics of the three options. The hydrodynamic behaviour of the detection units (including those of their anchors and dead-weights) are presented.

3.3.1 Common Issues

Many of the items in the subsystems are common to all design options.

Vertical Backbone

The link medium for bidirectional data transfer and power distribution is termed the Backbone. As discussed in Section 3.2, optical transfer of digital data will be used between the storeys and the shore station. The preferred solution is a point-to-point connection with a backup option based on a daisy chain connection scheme.

In the point-to-point data transmission scheme each storey is connected via a bidirectional mono-mode fibre to a DWDM multiplexer in a master unit, placed at the ninth storey (counting from the anchor) of the detection unit. The DWDM unit splits the 20 wavelengths of laser light, generated on shore and arriving via the input fibre, sending a unique wavelength to each storey. There the light is modulated by the digitized and serialized storey data and reflected back to the master module. Here the data from all storeys are combined onto a single output fibre. By placing the master module on the ninth storey, the lower half of the cable contains nine bidirectional fibres together with the input and output fibres, making a total of eleven.
The upper half contains eleven bidirectional fibres. One bidirectional fibre is branched out of the cable at each storey.

The cable also carries power, at 400 V, via copper conductors. The use of two conductors, each with a cross sectional area of 1 mm^2, leads to a voltage reduction at the top of the detection unit of around 3% assuming a power consumption of 15W per storey.

At each storey the power conductors are branched out. Only the input and output fibre and the power conductors are connected to the deep-sea network.

The key issue in the design of the backbone cable is the method for breaking out the fibre at each storey. This can be done by connecting sections of conventional deep-sea cable, with fibres protected in stainless steel tubes, to pressure resistant containers. Inside the containers one fibre is connected to a bulkhead dry-mateable connector whereas the through-going fibres are fusion-spliced to the fibres of the following cable section.

The cable can have an outer strength member if the particular detection unit design calls for this. This method was used successfully in the ANTARES experiment, where the electrical and optical backbone was combined with mechanical functions in a single inter-storey cable, deployed in more than 300 segments.

An alternative developed in cooperation with SEACON® is the use of a pressure-balanced oil- filled cable, in which the fibres and copper conductors operate under the ambient hydrostatic pressure. This system has two distinct advantages: the cable is made in one piece so that no fusion splicing is necessary and connector and breakout housings do not need to withstand the hydrostatic pressure. This can lead to a significant cost reduction and simplification of the breakout design.

In the case of the daisy-chain solution, two input fibres run to the top of the detection unit. One fibre enters and exits the even numbered storeys, the other the odd numbered storeys. At each storey the data is added to the data stream. The monochromatic signals are received and regenerated at each storey. In this scheme four fibres run along the length of the detection unit. At each storey two fibres are branched out and in. At each storey power conductors are also branched out. These cables can be produced in sections with dry-mateable connectors at each storey allowing for the breakout and power branching.

Pressure Balanced Oil Filled Backbone

Tests have been performed on a prototype oil-filled cable system. In order to keep the length manageable, 100 m of hose with three breakouts were produced. The hose was filled with Dow Corning DC200 oil which at 40 MPa has a density of 950 kg m-3. The hose contained four copper conductors (type 18 AWG with a cross sectional area of 0.82 mm2) and forty Corning Vascade® Leaf® fibres with a CPC8 coating. Stainless steel containers were used for the breakout units. To each of these an oil-filled breakout cable with two fibres and two copper conductors was connected, terminated by a SEACON® Mini-Con series connector. The backbone prototype cable had a 40-way fibre-optic connector at either end. By interconnecting the fibres a total fibre length of almost 4 km was produced. This system was pressure-tested at 60 MPa. No measureable deterioration of the attenuation in the fibres was observed. The copper conductors sustained a voltage 400 V with no measureable leakage.
After conclusion of the tests the design of a production cable has begun. A specialized company (Baas BV) has produced a first feasibility study. The main conclusions of this study were:

- A hose with inner diameter as small as 4 mm is possible for carrying 11 mono-mode fibres;
- The most suitable fibre is the DOW® carbon-polyamid-imid coated fibre for strength, hydrogen repulsion and size;
- The best hose material is Kynar®, as it is a plastic with superior resistance to seawater and has no plasticisers that can dissolve in the oil;
- The hose parts can be fused to form a single system.

Siemens has recently developed a transformer-oil (Midel 7131) that has excellent ecological characteristics and has a density very close to that of seawater (1001 kg m-3 at 40 MPa).

The present design consists of a 4 mm inner diameter and 6 mm outer diameter Kynar hose, containing 11 fibres. Spherical breakout units are fused to the hose and a SEACON® mini-con bulkhead connector (1 fibre, 2 conductors) is fused to each breakout unit (Figure 3-22). Two sections of 500 m are being prototyped.

A short inter connecting cable with at one end the mating SEACON® mini-con connector and at the other end a penetrator for use on a glass optical module or electronics container is being developed. Plans are to equip the penetrator with a DC/DC converter for converting the 400 V delivered via the backbone to 10 V. It will allow for galvanic separation of the optical modules or electronics containers, which will limit the damage, due to galvanic corrosion, in case of flooding of the modules.

Figure 3-22: Schematic of breakout.

The pressure will be equalised with a pressure compensator (Tecnadyne PC8X) located at the bottom of the detection unit, near the anchor. This will be fused to a container similar to the breakout unit that also has a fused connector connection to the interlink cable. The density of the oil is lower than that of seawater, which means that the full system including the connectors are at an overpressure of about 0.3 MPa at the top of the backbone.

The master module is a pressure resistant vessel containing circulators and a DWDM multiplexer as these components cannot sustain the hydrostatic pressure. This vessel will most likely be a glass sphere with holes for penetrators: one for the upper part of the backbone and one for the lower part.

If the prototyping is successful this backbone will be employed in the Bar and String detection unit designs. The cable design can readily be adapted for use in the daisy chain readout scheme. In case the prototyping shows that the cable design is unviable the traditional approach without strength member will be employed. As the triangle design relies on the strength properties of the backbone this design uses the more traditional cable design with an incorporated strength member.

Flotation Buoys

Even in the designs where most of the required buoyancy is provided by the OMs, a top buoy having a small intrinsic drag is added to help compensate buoyancy losses should any of the OMs become flooded. This also reduces the horizontal drift of the top of the detection unit in strong sea currents. An offset less than the horizontal spacing between detection units for a sea current velocity of 30 cm/s is considered safe (see Section 3.3.5). The top buoy will be composed of an ensemble of empty glass spheres, or of syntactic foam elements of varying shapes, qualified to the pressure at installation depth. The choice and segmentation of the top buoy will depend on the deployment and unfurling process adopted for the chosen design.

Sea-Floor Interlink cable

This EO cable connects the detection unit base to a primary or secondary junction box. All the designs propose, during deployment, to accommodate this cable wound on a reel fixed to the detection unit anchor. The free end of the cable terminates in a wet-mateable connector of a hybrid (electro-optical) type or in a pair of wet-mateable connectors, one electrical and the other optical. The unwinding of the reel and the connection to the junction box will be handled by a ROV.

The other end of the interlink cable is connected to the detection unit, through a penetrator, or if preferred, via a dry-mateable connector.

Deployment

The deployment of the detection units will need surface boats equipped with dynamic positioning capabilities and equipment including cranes, winches and cables. The number of detection units to be deployed in a relatively short time span requires this operation to be optimised in terms of cost, risk and duration. The use of compact detection units allows for transportation of many units on board a single deployment vessel. The detection units are deployed as a compact package. This concept method has advantages in terms of risk reduction for ship personnel and material during the deployment. It also improves tolerance to rough sea conditions.

The unfurling of the compact units is either autonomous, triggered acoustically any time after the deployment, or active using traction provided by a winch. An advantage of delayed unfurling is that it allows for connection of the detection units to the junction box and testing, while they are still compacted. In the event of malfunction recovery for repair is possible.

3.3.2 The *Bar* detection unit

The general description of this design has already been given in section 2. This section gives complementary details on this design option. The mechanical structure of the detection unit is a semi-rigid system composed of a sequence of horizontal elements (storeys) interlinked by a system of tensioning ropes arranged to force each storey to a position perpendicular to its vertical neighbours. The detection unit is anchored on the seabed. A buoy located on top of the structure provides the pull to keep the structure vertical and ensure its rigidity.

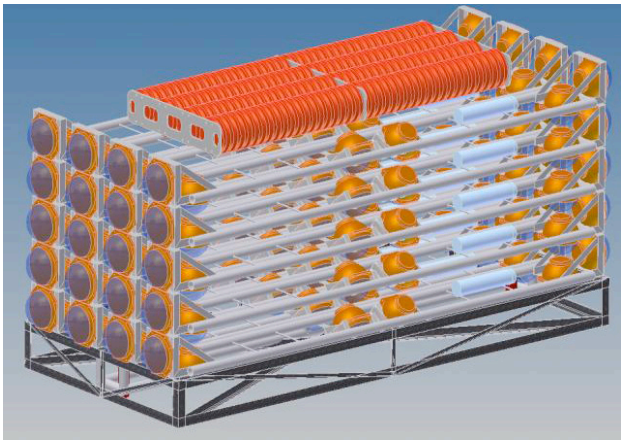

The storeys support the optical modules and the pressure vessels for the local storey electronics as well as the ancillary instrumentation needed (hydrophones for the acoustic positioning system, environmental probes, etc.).

Figure 3-23: The packed detection unit.

Product breakdown for the bar detection unit.		
Component	Description	Quantity
Anchor	Carbon steel structure to provide weight to keep detection unit on seafloor.	1
Detection unit base	Releasable metal structure forming connection between anchor and mechanical ropes.	1
Storey	Mechanical structure with optical modules and electronics container.	20
Mechanical ropes	Dyneema™ ropes, 4 mm diameter, running the full length of the detection unit. Supporting and orienting the storey. Length 900 m.	4
Backbone cable	Oil filled vertical cable providing power and fibre optic connectivity from detection unit base to the storeys. A dry mateable connector one fibre and two conductors at each storey.	1
Backbone master module	Pressure resistant vessel containing DWDM unit and optical circulator circuitry.	1
Floatation system	System of buoys at top of detection unit to keep it upright.	1
Interlink cable	Cable with two fibres and two copper conductors, dry mated to detection unit and with wet mateable connector at other end. Length as required by layout.	1

Product breakdown of storey.		
Component	Description	Quantity
Optical module	Described in Chapter 3.1.2	6
Electronics container	Described in Chapter 3.1.2	1
Storey structure	Aluminium structure 6 m x 0.4 m to support optical modules and electronics container.	1

Table 3.10: Product breakdown of Bar detection unit.

Anchor

A disposable anchor at the bottom of the structure provides the weight needed to anchor the detection unit on the seabed. This anchor is an anode-protected carbon steel trellis with length equal to that of the storeys (Figure 3-24).

During the integration, transport and deployment stages this structure also provides the support for the compact package of storeys.

The dimensions and characteristics of the detection unit anchor are given in Table 3.11.

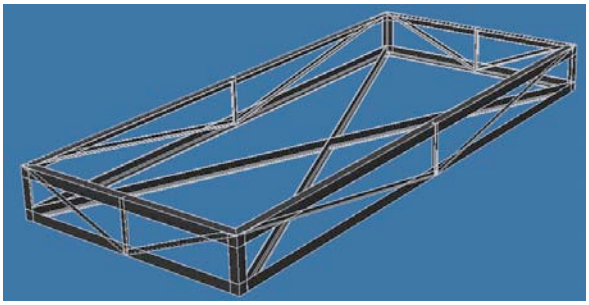

Figure 3-24: The detection unit anchor.

Anchor		**Base Unit**	
Length (m)	6	Length (m)	5.8
Width (m)	2.55	Width (m)	0.46
Height (m)	0.5	Height (m)	0.5
Mass (kg)	3000	Mass (kg)	65
Net buoyancy in water (N)	-25600	Net buoyancy in water (N)	-450
Storey		**Buoy**	
Length (m)	6	Length (m)	5
Width (m)	0.46	Width (m)	1.6
Height (m)	0.43	Height (m)	0.4
Mass mechanical structure (kg)	55	Mass (kg)	1500
Mass including OM and electronics container (kg)	115		
Net buoyancy in water (N)	300	Net buoyancy in water (N)	10000

Table 3.11: Bar detection unit characteristics.

Base Unit

The detection unit base (Figure 3-25) is a trellis structure built in series 5000 corrosion-resistant aluminium and attached to the anchor by means of an acoustic release system. It provides the link between the anchor and the vertical sequence of storeys.

The lower ends of the tensioning ropes linking the first detection unit storey are connected to this structure.

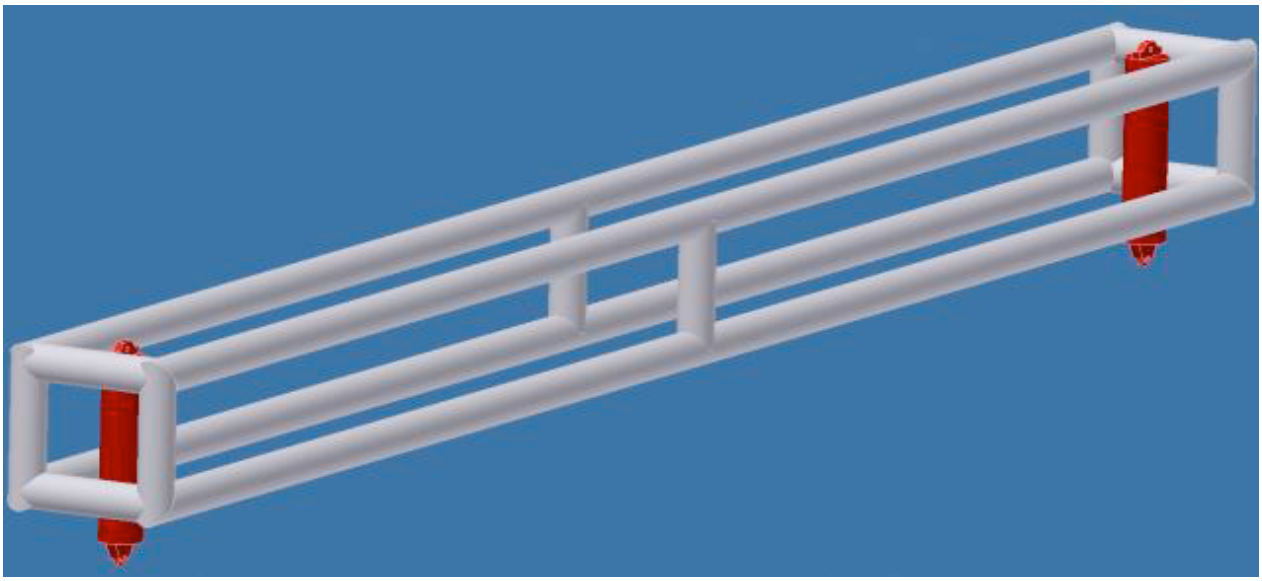

Figure 3-25: The detection unit base structure.

Storeys

The storeys (shown in Figure 3-26) are 6 m long mechanical bar structures in series 5000 Aluminium which support the OMs and the ancillary equipment.

The exact position and orientation of OMs on the storey will be defined following the results of simulations. The present hypothesis foresees three pairs of OMs, each housed in a 13 inch glass sphere. Two pairs are located at the ends of the bar, with one OM looking outwards and one looking downwards, while a third pair is located in centre of the storey, with the two OMs looking out perpendicular to the bar at 45° downward from the vertical.

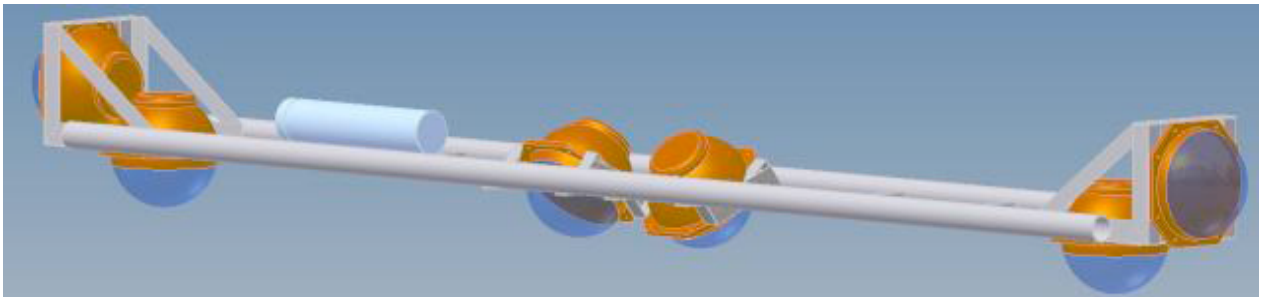

Figure 3-26: The storey for the Bar detection unit.

Dimensions and characteristics of the detection unit storey are given in Table 3.11. A sketch is presented in Figure 3-26.

The link between adjacent storeys is provided by means of a system of 4 mm Dyneema® ropes. These are fixed in pairs at each storey corner so that the set of two storeys and four ropes can assume a tetrahedral shape, as shown in Figure 3-27.

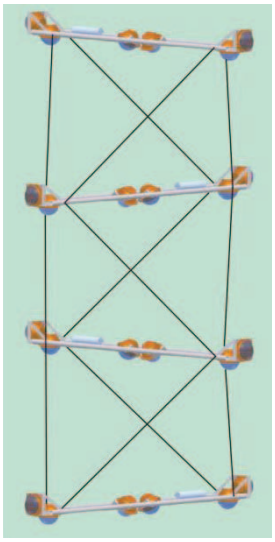

Figure 3-27: A few of storeys with interconnecting ropes for the Bar detection unit (vertical scale is reduced).

The configuration of the ropes forces the two storeys into a perpendicular orientation with respect to one another and gives structure rigidity against torsion.

Flotation Buoy

The flotation system is composed of a set of cylindrical syntactic foam floaters interconnected with aluminium plates in a rigid package.

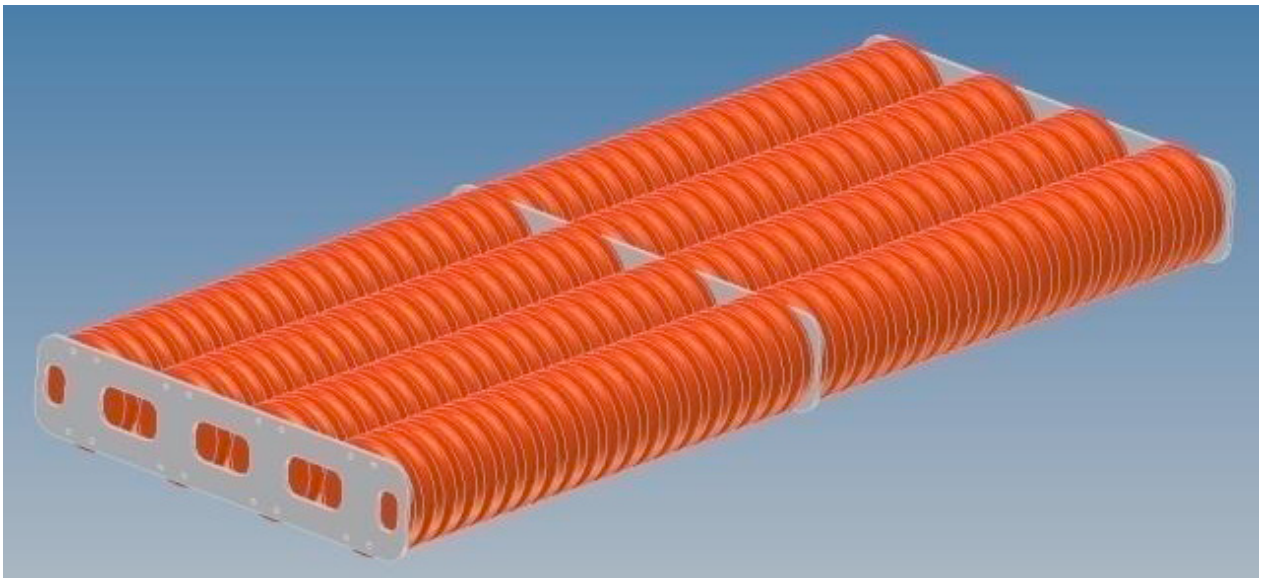

Figure 3-28: The flotation system for the Bar detection unit.

The flotation system is connected to the upper storey of the detection unit by ropes of the same type as those used for the inter-storey interconnection.
Dimensions and characteristics of the flotation system are given in Table 3.11

"Bar" design: Deployment

For deployment the detection unit is a compact package with the shape of a parallelepiped and size of 6 x 2.5 x 2.5 m. This package has to be deployed and positioned at depths beyond 2500 m.

The final working configuration will be reached, after deployment and connection of the structure, by remotely actuating an acoustic release system. The unfurling of the structure will be driven by the pull of the top buoy.

The operation sequence is the following:

- Lifting of the structure on the ship deck. This operation is performed using the ship's deck equipment.
- Immersion of the structure in the water. This operation is performed using the ship's deck equipment.
- Lowering of the structure close to the seabed. This operation requires a winch hosting a cable length sufficient for the site depth.
- Positioning of the structure on the seabed. The required accuracy (order of few metres) require the availability of an acoustic Long Base Line (LBL).
- Release of the structure. This operation will be performed by remotely actuating an acoustic release system placed at the end of the deployment cable.

Product breakdown for the bar detection unit.		
Component	Description	Quantity
Anchor	Concrete deadweight to keep detection unit on seafloor.	1
Storey	Mechanical structure with optical module.	1
Mechanical ropes	Dyneema™ ropes, 4 mm diameter, running the full length of the detection unit. Supporting and orienting the storey. Length 700 m.	2
Backbone cable	Oil filled vertical cable providing power and fibre optic connectivity from detection unit base to the storeys. A dry mateable connector for one fibre and two conductors at each storey.	1
Backbone master	Pressure resistant vessel containing DWDM unit and optical circulator circuitry.	1
Floatation system	System of buoys at top of detection unit to keep it upright.	1
Interlink cable	Cable with two fibres and two copper conductors, dry mated to detection unit and with hybrid wet-mateable connector at other end. Length as required by layout.	1

Product breakdown of storey.		
Component	Description	Quantity
Optical module	Described in Chapter 3.1.2	6
Electronics container	Described in Chapter 3.1.2	1
Storey structure	Aluminium structure 6 m x 0.4 m to support optical modules and electronics container.	1

Table 3.12: Product breakdown for the String detection unit.

3.3.3 The *String* detection unit

The general description of this design has already been given in section 2 and in Section 3.3.1. This section gives complementary details on this design.

The "string" detection unit is a lightweight structure of 20 storeys each comprising single OMs of the Multi-PMT type spaced vertically 30 m apart (see Figure 3-29). The structure is designed to have minimal hydrodynamic drag. The mechanical and electro-optical structures are separated, the former being provided by two ropes and the latter by a separate backbone cable. The detection unit is held on the seafloor with a deadweight connected to the ropes. The detection unit is held vertical mainly by the buoyancy of the OMs and in addition by extra buoyancy of the top buoy. Each OM is a self-contained unit whose failure does not influence the working of the remaining ones. OMs are connected to the vertical ropes at regular intervals via individual connection rings. The electro-optical backbone cable is an oil-filled equipressure cable that contains a fibre per OM together with two electrical conductors for the power distribution throughout the detection unit. The backbone has a branch out of an optical fibre and two electrical conductors at each OM. The connection from the base of the detection unit to the seafloor network passes via an electro-optic interlink cable terminating in a hybrid (EO) wet-mate connector for connection to the seafloor network. This interlink is an extension of the backbone cable containing two optical fibres and two electrical power conductors. The interface between the two unidirectional fibres to and from the seafloor network and the bidirectional fibres to each OM is placed within a "master module", a pressure vessel that contains the circulator and DWDM multiplexer (section 3.2.2)

The product breakdown for the detection unit is given in Table 3.12.

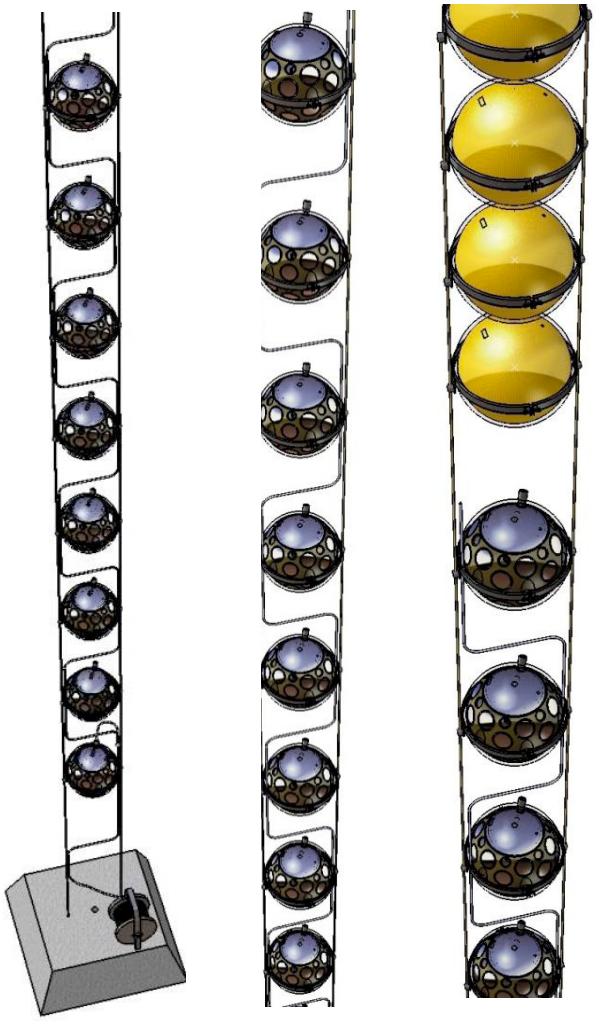

Anchor

The anchor in the string detection unit is a dead-weight to which the vertical mechanical ropes are connected. It will be constructed of concrete. Between 0.5 and 1 m3 will be required. The weight in air of 1 m3 of concrete is 2400 kg and therefore the negative buoyancy in water is 13240 N.

Mechanical Structure

The mechanical structure consists of two 4 mm Dyneema® ropes running the full length of the structure. The ropes will be delivered with length markings. The markings are made while the ropes are tensioned at the full tension expected during operation in the sea. At regular intervals thin Dyneema® strings are inserted through the ropes for attaching the electro-optical backbone cable.

Storey

For the string detection unit the storey is a single Multi-PMT optical module as described in section 3.1.4. The single sphere is connected to the ropes of the mechanical structure using a spring-loaded titanium ring. The ring has two sets of four titanium cleats. The ropes are run around the cleats and finally capped with a titanium cap. On one side of the ring there is also a provision for connecting the backbone cable. Figure 3-30 shows the ring structure.

Figure 3-29: Schematic layout of the String Detection Unit (from bottom at left to top at right)

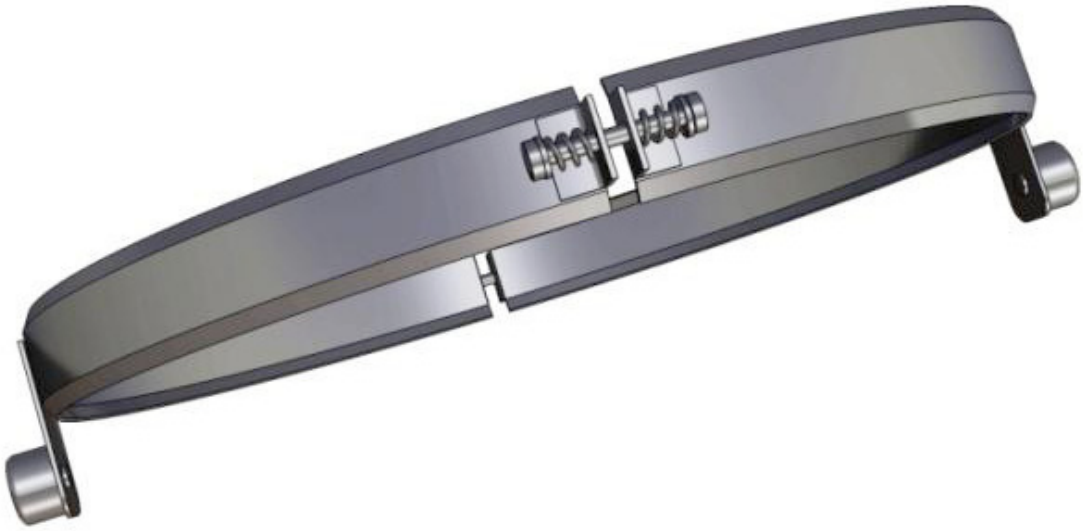

Figure 3-30: The spring loaded titanium connection ring

Deployment

There have been several requirements formulated for the deployment of the detection unit:

- It should fit in a standard transport container, to facilitate transport to the deployment port.
- At least eight detection units should be deployed in a single sea operation of three days otherwise these become prohibitively expensive both in time and money.
- These requirements have resulted in a number of restrictions on the deployment techniques:
- Deployment must proceed at least as a single unit (compact deployment)
- The detection unit must be in a compact transportable state when deployed (inner dimensions of a 20 ft container: 5.88 x 2.35 x 2.35 m^3)
- It must unfurl once on the seafloor
- Deployment frames must be reusable.

Deployment Structure

The deployment structure consists of a spherical aluminium structure (see Figure 3-31) with cable trays running round its circumference. The diameter is 2.1 m. The three sets of cable trays run from pole to pole and are offset by 60° Between the cable trays of each set, holes in the sphere provide the space for suspending the optical modules in the structure. The structure is loaded during assembly of the detection unit. First the five glass buoys are loaded on guiding rails through the hole at the North Pole. The first optical module is placed in the first hole next to the north pole and kept in place by a lever blocked by the ropes. The spherical structure is rotated around a winding axis perpendicular to the first cable tray. The Dyneema™ ropes and the backbone cable are laid in the trays. After five rotations the next optical module will be aligned with the next hole on the circumference and secured in it. This is continued until all holes in this first tray set are filled. (The holes at the poles are skipped). The spherical structure is rotated around the north-south axis by 60° to be able to fill the next cable tray set. The winding axis is changed accordingly. This cable tray is then filled followed by the last. During the loading of the last cable tray the hole at the South Pole is also filled. The final sphere is placed at the North Pole after which the remaining 100 m of ropes are wound round the spherical structure. The ropes are connected to the anchor. The sphere has three tubes (not shown) running through it so that during deployment cables can run through them from a spreader structure at the top to the anchor. In this way the deployment forces are taken by the deployment cable rather than the spherical structure.

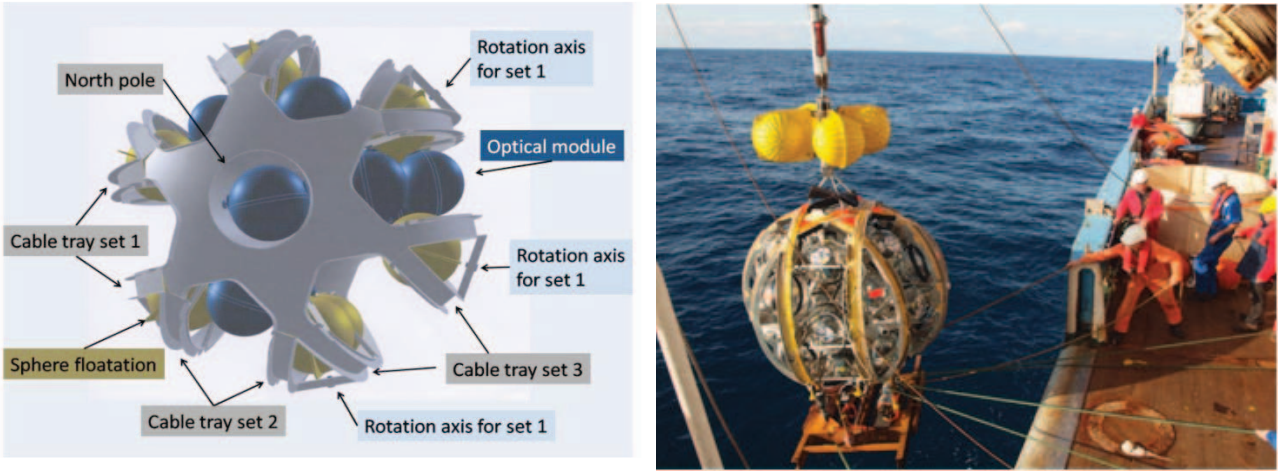

Figure 3-31: Spherical deployment structure, design and during deployment.

The spreader is secured to the anchor by an acoustic release mechanism. When released the spreader is winched to the surface and the structure rises due to its buoyancy. It rotates as it rises to the surface and unwinds the detection unit. When the last glass spheres have been released the spherical structure rises to the surface under its own buoyancy. This allows for recovery and reuse. Two of these structures fit into a 20 foot container. The deployment structure with all ancillaries takes up a deck-space of 2.2 x 2.2 m2. The units will be transported and stored on deck, two-by-two, in open top 20 foot containers. This will protect the units during transport and facilitate deployment. A minimum of eight units will be transported at a time on the deployment ship.

Maintenance

Following unfurling no maintenance of detection units is planned. When predicting the global performance of the detector, account must be taken of the probability that parts - storeys or optical modules - will become blind. The power and data network must be designed in such a way that in no case can the failure of a detection unit propagate to another part of the detector.

3.3.4 The *Triangle* detection unit

The general description of this design has already been given in section 2 and in Section 3.3.1. This section gives complementary details on this design.

The detection unit is inspired by ANTARES experience but represents an improved design in a compact string-type geometry allowing for easy transportation and deployment with remote unfurling on the sea bed. This unfurling requires a special apparatus, termed the "bell". The 6 optical modules of each storey are of the large PMT type (see Section 3.1.2) with the electronics housed in extra 7th glass sphere.

In the large PMT option, the 6 optical modules of each storey are grouped in 3 close pairs with adjacent pairs azimuthally separated by 120°. The two optical modules of each pair are used in coincidence with a PMT looking horizontally and the other looking downward, at 45°, both in direction at the opposite of the storey axis. The storey electronics sphere is linked electrically and optically - through a connector at one end and a penetrator at the other - to the backbone. The six OM spheres, each containing only a PMT and HV base, are linked electrically - through a connector at one end and a penetrator at the other - to the electronics sphere (see Figure 3-32).

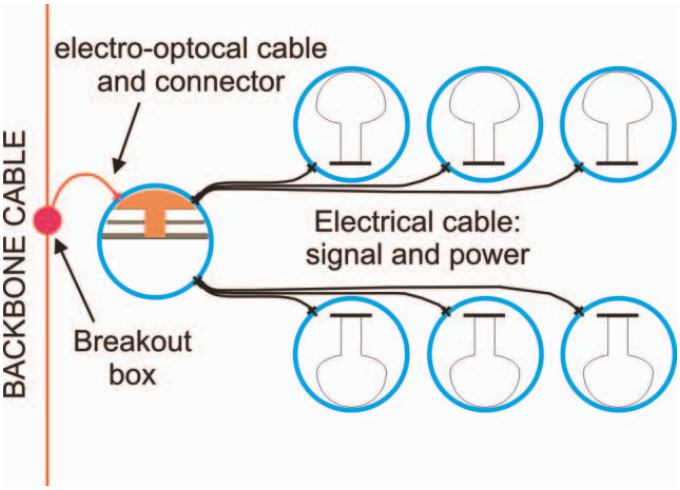

Figure 3-28: The flotation system for the Bar detection unit.

Product breakdown for the Triangle detection unit.		
Component	Description	Quantity
Anchor	The anchor is a dead weight to keep the detection unit on the seafloor. It carries the bell and the interlink mobile spool.	1
Storey	The mechanical structure with optical modules and an electronic container.	20
Backbone cable sections	It is meant to keep the optical modules spaced vertically in the water while distributing the power and the data. At regular intervals a storey is connected to the cable mechanically (by a pair of mechanical terminations and crow's foot riggings) and electro-optically (through a break out unit). Sections are connected through dry-mateable hybrid connectors.	4
Backbone master module	Pressure resistant vessel containing DWDM unit and optical circulator circuitry.	1
Floatation system	Buoy at top of detection unit to keep it upright.	1
Interlink cable	Cable with two fibres and two copper conductors, dry mated to detection unit and with hybrid wet-mateable connector at other end. Length as required by layout.	1

Product breakdown of storey.		
Component	Description	Quantity
Optical module	Described in Chapter 3.1.2	6
Electronics container	Described in Chapter 3.1.2	1
Storey structure	A welded structure of marine aluminium alloy, connecting the optical modules and the electronic container to the backbone cable.	1

Table 3.13: Product breakdown for the Triangle detection unit.

The storeys have a horizontal layout (overall diameter 2.5m) and, before the unfurling, they are stacked as "triplets" for compactness (see Figure 3-33).

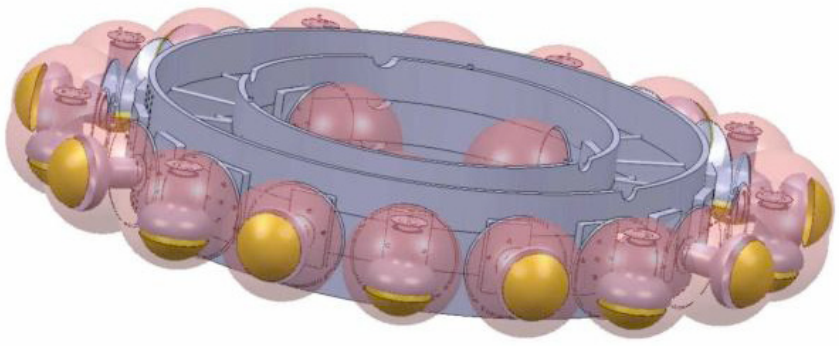

Figure 3-33: View of a nested pre-deployment triplet of three storeys of the Triangle detection unit.

In an alternative design each pair of OMs is replaced by a "capsule" (see Section 3.1.3) containing a pair of PMTs. In this design, each of the 20 storeys would house 3 OM/capsules which would also contain the OM electronics, eliminating the extra sphere.
The detection unit has 20 storeys (loaded on 7 pre-deployment "triplets", the last being incomplete) spaced 40 m apart after deployment between 100 and 860 m from the sea bottom. The backbone spaces the OMs spaced vertically in the water while providing the power and data flow. Storeys are mechanically connected to the cable - through a pair of mechanical terminations and crow's foot riggings - and electro-optically through a break out unit – an electro-optical "T" connection between two adjacent cable sections and the storey electronics.

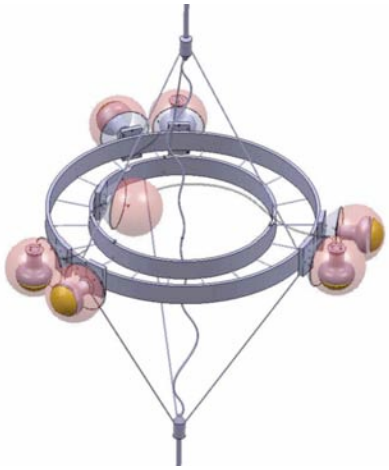

The detection unit anchor carries the "bell", the master module and the interlink cable wound on its mobile reel. The master module is a pressure vessel that contains the DWDM filter, and serves as a connection point between the backbone cable and the interlink cable to the deep sea network. Cable entries through the wall of the master module may use (connector-less) penetrators, or alternatively dry (surface-mate) connectors. The distant end of the interlink cable which connects with the seafloor network terminates in a hybrid wet-mate EO connector. The product breakdown for the Triangle detection unit is given in Table 3.13.

Figure 3-34: Triangle detection unit: detail of optical module and electronics sphere interconnections.

Storey

The mechanical structure of the storey is made of welded marine aluminium alloy (Titanium and composite material are also considered) with the following functions:

- to support the 6 OMs, the electronics sphere and the break out unit;
- to mechanically connect the up-going and down-going cable segments to neighbouring storeys, the buoy or master module;
- to hold, before unfurling, the 30m long cable sections (connecting a storey to its neighbours) in a safe way, avoiding any risk of blocking during the remote unfurling process;
- to constitute a stable stack in air as well as in water before unfurling.

The storey exhibits a 3-fold rotational symmetry around the detection unit axis. Figure 3-34 is a view of a single storey, whereas Figure 3-33 shows three consecutive storeys belonging to the same triplet stacked together, with the three corresponding cable sections wound in the middle. This assembly is the elementary brick of the whole stacked detection unit (see Figure 3-35) made of 7 such bricks. Figure 3-36 is a view of a central part of the unfurled detection unit.

- The weight in water of a storey, without the OM but with break out unit, electronics and cable mechanical termination, is 30kg.
- In the case of accidental corrosion of the structure of a storey, the damage will not propagate further; the mechanical, electrical and optical integrity of the vertical backbone will be preserved.

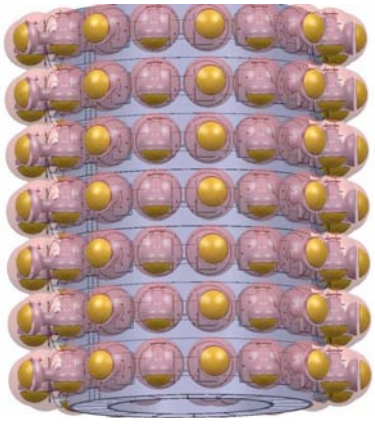

Figure 3-35: Triangle detection unit in stacked configuration with 20 storeys.

Anchor

The anchor is a heavy plate of anode-protected steel (or of concrete) having a weight in water of about -30000N (cf. Section 3.3.5). In addition, it carries the master module electronics container, the interlink cable reel, the acoustically triggered unfurling system and the bottom section of the vertical cable.

Buoyancy

Most of the detection unit's buoyancy is provided by the storeys but a top buoy is still needed to reduce the detection unit inclination in the case of strong horizontal sea currents (cf. the "detection unit stability" section). Each sphere has a buoyancy of 73 N. Taking into account the weights of the mechanical structure of the storey, the cable sections, their mechanical terminations and break out unit and of the electronic equipment, the net buoyancy of a storey will be 220 N. The top buoy will be a sphere of 1.4m diameter (or an ellipsoid of the same volume), made of syntactic foam of a density around 0.6 and located 10m above the top storey.

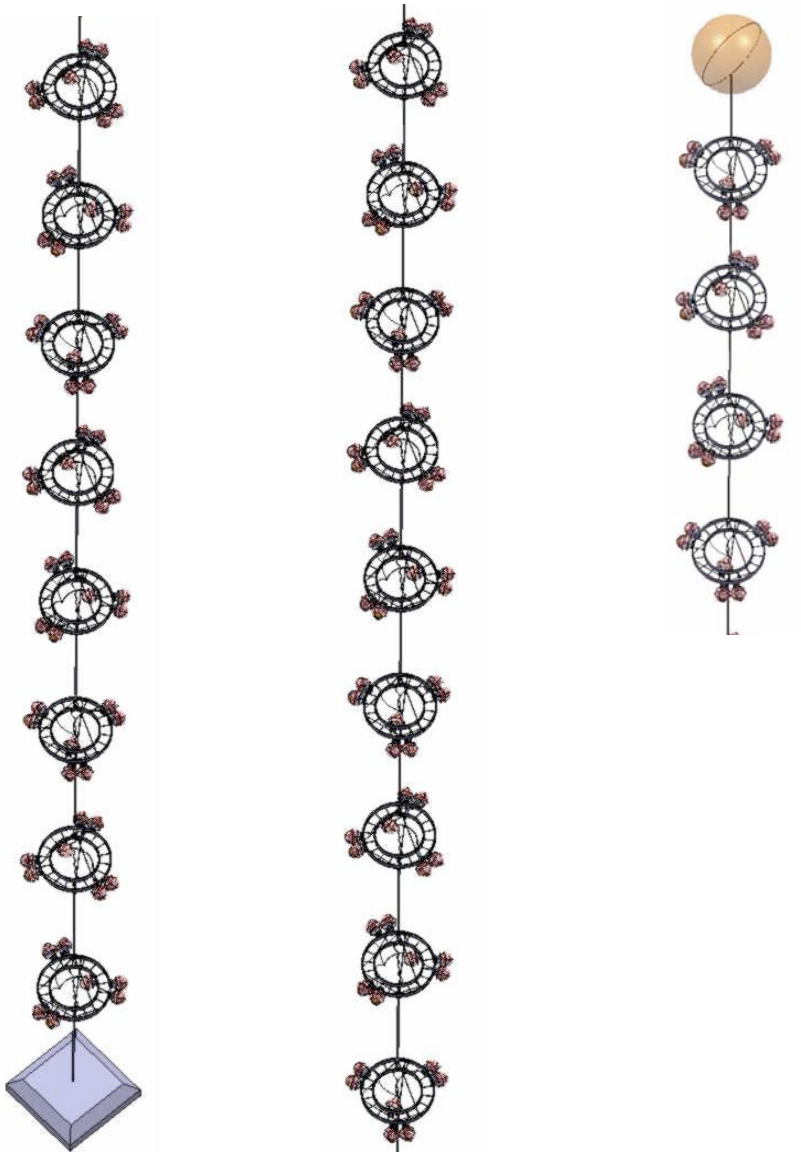

Figure 3-36: The unfurled detection unit. Bottom, central and top section.

Horizontal Interlink Cable

The detection unit interlink cable is coiled on a reel mounted on the detection unit anchor and connected to the sea floor network through a wet mate connector handled by a ROV. The possibility of unplugging interlink cables allows for the recovery of deep sea junction boxes for servicing, should this become necessary.

Vertical Backbone and Strength Cable

The backbone is inspired by the ANTARES implementation of an electro-optic core protected and surrounded by a layer of Aramid fibres under a polyurethane sheath.
The breaking load is reduced from the 180 kN ANTARES figure to around to 70 kN (still representing a safety factor of ~ 6) since the cable does not need to support the detection unit during deployment. The maximum stress is limited to that which occurs during the unfurling of the detection unit.

The break out is a delicate part of the backbone. A base solution under study employs a unique moulded part in which conditions close to equipressure are achieved, through the choice of moulding material. This solution would reduce the cost and provide a barrier at each storey as well as protection against short-circuit in the case of water ingress.

The mechanical part of the cable (the Aramid braid) ends around 1m above and below the storey in Titanium mechanical terminations. From this point, crow's feet rigging of triple Dyneema® ropes connect to the storey structure to maintain the plane of the storey perpendicular to the cable. The electro-optic core of the cable continues up to the break out unit with some additional length which allows the remaking of any faulty breakout at construction time and prevents accidental tensioning or over-bending of this part of the cable at unfurling time.

Logistics

We assume a maximum allowed volume for a furled detection unit of 2.5m (horizontal diameter) x 3.5m (vertical height) for road transportation. The bare furled detection unit (including the OMs and the base plate but without the deadweight, buoy and unfurling bell), fits easily within this volume and will be transported by road from the integration site to the deployment harbour. There the top buoy, the deadweight and the unfurling bell will be added and the whole assembly loaded onto the deployment boat. The foot-print of a detection unit on the deck will be 2.7m x3m =8.1m^2.

Unfurling

The stack of 20 storeys is initially held on the base within the unfurling bell. The base and the bell are linked by a rope that can be acoustically released to permit the unfurling. The bell containing the 20 storeys rises slowly under the action of the cable/winch system of the deployment boat. The bottom section of the vertical cable, initially wound on the base plate, is freely released during the ascent up to a height of 100 m, where the first storey is left automatically.
On this storey the next section of cable has been wound, ready for the nest step of the lift. The process continues until all the storeys and the top buoy are released below the bell. Then the bell continues alone, at the speed allowed by the winch, to the surface, where it is recovered by the deployment boat for reuse.
The shock occurring along the vertical cable each time a new storey is released from the raising bell will be limited by reducing the speed of the winch during the unfurling phase. The deployment hook will be equipped of a low friction swivel in order to avoid any transfer of torsion from the deep sea cable to the detection unit vertical cable during the unfurling.
The bell is a heavy object (at least 1.5T of protected steel) intended to keep the deep sea winch cable under tension during detection unit unfurling. Its centre of gravity will be significantly lower than the centre of buoyancy of the stacked detection unit inside it, in order to ensure the up-down stability of the assembly.

Maintenance

Following unfurling no maintenance of detection units is planned. When predicting the global performance of the detector, the probability that storeys and optical modules may become blind must be taken into account.. The power and data network must be designed in such a way that in no case can the failure of a detection unit propagate to another part of the detector.

Maintenance will be 'replaced' by a test of the detection unit in situ while still furled (which means still connected by the winch to the deployment boat). Several options are presently under study. In the event of failure at this stage, the furled detection unit will be recovered with its base for repair.

The partial loss of detection unit buoyancy which might cause it to interfere with its neighbours will of course require an emergency procedure. A ROV is needed to cut the vertical cable at a point where it is still under tension. Slow sea current conditions are mandatory. The released part of the detection unit is then recovered by a surface boat.

The only recovery of a detection unit after the unfurling will be during decommissioning following the end of detector operation. This could be done from a surface boat by dredging.

Component availability

Due to the large number of parts needed and in order to reduce the procurement risk, several sources are required for each single component. This should be easy for the mechanics, the cables and the electronics but more difficult for 3 critical parts: the glass spheres, the PMTs and the connectors. In the building phase, the production of these parts will be followed permanently by basing representatives of the project at the production sites.

3.3.5 Hydrodynamic behaviour

The behaviour of a generic detection unit under the effect of the sea currents is modelled considering the detection unit as a sequence of rigid *units*. Two adjacent units are supposed free to rotate around a horizontal axis perpendicular to the direction of the sea current:

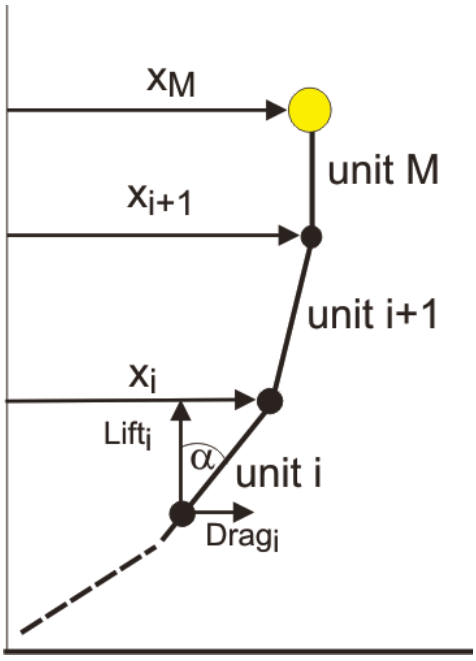

Figure 3-37: The detection unit approximated as a string of rigid units allows a simple derivation of the shape from lift and drag.

In the cases of flexible detection units (*String* and *Triangle* options), a unit is a storey (or top buoy) with the cable or ropes of various lengths attached *below* the storey (see Figure 3-37).

In the case of the bar design, due to its specific rigging, the unit is the parallelogram of Figure 3-38. It therefore consists of two adjacent storeys and ropes; the one perpendicular and the other parallel to the direction of the current.

The top buoy with its rigging constitutes an extra unit. At the bottom of the i[th] unit for the lowest unit, for the top unit), the total vertical force, lift, $(\mathcal{L}_i)$ and the total horizontal force, drag, (D_i) applied at this point of the detection unit are given by:

$$\mathcal{L}_i = \sum_{j=i}^{M} \ell_j$$

where $\ell_j = g(\rho_w V_j - m_j)$, $g = 9.804\ \mathrm{m\ s^{-2}}$, $\rho_w = 1040\ \mathrm{kg\ m^{-3}}$ and where V_j and m_j are the volume and mass of the j[th] unit respectively. The total drag at the ith storey is given by:

$$D_i = \sum_{j=i}^{M} d_j$$

The individual contribution to the drag by the j[th] storey is $d_j = \frac{\rho_w}{2}\left(S_j C_j + S'_j C'_j\right)v^2$. The cross sectional area of the storey or top buoy as seen by the current is denoted by S_j is and the dimensionless drag coefficient determined by the shape of the storey by C_j.
The quantities $S'_j(C'_j)$ denote the equivalent quantities for the cables and ropes. The sea current velocity is denoted by v.
The detection unit will adopt a shape such that:

$$\alpha_i = \tan^{-1}\left(\frac{D_i}{L_i}\right)$$

Here where α_i is the angle between the i^{th} unit axis and the vertical. Finally the horizontal excursion of the ith unit is given by:

$$x_i = \sum_{j=1}^{i} L_j \sin(\alpha_j)$$

with L_j is the total length of the j[th] unit.

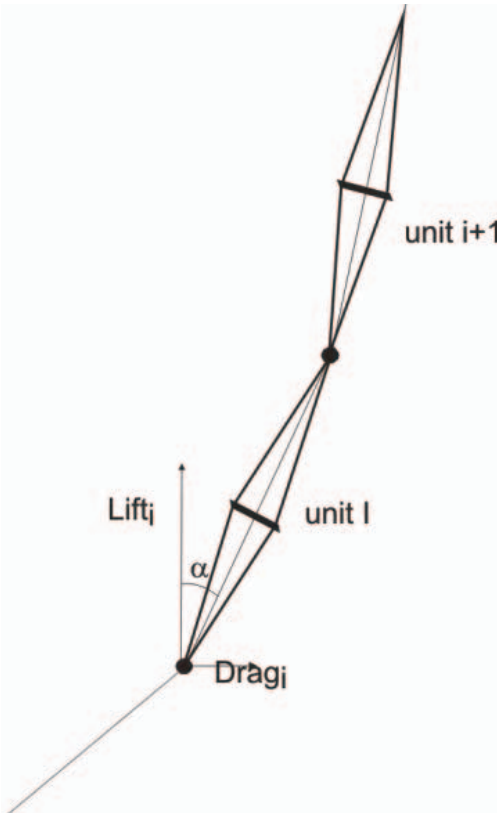

Figure 3-38: The elementary unit used for the drag calculation in the Bar design case.

Table 3.14 shows the various parameters and the calculated top offset M x for a current of 30 cm/s, considered as a maximum for any of the possible sites. Since the offsets scale with the square the velocity, the result for any other value of velocity can be easily computed. The drag coefficient C is 0.5 for a sphere (buoy or single OM) and 1.3 for a cylinder (cable, bar). Other shapes are approximated from these two primary volumes. It is clear that the deviation at the top of the detection unit can always be limited to within a fixed value, in this case 90 m. The requirement to compensate larger drag is results in added buoyancy and this in turn increases the mass required for the anchor. The calculations have been done for 30 cm/s, there is a finite probability that the current will exceed that number once in the ten year operating period by how much is a matter of speculation and also which form the large currents take: significant downward current, large turbulence or just steady state are all to a certain extent possible.

	String	Triangle	Bar
M	21	21	11
L_1 (m)	100	100	100
L_j $1 < j < M$ (m)	30	40	2x40
L_m (m)	5	10	20
ℓ_m (N)	1290	11096	10000
d_m (N)	34	75	135
ℓ_j: $1 < j < M$ (N)	140	220	2x300
d_j: $1 < j < M$ (N)	32	123	139+84
ℓ_1 (N)	140	220	300
d_1 (N)	86	233	100
x_M (m)	87	87	84
$\mathcal{L}_1$ (N)	4090	15510	16000
D_1 (N)	761	2645	2380
Dead weight W (N)	-8000	-30000	-30000

Table 3.14: Various parameters and calculated top offset x_M for a current of 30 cm/s in the 3 detection unit options.

Table 3.14 shows the various parameters and the calculated top offset x_M for a current of 30 cm/s, considered as a maximum for any of the possible sites. Since the offsets scale with the square the velocity, the result for any other value of velocity can be easily computed. The drag coefficient C is 0.5 for a sphere (buoy or single OM) and 1.3 for a cylinder (cable, bar). Other shapes are approximated from these two primary volumes. It is clear that the deviation at the top of the detection unit can always be limited to within a fixed value, in this case 90 m. The requirement to compensate larger drag is results in added buoyancy and this in turn increases the mass required for the anchor. The calculations have been done for 30 cm/s, there is a finite probability that the current will exceed that number once in the ten year operating period by how much is a matter of speculation and also which form the large currents take: significant downward current, large turbulence or just steady state are all to a certain extent possible.

Tests and measurements needed

Concerning the above calculation, the exact value of the drag coefficients still need to be measured in a test pool, at reduced scale if needed, with the absence of vibrations in the rigging verified. The resistance to torsion, and the possible asymmetries that would lead to torque being applied through the sea currents to the detection units is yet to be determined.

Concerning the dimensioning of the dead weight (i.e. to make sure that the current will not displace the detection unit), the following rule, used commonly by the oceanographers, will be used, again for 30 cm/s current speed:

$$B = -1.5\left(\mathcal{L}_1 + \frac{D_1}{0.6}\right)\,[\mathrm{N}]$$

Where B is the required net buoyancy in water (obviously negative) of the dead weight (including the attached detection unit base in the case of the *Bar* option).

3.4 Telescope Deep Sea Network

The building blocks described in the previous chapters have not at this point been optimised. The inter-unit distance has to some extent been optimised, but the layout on the seafloor still needs tuning. In addition the number of detection units in the building blocks depends strongly on the detection unit design. The full detector, equivalent to about 2 building blocks contains about 320 bar, 280 triangle units or 650 string units. This has a consequence that the description of the seafloor network will only be possible in terms of general architecture and operation principles rather than a full completely worked out design. The architecture that will be described is a star network with successive branching from the main electro-optical cables to the detection units. The implementation of this branching will depend on available technology, the efficiency of power distribution, the number of wavelengths carried on each data transmission fibre and of course the exact layout of the detection units on the seafloor.

The power transfer from the shore to the primary junction box is performed at high voltage, of the order of 10 kV, whereas the network from primary junction box onward operates at 375 V. The power losses in the different parts of the seafloor network have significant implications for the overall network requirements.

3.4.1 Network Components

In general the system consists of

- Power feeding equipment;
- Main electro-optical cables: the connection of the detector to shore for power, data and control signal transmission;
- Primary junction box(es): Conversion of high voltage to medium-voltage;
- Secondary junction boxes;
- Cables between primary and secondary junction boxes;
- Interlink cables from secondary junction boxes to the detection units.

Overall Power Requirements

The power requirements are determined mostly by the detection units. Each of the 320 (650) units have a consumption of 300 W (150 W). In addition there are power losses at the different stages of the system. The total power requirement of the detection units is 96 kW. The associated sciences node requires 10 kW. The additional power due to losses, predominantly in the main electro-optical cable and the medium voltage converters, is around 30 % so that the total required power on the shore is 155 kW. (See Table 3.15)

Total load detection units	96 kW
Interconnecting cable losses (375 V DC)	4 kW
Interconnecting cable voltage drop	<4%
Associated science power	10 kW
Medium-voltage converter power loss (η=80%)	27.5 kW
Total power at deep see	137.5 kW
Main cable loss	17 kW
Total power loss	30%
Shore power required	155 kW

Table 3.15: Power budget for full detector.

Power Flow Scheme

The power transmission system consists of two shore based 85 kW, 10 kV DC, 8.5 A power supplies, the main electro-optical cables operating at 10 kV DC, each with one power conductor with the return current being led through the seawater. The alternative cable solution, with copper return will be considered should environmental laws, at the time and site of deployment, exclude operation of a sea return. This will then have consequences both in financial and power terms.

A schematic view of power flow in the sea floor network is presented in Figure 3-39. At the end of each cable the 10 kV DC is transformed down to 375 V DC for supply to the detection units. This is done using 14 10 kW medium-voltage converters. These converters can be located close together or in principle separated so that each converter feeds a part of the detector in situ. This then requires additional equipment to split the main electro-optical cable, that are commercially available.

Because of power losses in the medium-voltage converter a maximum of 8.0 kW of power is provided to the detection units from each converter. The units are reached via the secondary junction boxes. A similar path is followed by the fibre optics network used for bi-directional data transmission and control. The fibre optic network was described in section 3.2 and will not be discussed further in this section. The only requirement stemming from the fibre network is that in the secondary junction box the communications wavelengths from four detection units are multiplexed onto a single fibre. The secondary junction box should therefore feed multiples of four detection units. The description below assumes a secondary junction box connecting to eight detection units. The detection units are designed to operate at a minimum voltage of 350 V corresponding, in the worst case, to a drop of no more than 25 V from primary junction box to detection unit.

The primary-to-secondary junction box cables have four copper conductors, with 13 mm^2 cross section each, rated for 600 V operation and have an assumed maximum length of 1500 m leading to a voltage drop of 12.7 V; the cables running from the secondary junction box to the detection units have four copper conductors, with 2.5 mm^2 cross section each, rated for 600V operation and at a length of 400 m lead to an additional 2.2 V loss. The power lost in the cables is around 4 kW for the full system.

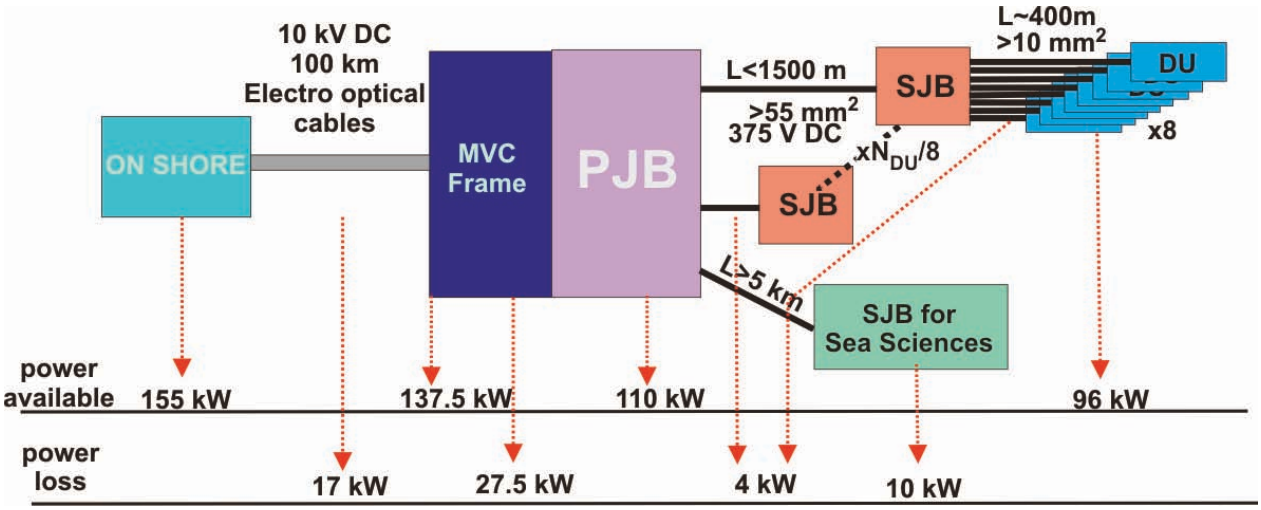

Figure 3-39: Power flow block diagram.

3.4.2 The Main Electro-Optical Cable

The KM3NeT site-to-shore main cables, which carry the optical fibres and electrical conductors, must survive both the rigours of installation (torsion, tension due to its own weight and ship movement) and the seabed conditions (high ambient pressure, abrasion risk and unsupported spans). Furthermore, the longevity of the read-out system depends on minimizing the strain induced on the optical fibres.
Submarine telecommunication cables satisfy these requirements. They have to provide service lives of at least 25 years and they must be easy to deploy and repair at sea. In addition, standard telecommunication cables have the advantage of working with a wide range of industry-approved accessories (such as connection boxes, couplings and penetrators). These accessories have shown very low failure rates and can be readily used to interface with scientific equipment. Thus the KM3NeT main electro-optical cables will be, to the extent possible, standard submarine telecommunication cables.

The solution where submarine cables with a single copper core are used will require two cables for the full detector. Then 96 fibres in each of the cables are necessary for the data transport.

The fibre types used for submarine transmission are optimised for minimum attenuation over the full C-band (1530-1570 nm) with dispersion characteristics that depend on the application. The main electro-optical cable has to be equipped with standard mono-mode fibres conforming to ITU-T standard G.655.

A single conductor power transmission system with current return via the seawater would allows for a light cable. The extremely small resistance of the sea return also implies a system with lower power losses. Such systems must incorporate sea electrodes both at the shore and in the deep sea. An issue with a DC single conductor system is the corrosion of neighbouring structures and installations. The anode is placed on shore in wet ground. Provisions will be made to capture any liberated chlorine gas. At the kathode a depletion of the H+ ions leads to a reduction of the pH of the seawater in the vicinity of the electrode. This issue will have to be addressed.

Length [km]	100
Type of power to be transmitted	DC, sea return
Maximum Voltage [kV]	10
Maximum Current [A]	10
Cable resistance [Ω/km]	1
Number of fibres	96

Table 3.16: Main Electro-Optical Cable characteristics.

A system providing data and power transmission over 100 km is in use between the Capo Passero on-shore laboratory and the deep sea site at 3500m depths. The cable was manufactured by Alcatel-Lucent and deployed in July 2007. The system can be operated at up to 10 kV DC at a power level of more than 50 kW.
The KM3NeT main electro-optical cable characteristics for the data and power transmission are summarized in Table 3.16.
There exist many kinds of submarine cable armouring. The armour is selected to be compatible with the specific cabling route on the seafloor. The final characteristics of the main electro-optical cable will therefore depend strongly on the deployment site.

Medium Voltage Converter

At the end of the main electro-optical cable there will be a frame termination assembly that will contain:

- a cable termination assembly that separates the power and fibre optic paths;
- a system of Medium Voltage Converters;
- a patch panel with several output wet-mateable connectors.

The medium-voltage converter transforms 10 kV DC input to an output of 375 V DC. An example of such a converter is the 10 kV to 375 V DC, 10 kW medium-voltage converter built by Alcatel for the NEMO project, which in turn was based on a design developed by JPL-NASA for the NEPTUNE project[15]. The measured efficiency is 87% at full load.

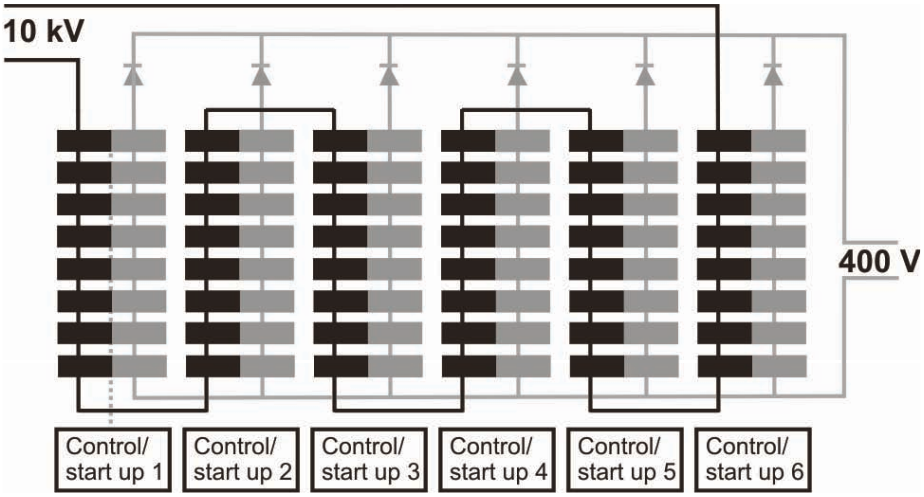

Figure 3-40: The DC/DC Medium Voltage Converter layout.

The converter is configured as a matrix of 48 power converter building blocks arranged in 6 columns connected in parallel, each having 8 blocks in series (Figure 3-40). This arrangement allows for the converter to continue operating, even with some faults in the printed circuit boards. Each building block is a pulse width modulated switching forward converter with an input of 200 V and an output of 50 V with a capacity of roughly 200 W. Each block has four MOSFETs, two working as a primary switch and two on the secondary side as a synchronous rectifier. A block diagram of the circuit is shown in Figure 3-41. The various transformers are able to withstand continuous 10kV operation

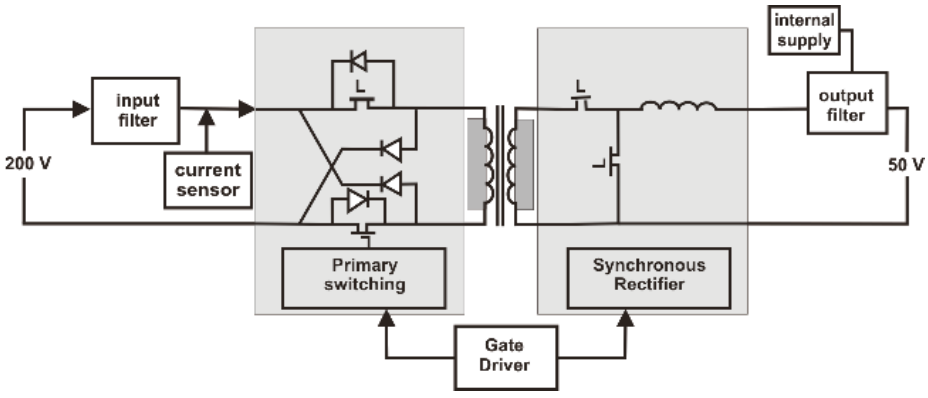

Figure 3-41: The DC/DC Medium Voltage Converter PCBB block diagram.

The entire power converter is housed in a pressure vessel filled with a dielectric fluid (Fluorinert®) for cooling and insulation. The complete medium-voltage converter is shown in Figure 3-42.

Figure 3-42: The Medium Voltage Converter.

The main characteristics of the medium-voltage converter, as measured on a functioning device, are shown in Table 3.17

Input Voltage	5.7 - 10 kV
Output Voltage	375 V
Output current	25 A
Input shut down voltage	5,2 kV
Efficiency at 10kV, full load	87%
Voltage undershoot at 10kV -10% to 90% step up	40 V
Voltage overshoot at 10kV -90% to 10% step down	43 V
Output Ripple Voltage, rms at 100 kHz	1,5 V

Table 3.17: Medium-voltage converter characteristics.

Primary Junction Box

The block diagram of the primary junction box is shown in Figure 3-43. Its main function is to route the 375 V DC power from the medium-voltage converters to the secondary junction boxes. The power from the medium-voltage converters will be connected inside the primary junction box in such a way that a secondary junction box can be fed by more than one medium-voltage converter, thus providing redundancy. Another functionality of the primary junction box is the monitoring and control of the output lines. The primary junction box also has remotely actuated relays that connect the secondary junction box to the medium-voltage converter system, that are used to switch on and off the feed lines during normal operation and to automatically isolate a faulty line. The bi-directional communication of control and data between the primary junction box and the shore station is achieved via a fibre optic connection. The primary junction box will have acoustic transponders so that its location on the sea floor can be easily determined. It must have a highly reliable operation and also it should allow for its recovery for maintenance or replacement, since it is a point where a single point failure may have truly severe consequences for the detector's operation. In addition a layout that allows for easy access of an ROV to the wet-mateable connectors is required.

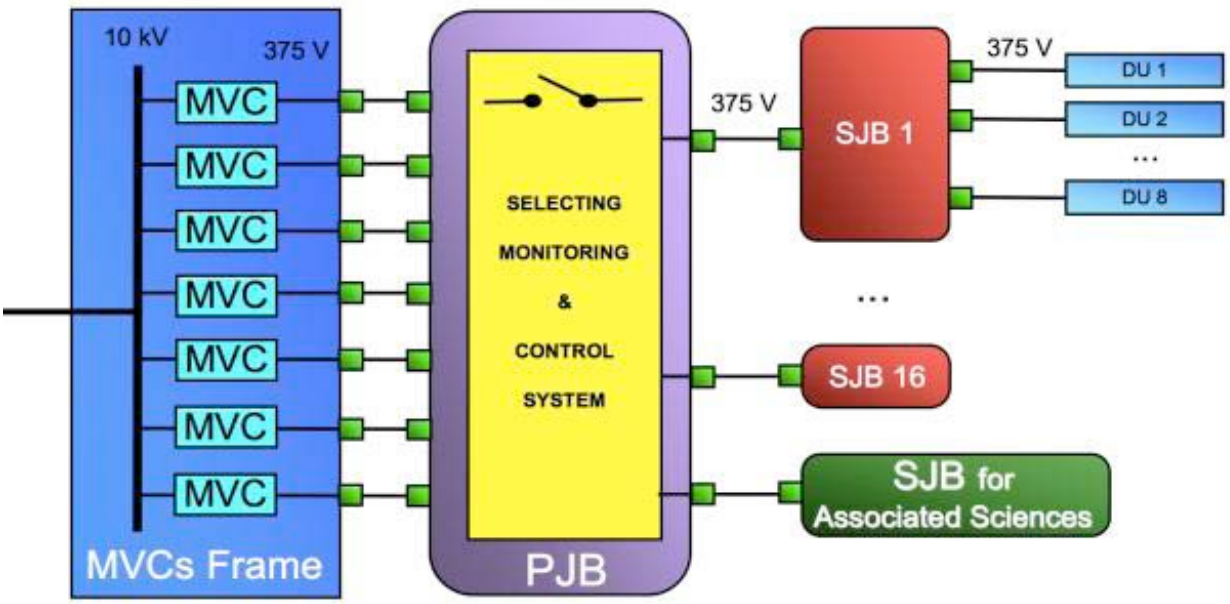

Figure 3-43: Block diagram of the sea-floor power distribution chain.

The specific details of the primary junction box depend on the exact configuration of the detector to be built, and thus the primary junction box will be one of the last components to be detailed. Both the ANTARES and NEMO projects have deployed and operated junction boxes in the deep sea with all the required functionalities. Descriptions of the various junction boxes are given elsewhere[16]. Salient features of the NEMO junction boxes are: (i) one incorporates the medium-voltage converter described above connected to the main electro-optical cable's cable termination assembly via a 10 kV DC connector which is designed to be wet-mateable, and (ii) another one makes an innovative use of an external light-weight fibreglass oil-filled tank to prevent the corrosion of inner pressure resisting steel tanks containing the electronic components. The use of regular steel tanks rather than titanium containers allows for a more economical structure. In contrast, the ANTARES junction box has a dry mateable main electro-optical cable connector and employs a titanium sphere as its electronics container.

Secondary Junction Box

Each secondary junction box serves a group of 8 detection units and is located near them so that the distance to the detection units is as short as possible. Its function is to distribute the power coming from the primary junction box to the detection units. The power distribution network inside the secondary junction box is shown in Figure 3-44.

The secondary junction box contains:

- a power feed system able to supply all the internal loads;
- a monitoring & control system that will monitor and switch on and off the output lines;
- input and output 600 V wet-mateable connectors including some spare connectors.

The sum of conductors and fibres in each connector should not exceed 8 to allow the use of available hybrid electro-optical connectors.

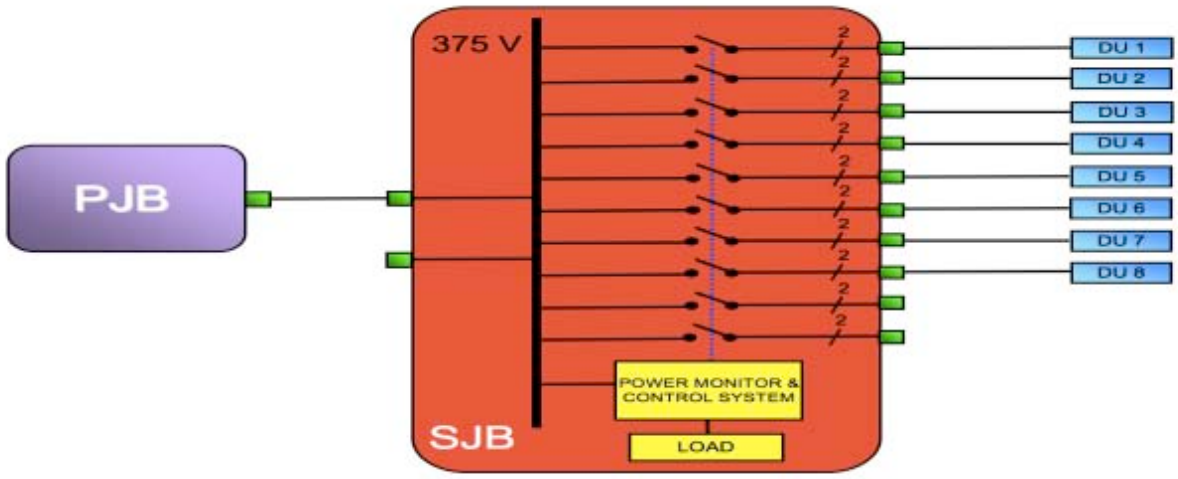

Figure 3-44: Block diagram of the Secondary Junction Box.

Examples

Just as examples of the different layouts that can be achieved using the architecture described above two options that could be used to power the building block are described in the following.

A star cabling layout

Figure 3-45 shows the "star" scheme of the power and fibre optic distribution.

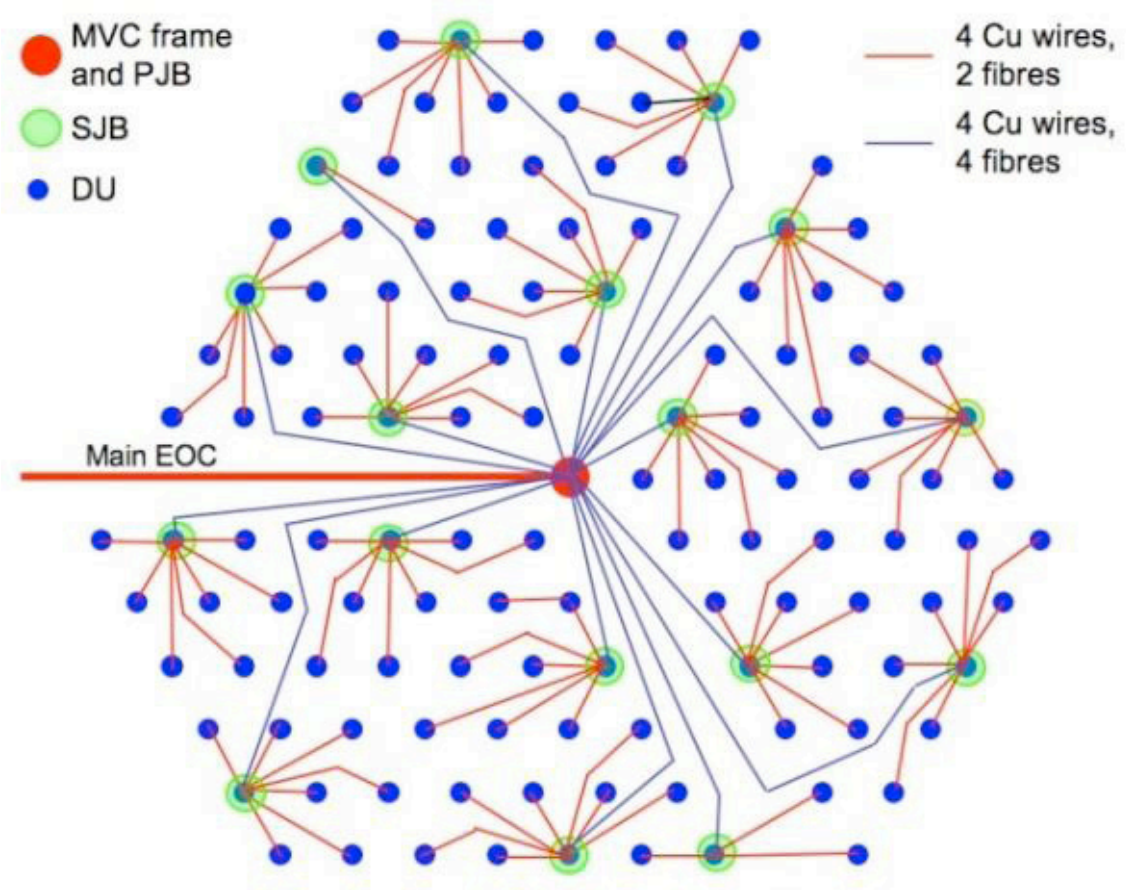

Figure 3-45: Star scheme of power and fibre optic distribution.

This scheme takes into account limitations dictated by the deployment and interconnection of the main electro-optical cable, primary and secondary junction boxes and detection units. Three corridors, ~ 300m wide, separate the whole detector into three parts to allow for the routing of the main electro-optical cable and for the passage of a remotely operated vehicle during deployment, connection and maintenance operations. The primary junction box structure is located at the centre of the detector. All the secondary junction boxes are located either along the corridors or to the outside of the detector. Each secondary junction box is connected to eight detection units in order to comply with the chosen data transmission scheme on optical fibres. The cables do not cross each other and cable lengths are kept as short as possible.

A ring layout

The alternative ring-configured geometry of junction boxes arranged around the circumference of the neutrino telescope is shown schematically in Figure 3-46. All junction boxes are combined function devices in the sense that they are attached to the main electro-optical cable from shore and contain a medium-voltage converter but also supply the detection units directly through radial interconnecting cables equipped with wet mate-able connectors.

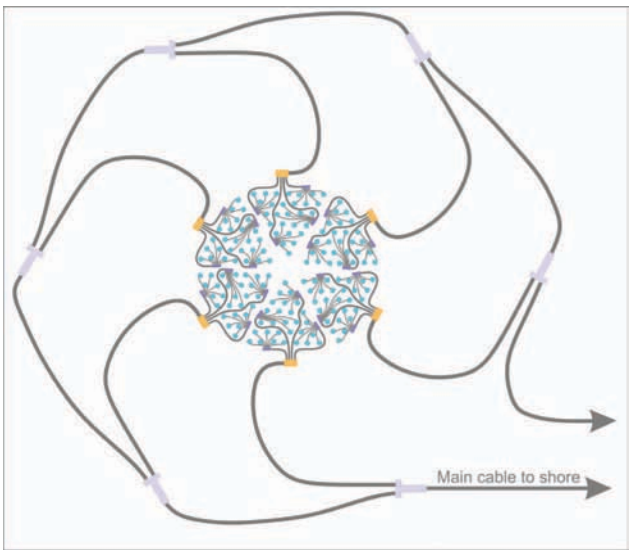

Figure 3-46: Possible ring geometry for sea floor infrastructure of junction boxes. Drawing not to scale, the diameter of the inner detector is ~2 km, and of the outer main electro-optical cablering is ~10 km.

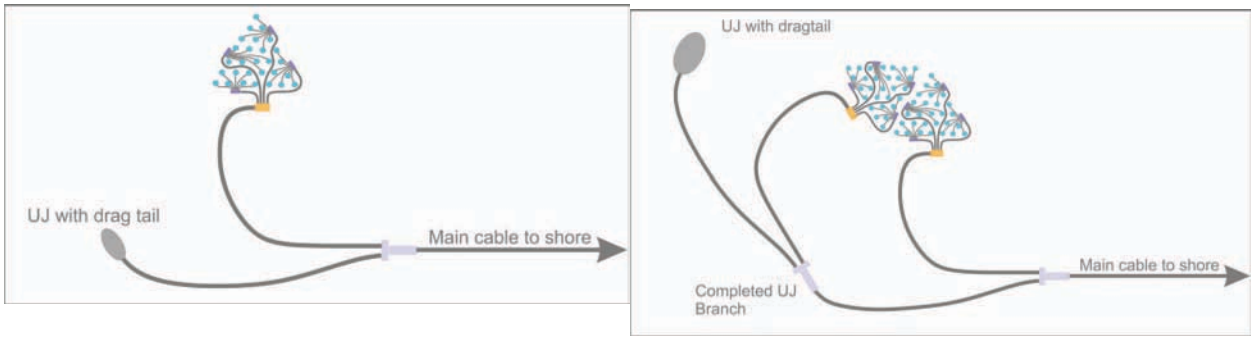

Figure 3-47: Progressive deployment of a circumferential ring sea floor power and data flow topology. The drawing is not to scale.

The junction boxes are connected to the circulating cable main electro-optical cable ring using commercially available branching units which allow for power to be switched individually onto each output arm. All connections of junction boxes and branching units in the circumferential ring use the same cable type as in the main electro-optical cable. Furthermore, all connections are connectorless, instead penetrators are used. These penetrators conform to the Universal Joint Standard of industry qualified components for the termination, repair and jointing of deep sea telecommunications cables [17] from a variety of manufacturers.
The use of Universal Joint technology allows for the staged deployment of the ring topology, as illustrated in Figure 3-47. On the upper part of the figure the first junction box is installed together with its BU and an unconnected, recoverable cable stub terminated in a blind Universal Joint jointing box and equipped with a 'dragging tail' allowing for later lifting with a trawled grapnel. This cable stub and its dragging tail have a length of at least twice the water depth, a factor generally considered the safe minimum for grapnel

3.4.3 Deployment and maintenance

The main electro-optical cable will be deployed, following consolidated experiences, from the shore laboratory to the off-shore site. The off-shore termination of the main electro-optical cable will be mechanically inserted into a frame than hosts also the main electro-optical cable termination and the medium-voltage converter system.

The primary junction box will be built in such a way that, in case of fault, it will be possible to recover it, to bring it on shore and to repair it. The connections between the primary junction box and the medium-voltage converter system will be implemented by means of "Jumpers" equipped with ROV operated electro-optical connectors. The same will apply to the connections between the primary junction box and the secondary junction boxes. This choice allows the possibility to disconnect, in case of fault, the primary junction box, to recover it and to repair it on shore.

3.5 Calibration and Positioning

In order to achieve the excellent angular resolution of the neutrino telescope an adequate knowledge of the position of the optical modules and of their timing is required. The energy measurement of the telescope requires an appropriate charge calibration. In addition, measurements of water properties are important for evaluating the detection efficiency.

With the precautions taken in the design, it is expected that the timing offsets of the optical modules will be stable such that after the initial calibrations, the subsequent calibrations will only be necessary for verification. For the positioning, the flexible nature of the detection units means that continual measurements in real time are necessary because of the displacements of the detector elements in the sea current.

For both timing and positioning calibrations there will be a relative calibration inside the detector and an absolute calibration against external reference systems.

3.5.1 Time calibration

The absolute time can be determined with a precision of 1 10ns, with respect to UTC, which is well below the time variability of any conceivable astrophysics process observed through a neutrino signal.

The precision necessary for the relative timing calibration requirement is specified so as not to degrade the overall accuracy.

For a large water-based neutrino telescope the chromatic dispersion of light in water is an intrinsic limitation to the timing precision. It amounts to an uncertainty of $\sigma \sim 2$ ns for light travelling a distance of 50 m. All contributions in the design from PMTs and electronics are less than 2ns and so the timing calibration system is required to have a precision of $\sigma \leq 1$ ns.

As already mentioned, the clock system will distribute the time reference signal required to synchronize all the front end digitizing elements and the reference clock in the shore station. The delay between the arrival of the photon to the photocathode and the time stamping (i.e. the transit time of the PMT plus the one of a part of the front end electronics) will be measured for all the PMTs before deployment during the on-shore detection unit calibration. These delays together with the clock phases (measured *in situ*) will enable time calibration of the data coming from different PMTs anywhere inside the detector.

After deployment *in-situ* of the detection units, time calibrations will be performed to make corrections in the calibration constants determined on-shore. Such changes will be necessary to correct for different temperature and for any adjustments of the PMT high voltage. This off-shore time calibration will use four methods:

- ^{40}K coincidences;
- LED light emitter: "nanobeacon";
- Lasers: "laser beacon";
- upward and downward going muons.

All these methods are based on the experience gained from the ANTARES project and together, they constitute a redundant and robust timing system, given that each method has its own set of systematic errors.

Cherenkov light from ^{40}K

Cherenkov light emitted in the decays of ^{40}K in the sea-water around the storeys gives coincident signals in nearby PMTs which can be used to determine the relative time offsets.

Nanobeacon

A nanobeacon, containing a small number of LEDs pointing upwards and pulsed by self-triggering electronic circuits, will be mounted on the inner surface of each OM. The nanobeacon will be at a 30° angle from the vertical where the long term absorption of the emitted light by bio-fouling should be small.

After characterization of several types of commercial LEDs, the CB30 from Avago has been selected. Pulsed by a modified version of the pulser circuit used in ANTARES, this LED emits with a rise-time of ~ 2.0 ns, a total width at half maximum (FWHM) of 4 ns and an angular spread of 28° (FWHM). The light emission is in the blue region peaking at 473 nm with a width of 15 nm (FWHM). Energies per pulse of ~ 90 pJ (~ 2 x 10^8 photons) are reached at the full voltage of the pulsing circuit. Based on the results in ANTARES results, ranges exceeding 200 m can be reached. Some LEDs with different wavelengths (400 nm, 450 nm and 500 nm) will be included for the measurement of water optical properties. The LED intensity is controlled by the variation of a 24 V DC voltage, and the power consumption of each nanobeacon is less than 0.5 W. The nanobeacon circuit has the options of an internal 20 kHz oscillator or an external trigger.

Laser beacon

The laser beacons used in ANTARES employed compact solid state Nd-YAG pulsed lasers emitting in the green (532 nm). Recently, compact pulsed lasers emitting blue light (470 nm) have become available and are under investigation. The scattering length of green light is larger than that of blue light, while the blue light has a larger absorption length. Both types of lasers can emit pulses with energies of a few μJ, so that distances of a few hundred meters can be reached in both cases, with less time dispersion for green light. Green lasers have pulses with rise times below 0.5 ns, while the presently available blue lasers give rise times below 1.5 ns. Either a blue or a green laser will be housed in a pressure container located near the sea floor and pointing upwards. Anti-fouling devices, successfully used in ANTARES will be applied.

These laser beacons will enable the relative calibration between several OMs of different detection units. One laser beacon for every six detection units will be sufficient to ensure redundancy of coincident signals.

The laser beacons will either be located on the bases of the detection units or on the junction boxes on the sea floors.

Muons

Reconstructed muons can be used to further refine and cross-check the determination of the time constants. For downward going atmospheric muons there is a limitation in the precision achievable due the light scattering needed to reach downward looking PMTs. Upward going muons from atmospheric neutrinos or optical modules with upward looking photomultipliers can be used to avoid this limitation.

3.5.2 Positioning

The positioning system supplies information for both the installation and operation phases of the project. During the deployment of the detector, the positioning system must provide the position of the telescope's mechanical structures, in a geo-referenced coordinate system, with accuracy of the order of a few metres. This is important both for the safe deployment of the mechanical structures and for the determination of the absolute position and pointing direction of the telescope. During the operation phase, the positioning system must give the positions of the optical modules with the necessary accuracy for the muon tracking. For this requirement the optical module coordinates must be measured, in a local reference system, with accuracy better than 20 cm with a frequency of one measurement per 30 s in order to correct for the movement of the detection units due to the sea currents.

The positioning system has four elements:

- acoustic transceivers, anchored on the seabed in known positions in a "Long Base-Line (LBL)" reference system;
- acoustic receivers (hydrophones) rigidly connected to the telescope's mechanical structures holding the OMs;
- devices (compasses) to measure the orientation of each storey;
- computers on-shore for data analysis.

The optical module positions are extracted by measuring the acoustic travel time between the transceiver signals from the long base-line reference array and the receivers on the detection units. With a set of at least three acoustic travel times for each receiver to a different transceiver, the positions in space of the hydrophone can be determined by triangulation with respect to the long base-line system.

The KM3NeT positioning system is based on experience of the systems developed for ANTARES [18] and NEMO [19] but with better accuracy due to absolute time synchronization between transceivers and receivers. It is fully integrated with the detector electronics. The components are commercially available and have been tested to 3500 m depth by the pilot projects..

Commercial hydrophones are the default choice for the acoustic receivers; however a promising option, to use a piezoelectric sensor directly glued inside the glass container of the optical module, is under development.

Acoustic Long Base-Line System.

The best resolution for acoustic distance measurements is obtained from the higher frequencies which however limits the range. ANTARES had two distinct long base-line systems:

- a high frequency system used for the high resolution relative positioning of the detector
- a low frequency system used for the long range deployment, ROV navigation and absolute calibration of the detector.

The KM3NeT design combines these functions in a single system based on a unique long base line system, inspired by the system developed for NEMO that has both the required resolution and the range needed for a larger detector at greater depth.

This is made possible by:

- using an intermediate frequency;
- modulating the emitted acoustic signal;
- sampling this received signal permanently at high frequency and high resolution;
- sending all the samples to shore for processing.

Each transceiver has its own modulation signature, allowing the simultaneous detection by one hydrophone of several overlapping signals with an optimal noise rejection and phase detection. The signal carrier frequency will be between 10 and 40 kHz and can change depending on the operation and the range needed. The signals will be continuously at about 200kHz in at least 16 bits, also making possible the detection of acoustic neutrino signals from showers and the detection of marine mammals.

The long base-line systems will consist of around 10 transceivers fixed on the seabed and distributed all over the site. The physical support of the transceivers could be the junction boxes or the detection unit bases. These devices will require the same local clock and data transmission capabilities as a storey.

Absolute calibration of the position

After the triangulation procedure the storey positions are known in the local frame of the long base-line system. For a site with a flat sea bed there is an ambiguity in the relative heights (depths) of the long-base-line transceivers. An absolute positioning calibration is necessary to relate this local frame to a geographic reference system. The absolute calibration measures the orientation (i.e. three independent angles) of the long-base-line frame with respect to the geographic references: the local gravity (i.e. the absolute north-south and east-west tilt angles) and the local North (i.e. the absolute azimuth with respect to the projection of the earth rotation axis on the local horizontal plane). The methods used are summarised in Table 3.18.

Type of calibration	Relative (+-10cm)	Absolute (+-1m)
X/Y coordinate	Triangulation inside long-base-line system	Surface boat and GPS
Z coordinate (=vertical)	Long-base-line surface echo or triangulation with hydrophones	Long-base-line surface echo or surface boat

Table 3.18: Methods used for the relative and absolute calibration of the LBL.

In ANTARES, the absolute tilts were measured by a remotely operated vehicle equipped with a high resolution and high stability pressure meter which successively visited each of the acoustic transceivers to record their relative depths. This operation is difficult to perform with the required <10 cm accuracy. For example, it must be done in a short time (<1 hour) since the tide and the drift of the device corrupt the data. For KM3NeT, this will only be a back-up solution and the default method will use acoustics, for which two methods are under investigation. One method is for each long-base-line transceiver to detect its own surface echo and the other is, during a period of low current, for the storey hydrophones to determine the missing relative altitudes.

For the absolute azimuth measurement of the long-base-line system, a surface boat equipped with an acoustic fish with a position known from differential GPS, moves around the detector while measuring periodically its distance to each of the long-base-line transceivers. The geodetic positions of these transceivers are then determined by triangulation and minimisation with accuracy ~1 m radius for the GPS or better for the Galileo system. The global long-base-line system azimuth is a natural output of this minimisation, as well as the depths if needed. For geometrical reasons and also since the exact altitude of the acoustic fish is poorly known, the best accuracy in x and y positions (i.e. in the horizontal plane) is achieved for a boat at a relatively long distance from the vertical of the site, needing an acoustic range of at least twice the depth.

The goal is an accuracy of better than 0.10°, for all the three angles, i.e. less than 1 m radius error in x, y and z at both ends of a detector diameter of about 1 km. A set of celerimeter (sound velocity profilers), current-temperature-density (CTD) probes and current meters at different altitudes above the seabed is needed to reach the ultimate accuracy of the acoustic system. Since the absolute calibration must only be performed occasionally it is possible to wait for a period of good sea conditions, i.e. low acoustic noise from the surface, small oscillations of the sea surface and good amplitude of the surface echo.

Check of the absolute positioning and orientation

Knowledge of the absolute orientation of the detector is essential to perform neutrino astronomy and so two independent check of the absolute orientation calibration are planned: one using the Moon's shadow in cosmic rays and the other using the synchronous detection of Extensive Air Showers (EAS) with the neutrino telescope and floating scintillator arrays.".

The moon absorbs charged cosmic rays and so the flux of down going muons detected has a deficit or shadow in the exact direction from the moon with size 0.25° in radius. At the relevant energies, the magnetic field of the Earth does not perturb the effect. IceCube [20] used this method with success. Several months of data taking will be needed to distinguish the moon shadow from the background. For the second check, Extensive Air Showers are detected by a geo-referenced floating surface array, while the atmospheric muons produced by these Showers are detected by the KM3NeT [21,22,23]. The direction of the shower's axis is estimated by the floating surface array and compared, event-by-event, with the direction of the reconstructed muon by the underwater detector. Three floating EAS detector arrays placed above the underwater detector and taking data for a period of 10 days could detect an offset in the reconstruction by the KM3NeT of 0.01 degrees in the zenith angle and 0.07 degrees in the azimuth angle. Each such array is made of 16 scintillator counters (1 m^2 each) placed on a floating platform with surface 360 m^2.

Magnetic heading measurement

Even with the acoustic positioning measurements, knowledge of the heading of each storey is needed to derive the final position and orientation of each photomultiplier. The required resolution is of the order of one degree but depends on the detection unit design. Magnetic compasses having this resolution using the new magneto-resistant sensors are available at low cost, for low size and low power. This device is incompatible with a mu-metal cage or any other ferromagnetic material in the vicinity.
In principle tilt angle measurements are also needed to correct the compass reading and the vertical optical module position, but since there will be a hydrophone per storey these data can be derived from the detection unit positioning.

3.5.3 Charge calibration

The threshold level and high voltage combination convenient for each PMT in order to achieve an effective threshold of 1/3 of a photoelectron will be adjusted for all the PMTs before deployment, during the on-shore calibration. Adjustments might be needed after the deployment of the detection units and will be performed using the single photoelectron peak in the charge spectrum as well as the rate of detected coincidences from ^{40}K decays as input.

3.5.4 Water and Environmental monitoring

The performance of the neutrino telescope strongly depends on the environmental conditions. The water transparency affects the propagation of the Cherenkov light in sea water reducing the visible volume and worsening the angular resolution. As already discussed, the deep sea current displaces positions of the optical modules and must be taken into account. The salinity and the temperature of the sea water affect sound transmission in the acoustic positioning system. All these environmental properties will be monitored continuously by means of dedicated specialized instruments placed in the active volume of the detector.
Optical water properties such as absorption length and scattering length have a big influence on the track reconstruction efficiency. The devices used for these measurements are the nano-beacons and laser beacons described earlier. The characterization of the water optical properties will be possible by analysing the information of the amplitude and the time of pulses collected by optical modules located at several distance from the light sources. The nano-beacons will be located on all lines and the laser beacons on a few line bases or on junction boxes. Deep sea currents will be measured by Acoustic Doppler Current Profiler (ADCP) which permits measurements of the current at different distances, up to ~150m, from the instrument simultaneously. Several ADCP devices (e. g. the RDI Workhorse) will be located on the same vertical detection unit to characterize the full vertical water column around the detector. Only a few (3 or 4) detection units will be equipped with ADCPs in this way.
The physical-chemical environmental properties will be measured by means of CTD (Conductivity, Temperature, Depth) instruments like the SBE 37-SI MicroCAT. As with the ADCPs, only a few lines will be equipped with a series of CTD instruments to characterize the full detector volume. The instruments on these special detection units will operate at regular interval of time (15-30 minutes. An alternative to equipping the standard detection units with instruments would be to have dedicated instrumentation lines.

3.6 Assembly of optical modules

Detailed list of the assembly procedures for the optical module with large PMT with its associated electronics module is given in Table 3.19 and Table 3.20. Table 3.21 shows the steps for the Multi-PMT optical module and finally Table 3.22 gives the details for the capsule optical module. The time required for the steps have been deduced from experience with the ANTARES experiment and from mechanical prototyping. It is clear from the tables that the workforce can be optimized by performing several of the tasks in parallel. This however then does require that the workforce can only occur in multiples of the numbers given below. In addition they of course must be matched to the integration of the storeys and detection units.

For the optical module with the large PMT the estimate is that 6 optical modules can be produced in 4 full time equivalent (fte) days. The associated electronics module takes a further 2 fte days.

For the Multi-PMT optical module 10 optical modules can be produced in 5 days with a fte workforce of 6. The capsule requires 2 fte days for production and testing.

Single Large PMT optical module		
Components	1. Glass hemispheres 13 inch (2)with fitted bulkhead connector(1) 2. 8 inch PMT (1) 3. Optical Gel (2 components) 4. Magnetic field cage (1) 5. Pressure gauge (1) 6. High voltage base(1)	
Lower hemisphere assembly	PMT and magnetic field cage positioning; establishing optical contact	1. Placement of the hemisphere on the dedicated assembly table using dedicated tooling; 2. Cleaning of hemisphere (ethyl alcohol); 3. Cleaning the mu-metal shield; 4. Mix the 2 components of Wacker Silgel 612A/B in ratio 60/40; 5. Pouring the gel into a hemisphere 6. Placement of the hemispheric part of the mu-metal® magnetic shield in the optical gel; 7. Out-gassing of the optical gel; 8. Placement of the PMT in the optical gel with a 5mm gap between the glass and the PMT, 9. Out-gassing repeatedly; 10. Leave optical gel to polymerise over a period of 8 hours; 11. Placement of the ring segment of the mu-metal shield; 12. Placement of the pressure gauge
	PMT acceptance test	13. Storage of the hemisphere in dedicated dark box to restore the capacity of the PMT photocathodes of the PMTs; 14. Test dark current and single photon response; 15. Record results in a test report and in the data base; in case of failures replace PMT and base

Upper hemisphere assembly	Hemisphere preparation	16. Cleaning of the hemisphere;
Sphere assembly	Sphere assembly	17. Soldering the PMT high-voltage base to the wires projecting from the connector in the upper hemisphere; 18. Connecting high-voltage base to the PMT in the lower hemisphere; 19. Placement of the two assembled hemispheres in dedicated tooling and closure of sphere; 20. Placement of sphere in a vacuum glove box; 21. Reduction of pressure to 700mbar$_{abs}$; 22. Sealing "equator" with putty; 23. Taping equator;
Conformity test	Test procedure	24. Using dedicated tooling the OM is placed in a dark box with LEDs for functionality tests and electronics circuits to perform acceptance tests: 25. Measurement of power consumption of the OM; 26. Measurement of dark current rate for each PMT; 27. Storage of test results in database;
Sign off	Final procedures	28. Packaging of optical module 29. File optical module documentation 30. Update database.

Table 3.19: Assembly steps for the large PMT optical module.

Storey electronics module	
Components	1. Glass hemispheres 13 inch with fitted Bulkhead connectors for optical modules (2) 2. Storey logic board including 6 FE electronics chips(1) 3. Converter board (1) 4. Support and cooling element (1) 5. Nano –beacon with electronics board (1) 6. Piezo acoustic sensor with electronics board (1) 7. Outer connection: penetrator – cable-connector to backbone(1) 8. Pressure gauge (1)

Upper hemisphere assembly	Hemisphere preparation	1. Cleaning of hemisphere 2. Mounting a EO penetrator in glass hemisphere 3. Fibre splice of readout fibre to penetrator 4. Gluing of the cooling element at a predetermined location to the glass hemisphere; 5. Soldering of power conversion board to input wires on penetrator 6. Mounting the converter board on the cooling element; 7. Mounting pressure gauge
	Electronics installation	8. Connection of the nano-beacon with its electronics board 9. Mounting the electronics board of nano-beacon on the cooling element 10. Gluing the nano-beacon to the glass of the hemisphere 11. Mounting the electronics board of piezo acoustic element on the cooling element 12. Making power connections to storey logic board 13. Mounting the storey logic board to the cooling element
Lower hemisphere assembly	Hemisphere preparation	14. Glue piezo acoustic sensor to predetermined position on the hemisphere;
Sphere assembly	Sphere assembly	15. Placement of hemispheres in dedicated tooling close to each other 16. Soldering connections to Optical Module connectors 17. Soldering connections to piezo acoustic sensor 18. Closure of sphere 19. Placement of sphere in an assembly tool inside a vacuum glove box 20. Flush with dry nitrogen 21. Reduction of pressure to 700 $mbar_{abs.}$ 22. Seal "equator" with putty 23. Tape equator
Conformity tests	Test procedure	24. Placement of electronics module on a test bench using dedicated tooling; 25. Acceptance testing of the electronics on a test bench; 26. Storage of test results in database;
Sign off	Final procedures	27. Packaging of storage electronics module 28. File storey electronics module documentation 29. Update the database

Table 3.20: Assembly steps for the storey electronics module.

Multi-PMT		
Components	1. Glass hemispheres 17 inch (2) 2. 3 inch PMT including high voltage base(31) 3. Foam core for 19 PMTs and piezo acoustic sensor(1) 4. Foam core for 12 PMTs and pressure gauge(1) 5. Optical gel (2 components) 6. Outer connection: penetrator-storey cable-connector (1) 7. Signal collection board (2) 8. Storey logic board containing compass/tiltmeter(1) 9. Converter board (1) 10. Cooling mushroom (1) 11. Pressure gauge (1) 12. Nano-beacon with electronics board (1) 13. Piezo acoustic sensor with electronics board (1) 14. Storey connection ring (1)	
Lower Hemisphere assembly	PMT and Piezo-acoustic sensor positioning	1. Placement of the foam core on a dedicated assembly table in the clean room; 2. Positioning of 19 PMTs with bases in the foam core; 3. Connection of the PMTs to their signal collection board; 4. Placement of the hemisphere on the dedicated assembly table using dedicated tooling; 5. Cleaning of the hemisphere; 6. Electrical acceptance test of the piezo-acoustic sensor; in case of failure replace; 7. Gluing the piezo-acoustic sensor at a predetermined location to the hemisphere; 8. Placement of the foam core with PMTs - using additional tooling - in the hemisphere;
	PMT acceptance test	9. Storage of the hemisphere in dedicated dark box to re-s tore the capacity of the PMT photocathodes of the PMTs; 10. At 400 V test and record power consumption with electronic circuits off; 11. Switch on electronic circuits and measure and verify dark count rate and power; 12. Record results in a test report and in the data base; in case of failures replace PMT and base.
	Establishing optical contact	13. Mixing the 2 components of Wacker Silgel 612A/B in ratio 60/40; 14. Pouring of the optical gel between the glass hemisphere and foam core carrying the PMTs; 15. Out-gassing the optical gel and waiting for it to polymerize.

Upper hemisphere assembly	Hemisphere preparation	16. Placement of the foam core on a dedicated assembly table in the clean room; 17. Cleaning of the hemisphere; 18. Mounting of the EO penetrator in the glass hemisphere; 19. Gluing of the cooling mushroom at a predetermined location to the glass hemisphere; 20. Mounting the converter board 21. Connection of converter board to penetrator; 22. Mounting of the auxiliary boards on the storey logic board; 23. Performance of electrical acceptance tests of the "nano-beacon"; in case of failure replace; 24. Gluing of the "nano-beacon" to the hemisphere at a predetermined location; 25. Connection of the storey logic board with compass and tilt-meter to the power converter board; 26. Connection of the "nano-beacon" to the auxiliary board; 27. Mounting storey logic board on the cooling mushroom;
	PMT positioning	28. Fibre splice of readout fibre; 29. Placement of the foam core on the assembly table in the clean room; 30. Insertion of the 12 PMTs with bases and a pressure gauge (0-1 bar_{abs}) in the foam core; 31. Connection of the PMTs to the "Oktopus" signal collection board; 32. Placement of the core over the stem of the cooling mushroom; 33. Mounting of the "Oktopus" board on the cooling mushroom;
	PMT acceptance test	34. Storage of the hemisphere in a dedicated dark box to restore the capacity of the cathode of the PMTs; 35. Performance of acceptance tests on the PMTs in the dark box (identical to lower hemisphere). In case of failure replace;
	Establishing optical contact	36. Mixing the 2 components of Wacker Silgel 612A/B in ratio 60/40; 37. Pouring of the optical gel between the glass hemisphere and foam core carrying the PMTs;
		38. Out-gassing the optical gel and waiting for it to polymerise.

Sphere Assembly	Sphere assembly	39. Placement of assembled lower and upper hemispheres in dedicated tooling and closure of sphere; 40. Placement of sphere in a vacuum glove box; 41. Flushing with dry nitrogen; 42. Reduction of pressure to 700mbarabs; 43. Applying protection to the external joint between the two hemispheres;
Conformity test	Test procedure	44. Using dedicated tooling the OM is placed in a dark box with LEDs for functionality tests and the results of the following tests will be stored in a data base: 45. Powering all electronic circuits; 46. Measurement of the power consumption of the OM; 47. Creation of a look up table with an electronic ID for each PMT; 48. Mapping of the location of each PMT by switched fibres to each PMT, driven from a central LED; 49. Measurement of the dark current rate for each PMT; 50. Switching between several wavelengths, checking and logging communication; 51. Switching between several attenuations in the optical system; 52. Testing of the minimum OM switch-on voltage level and the auto shutdown level; 53. Testing of the slow control communication; 54. Calibration of the compass/tiltmeter, "Nano-beacon" and piezo-acoustic sensor; 55. Storage of test results in the data base
Sign off		56. Attachment of the storey connection ring 57. Packaging of optical module 58. File optical module documentation 59. Update database.

Table 3.21: Assembly steps for the Multi-PMT optical module.

Capsule		
Components	1. Glass half capsules (2) 2. 8 inch PMT (2) 3. Magnetic field cage (2) 4. High voltage base (2) 5. Voltage converter board (2) 6. Storey logic board including 2 frontend chips (1) 7. Cylindrical supports (2) 8. Outer connection: penetrator-cable-connector (1) 9. Pressure gauge (1) 10. Piezo acoustic sensor with electronics board (1) 11. Nano-beacon with electronics board (1)	
Half-capsule production (2x)	PMT and magnetic field cage positioning; establishing optical contact	1. Placement of the half-capsule on the dedicated assembly table using dedicated tooling; 2. Cleaning of half-capsule (ethyl alcohol); 3. Cleaning of mu-metal magnetic field cage; 4. Mixing the 2 components of Wacker Silgel 612A/B in ratio 60/40; 5. Mounting the EO penetrator only in one half-capsule; 6. Pouring the gel into half-capsule 7. Placement of the hemispheric part of the mu-metal® magnetic field cage in the optical gel; 8. Outgassing the gel; 9. Placement of the PMT in the optical gel with a 5mm gap between the glass and the PMT; 10. Repeated out-gassing; 11. Polymerisation of the optical gel over a period of 8 hours; 12. Installation of the ring segment of the mu-metal magnetic cage; 13. Mounting pressure gauge in one of the half-capsules
	PMT acceptance test	14. Storage of the hemisphere in dedicated dark box to restore the capacity of the PMT photocathodes of the PMTs; 15. Test dark current and single photon response; 16. Record results in a test report and in the data base; in case of failures replace PMT and base

	Electronics installation, piezo acoustic sensor and nano-beacon positioning	17. Soldering of power conversion board to input wires on penetrator 18. Mounting the converter board in cylindrical support; 19. Placement of piezo acoustic sensor electronics board in cylinder 20. Testing electrical connection piezo acoustic sensor 21. Placement of nano-beacon acoustic sensor electronics board 22. Testing electrical connection nano-beacon 23. Mounting the storey logic board in cylinder 24. Gluing cylindrical support to glass of one of the half-capsules; 25. Gluing piezo acoustic sensor to the glass of one of the half-capsules 26. Gluing nano-beacon to the glass of one of the half-capsules 27. Soldering the storey logic board to the PMT signal wire 28. Soldering the HV base to electronics boards. 29. Connection of the HV base to the PMT;
Capsule assembly	Capsule assembly	30. Placement of assembled half-capsules in dedicated tooling and closure of capsule; 31. Placement of capsule in a vacuum glove box; 32. Reduction of pressure to 700mbar$_{abs}$; 33. Sealing "equator" with putty; 34. Taping equator;
Conformity tests	Test procedure	35. Using dedicated tooling the OM is placed in a dark box with LEDs for functionality tests and to perform acceptance tests: 36. Measure the power consumption of the OM; 37. Creation of lookup table with electronic ID for each PMT; 38. Measure the dark current rate for each PMT; 39. Test the minimum OM switch-on voltage level and the auto shutdown level; 40. Test the slow control communication; 41. Storage of test results in database; 42. Packaging of optical module 43. File optical module documentation 44. Update database

Table 3.22: Assembly steps for the capsule optical module.

3.6.1 Detection unit integration

The integration of the detection units is described in Table 3.25 for the bar detection unit. Table 3.26 describes the production steps for the triangle detection unit and finally Table 3.27 gives the integration procedures for the string detection unit.
The time estimated for full integration and testing of both the bar and the triangle detection units is 20 fte days. As in the string case a single multi-PMT optical module is also the full storey the integration time of the string detection unit is 5 fte days. In all cases there is a workforce of 2 at all times. Table 3.23 and Table 3.24 show the summary of the times required and the total fte days required to build the full detector of either bar or triangle and string design. Also indicated is the spread of the workforce over optical module, electronics module and detection unit integration, in order to achieve matching of the production speeds. The workforce required for completion within 5 years is in both cases around 50. Split 3:2:1 over optical module, electronics module and detection unit assembly for the bars and triangles. The workforce is spread over optical module production and detection unit assembly in the ratio 12:1 for the string detection unit. A production rate of 5 years requires a large yearly production rate of some items, most notably the photomultiplier tubes and glass spheres. The numbers required for the main items for the different design options are given in Table 3.28. The production rate for the photomultipliers is 80000 3 inch or 8000 8 inch tubes per year. These numbers have been discussed with the two available manufacturers and although this is a large number neither manufacturer saw significant problems. For most other items the production rate is not severely challenging.

	# units	Fte days per unit	Total
Optical module	38400	0.67	25600
Electronics module	6400	2	12800
Detection unit	320	20	6400
Total fte days per detection unit			44800
Total fte years			224

Table 3.23: Required work force for the assembly of a bar or triangle detection unit.

	# units	Fte days per unit	Total
Optical module	13000	3	39000
Detection unit	650	5	3250
Total fte days per detection unit			42250
Total fte years			211

Table 3.24: Required work force for the assembly of a string detection unit.

Storage and stock management

Secure storage facilities will be needed at component and detection unit integration sites and at the on-shore final assembly point before loading onto the deployment ship. The appropriate storage conditions (temperature, humidity, ambient light levels…) will depend on the nature of the product and the degree of completion.

Transportation

During production many thousands of items will have to be delivered to assembly sites around Europe (and perhaps outside). The detection units must then be delivered to the deployment harbour. The organisation of the logistics will most likely be outsourced. ANTARES, for instance, successfully used the CNRS-IN2P3 "Ulisse" (Unité de logistique international), which is a user-friendly web-based logistics system with transportation units around Europe. "Ulisse" could also be a good candidate for KM3NeT.

Bar DU assembly Components		
	1. Storey frames (20) 2. Optical modules (6x20) 3. Optical module storey cables (6x20) 4. Dyneema® tensioning ropes on reels (19x4 of ~40 m; 4 of ~100m; 4 of 20m between highest storey and buoy) 5. Backbone cable on reel (including master module) (1) 6. Buoy (1) 7. Anchor trellis (1) 8. DU base structure (1) 9. Master module (1) 10. Interlink cable on drum (1) 11. Acoustic release system (1)	
Storey assembly (20x)	Preparing the assembly location	1. Using a crane placement at the storey assembly location: 2. Storey frames (55 kg) 3. Electronic modules (20 kg) 4. Optical module storey cables 5. Optical modules using dedicated tooling (12 kg)
	Storey assembly and calibration	6. Using dedicated tooling placement of the optical modules (12 kg) on the storey frame 7. Using a crane placement of the storey electronics module (20 kg) on the storey frame 8. Connections between the optical modules and the storey electronics module 9. Using a crane placement of storey (115 kg) in the dark room with dedicated test setup 10. Performance of calibration tests 11. Storage of results in data base 12. Using a crane to store/transport storey (115 kg) to DU integration location
DU assembly	Preparing the assembly location	13. Using a crane, placement at the DU assembly location of: 14. Anchor trellis (3000 kg) 15. DU base plate (65 kg) 16. Buoy (1500 kg) 17. Interlink cable at its drum 18. Storeys (115 kg) 19. Backbone cable on reel 20. Tensioning ropes
	Assembly of DU base	21. Placement of DU base structure (65 kg) on the anchor trellis using a crane 22. Mounting acoustic release system between trellis and base structure

		23. Placement of the interlink cable drum on the DU base structure using a crane 24. Attachment of 100 m backbone cable section 25. Connection between interlink and backbone cable 26. Attachment of 4x100 m rope to DU base structure
	Stacking storeys and buoy	27. Placement of a storey (115 kg) on the previous one (or on the anchor trellis) using a crane 28. Connection of the electronics module to the backbone cable 29. Testing of optical and electrical connectivity of the optical modules 30. Measurements of signal and clock transit time without powering the optical modules 31. Storage of test results in data base 32. Repetition of steps 23-28 for 20 storeys 33. Attachment of 20 m ropes between and last triplet and buoy 34. Placement of the buoy (1500 kg) on top of the DU using a crane 35. Using a crane storage/transport of DU (7500 kg) for 'ready to deploy' phase
Deployment	At sea	36. Deployment of the detection unit (7000 kg) using a crane

Table 3.25: Assembly steps for the bar detection unit.

Triangle DU assembly	
Components	1. Storey frames (20) 2. Optical modules (6x20) 3. Optical module storey cables (6x20) 4. Storey electronics module (with storey cable and connector)(20) 5. Segments of backbone cable with 3 breakouts (7x150 m) 6. Segment of backbone cable (100 m) 7. Dyneema® tensioning ropes (20x6) for the crow-foot rigging of the storey 8. Buoy (1) 9. Base plate (1) 10. Anchor dead weight (1) 11. Master module (1) 12. Interlink cable on drum (1) 13. Reusable deployment "bell" (1) 14. Reusable acoustic release system (1)

Pre-deployment triplets	Preparing the assembly location	1. Using a crane, placement at the triplet assembly location: 2. Storey frames 3. Electronic modules 4. Optical module storey cables
	Storey assembly, calibration and integration into triplet	5. Using dedicated tooling placement of optical modules 6. Using dedicated tooling placement of the optical modules on the storey frame 7. Using a crane placement of the storey electronics module on the storey frame 8. Connections between the optical modules and the storey electronics module 9. Using a crane placement 10. Performance of calibration tests 11. Storage of results in data base 12. Step 6-11 is repeated 3 times 13. Using a crane integration of the 3 storeys into a nested pre-deployment triplet
DU assembly	Preparing the assembly location	14. Using a crane, placement at the DU assembly location of: 15. Base plate and buoy 16. Master module and interlink cable at its drum 17. Nested pre-deployment triplets 18. Backbone cable segments and tensioning ropes
	Assembly of DU base	19. Placement of the master module on the base plate using a crane 20. Placement of the interlink cable drum on the base plate using a crane 21. Attachment of 100 m backbone cable section 22. Connection of interlink cable to backbone cable
	Stacking storey triplets	23. Placement of a storey triplet on the previous triplet (or on the base plate) using a crane 24. Placement of a backbone cable segment into the cable tray of the triplet using a crane 25. Attachment of the cable segment to the previous segment 26. Attachment of all the storey electronics modules in the triplet to a break out of the segment backbone cable 27. Testing of optical and electrical connectivity of the optical modules 28. Measurements of signal and clock transit time without powering the optical modules 29. Storage of test results in data base

		29. Storage of test results in data base 30. Repetition of steps 22-28 for 7 triplets 31. Using a crane storage/transport of the pile of triplets (supporting frame??)
Ready to deploy	Anchor	32. Using a crane placement of dead weight anchor 33. Using a crane placement of detection unit on the dead weight 34. Connection of DU base plate to dead weight
	Buoy integration	35. Attachment of 20 m ropes between and last triplet and buoy
	Bell	36. Placement of the buoy on top of the DU using a crane 37. Using a crane placement of the "bell" (1500 kg) over the detection unit 38. Attachment of the "bell" to the anchor dead weight using acoustic release system

Table 3.26: Assembly steps for the Triangle detection unit.

String DU Assembly Components		
	1. Storey (optical module with storey cable and connector) (20) 2. Dyneema® ropes on reel(2 x 880 m) 3. Backbone cable on reel (including master module) (1) 4. Empty spheres for buoyancy (13) 5. Concrete anchor dead weight (2x2x0.25m^3) (1) 6. Reusable deployment frame with empty glass spheres for buoyancy of the frame (300 kg) (1) 7. Interlink cable on drum (1) 8. Reusable acoustic release system (1)	
DU assembly	Preparing the DU assembly location	1. Using a crane placement of at the DU assembly site: 2. Anchor dead weight (2000 kg) 3. Deployment frame in the dedicated tooling for winding the string (300 kg) 4. Backbone cable at reel 5. Ropes 6. Interlink cable at its drum 7. Using dedicated tooling placement of the optical modules
	Buoy integration	8. Attachment of the ropes to an empty glass sphere; 9. Placement of the glass sphere in the deployment frame; 10. Repetition of steps 5 and 6 for all empty glass spheres that form the buoy of the string.

Ready to deploy	Storeys and backbone cable integration	11. Attachment of the backbone cable to one of the ropes near the location of a break out; 12. Connection of the optical module to the backbone cable; 13. Testing of optical and electrical connectivity of the
		optical module (optical module replaced in the event of failure); 14. Storage of test results in data base 15. Attachment of the storey to the ropes; 16. Placement of the storey in the deployment frame; 17. The winding of the backbone cable and the ropes onto the deployment frame until the next break out; 18. Repetition of steps 8-14 -until all storeys and the master module are mounted in the deployment frame changing orientation of winding twice; 19. The winding of the rest of the backbone cable and ropes onto the frame; 20. Using crane storage/transport of the DU (800 kg + weight of backbone cable and ropes) for the 'making the DU ready-to-deploy' phase of the integration procedure. 21. Placement of the anchor (2000 kg) at the 'ready to deploy' location using a crane. 22. Placement of the DU in the deployment frame (1000 kg) on the anchor using a crane; 23. Mounting of the drum with the interlink cable on the anchor using a crane; 24. Attachment of the ropes to the anchor; 25. Connection of the interlink cable to the backbone cable; 26. Mounting the acoustic release system to the deployment frame
	At sea	27. Deploy the DU and its anchor (3100 + weight of interlink, release) using a crane

Table 3.27: Assembly steps for the string detection unit.

3.7 Marine Operations

Marine operations are required for the transfer of the assembled detection units from the supply harbour at the coastline to the intended offshore site and then for the deployment of the telescope parts on the sea-bed at a depth of 3000 – 5000 m.
In order to perform marine operations specialised equipment, has to be available. This equipment includes cranes, winches, A-frames, deck space for storage, handling facilities for underwater vessels, dynamic positioning according to GPS. These items are in routine operational use on cargo vessels, research vessels or offshore supply vessels.

		Tower	String	Triangle
Photo-multipliers	8"	40000		40000
	3"		400000	
Glass spheres	13"	45000		45000
	17"		13000	
Dyneema® rope (km)		1150	880	
Backbone cable (860 m)		320	650 (670 m)	320
Wet mateable connectors		320	650	320
Backbone storey connection cable		6400	13000	6400
Electronics to optical module cable (triple)		12800		12800
Bulkhead connectors (4 copper)		80000		80000
Mechanical storey frame		6400		6400
Converter board		6400	13000	6400
Storey logic board (capsule)		6400 (19200)	13000	6400 (19200)
Frontend electronics board		40000	On SLB	40000

Table 3.28: Quantities required of the major items in the detection units.

A detailed description of marine operations cannot be presented here because the specific requirements depend largely on the design of the telescope and the location of the offshore site. Therefore only general aspects of the deployment can be discussed at this time, and specifics will have to be deferred to a time when the design is finalized.

3.7.1 Deployment and connection

The detector deployment concept is based on the idea of deploying the detection units as compact packages to the seabed. After the correct positioning on the seabed, the structure is connected to the sea-floor cable network. Unfurling of the detection unit to reach its working configuration is obtained by actuating an acoustic release system. The detection unit self-unfurls under the pull provided by its buoyancy.

This deployment concept has several advantages:

- easy handling of the structures on-shore for loading on the surface vessel;
- reduced space requirements on the ship deck so that an increased number of structures can be deployed in a single operation;
- less time needed to lift and immerse the structure in the water, providing increased safety for the operating personnel.

Deployment of Detection Units

During the deployment the detection unit is a compact package. This package has to be deployed and positioned at depths beyond 2500 m. The final working configuration will be reached, after deployment and connection of the structure, by remotely actuating an acoustic release system. The unfurling of the structure will be driven by the pull of the top buoy. The operation sequence is the following:

- Lifting of the structure on the sea surface vessel deck;
- Immersion of the structure in the water. This operation and the previous one are performed using the vessel's deck equipment;
- Lowering of the structure close to the seabed. This operation requires a winch with a cable length sufficient for the site depth;
- Positioning of the structure on the seabed. The required accuracy (order of few metres) requires the availability of a long-baseline acoustic positioning system ;

Deployment of Junction Boxes

A design of the junction box has not been developed yet. For the deployment considerations we will assume that each junction box is a structure with size 3 m x 3 m, a height of 2 m and a weight of no more than 3000 kg.
The deployment procedure is then analogous to the one described for the detection unit.

Connection of Detection Units and Junction Boxes

After the deployment of the telescope components an ROV will be used to connect them to the seabed network. The ROVs are described in some detail in Section 3.7.2. The detection units and junction boxes are interconnected by a network of electro-optical cables with lengths of the order of a few hundreds metres. These cables have to be accurately laid on the seafloor along well-determined paths in order to avoid damage to the network during successive deployment of telescope components and ROV operations. Interlink cables that connect detection units to the secondary junction boxes will be deployed to the seabed together with the detection unit on drums. The drums are taken by the ROV and the cable unrolled on the seafloor. This method has been well tested in the installation of ANTARES.

3.7.2 Vessels

The surface and deep-sea vessels needed are:

- a sea surface vessel, used to transfer, deploy and install components of the deep sea neutrino telescope at the bottom of the sea, equipped with a Dynamic Positioning (DP) system;
- a deep-sea ROV.

Sea surface vessels

The sea surface vessel used in deploying the telescope components has to be equipped with a dynamic positioning system in order to allow for accurate positioning of the detection units. For safety reasons a vessel equipped with a fully redundant dynamic positioning system would be advisable. In addition, the ship deck should have a size adequate for many detection units and be equipped with lifting equipment.
The minimal characteristics of the sea surface vessels are:

- Dynamic positioning system able to maintain the ship position to within 1 m for sea states up to level 5;
- Available space on the ship deck of ~250 m^2;
- Crane for 10 t load;
- A winch with a long cable, a cable speed control for between 0.1 m/s and 1 m/s, a load measuring system with 100 kg accuracy and heave compensation;
- Ship deck allowing at least 1500 kg/m^2 load;
- Extra space on the ship deck for two standard 20 foot equipment containers.

Two general variants of the deployment operations are being considered:

- A surface vessel equipped with a dynamic positioning system is used both for the transportation of the detection units from shore and for the deployment operation. Such vessels can be contracted for defined periods of time and are permanently shuttling between shore and site.

- An adequate vessel (e.g. a transport barge) is used for the transfer of the components to the site. A surface platform, equipped with a dynamic positioning system and the other required equipment is used for the actual deployment. This deployment platform could be an offshore supply vessel with an adequate deck space for storage of the detector parts to be deployed.

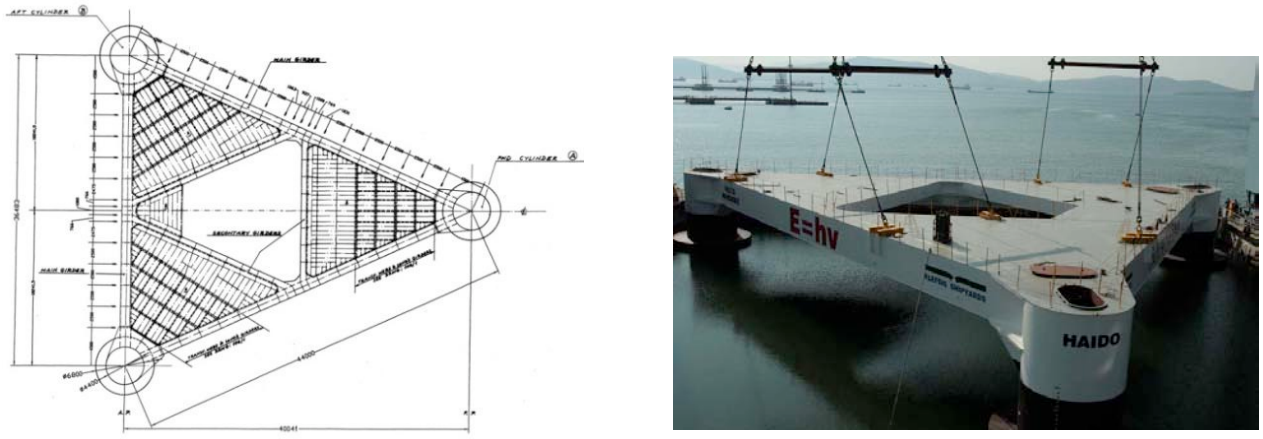

Figure 3-48: Surface platform "Delta Vereniki" Left: Mechanical drawing of girder structure; Right: Photo during launch.

The surface platform considered here is, for instance, "Delta Verenike" of the NESTOR Institute (see Figure 3-48). This platform has all the necessary equipment for station keeping and deployment. It is able to stay at the site for prolonged periods of time, while performing deployment operations. The transport barge meanwhile shuttles between shore and site bringing more detection units to be deployed. The platform has a large opening at the centre of its deck for deployment operations. It is equipped with several winches, a standard crane for lifting and lowering equipment to and from the working deck, a movable crane structure across the central opening.

Underwater vessels

Operations on the seabed will be performed by means of a ROV controlled from the surface. It is an underwater robot that allows the vehicle's operator to remain in a sea surface control room while the ROV performs the work underwater following the operator's commands. An umbilical cable carries power and command and control signals to the vehicle and status and sensor data back to the operator. This method was extensively used during the deployment of the ANTARES pilot project.

The ROV used in this case was the VICTOR (see Figure 3-49) that has an operating depth of 6000m and is capable of lifting and manipulating objects with an underwater weight of up to 100 kg. It is owned and operated by Ifremer. An example of a light work class ROV is the specially modified Seaeye Cougar-XT ROV (see Figure 3-49) which was used in the PEGASO project. This ROV is of the tethered kind, i.e. one in which the main umbilical cable runs from the surface support vessel to a garage that carries the ROV and is deposited at the sea floor. The ROV travels from this garage on the sea floor to the desired location while being connected to the garage by a light-weight tether. This particular ROV had a maximum operating depth of 4000m, a 250m long tether, a system for connecting and disconnecting wet-mateable connectors, a connector cleaning system, and two manipulators with five degrees of freedom. Similar ROVs exist that can go down to depths of 5000 m and can be used at any of the proposed sites.

Figure 3-49: The Ifremer VICTOR ROV and a light class Seaeye Cougar-XT ROV shown at the right in its subsea "garage".

4. Earth and sea sciences infrastructure

The Earth-Sea Science infrastructure is designed to be site independent to ensure the experienced gained in building and operating the node can be shared by future cabled observatory programmes around Europe. As a result this report deals with the seafloor infrastructure and not the instrumentation.
The list of functions of an ESONET/EMSO subsea observatory will be either shared with KM3Net telescope *(Shared)* or provided by the KM3Net telescope *(telescope)* or specific to the Earth-Sea science segments *(Specific)*:

The functions and components of a subsea observatory are:

1) Management of the infrastructure *(Specific)*
2) Dissemination and user interfaces *(Specific)*
3) Data bases *(Specific)*
4) Technical supervision infrastructure *(Specific)*
5) Onshore network *(Specific)*
6) Land Base termination of sea infrastructure *(telescope)*
7) Land sea communication segment *(Shared)*
8) Node from branching unit to Main junction box *(Shared)*
9) Branch extension of the network - uplink *(Specific)*
10) Secondary junction box *(Specific)*
11) Link to instruments - downlink *(Specific)*
12) Individual instrument *(Specific)*

The following sections describe components 9 to 11

4.1 General description

The Earth-Sea Science node will be connected to the KM3NeT main electro-optical cable via a primary junction box to which up to three secondary junction boxes, distributed around the neutrino telescope, will provide the required infrastructure.

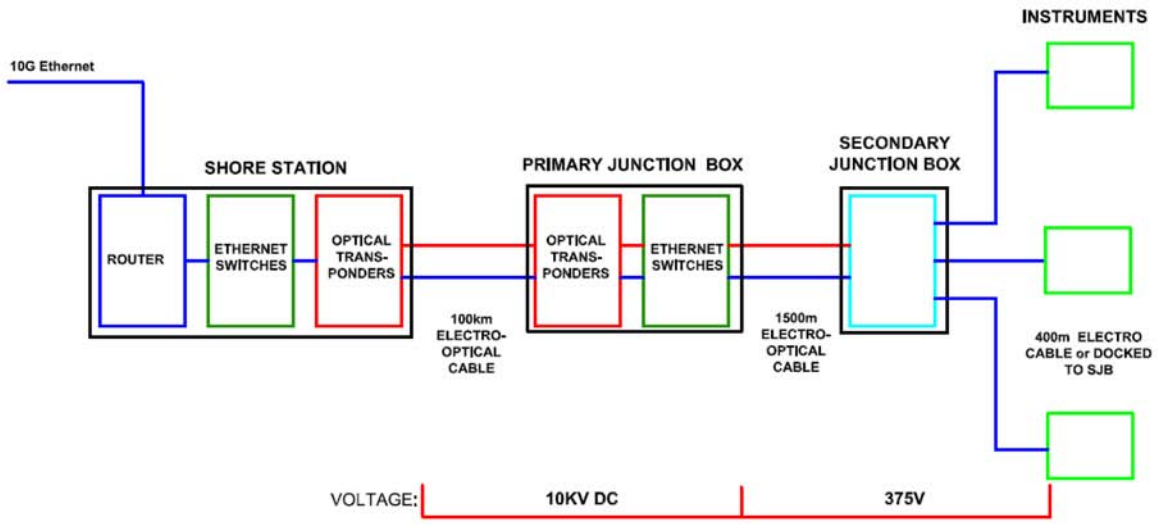

Figure 4-1: KM3NeT Earth-Sea Science node Network Architecture.

This infrastructure may consist of combinations of the following:

- Lines of autonomous sensors such as seismographs
- Moorings containing suites of instruments to monitor surface water, water column, sea bed and sub sea-floor
- Fixed structures with removable modules containing instruments such as cameras and flash lights, acoustic sensors and suites of oceanographic sensors such as the proposed ESONET standard instrumentation module

The electro optical cable and primary junction box will have identical specifications to those of the neutrino telescope and will be part of the common infrastructure. The secondary junction boxes however will have different requirements and will therefore be specific to the Earth-Sea science infrastructure.

The optimal layout of the Earth-Sea Science cable would be circular around the foot print of the telescope array however that will depend on the topology, telescope expansion plans and costs.

4.2 Junction box

The KM3NeT Earth-Sea science junction box will be based on the commercial junction box designed by OceanWorks International for the Neptune Canada deep-sea observatory. Some parts of the design may, however, need changing in order to meet the KM3NeT requirements.

The network architecture for the Earth-Sea science node is shown in Figure 4-1.
Note that in this architecture the node is the equivalent of the KM3NeT primary junction box and the primary junction box is the equivalent of the Earth-Sea science secondary junction box. The instruments are connected to the OceanWorks International junction box shown in Figure 4-2.

Figure 4-2: OceanWorks International Junction box.

The junction box supports a maximum of ten downlink interfaces and one uplink interface. It receives an input of 300-400 volts DC at up to 22.5 amps on the uplink interface from which all external and internal loads are powered.

The 400V power bus is referenced to seawater ground at the node such that two power leads are nominally +200V and -200V with respect to sea water. In case of a seawater ground fault, the junction box is designed to continue operating on either of the lines. The uplink power conductors have an isolation potential of at least 600V from seawater or pressure case. Figure 4-3 shows the Neptune Canada infrastructure.

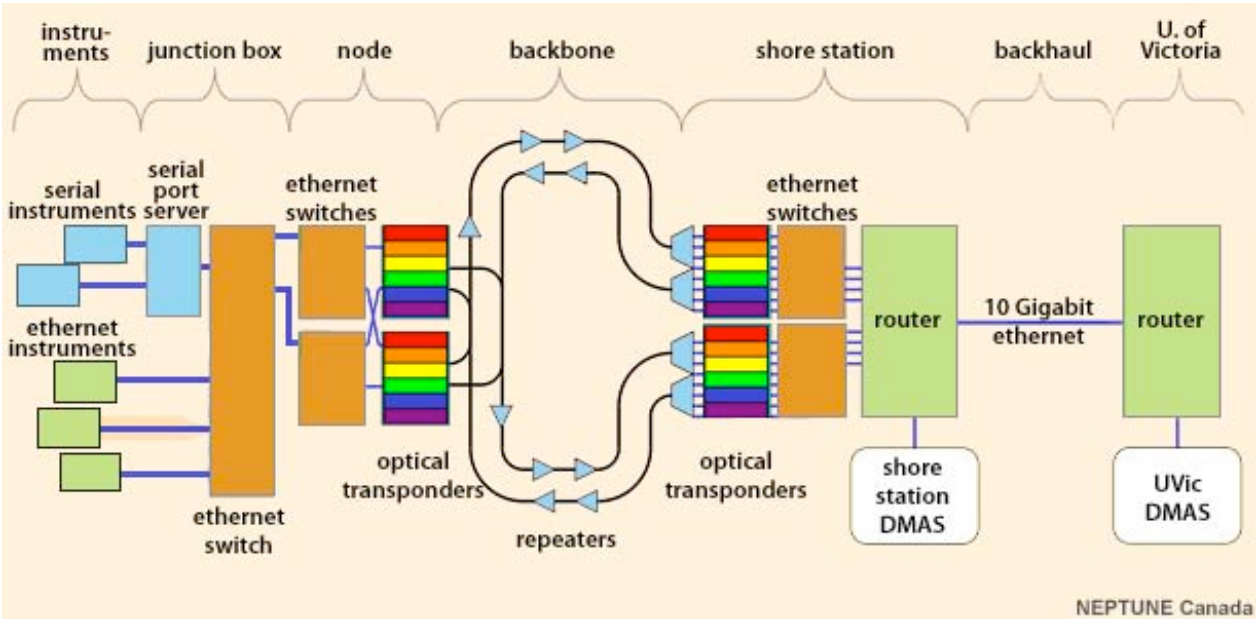

Figure 4-3: Neptune Canada Network architecture from data centre to instrumentation.

Cable Interface

The communications interface for the uplink interface is provided via one of the following:

- 100Base-T Ethernet;
- 1000Base-LX Ethernet on two single mode fibres;
- Dual 1000Base-LX Ethernet Links using four single mode fibres.

Each downlink provides a DC power supply circuit and a communications link which may consist of a combination of the following:

- Up to 600 watts at 48 volts;
- Up to 75 watts at 12V, 15V, 24V or 48V;
- Up to 150 watts at 24V or 48V;
- Other power levels at 12V, 15V, 24V or 48V are determined by the thermal limitations within the junction box;
- 10/100Base-T Ethernet;
- EIA-232, EIA-422 or EIA-485 serial data at up to 115.2 Kb/s;
- 1000Base-LX Ethernet.

The Ethernet uplinks comply with IEEE 802.3-2005 protocol. Optical uplinks consist of one or two bi-directional 1000Base-LX, each using two single mode fibres for a total of two or four fibres and support IEEE 802.3ad Link Aggregation Control Protocol (LAPC).
Each Ethernet downlink interface supports one 100Base-T communications link compatible with any of the following output voltage levels: 12V, 15V, 24V, 48V, 300 to 400V. Each signal line is transformer coupled to maintain isolation in the event of a connector leak. They are IEEE 802.3-2005 compliant. Each junction box has a maximum of four serial communications downlink interfaces to connect the instruments. They support one of EIA-232, EIA-422, or EIA-485 communication link at operating up to 115.2 kb/s. The interface is software configurable. Each serial downlink interface is compatible with any of the following output power voltage levels 12V, 15V, 24V, 48V, 300-400V. Each signal line is optically isolated to maintain isolation in the event of a connector failure.

Downlink power conductors have an isolation potential of at least 100V from seawater or pressure housing. Conductors enter the pressure vessel through a Seacon MINK-10 (2#14, 8#20)-FCRL-TI penetrator.
Each junction box allows for the addition of two optical downlink interfaces supporting one 1000Base-LX Ethernet communications link and compatible with any of the following output power levels: 12V, 15V, 24V, 48V, 300-400V.
Conductors and fibres for an optical downlink enter the pressure vessel through an ODI Hybrid Bulkhead Penetrator having a 1.312 inch diameter bore and a 3 inch diameter flange. The Ethernet downlinks comply with IEEE 802.3-2005.

Communications Interface

The communications switch is equipped with a fully managed Ethernet switch or multiple connected switches to satisfy the number of interfaces. The switch is software configurable and can be accessed via remote control either via telnet or http. It can also be upgraded remotely.

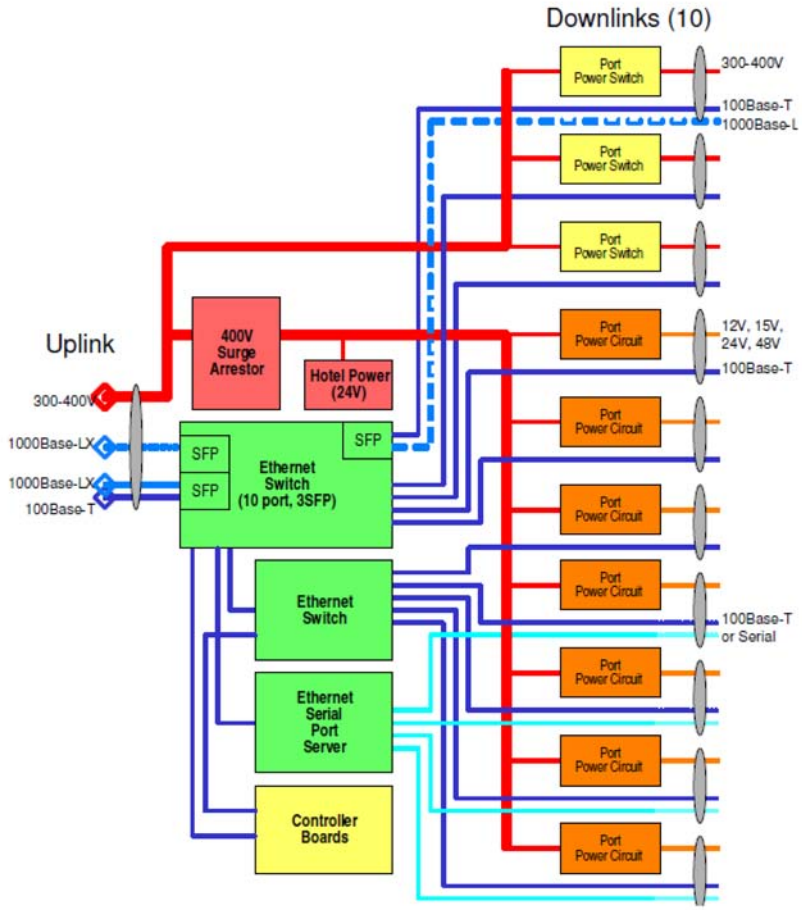

Figure 4-4: OceanWorks junction box block diagram.

The junction box supports IPv4 and IPv6 internet protocols. It tolerates a bit error rate for underwater interface to shore interface link of 1×10^{-12} or the equivalent packet loss rate of 1.2×10^{-8}. The Junction box switches support IEEE 802.1Q virtual local area network tagging for data routing and prioritisation, IP multicast and IEEE 802.3ad link aggregation control protocol on the 1000Base-LX uplinks only. The junction box controller uses TCP/IP or UDP only (IP broadcast is only ever used for address resolution).

The junction box is equipped with one or more fully managed Ethernet Serial Server(s) (ESS) satisfying the number of interfaces. Where instrumentation is limited to serial communications only, the data is encapsulated in IP for transmission to the shore station using the ESS. The ESS software can be reconfigured or upgraded remotely via telnet. Figure 4-4 depicts a block diagram of the Oceanworks junction box.

Electrical interface

The junction box supports a maximum of three interfaces. Each interface is capable of 15 A output at 300-400V.
At least one interface per junction box shall support a 600 watt output at 48V.

The available electrical interface configurations are as follows:

- 15 A at 300-400 V;
- 600 W at 48 V;
- 150 W at 48 V;
- 150 W at 24 V;
- 75 W at 12 V;
- 75 W at 15 V;
- 75 W at 24 V;
- 75 W at 48 V.

The voltage regulation from no load to full load steady state is better than 1%. Interfaces supporting other power levels can be supported provided the thermal design of the junction box can accommodate them.
The voltage level received on the uplink interface is delivered to any 300-400V output and is not required to be stabilized or adjusted.
The voltage converter efficiency is 80% or better at full load.

The junction box is designed such that a dead short applied to any downlink interface will not cause permanent damage to any other interface. Both power and return paths are isolated from seawater and neither the metal chassis nor the pressure housing is used as the current return path. There is no low resistance connection between either side of the power supply or any communications line and the ground within the junction box.
The junction box has active and passive surge arresting capability to prevent overvoltage up to 800 V on any 400 V uplink or downlink from damaging the junction box components. Peak voltage, peak current and maximum energy dissipation are to be confirmed.
Mechanical and Environmental Interfaces
The junction box enclosure provides a 1 Bar air-purged environment for the internal components. The housing is designed for a fifteen year operational life cycle of continuous sea water submersion with no degradation to system performance. Provision is made to recover the junction box every five years for refurbishment and redeployment. The operational depth of the junction box is 3000 m and may need to be upgraded.
The junction box is designed to operate in ambient water temperatures down to 3˚C and be able to tolerate temperatures of between -20˚C and 70˚C during transport and installation.

Operational and Control Procedures

The junction box is operated continuously and reports its status on a regular basis as well as on request. The junction box will start up automatically once power is provided either from a primary or another secondary junction box. It returns to a safe state when power is withdrawn.

Each instrument is monitored for power consumption and fault diagnostics. The following are measured and reported by the junction box at a rate of at least 1 Hz:

- Voltage levels on 12 V, 15 V, 24 V and 48 V outputs with a 100 mV resolution and a ± 0.5 V accuracy;
- Current levels on all outputs are measured with a resolution of 20 mA and ±100 mA accuracy;
- Ground faults with resistances between 5 kΩ and 5 MΩ shall be detected on the 12 V, 15 V, 24 V and 48 V outputs with an accuracy of ±20 % ;
- Alarm thresholds for each interface shall be configurable via software.

Each interface can be remotely disabled to prevent damage to the junction or other instrumentation and re-enabled once problems have been solved. In such instances power and communication lines are isolated such that they provide no current path from any external connector pin to any internal component or chassis. The temperature within the junction box housing shall be monitored with a resolution of ±1 ˚C. The junction box input power supply is measured and monitored with ±1 V accuracy.
Data is transmitted via a continuous UDP stream at a rate of at least 1 Hz. The junction box is equipped with a controller to communicate with the control centre, monitor interfaces and internal sensors, and control the interfaces. The controller has an IP address, is software configurable and can be controlled and upgraded remotely. The junction box responds to commands sent asynchronously from the shore station such as requests for status information and data transmission. Command execution is always acknowledged.
The junction box internal clock can be set by command to within 2 seconds accuracy. There is no requirement for the junction box to pass timing signals to the instruments. Instruments are required to acquire timing signals using network time protocol or precision time protocol. The junction box provides a means of locating and isolating faults in internal components, including but not limited to power converters, optical transmitters and receivers, switches, ESS, and other communications equipment, without underwater intervention. Performance, fault, configuration and security information is transmitted to the shore station.
Estimates of the overall reliability based on components, sub-assembly, or sub-system reliability data and using appropriate calculations or modelling are included. They are calculated based on Telcordia, MIL-HDBK-217F, or other recognised standards. FIT (Failure in Time) & MTBF (Mean Time Between Failure) figures are provided together with their source. The probability of complete failure within the first year of operation does not exceed 10% where complete failure means a failure of all junction box ports. Assuming there are no duplicated or redundant components within the instrument, this probability of failure is equivalent to a total FIT for core components of 12,000 or less where core components are those whose failure would cause all ports to become unusable.
For a system with no redundant components, FIT and probability of failure over a given time period are mathematically linked as follows:
$MTBF\ (hours) = 10^9 / FIT$;
$MTBF\ (years) = MTBF\ (hours) / 8760$;
The failure rate: $R_{fail} = 1 / MTBF$;
The failure probability in time t: is given by $P_{fail}(t) = 1 - e^{-R_{fail}\,t}$.

4.3 Connectivity

The earth-Sea science node consists of several electrical, mechanical and power components which need to meet deployment, safety and environmental constraints and will likely vary depending on the final site selection. This section identifies the components individually and suggests technologies that may be used to address the safety and environmental requirements. A block diagram representing these components is shown in Figure 4-5.

4.3.1 Main Uplink Cable

This cable must be compatible with KM3NeT neutrino telescope which currently is in the order of 400 V input delivering in the order of 125 kW power of which 10 kW is reserved for the Earth-Sea science node.

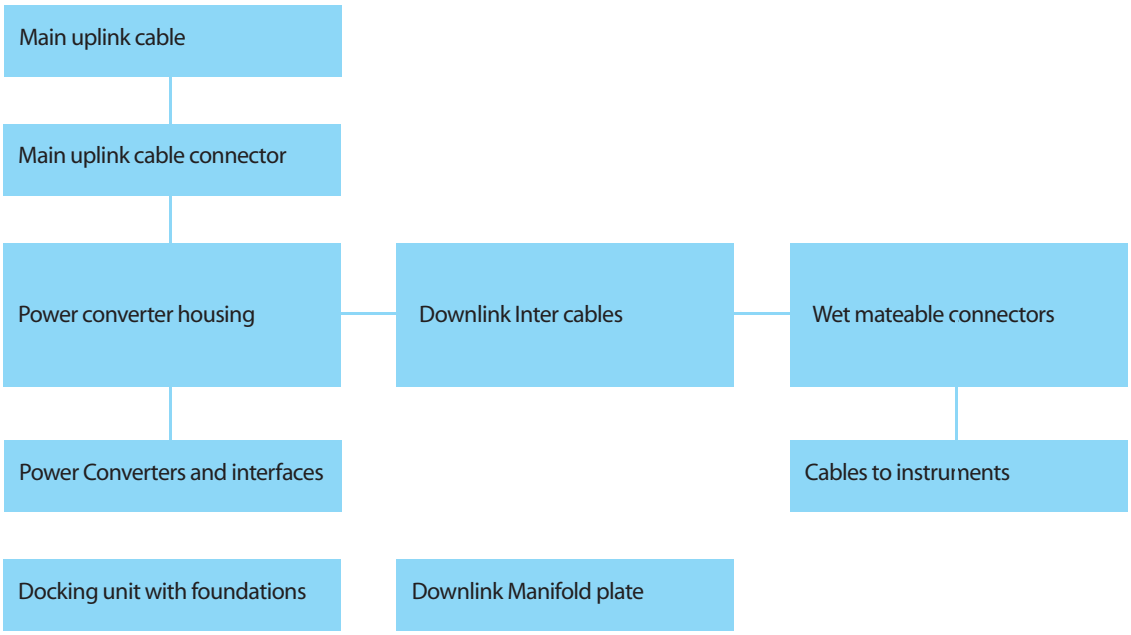

Figure 4-5: Earth-Sea Science node component breakdown.

4.3.2 Uplink Cable connection

This may be a wet or dry mated connection depending on deployment method and available technology.

4.3.3 Power Converter and interfaces

These are similar to the Neptune Canada power-system requirements and if possible have the option to be reconfigurable as the instrumentation changes over the 20 year life cycle of the observatory.

4.3.4 Downlink Cables

Options may be to install the cables with dry mateable connectors or oil filled tubes on deck before deployment of the junction box.

4.3.5 Connector Manifold plate

This could be like an ROV tool plate with wet mateable connectors. Recommendation for parameters such as the distance between connectors and grabbing pressure will be set for the design and included in the operation guide. The connectors and associated hardware can be spaced at a given distance apart and a given height above the sea floor. It will require a grab bar for ROV operations with the grab.

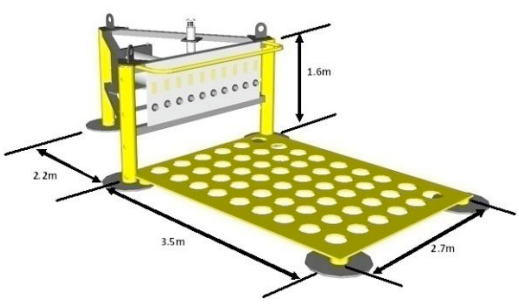

Figure 4-6: Docking unit with foundations and approximate dimensions.

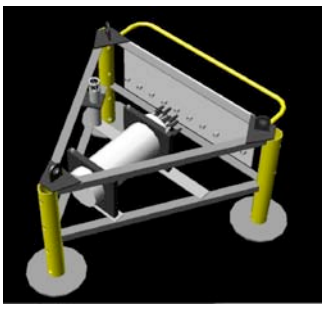

Figure 4-7: Sketch of junction box frame.

4.3.6 Docking Unit with foundations

The experience with subsea observatories used for Earth-Sea science as well as neutrino telescope first generation projects demonstrated the need to offer an easy interface for connection with an ROV. The connecting phase is critical for the reliability of the whole infrastructure.

A docking underwater structure supports the secondary Junction box and allows for easy access to any of the connectors with well defined coordinates, thus enabling the operation of the ROV according to well defined procedures. Figure 4-6 and Figure 4-7 give an impression of the dimensions of such a junction.

4.4 Deployment and Maintenance

Most components will be commercially available and therefore testing certificates will be provided on delivery demonstrating, where necessary, results of the relevant quality control tests. If a different use from the operational references of the sensor or component is foreseen, the instrument may be validate on an Earth-Sea Science test bed in a laboratory or using a sea-bed test node developed by the ESONET Network of Excellence.

4.5 Marine Operations

All Earth-Sea science data obtained from both the science node and instruments positioned within the array for calibration purposes will be made available to the science community, government agencies, outreach programmes and monitoring agencies. The raw data will be stored in real time at the shore station and disseminated according to the ESONET data management methods as shown in Figure 4-8, complying with GMES-GEOSS, INSPIRE and other policies on ocean environment. Existing data networks and data centres will be used to provide access for registered users. When the background knowledge is sufficient, standard data quality checks will be performed prior to distribution. Further processing may be done at the holding data centres.

4.6 Additional Features

Together with the ESONET group working on smart sensors, Ifremer proposed an adapted secondary junction box specification. It takes into account the advances of technology since the Neptune Canada design, additional operational constraints for the KM3NeT project and enhances the versatility.

A major input took its root in the KM3Net project thanks to the technological comparison of potential technologies for the downlink between secondary junction box and instrumentation (cf NIKHEF studies). Both fibre-optic communication and VDSL2 communication on twisted pairs are capable of the high data transmission rate.

A project called DeepSeaNet involving a low cost fibre optic solution without the need for power transmission will also be considered. It will allow the collection of data from areas several kilometres away from the KM3NeT site, such as zones threatened by geo-hazards. Validation of this technology is taking place in 2010 at the Antares site.

A low cost connection will also be implemented, allowing for the hosting of experiments without requiring the purchase of expensive connectors. This feature has been demonstrated during several projects (such as the FP5 Assem project [24]) and will be implemented at Antares and Neptune Canada.

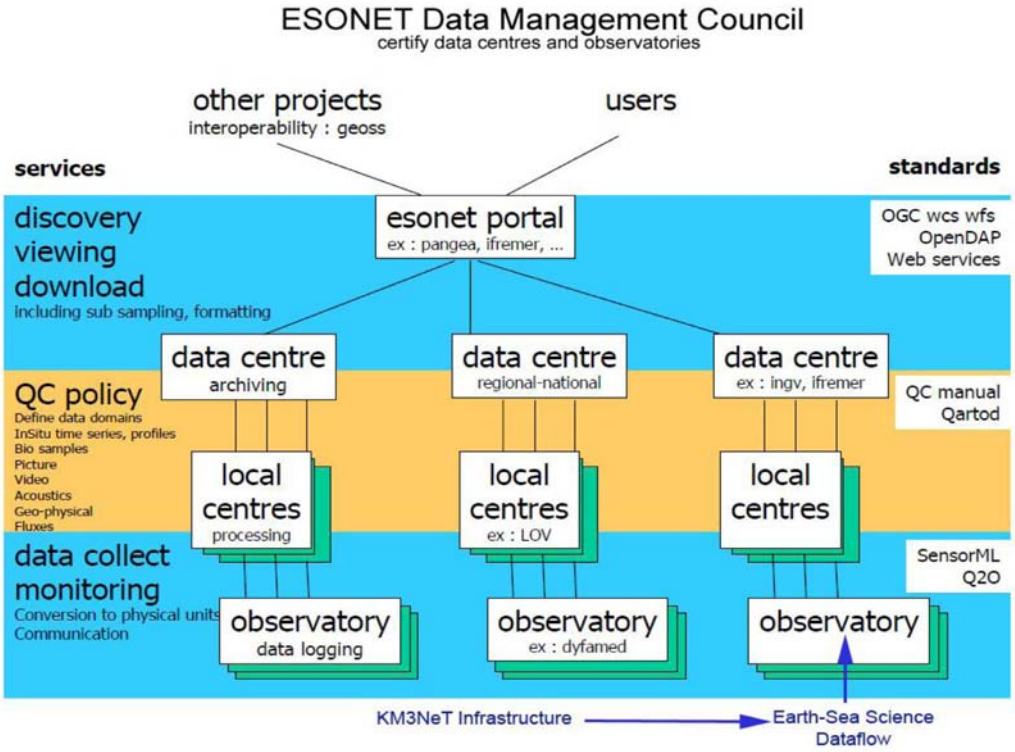

Figure 4-8: KM3NeT Earth-Sea Science dataflow with respect to ESONET data management plan.

5. Site Characterisation

The Mediterranean Sea offers optimal conditions, on a worldwide scale, to host an underwater neutrino telescope. Several suitable sites have been identified and their physical, geophysical and oceanographic properties investigated in detail. In the following, the most relevant results of these studies are presented. In assessing them, it has to be kept in mind that measurements have been performed with different devices and at different points in time.

The most relevant requirements for candidate sites to host the KM3NeT infrastructure are:

- Proximity to coast to ease deployment and reduce the expense of the power and signal cable connections to shore;
- Sufficient depth to fully shield the day light and reduce background from atmospheric muons, in particular from those that are falsely reconstructed as up-going;
- Good optical properties of the water, i.e. absorption and scattering lengths close to the ones of optically pure sea water for light in the wavelength range of about 350 nm to 550 nm;
- Low level of bioluminescence;
- Low rate of biofouling (bacterial film deposition and marine life accretion) on optical surfaces;
- Low rate of sedimentation;
- Low sea current velocities;
- Low risk of significant seismic events.

A geographic information system tool has been developed that allows parameters such as depth, distance from shore, costs, water properties to be given a weighting to help with site selection. An in depth description of the method and its flexibility is given [25].

5.1 Locations

The ANTARES, NEMO and NESTOR Collaborations have carried out dedicated research programmes to characterise the candidate sites, which are currently pursued within the context of the KM3NeT project. The locations of the three candidate regions, shown in Figure 2-2 are:

Toulon - Ligurian Sea (ANTARES):

- 42°48′ N 06°10′ E; depth: 2475 m; cable length to shore 40 km.

Capo Passero - West Ionian Sea (NEMO):

- 36°16′N 16°06′E; depth: 3500 m; cable length to shore 100 km.

Pylos - East Ionian Sea (NESTOR):

- 36°33′N 21°08′E; depth: 5200 m; cable length to shore 50 km;
- 36°33′N 21°29′E; depth: 4500 m; cable length to shore 30 km;
- 36°38′N 21°35′E; depth: 3750 m; cable length to shore 20 km;
- 36°50′N 21°32′E; depth: 3000 m; cable length to shore 15 km.

5.1.1 Bathymetry

The topology of the seafloor has been measured for all three candidate site regions, see for instance Figure 5-1 for the Pylos site and Figure 5-2 for the Toulon site. These measurements show that sufficiently large, approximately plane areas are available at each site.

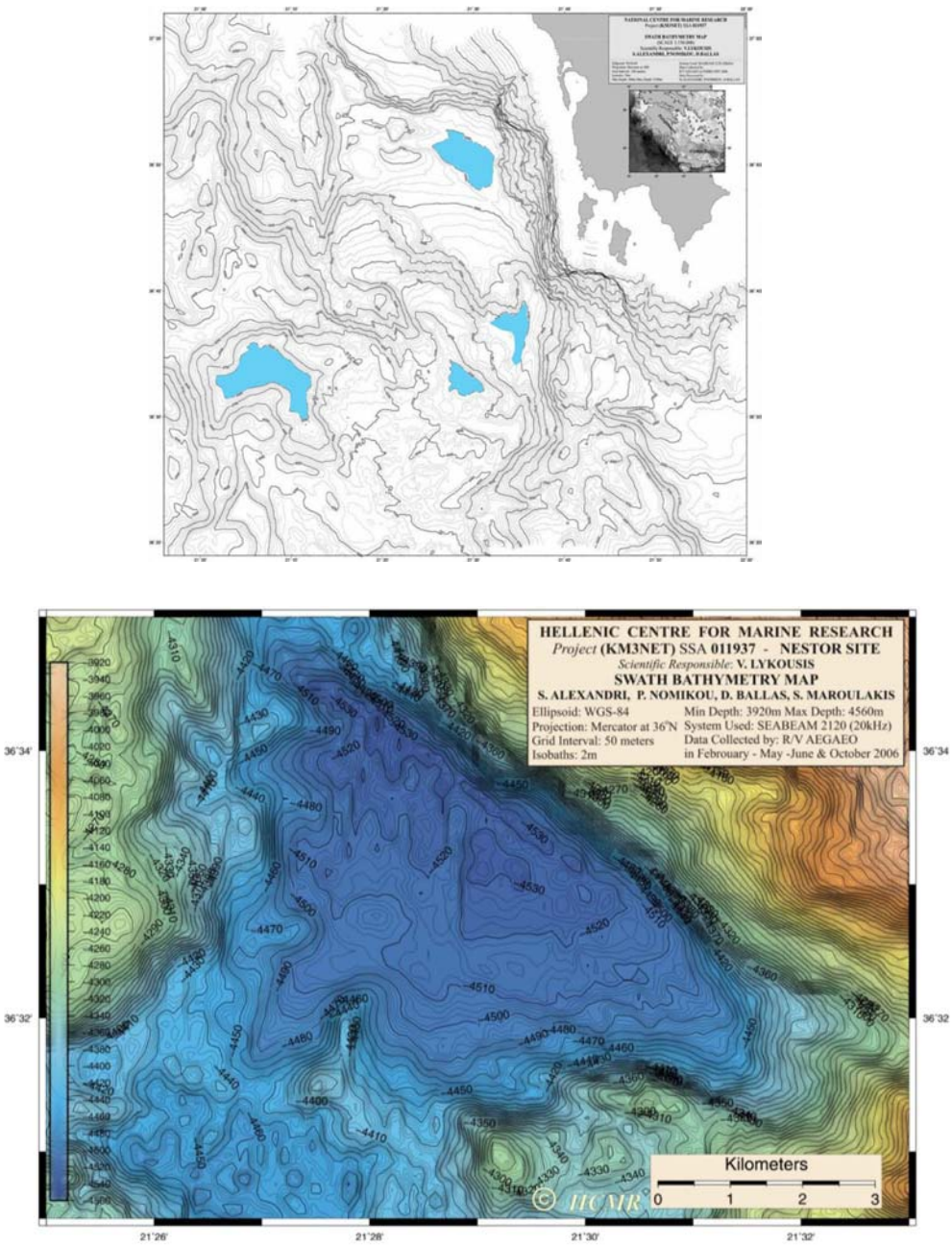

Figure 5-1: Bathymetry maps of the Pylos area. The top panel shows an overview with the 4 possible locations indicated in blue (the northern-most location is 3000 m deep, the others 5200 m, 4500 m and 3750 m (from west to east). Subsequent isobars indicate elevation differences of 50 m. The bottom panel shows a high-resolution map of the 4500 m location; here, subsequent isobars indicate elevation differences of 2 m.

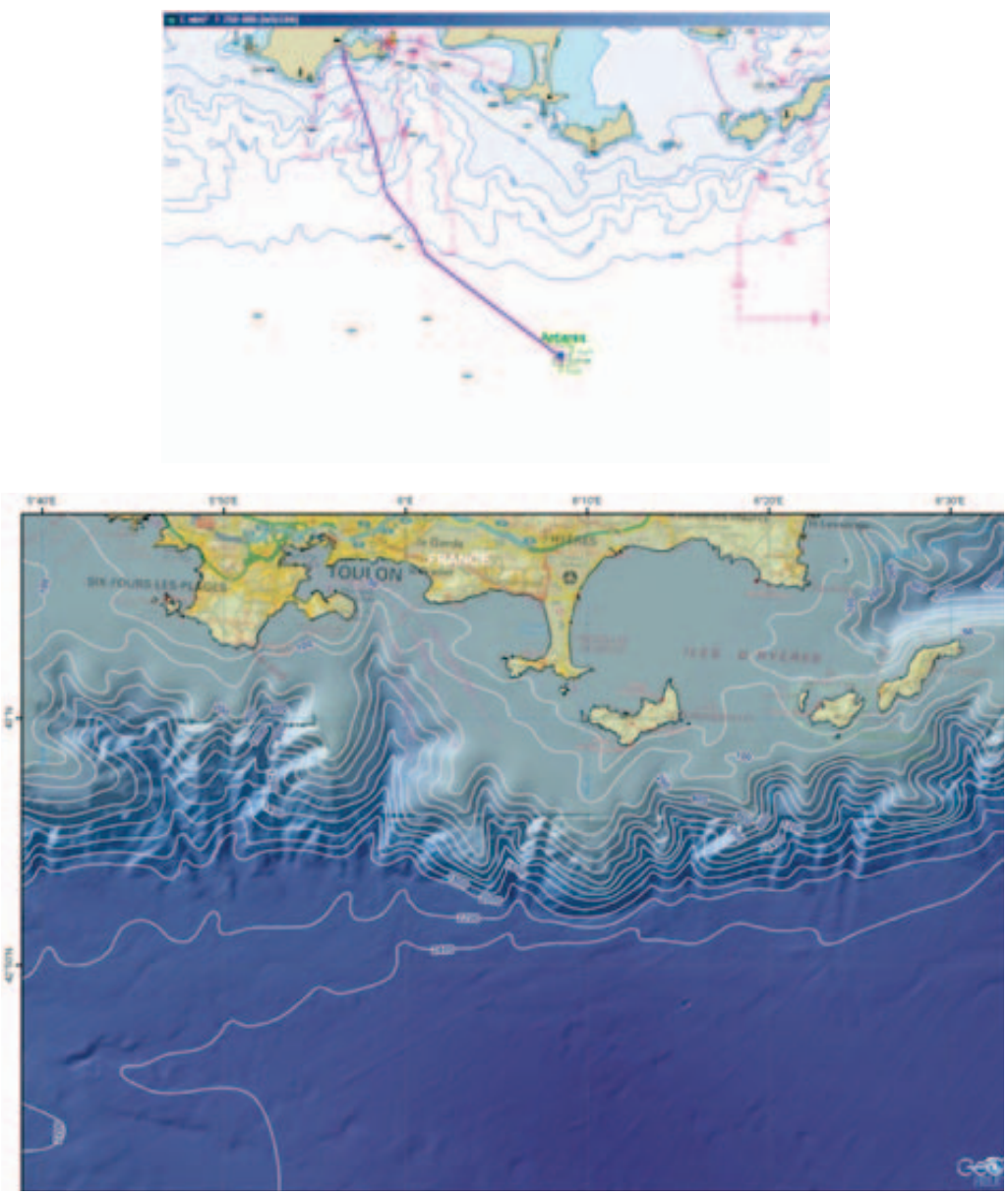

Figure 5-2: Bathymetry map of the Toulon site. The position of the existing ANTARES telescope is indicated on the top map. The lower panel shows a more detailed map of the ANTARES site area.

5.1.2 Weather and Sea Conditions

The weather and in particular the sea state is highly important for deployment operations. Experience of the pilot projects shows that a sea state of 3 at maximum, with wave heights below a metre, is required for safe sea operations. Using modern heave compensation and dynamic positioning technology these requirement could be relaxed to 4 beaufort and 2m waves. The candidate sites provide sufficiently long and frequent periods of calm sea. As examples, Figure 5-3 shows the fraction of time in periods of calm conditions, as a function of the period length, for the Pylos area. Figure 5-4 shows the distribution of wave heights for the Toulon area. It can be concluded that at both sites the sea state is acceptable for deployment operations for more that 50% of the time. The duration of individual deployment operations should be limited to periods of a few days.

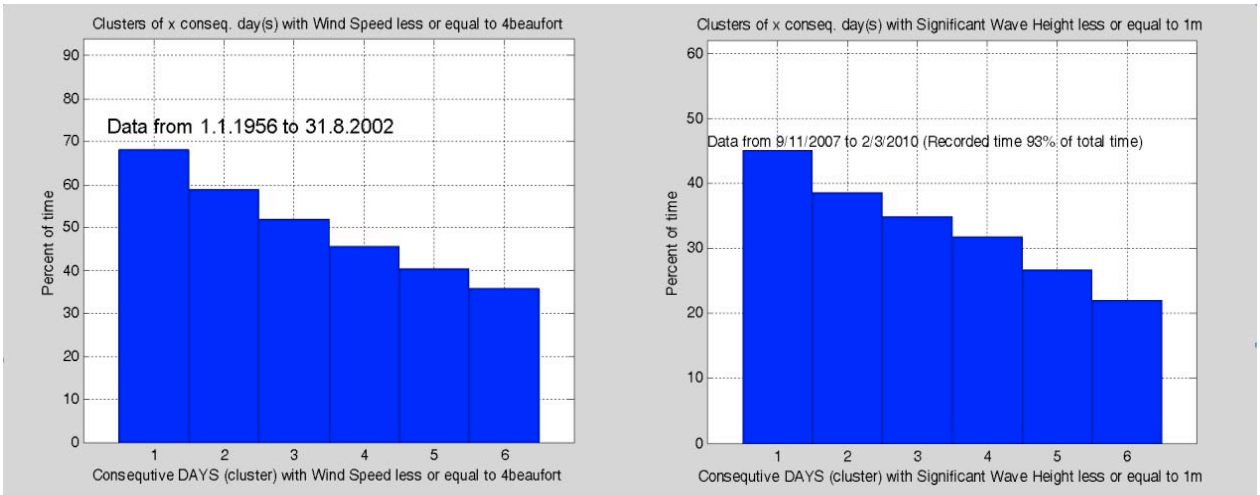

Figure 5-3: Wind speed and sea state conditions at the Pylos site. The left panel shows the fraction of time in periods with wind speed less than or equal to 4 Beaufort (15 knots = 7.9 m/s), as a function of the period length (Source: Greek National Meteorological Service). The corresponding graph for wave heights below 1 m is shown in the right panel. The data are from continuous measurements over 46 years (left) and 29 months (right), respectively. (Source: Hellenic Centre for Marine Research).

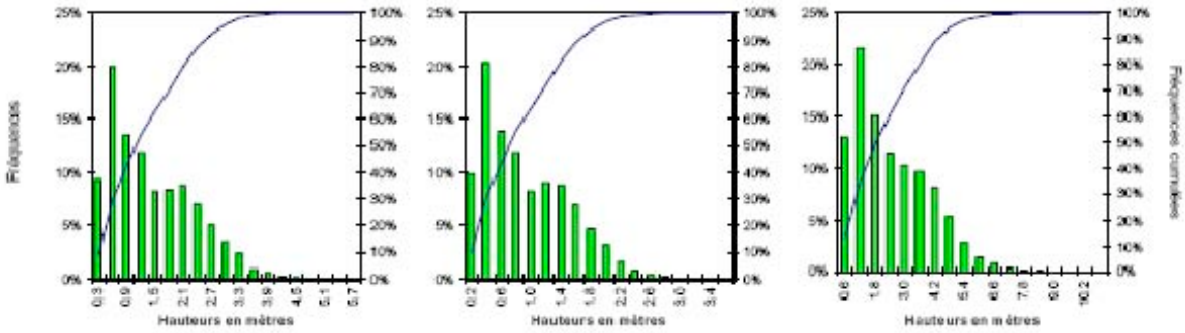

Figure 5-4: Surface wave characteristics at the Toulon site. Shown is the relative abundance of wave heights; the panels from left to right indicate the average height of the 30% largest waves (H1/3); the average wave height; the maximum wave height. The data are from continuous observations over more than 9 years in the period 1992-2001.

5.1.3 Geology

Risks for the operation of the KM3NeT research infrastructure may come from geological processes such as underwater landslides, earthquakes, volcano eruptions or turbidity events. Bore cores of the sediment layer at the sea floor have been taken at all three candidate site areas. Their investigation provided no evidence for major events of these types over the last tens of millennia [26.

5.2 Environmental Site Characteristics

Since the neutrino telescope, as well as the earth and sea science devices, will be operated in the unsheltered natural deep-sea environment, the operation conditions have to be carefully studied to assess their impact on data quality, long-term performance and associated risks.

5.2.1 Temperature

The sea water temperature directly impacts on the temperature at which off-shore components, such as front-end electronics and photomultipliers, are operated. Since their performance typically is temperature-dependent, both local and temporal variations of the water temperature are of concern. Measurements at the different sites have shown that the temperature is stable to within 0.2°C, both as a function of depth (below about 1.5 km) and as a function of time. The average temperature varies from 13.3°C in the Ligurian Sea to 13.5°C in the Ionian Sea.

5.2.2 Salinity

The salt content of the sea water determines its physical and chemical properties, such as conductivity, density and chemical reactivity. These parameters are relevant for KM3NeT as they impact on the design of the telescope. The observed temporal or local salinity variations are small. Measurements show that the salinity in the Mediterranean Sea increases slightly from West to East, from about 38.45 psu[5] at the Toulon site to 38.75 psu at the Pylos site.

Probably the most important aspect of the prevailing salinity value is that it is directly proportional to the potassium (K) content of the sea water, which contributes to the optical background through decays of the natural radioactive isotope 40K. See Sections 6 for more details.

5.2.3 Deep-sea Currents

Since the Detection Units are flexible, the optical modules are displaced from their nominal positions (corresponding to a vertical line shape) due to the drag forces of deep-sea currents. These displacements need to be continuously monitored (see Section 3.5.4), and they have to be limited in magnitude to guarantee the mechanical stability of the detection units (see Section 3.3.5).

Using moorings of current-meters and the ANTARES data, the long-term distribution of current speed and direction has been monitored over several years at all three candidate sites. The results are shown in Figure 5-5 (Toulon), Figure 5-6 (Capo Passero) and Figure 5-7 (Pylos). Whereas for 90% of the time, the current velocity is below 12 (8, 5) cm/s at the Toulon (Capo Passero, Pylos) sites, occurrences of currents with up to about 30 cm/s have been observed at the Toulon site. Any design is therefore required to withstand such currents.

It is known that instabilities of the water column can occur, which are unpredictable in time and location and lead to turbulent downflows of large water masses, causing deep-sea currents of the order 50 cm/s or more. However, no evidence for such events has so far been observed in the candidate site regions over extended measurement periods of up to five years.

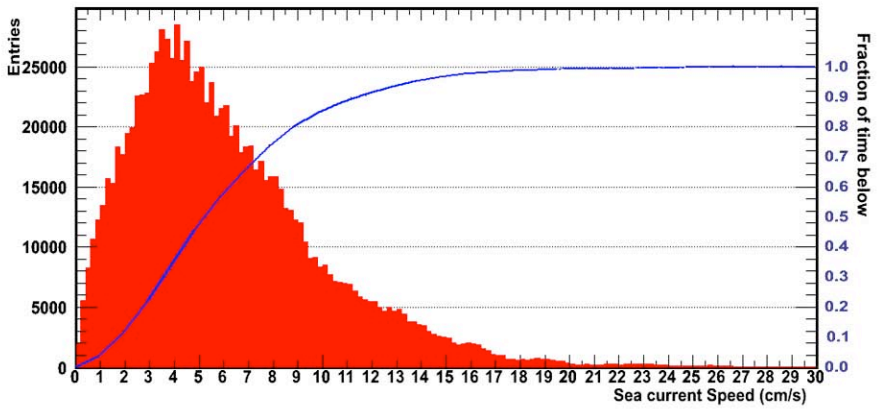

Figure 5-5: Distribution of the deepsea current velocity measured at the Toulon site during the period September 2005 - October 2009 using ANTARES instrumentation. The blue line represents the integrated content of the histogram, normalised to unity.

[5] *Practical salinity units, based on conductivity measurements. 1 psu is approximately equal to 1 g of salt per litre of water.*

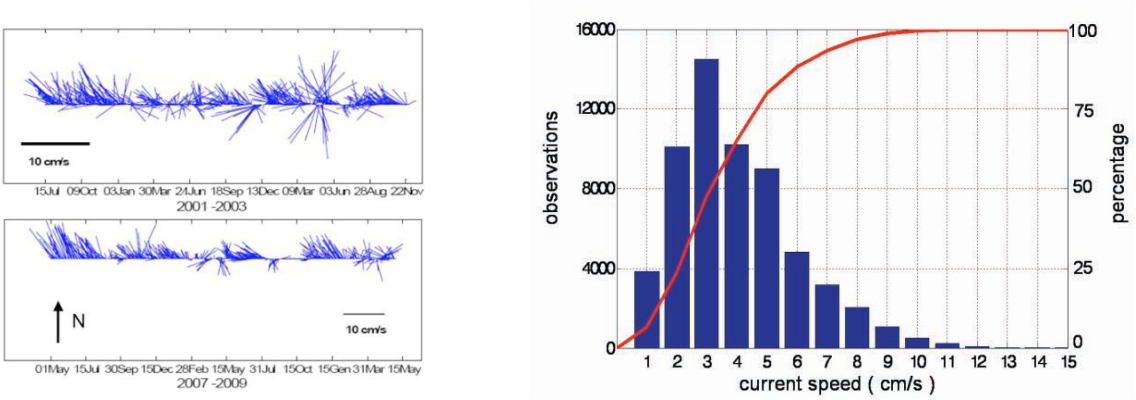

Figure 5-6: Deep-sea current velocities from measurements performed in the periods 2001-2004 and 2007-2009 at the Capo Passero site. The graphs in the left panel indicate the development of direction and speed over time; the plot in the right panel shows the speed distribution (blue histogram) and its integral, normalised to unity (red line). The measurements have been performed at depths up to 500 m above seabed. No significant depth dependence of the currents was observed.

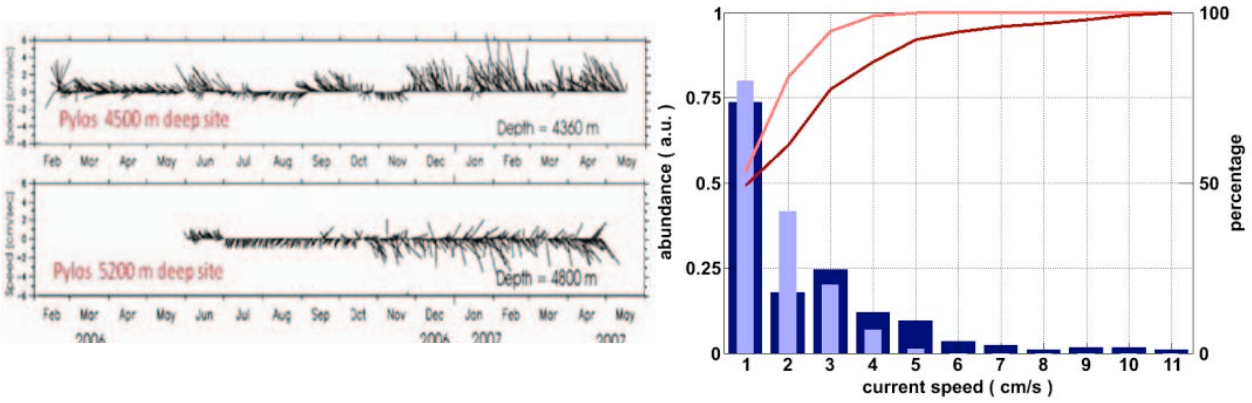

Figure 5-7: Deep-sea current velocities from measurements performed in the period 2006-2007 at the Pylos site. The graphs in the left panel indicate the development of direction and speed over time at the two deepest locations (North is towards the top); the plot in the right panel shows the speed distributions (4500 m: dark blue histogram; 5200 m: light blue) and their integrals, normalised to unity (4500 m: dark red line; 5200 m: light red). Measurements have been made every 8 hours. Velocities measured at intermediate depths between 2000 m and 4000 m show a very similar behaviour.

5.2.4 Sedimentation and Biofouling

The downward flux of sediments can cover the optical modules and reduce the transmittance for Cherenkov light, thus decreasing the neutrino telescope's sensitivity. This effect depends on the angle of view (it is stronger for upward-pointing than for downward-pointing parts of an optical module). It may be supplemented by biofouling, i.e. the growth of a layer of biological organisms (bacteria etc.) on the glass surface, which further reduces the transmittance and in addition provides a "capture ground" for sediments.
The sediment flux has been measured using sediment traps on mooring lines that have been deployed regularly over periods of 1-2 weeks (see e.g. [27,28].) Example results are presented in Figure 5-8. There is a significant seasonal variation in the sediment flux. Even stronger variations are observed from year to year, presumably related to changes of the prevailing weather conditions (in particular wind speed and direction) and to singular occurrences of additional sediment material sources such as ashes from forest fires or sand from the Sahara.

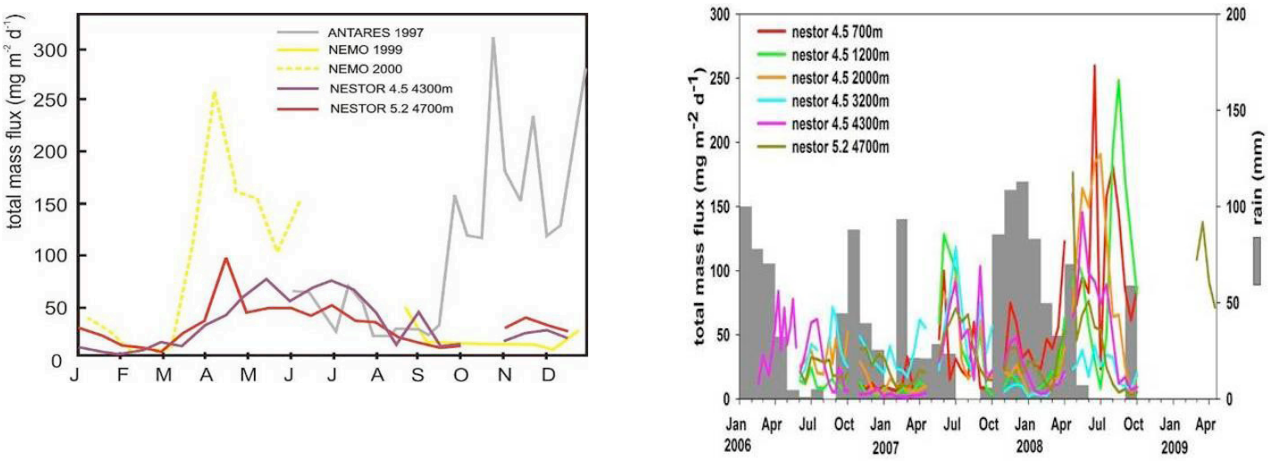

Figure 5-8: Downward total mass fluxes measured at the three candidate sites. The plot in the left panel shows a comparison of the seasonal variation for selected years (averaged over several years for Pylos). In the right panel, the sediment flux as measured at different locations and depths at the Pylos site during the period 2006-2009 is shown. Times and intensity of precipitation are also indicated.

Longer-term average rates of sedimentation can be inferred from the bore cores. The results are 0.2-0.5 mm/year for the Toulon site, about 0.04 mm/year for Capo Passero and 0.02 mm/year for Pylos [26,29].
The combined effect of sedimentation and biofouling on the transmittance of optical modules has been investigated in long-term measurements with dedicated instruments. In Figure 5-9, the LIMS[6] device [30] is presented as an example; 20 LIMS instruments have been produced and operated from May 2007 to October 2009 (260 LIMS-months). The measurement principle is to instrument the inner surface of an optical module with light sensors at positions corresponding to different polar angles and monitoring their response to external light sources at fixed positions and with constant intensity.
Typical data retrieved from these measurements are shown in Figure 5-10 for the Pylos site and in Figure 5-11 for the Toulon site (from a similar device deployed earlier by the ANTARES collaboration [27]). The measured reduction rates of transmittance are shown in Figure 5-12 as functions of the polar angle. In all sites, these rates roughly coincide for downward directions between nadir and horizontal (a few percent reduction per year), but they somewhat differ for upward directions of view, as to be expected from the different sedimentation rates.
It is to be noted that during and after periods of stronger currents an increase of the transmittance was observed (see Figure 5-11), indicating that the biofouling and sedimentation layer is washed off to some extent.

[6] *Light Intensity Measuring Device.*

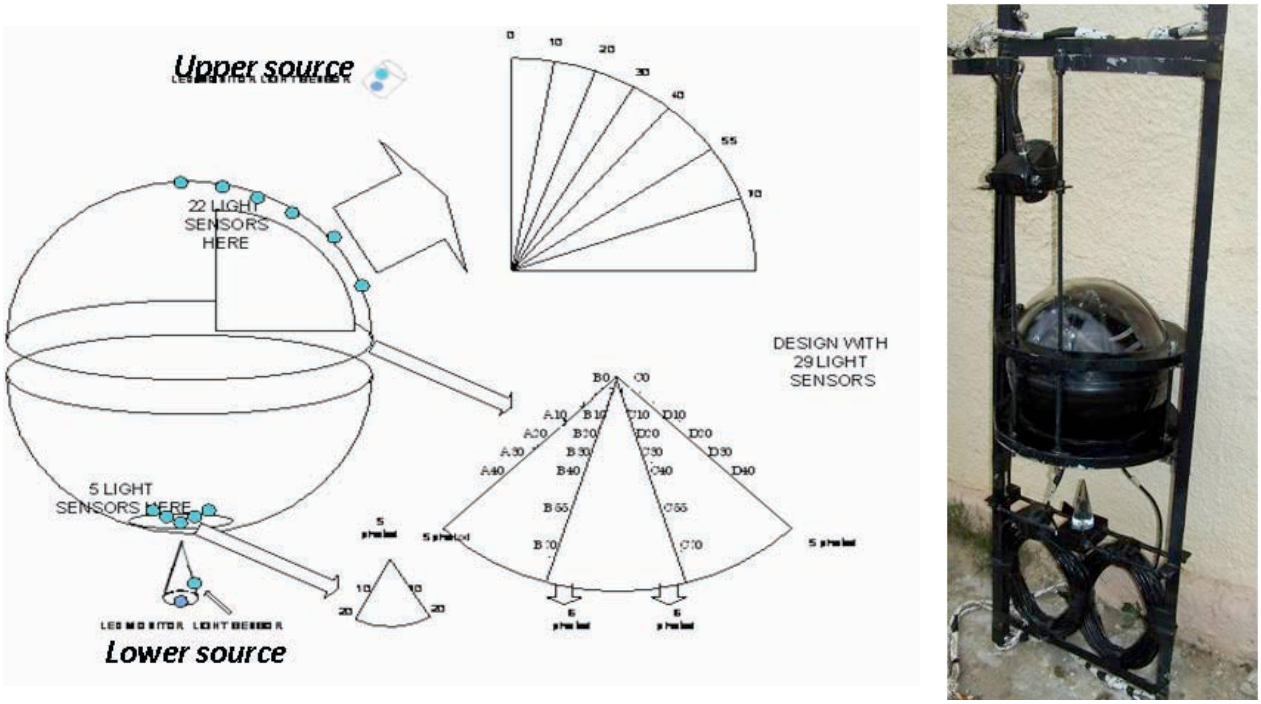

Figure 5-9: The LIMS instrument for long-term transmittance measurements. The left panel shows the geometry of light sources and sensors placed inside a glass sphere as used for optical modules. 22 sensors are upwards-pointing at zenith angles between 0° and 70°, 5 sensors are installed close to the nadir (180°). Two light sources are operated alternating to illuminate the upper and the lower part of the sphere. The right panel shows a LIMS instrument ready for deployment.

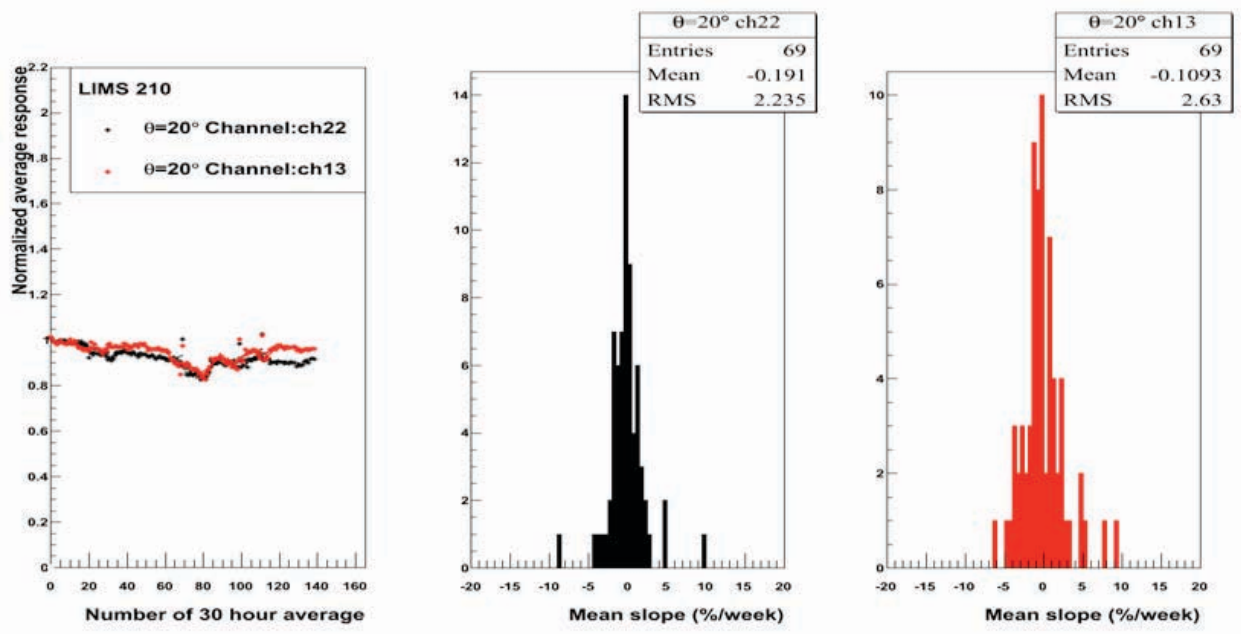

Figure 5-10: Typical example data taken with a LIMS device over a 6-month period at the Pylos site, at a depth of 3240 m. The data of two sensors, averaged over 30-hour periods and normalised to unity at the start of the measurement, are shown in the left panel. The middle and right panels show the distribution of weekly variations in percent of the corresponding transmittances.

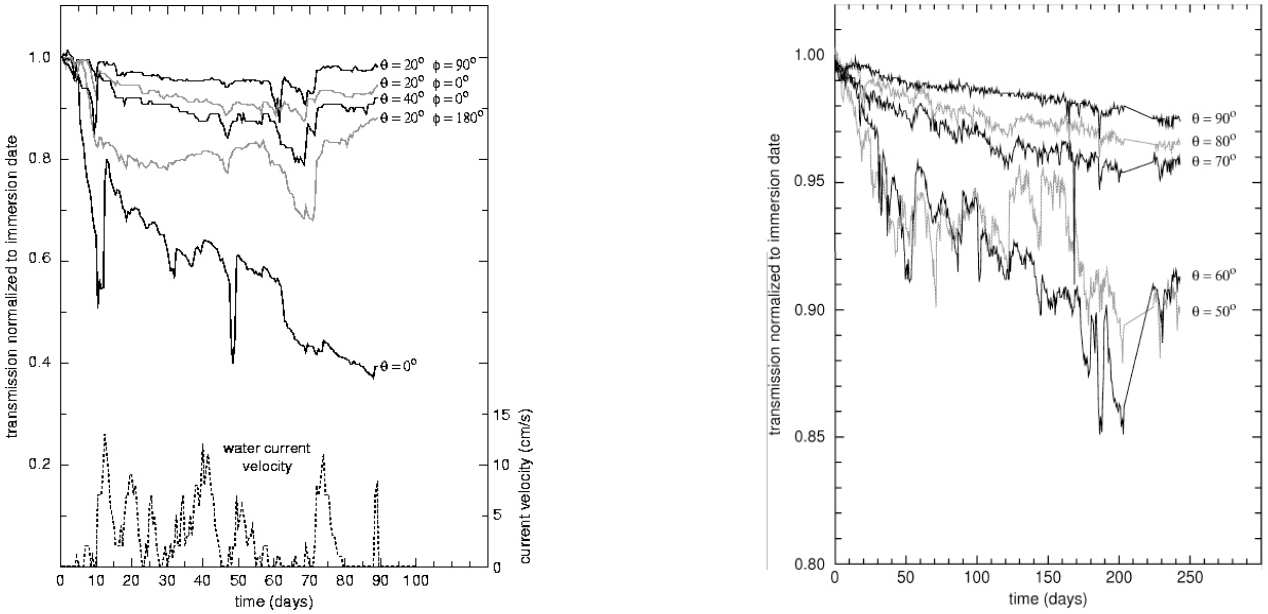

Figure 5-11: Time dependence of transmittance measured at the Toulon site in two campaigns in 1997-1998. The left panel shows the results of a 3-month measurement with the sphere illuminated from above; the right panel is from a 8-month period, where the illumination was horizontal. The θ values indicate the zenith angles of the photo-sensors inside the sphere. The water current speed is indicated for the first measurement.

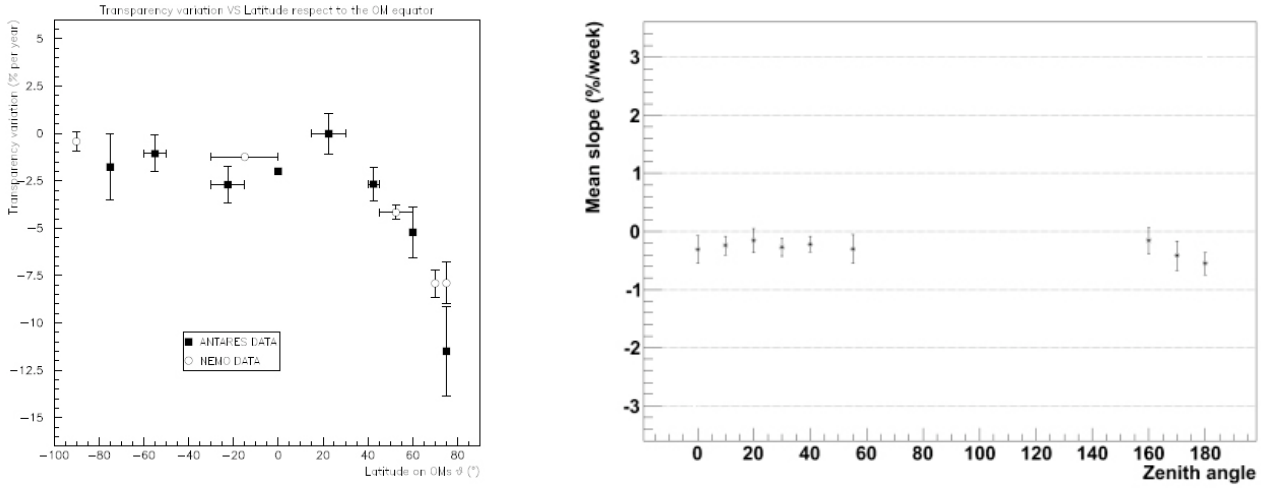

Figure 5-12: Decrease of transmittance with time. The left panel shows a comparison of measurements at the Toulon (black squares) and the Capo Passero (open circles) sites. The polar angle is given as latitude (-90° is downwards-looking, 90° is upwards-looking). The right panel shows results obtained with LIMS at the Pylos site in 3240 m depth.

A growth of peculiar organisms was observed when recovering an ANTARES detection unit after 2.5 years in the deep sea. The exact classification and properties of these organisms, the conditions for their growth, their abundance throughout the Mediterranean, as well as longer-term investigations of their impact on the neutrino telescope performance need to be further investigated. The transmittance reduction after the 2.5 years due to this growth is of the order of 1% and thus has no significant adverse effect on the sensitivity of the neutrino telescope. Other spheres have been recovered at this and the other sites after similar time in the deep sea and have shown no growth.

5.2.5 Radioactivity

Radioactive β and γ decays in the sea water cause continuous, homogeneous and isotropic emission of Cherenkov light. The dominant contribution to this background light is from ^{40}K decays. The K concentration in sea water is 0.010 mol/litre; the relative abundance of ^{40}K is 0.012% and its half-life 1.25x10^{9} years. The resulting activity is about 13 Bq/litre, causing a typical count rate of 40 kHz on an 8-inch photomultiplier (threshold at 0.3 photo-electrons). In order to investigate possible additional contributions or temporal variations of this rate due to other radio-nuclides, in particular from anthropogenic sources, a radioactivity probe (see Figure 5-13) was constructed and deployed at the Capo Passero site for 6 months. The probe uses a NaI(Tl) crystal to measure the γ spectrum of radioactive decays in sea water. The expected activity level from ^{40}K decays was confirmed (see Figure 5-14) and no significant additional activity rates were observed. Water samples from the Pylos site have been collected and analysed in the laboratory. Also here, the ^{40}K activity was confirmed (14±1 Bq/litre) and the overall activity from anthropogenic isotopes (^{137}Cs, ^{243}U, ^{238}U) found to be of the order of 0.05 Bq/litre.

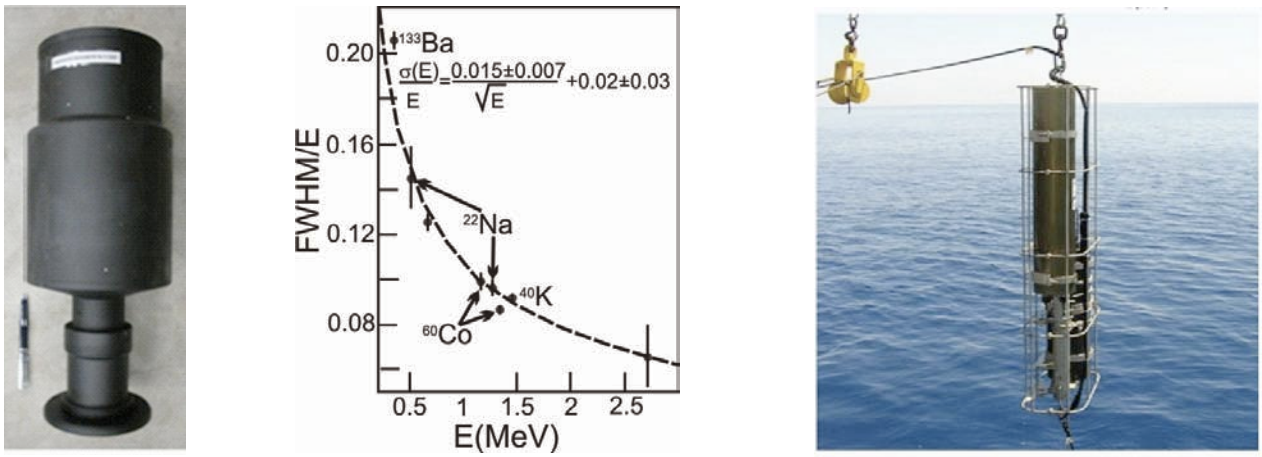

Figure 5-13: The gamma spectrometer developed for gamma activity measurements in the deep sea. The left panel shows a photograph of the instrument, the middle panel the result of calibration obtained with radioactive sources and the right panel the instrument during deployment as part of a mooring operated for six months at the Capo Passero site.

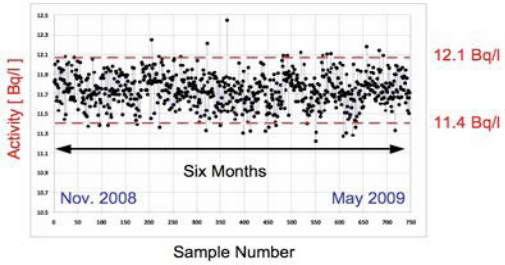

Figure 5-14: ^{40}K activity at the Capo Passero site, measured over 6 months using the radioactivity probe shown in Figure 5-13. The measurement is based on the γ decay mode of ^{40}K.

5.2.6 Bioluminescent Organisms

Further sources of background light are bioluminescent organisms, which typically emit light in the blue wavelength regime, where water has maximal transparency [31,32]. There are two contributions to bioluminescent light, one varying on time scales of hours to days (presumably from bacteria) and one coming in "bursts" with durations of a few tenths to a few tens of seconds (assigned to larger organisms). The photomultiplier count rate from the steady component can be of similar size as that from ^{40}K and is typically homogeneous over the full detector; a burst can cause rates that are larger by orders of magnitude, but affect only a local group of optical modules. Both components thus differ significantly in their impact on data taking, filtering and analysis (see Section 6.1).

The most direct assessment of bioluminescence and its impact on the neutrino telescope is by measuring the intensities of deep-sea background light over long-term periods. The corresponding results are presented in Section 5.3.3.

To investigate the occurrence of bioluminescent organisms, water samples have been retrieved from different depths at a location near the Capo Passero site. Subsequently, the density of luminescent bacteria cultivatable at atmospheric pressure has been determined. The results (see Figure 5-15) indicate that such bacteria are essentially absent at depths beyond 2500 m [28].

To compare the abundance of bioluminescent animals at the Capo Passero and Pylos sites measurements were made with the ICDeep camera (I^{2}CCD (Image Intensified Charge Coupled Device) for Deep-sea research). Measurements were made in autumn 2008 and spring 2009 to investigate seasonal changes at each site. The ICDeep camera is more sensitive than the ISIT camera, which was used for previous measurements at the Pylos and Ligurian sea sites[33,34] resulting in higher abundance values.

A seasonal effect was found at the Capo Passero site where abundance values were higher in the autumn than in spring between 500-2400 m depth. No seasonal effect in the abundance of bioluminescent animals was found at the Pylos site. Comparing the two sites higher abundance values are found at the Capo Passero site in spring and autumn than at the Pylos site (Fig XX). In water 2500-3500 m densities of bioluminescent animals were 2-3 times higher at the Capo Passero site (0.4-0.6 m^{-3} in autumn and spring, respectively) than the Pylos site (0.24 – 0.17 m^{-3})

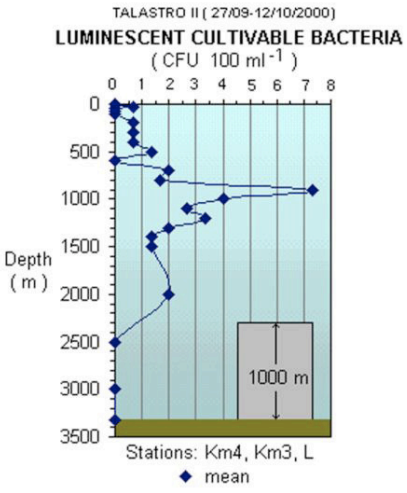

Figure 5-15: Concentration of luminescent bacteria cultivatable at atmospheric pressure, as a function of depth. The data have been obtained from water samples taken at the Capo Passero site.

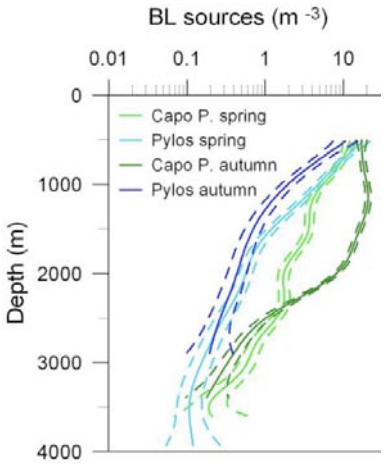

Figure 5-16: Density of bioluminescent animals at the Capo Passero and Pylos sites, in autumn 2008 and spring 2009. (Dashed lines show 95% c.l.)

5.3 Optical Properties of the Deep-Sea Environment

The study of the deep-sea water optical properties has been performed through a long-term programme carried out spanning all seasons. Sea water absorbs and scatters light depending on the water temperature, salinity, as well as the characteristics and concentration of the suspended particulate. These parameters are different at different marine sites and may vary as a function of time. Furthermore, the intensity and time dependence of background light from radioactivity and bioluminescence (Section 5.3.3) has been measured in long-term exploratory campaigns and by the ANTARES experiment and is reported in the following.

5.3.1 Light Transmission Parameters

Light transmission through media is affected by absorption and scattering. Scattering processes in which only the direction of the light is changed are dominant, whereas scattering phenomena in which also the photon wavelength changes (e.g. the Raman effect) happen less frequently. Scattering can take place either on molecules (Rayleigh scattering) or on particulate matter (Mie scattering). In order to properly describe the transparency of sea water as a function of wavelength, it is necessary to measure the parameters describing absorption and scattering, such as the absorption length $L_a(\lambda)$ scattering length $L_b(\lambda)$ and attenuation length $1/L_c(\lambda) = 1/L_a(\lambda) + 1/L_b(\lambda)$. Each of these lengths represents the path after which a beam of initial intensity I_0 and wavelength λ is reduced in intensity by a factor of 1/e through absorption, scattering or both according to

$$I_{a,b,c}(x) = I_0 e^{\left(-\frac{x}{L_{a,b,c}}\right)}$$

where x is the optical path traversed by the beam. In the literature, also the coefficients of absorption, $a = 1/L_a(\lambda)$, and scattering, $b = 1/L_b(\lambda)$, are used to characterise the light transmission through matter. The sum of scattering and absorption coefficients is called attenuation coefficient c. Other parameters commonly used in the literature are the effective scattering length

$$L_b^{eff} = \frac{L_b(\lambda)}{1 - \langle \cos\vartheta \rangle} = \frac{1}{b_{eff}}$$

and the effective attenuation length

$$L_c^{eff} = \frac{1}{c^{eff}} = \frac{1}{a + b^{eff}},$$

where $\langle \cos\vartheta \rangle$ is the average cosine of the scattering angle. The estimation of the latter parameter is difficult since it needs the knowledge of another inherent optical property, the volume scattering function $b(\vartheta)$, which must be measured with appropriate devices. Using an isotropic light source, it is also possible to measure the so-called transmission length, $L_\beta(\lambda)$ characterising the variation of light intensity as a function of the distance, R, between the source and the detector:

$$I(\lambda, R) = \frac{I_0(\lambda)}{4\pi R^2} e^{-\frac{R}{L_\beta(\lambda)}}$$

The transmission length can be determined, for specific values of λ, by fitting $I(\lambda,R)$ to data taken with fixed $I_0(\lambda)$ and several values of R.

A direct comparison between measured values of $L_\beta(\lambda)$ and L_c^{eff} requires the knowledge of the volume scattering function as a function of λ, or of the value of $\langle \cos\vartheta \rangle$. This knowledge is still lacking for the Mediterranean Sea.

5.3.2 Light Transmission Measurements

The Toulon site has been studied for many years with dedicated setups designed to characterise water optical properties. Early measurements [35] taken between 1997 and 2000 were made for blue (473 nm, with 10 nm of FWHM) and UV (375 nm, with 10 nm of FWHM) light. The resulting absorption, scattering, and effective attenuation lengths are summarised in Table 5.1 and Table 5.2 .
Using data from the ANTARES instrumentation, the transmission length is being monitored continuously since 2008. Light signals from optical beacons (wavelengths 400 and 470 nm, operated periodically for calibration purposes) registered by optical modules placed at various distances allow for measuring in situ the light transmission as a function of distance. Figure 5-17 shows the results of these measurements. Monte Carlo simulations indicate that, for reasonable scattering models, the absorption length at 470 nm is typically 5 m larger than the transmission length.

Date	Effective attenuation length (m)	Absorption length (m)	Effective scattering length (m)
July 1998	60.6 ± 0.4 ± 5	68.6 ± 1.3 ± 5	265 ± 4 ± 28
Mar. 1999	51.9 ± 0.7 ± 1	61.2 ± 0.7 ± 1	228 ± 11 ± 24
June 2000	46.4 ± 1.9 ± 2	49.3 ± 0.3 ± 2	301 ± 3 ± 27

Table 5.1: Water optical properties measured at the Toulon site using blue light (λ =470nm). The first error is statistical and the second one is systematic.

Date	Effective attenuation length (m)	Absorption length (m)	Effective scattering length (m)
July 1999	21.9 ± 0.8 ± 2	23.5 ± 0.1 ± 2	119 ± 2 ± 10
Sept.1999	22.8 ± 0.3 ± 2	25.6 ± 0.2 ± 2	113 ± 3 ± 10
June 2000	26.0 ± 0.5 ± 1	28.9 ± 0.1 ± 1	133 ± 3 ± 12

Table 5.2: Water optical properties measured at the Toulon site using UV light (λ =375 nm). The first error is statistical and the second one is systematic.

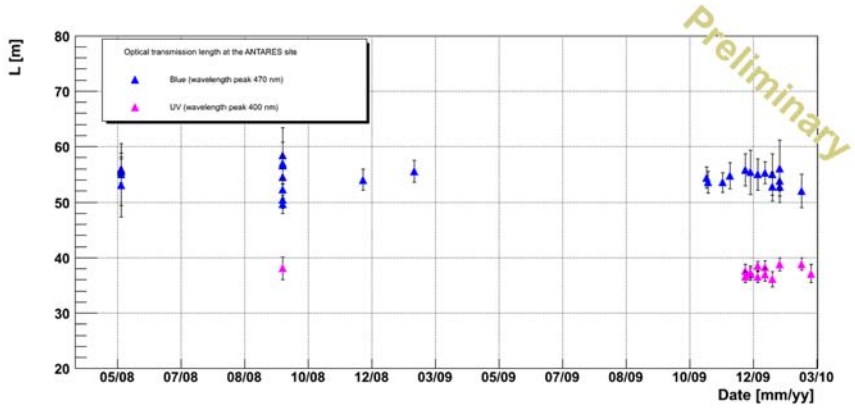

Figure 5-17: Results of in situ measurements of the transmission length at the Toulon site. The Measurements were performed using ANTARES instrumentation. The blue symbols are for a wavelength of 470 nm, the magenta ones for 400 nm.

The light transmission at the Capo Passero site has been investigated [36] using a setup including a commercial instrument (the AC9 by WETLABS) capable of measuring, in a collimated geometry, the absorption and the attenuation coefficients for nine wavelengths ranging from 410 nm to 715 nm. The values of the absorption and attenuation lengths have been determined for each measurement by averaging the data for depths greater than 2850 m [37]. The results of four sets of measurements taken in different seasons are shown in Figure 5-18. For comparison, light absorption and attenuation data for optically pure sea water [38] are also shown. At all wavelengths, deep waters at that location have an absorption length compatible with that of pure sea water. There is no evidence of a seasonal dependence of the optical parameters.

The NESTOR group has developed and operated a device (Long-Arm Marine Spectrophotometer, LAMS) to determine the transmission length by means of a rigid structure that allows for measuring the intensity of light from an isotropic, constant source at distances of R=10, 15, 17, 22 m (see Figure 5-19). Measurements have been performed at 8 wavelengths ranging from 376 nm to 520 nm and at different depths, at the Pylos and Capo Passero sites.

Table 5.3 shows a comparison of the corresponding results, for similar depths and at about 200 m above seabed at both sites. More details can be found in [39]. The transmission length measured by LAMS cannot easily be related to absorption or attenuation length (see Section 5.3.1). The transmission length was previously measured at different locations in the Pylos area using a non-collimated light source at a wavelength of 460 nm; a result of 55 ± 10 m was found[40].

The results in Table 5.3 indicate a transmission length that is roughly 10% larger at the Pylos than at the Capo Passero site; however, it must be noted that these measurements represent a snapshot at a given time (the campaign at both sites was performed within a few days) and the systematic uncertainties quoted do not account for longer-term variations of the respective optical properties.

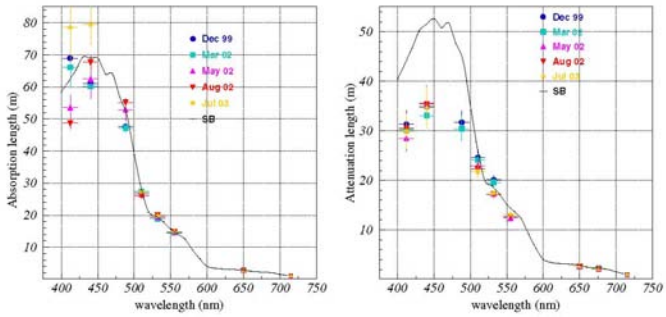

Figure 5-18: Absorption length (left panel) and attenuation length (right panel) measured at the Capo Passero site at four seasons. Also indicated are the the values for optically clean salt water (black lines). Figure taken from [36].

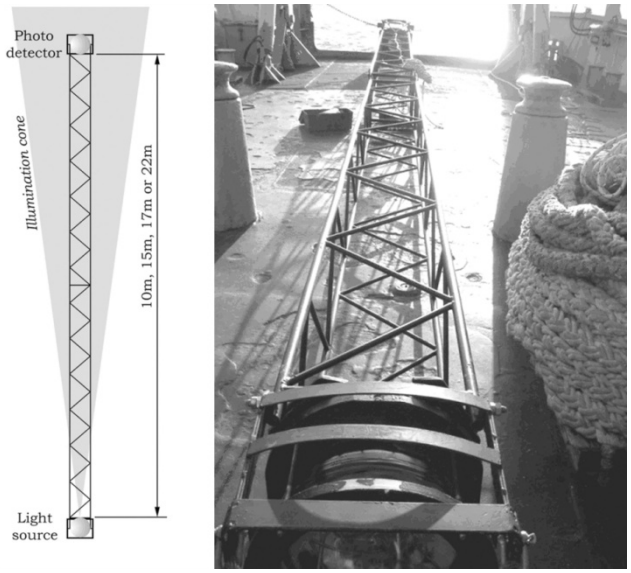

Figure 5-19: Schematic of the LAMS instrument (left), and photographs of it shortly before deployment (upper right) and during deployment (test operation with green light, lower right).

Site	Depth m	376 nm	386 nm	400 nm	425 nm	445 nm	463 nm	502 nm	520 nm
N4.5	4100	21.0±0.5	24.8±0.7	29.2±0.9	36.0±1.3	42.3±1.8	46.1±2.0	28.7±0.8	21.3±0.5
CP2	3400	18.6±0.4	21.8±0.5	25.6±0.7	32.4±1.1	38.5±1.5	42.0±1.7	27.1±0.8	20.9±0.5
N4.5	3000	21.9±0.5	25.7±0.7	30.5±1.0	37.8±1.5	43.8±1.9	47.2±2.2	29.3±0.9	21.5±0.6
CP1	3100	19.9±0.4	23.2±0.6	27.8±0.8	34.6±1.2	41.5±1.7	44.1±1.9	28.5±0.8	21.8±0.5
CP2	3000	19.5±0.4	23.0±0.5	27.3±0.8	34.1±1.2	39.6±1.6	43.7±1.8	27.6±0.8	21.1±0.5

Table 5.3: Transmission lengths (in metres) for light of different wavelengths at Pylos (N4.5), and Capo Passero (CP1 and CP2) sites for the largest and similar depths.

5.3.3 Background Light Measurements

Before detector construction, the ANTARES Collaboration performed a series of in situ measurements of the background light in the Toulon site using 8-inch photomultiplier tubes on autonomous device systems[41]. These measurements revealed the two contributions to the optical background described above: a continuous base rate ("baseline") of a few tens of kHz, varying slowly on time scales of a few hours, and sharp peaks lasting a few seconds and rising to tens of MHz ("bursts"). A typical time stream of data, acquired in April 2005 [42]., and the median counting rate of single optical modules during almost 5 year are shown in Figure 5-20. Counting rates were acquired with a threshold of 0.3 photoelectrons. The two components of optical background described above are clearly visible.

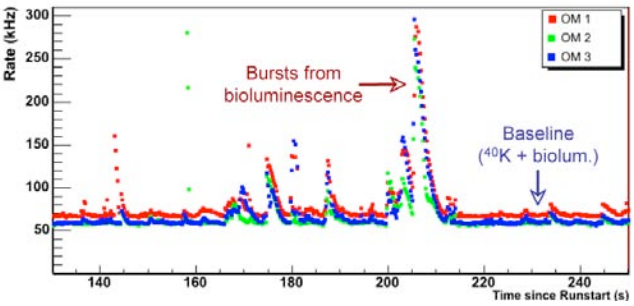

Figure 5-20: Upper panel: Counting rates in three optical modules of an ANTARES storey over a period of 4 minutes. The small differences in the baseline are due to slightly different sensitivities of the photomultipliers. Lower panel: Median counting rates in different ANTARES optical modules over a period of almost 5 years. The colours indicate different optical modules.

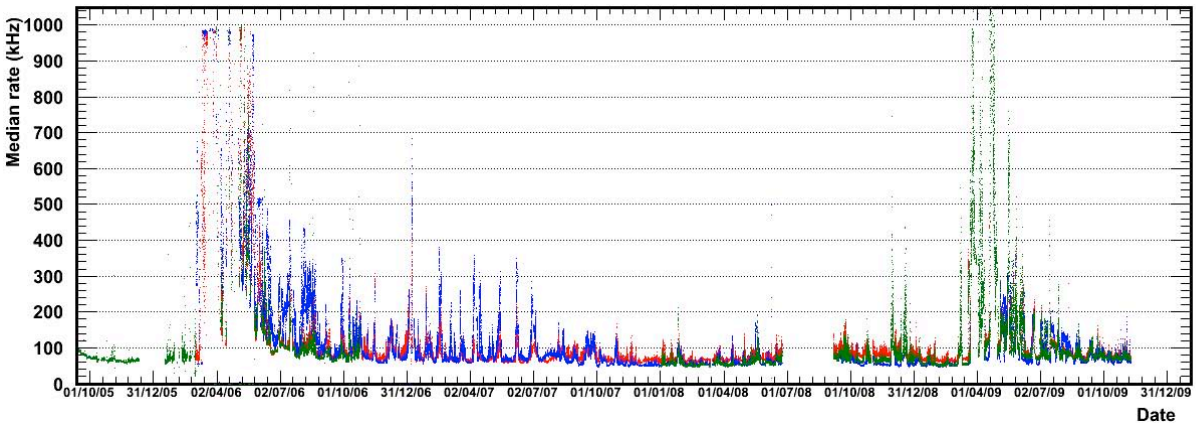

The baseline component is neither correlated with the sea current, nor with the burst frequency; however, long-term variations of the baseline rate were observed in the ANTARES detector. Periods of high burst activity are uncorrelated with variations of the baseline component, suggesting that each of the two contributions is caused by a different population. Moreover, a strong correlation is observed between burst activity and the current velocity, as shown in Figure 5-21 [43].

Optical background data in Capo Passero were collected by means of two different setups. One, built by the NEMO Collaboration, consisted of two 8-inch photomultipliers and the associated electronics, the second, built by the ANTARES Collaboration, used an optical module containing a 10-inch photomultiplier. The two devices have been used to collect data separately, but also together in order to assess systematic uncertainties. Figure 5-22 shows the photomultiplier count rate as a function of time, as obtained with the NEMO setup [28] using a threshold equivalent to 0.33 photo-electrons. After subtracting the dark count rate of 7 kHz an average counting rate of 28.4 ± 2.5 kHz is obtained. This background is rather constant and shows only rare bioluminescence bursts. From this rate, taking into account the properties of the optical module and the photomultiplier, an isotropic photon flux of 360 ± 40 $cm^{-2}s^{-1}$ in the wavelength range of sensitivity of a bi-alkali photocathode is derived. This flux is consistent with the expectation from just the ^{40}K decays.

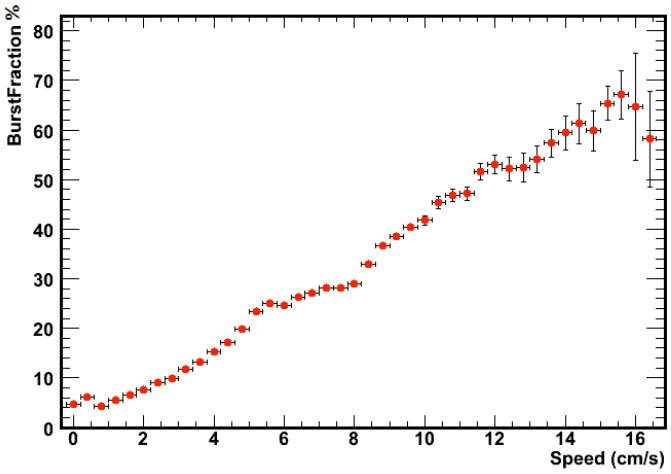

Figure 5-21: Correlation of burst fraction (the fraction of time with count rates exceeding 120% of the baseline rate) and deep-sea current speed. The data have been collected with the ANTARES detector from summer 2005 to summer 2006 at the Toulon site.

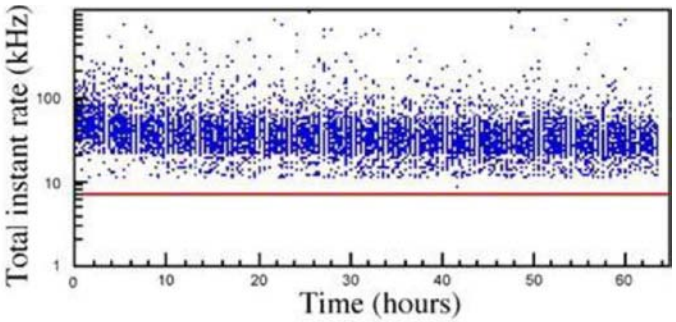

Figure 5-22: Count rate of a single 8-inch photomultiplier at the Capo Passero site, for a measurement period of approximately 3 days. The threshold was set to 0.33 photoelectrons. The red line indicates the dark current count rate.

Also in the Pylos area the optical noise has been measured on several occasions and with different devices. A number of free-drop experiments have been performed since 1996, at a depth of 4000 m, with an apparatus composed of two optical modules. The NESTOR floor deployed and operated in 2003 was also used to study the optical background [44]. A data sample of 100 s duration is shown in Figure 5-23 [45]. From the analysis of the full data sample it is concluded that bioluminescence occurs during 1.1% ± 0.1% of the time, consistent with earlier measurements using autonomous optical modules.

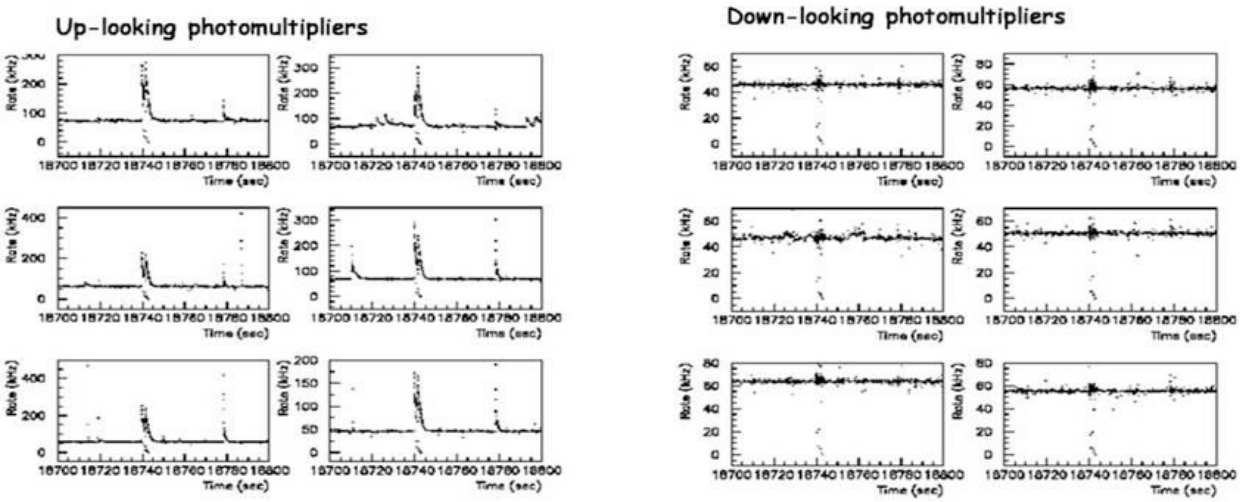

Figure 5-23: Count rates measured with the 12 optical modules of the NESTOR floor operated in 2003. A period of 100 s is covered.

6. Telescope Performance

This chapter presents the expected performance of the KM3NeT neutrino telescope. Detailed detector simulations have been performed, and expected neutrino rates from some example astrophysical sources estimated. From these, in particular, the sensitivity to point sources (assuming a pure E^{-2} neutrino spectrum) has been computed.

Given that as yet no observations of high energy neutrinos from extra-terrestrial sources have been made, these rate estimates must rely on models of neutrino production in the sources. These estimates have significant uncertainties, the magnitude of which depends on the nature of the source.

In many models of production of high energy astrophysical radiation, charged particles are accelerated in shock waves and neutrinos are produced in interactions of these accelerated particles with matter or radiation fields in the vicinity of the source. A typical reaction is $pp \rightarrow \pi + X$, followed by the decay of the charged pions $\pi \rightarrow \mu\nu_\mu$. In the same reaction, gamma rays are produced in the decay of neutral pions $\pi^0 \rightarrow \gamma\,\gamma$ and so a link can be made between the neutrino and gamma production rates. In general, many final states contribute to the full neutrino rate and detailed predictions must be based on Monte-Carlo simulations of the interactions [46,47]. Pion production and decay are well understood from particle physics. Uncertainties arise from using approximations and simplified parametric approaches and from considering incomplete sets of neutrino production channels. Furthermore, in dense source environments multiple interactions are important and the rate of particle decay compared to further interaction must be taken into account. In some models of dense sources [48], e.g. in the case of gamma ray bursts, the high-energy neutrinos are dominantly produced from kaon decays rather than pion decay because of the shorter meson lifetime.

For sources with low matter density, where secondary particle absorption is small, a fairly reliable neutrino rate prediction can be made based on the observed gamma fluxes. This class of sources includes supernova remnants such as RX J1713.7-3946 and RX J0852.0-4622 which are observed in gamma rays as extended objects with angular sizes of 1-2°. For compact objects such as microquasars, absorption of gammas could be important and so neutrino rate predictions must be based on modelling of the corresponding processes. For even denser environments, in particular observed GRBs and the hypothesised "failed GRBs", the predictions are very uncertain.

For the event rate predictions presented in this chapter, the uncertainty of the assumed neutrino fluxes from supernova remnants can be estimated to be roughly a factor of 2. For other sources the predictions must be taken as order-of-magnitude estimates.

6.1 Analysis Techniques

In this section the techniques are presented to identify event candidates in the data, reconstruct them, suppress background and search for signals of cosmic neutrinos.

6.1.1 Background Suppression

There are two different kinds of background related to high-energy particles: atmospheric muons and atmospheric neutrinos. Both are produced by the interaction of primary cosmic rays with the atmosphere. The flux of atmospheric muons at sea surface exceeds that of neutrino-induced muons in the detector by about 10 orders of magnitude. These muons, however, are attenuated in flux and energy below sea surface as a function of depth and zenith angle. Their flux falls to zero near and below the horizon where they are stopped by the water and earth shielding. For this reason astrophysical neutrino signals are mainly searched for among muons from the downward hemisphere. Accurate reconstruction procedures and quality cuts on reconstructed tracks are needed to eliminate atmospheric muon tracks that are mis-reconstructed as up-going.

Atmospheric neutrinos traverse the Earth and are detected in the same way as signal neutrinos. They are thus an unavoidable source of background and must be discriminated from the signal in the data analysis with energy cuts and on statistical grounds.

For atmospheric neutrino simulation, the Bartol flux [49] was used. A prompt contribution from charm decays is included according to the highest prediction of the Recombination Quark Parton Model [50]. The atmospheric neutrino flux has an energy spectrum approximately proportional to $E^{-3.7}$ and an isotropic distribution, while neutrinos from astrophysical point sources point to their origin and are expected to follow an energy spectrum close to E^{-2}. Applying a search cone around the source position with a width reflecting the angular resolution of the detector and energy cuts are thus the prime methods to increase the signal-to-background ratio for point source searches.

A different source of background is the optical noise in sea water that superimposes random hits that are not correlated to the neutrino signal. This background is due to the presence of radioactive isotopes (mainly ^{40}K) and bioluminescent organisms (see Sections 5.2.5 and 5.2.6). The uncorrelated background produced by ^{40}K decay is about 40 kHz for 8-inch PMTs (at a threshold of 0.3 photoelectrons). Bioluminescent bacteria may produce an additional slowly varying background level. To cope with the optical backgrounds, specific online data filter procedures and offline hit selections are applied.

Larger bioluminescent organisms (from plankton to fish) produce bursts of light that saturate close-by PMTs which are then excluded from the data analysis.

6.1.2 Online Data Filter

The data stream to shore contains information of all PMT signals above a given threshold. Online filters based on high amplitude and coincident signals on adjacent PMTs are applied to select candidate events from this stream, which are then stored for further analysis (see Section 3.2). For the sensitivity studies presented here, no simulation of this online filter was necessary since the quality and selection cuts applied at later analysis stages are much more selective than the filter criteria.

6.1.3 Muon Reconstruction

The central challenge in measuring muon neutrinos is the reconstruction of the muon trajectory from the PMT signals. For an assumed muon trajectory the expected arrival times of the Cherenkov photons at the optical modules are calculated, using the geometrical positions of the PMTs, the group velocity of light in water and the Cherenkov angle of about 43°.

Time residuals are determined as the differences between the expected and the measured arrival time of the photon(s) on a given PMT. Photons that scatter in the water and photons emitted by secondary particles lead to residuals with increased magnitude. The reconstruction algorithms aim at finding muon track parameters for which the residuals are small in magnitude. This is done by maximising the sum over PMTs of a "score function" that is designed to be large when the residuals are small. In the final stage of the algorithm, the score function is the logarithm of the probability (log-likelihood) of a residual.

The background light from ^{40}K and bioluminescence potentially degrades both the angular resolution and the reconstruction efficiency. The algorithm accounts for this background by incorporating it into the probability function. A full description can be found in [51].

The probability density function of the arrival time residuals has been derived from simulations with the ANTARES software. It takes into account the probability of photons arriving late due to scattering or emission from secondary particles. Moreover, the probability of a hit being due to background is accounted for as a function of the hit amplitude. The overall log-likelihood value per degree of freedom obtained from the final fit is used as a measure of the fit quality.

The contribution of the background hits results in a likelihood function that has many local maxima as a function of the track parameters. As a consequence, the fit only converges to the correct solution if the start values are already a good approximation to this solution. The final likelihood fit is therefore preceded by a series of prefit algorithms of increasing sophistication.

The score functions used in these prefits are designed to yield an adequate trade-off between an accurate description of the true hit residuals and high efficiency for finding the global maximum. They allow for convergence to a solution which is typically within a few degrees of the true muon direction, while being robust against the presence of background hits with large residuals. Since not all parameters and probability density functions used in the muon reconstruction could as yet be optimised to KM3NeT in its different design options, there is room for further improvement of reconstruction efficiency and precision. For example, it has recently been demonstrated that an increase of the reconstruction efficiency in KM3NeT is achievable by replacing the prefits by a scan of the trajectory parameter space to define appropriate starting points for the final track optimisation. An alternative reconstruction algorithm is used in the SeaTray framework described in Section 6.2.2. This algorithm uses the Pandel parameterisation of the time residual distribution [52,53,54], which is a function derived from the physics laws of the underlying processes, with three free parameters determined from Monte Carlo simulations for various distances from point light sources. Despite the fact that it only has a small number of free parameters, it can accurately parameterise a large range light transmission phenomena. It is for this reason that it can also be used for muon tracks, which in principle have a light emission profile different from point sources of light.

6.1.4 Sensitivity Calculation

The number of detectable events from a neutrino source is related to the neutrino flux and to the detector response by the following relation:

$$N_s = \iint A^{\nu}_{eff}(E_\nu, \theta_\nu) \frac{d\Phi_\nu}{dE_\nu d\theta_\nu}\, dE_\nu\, d\theta_\nu$$

In this definition, $\frac{d\Phi_\nu}{dE_\nu d\theta_\nu}$ is the predicted astrophysical neutrino flux, E_ν is the neutrino energy and θ_ν is the neutrino angle with respect to the detector coordinate system. The neutrino effective area A^{ν}_{eff} is given by:

$$A^{\nu}_{eff}(E_\nu, \theta_\nu) = V_{eff}(E_\nu, \theta_\nu) \times \rho N_A \times \sigma(E_\nu) \times P_{earth}(E_\nu, \theta_\nu)\,,$$

where ρN_A is the number of nucleons per unit volume (ρ is the effective matter density in mol per volume and N_A the Avogadro number), $\sigma\,(E_\nu)$ is the neutrino cross section in the reaction channel considered, and P_{earth} is the neutrino transmission probability through the Earth. The quantity $V_{eff}\,(E_\nu, \theta_\nu)$ is the detector effective volume which is evaluated from the ratio between the numbers N_{rec} of reconstructed events and N_{gen} of neutrino interactions inside a generation volume V_{gen}, generously encompassing the instrumented volume. The effective volume is then given by:

$$V_{eff}(E_\nu, \theta_\nu) = \frac{N_{rec}(E_\nu, \theta_\nu)}{N_{gen}(E_\nu, \theta_\nu)} V_{gen}$$

The search for cosmic neutrino signals is based on statistical techniques that are appropriate for the detection of small numbers of events. The discovery potential of the neutrino telescope is evaluated using the model discovery potential (MDP) [52] calculated for a given level of significance (3σ, 5σ, …) and probability to make a discovery (70%, 90%, …). In this case cuts are optimised in order to obtain the least signal necessary to claim a discovery.

When no significant signal is observable, limits are set using the model rejection factor (MRF) [55]. In this case, the cuts are optimised to obtain the lowest possible expected upper limit for the experiment, assuming that no true signal is present. The average flux limit that can be placed on a neutrino flux model is defined by

$$\Phi_{90} = \Phi_S \cdot MRF = \Phi_S \frac{\bar{\mu}_{90}\big(\langle N_{bkg}\rangle\big)}{\langle N_s\rangle},$$

where Φ_S is the normalisation factor of the flux model. The MRF is defined as the ratio between the average upper experimental limit $\bar{\mu}_{90}$ on the number of signal events and the expected average number of signal events from the source for given Φ_S. The parameter $\bar{\mu}_{90}$ depends on the mean number of background events and is calculated following the Feldman-Cousins approach [56]. The sensitivity values reported in this document are obtained by minimising the Model Rejection Factor, unless explicitly stated otherwise.

6.2 Simulation

This section describes the software packages used for the Monte Carlo simulation. These packages generate neutrinos from astrophysical sources as well as atmospheric muons and atmospheric neutrinos. The code simulates the particle interactions with the medium surrounding the detector, light generation and propagation as well as the detector response.
Two principal and two alternative simulation chains have been used during the Design Study. The results presented in this chapter are produced by the two principal chains, one based on the ANTARES software and the other, named SeaTray, based on the IceCube software framework. Cross- checks on results have been made using these two chains and with the two alternative codes.
In all simulation chains a volume surrounding the instrumented volume, called "can", is defined. The can volume is a cylinder with height and radius exceeding the instrumented volume by about 3 absorption lengths. In the can volume, muons, taus and electrons are propagated and the Cherenkov light is generated.

6.2.1 ANTARES Software

Neutrino and anti-neutrino induced events are generated with the code GENHEN. Within GENHEN, neutrinos of all flavours with energies up to about 10^9 GeV are propagated through the Earth and their interactions simulated. Both charged current (CC) and neutral current (NC) reactions are implemented. The deep-inelastic scattering is simulated with the LEPTO code [57]. The quasi-elastic scattering and resonance production, dominant at low energies, are also taken into account. The propagation of muons and taus in rock or water up to the can surface is performed with MUSIC and TAUSIC [58], respectively.
The background due to down-going atmospheric muons is generated with the code MUPAGE [59] . MUPAGE provides a parameterised description of the underwater flux of atmospheric muons including also multi-muon events. The parameterised muon flux was obtained starting from full simulations with HEMAS [60]and cosmic ray data.
Muons inside the can are tracked with the code KM3 which generates and propagates the light produced by the muons and their secondary particles, taking into account the optical properties of the water. For the photon propagation, the code uses tables containing parameterisations obtained from a full GEANT3 [61] simulation. The code simulates the PMT hit probabilities and the response of the PMTs including the readout electronics. The PMT photocathode area, quantum efficiency and angular acceptance, as well as the transmission of light in the optical module glass sphere and in the optical gel are taken into account.
In order to reproduce the randomly distributed background hits due to optical background (^{40}K and bioluminescence), single photoelectron hits can be added to the muon-induced hits inside a chosen time window. Bursts of bioluminescence, whose effect is to saturate a small number of PMTs over a short period, are estimated to have a negligible effect and are not simulated.

6.2.2 SeaTray

The SeaTray software chain consists of modules organised in the IceTray software framework which has kindly been provided by the IceCube collaboration. The SeaTray package [62] has been specifically developed for use in KM3NeT, both for

the present simulation study and also for the future. SeaTray is a full replacement for the ANTARES software chain presented above and provides the same functionality either using ANTARES packages ported to SeaTray or using alternative modules. In this section only the alternative modules which have been used for the presented results are described.

The propagation through the Earth and the interactions of neutrinos of all flavours are simulated using the ANIS package [63] . Neutrino-nucleon interactions are generated using the CTEQ5 parton distribution functions [64]. CORSIKA [65] is used to generate the atmospheric muon background.

The MMC package [66] performs lepton propagation through matter, which is primarily used to track muons from their point of generation to the detector. The package provides a list of secondary particles above a certain energy threshold produced along the muon trajectory. After a muon has been tracked to and through the detector, light from the muon and its secondary particles is generated and propagated through the detector using the muon-sim[67] package. This package generates Cherenkov photons according to parameterisations produced using a full GEANT4 [68] simulation. Using a set of pre-generated lookup tables, these photons are then tracked through the water taking into account scattering and absorption.

For optical modules with a single PMT, the photons arriving at the optical module are converted into hits using a parameterisation of the angular acceptance. For optical modules containing multiple PMTs, an improved version of this algorithm was developed which performs a simple ray-tracing to identify the PMT that was hit by a particular photon. The PMT readout is simulated with a full time-over-threshold scheme, including a waveform simulation and a time/charge calibration with a time-walk correction. Both reconstruction algorithms described in Section 6.1.3 are implemented in SeaTray.

6.2.3 Alternative Simulations

Beyond the principal simulation chains a fast simulation tool has been developed to compare multiple detector configurations. The software package [69] is a detailed semi-analytic simulation based on the Mathematica software. This flexible tool makes it possible to scan relatively quickly a large parameter space, including design properties (distance between lines and storeys, PMT configurations) and the environmental characteristics (water optical properties, 40K and bioluminescence background). A further complete and independent simulation software [70,71], using GEANT4 for muon propagation and for light simulation, has also been developed. A reconstruction algorithm based on -2 minimisation and driven by Kalman filters is part of this package [72]. The results obtained with these alternative packages are in agreement with those of the ANTARES software and the SeaTray framework.

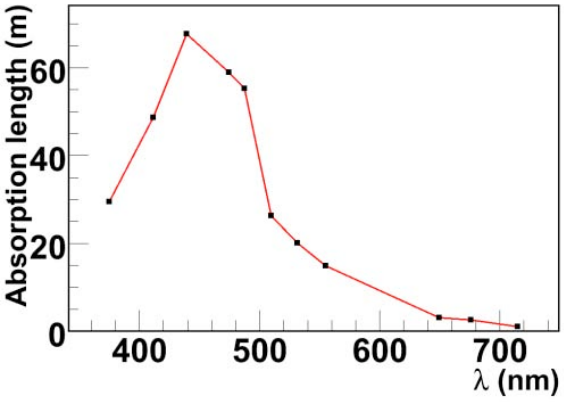

Figure 6-1: Absorption length used in the simulations as a function of wavelength.

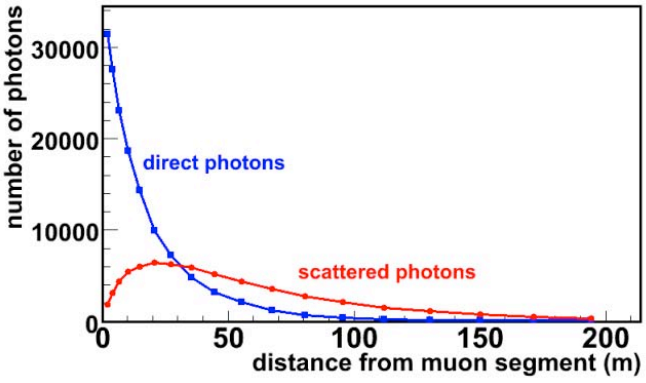

Figure 6-2: Number of Cherenkov photons, from 1 metre of muon path, reaching the given distance from the muon segment.

6.2.4 Sea water properties used in simulations

The simulations are based on the following sea water properties:

- The absorption length, shown in Figure 6-1, corresponds to a measurement at the Capo Passero site, at a depth of 3500m (see Section 5.3.2).
- Light scattering in water has been parameterised according to [73]. This model uses a combination of Rayleigh and Mie scattering, with a relative probability of 0.17 for Rayleigh scattering. The scattering length is computed assuming a concentration of small particles (size < 1μm) of 7.5 per m^3 of water. The same volume concentration is assumed for particles having sizes larger than 1μm.
- The refractive index used for the medium is taken from [74], resulting in 1.35 at 470 nm.

Figure 6-2 shows the number of Cherenkov photons produced per metre of muon trajectory reaching a certain distance. Both absorption and scattering effects are taken into account. This parameterisation is used in the simulation of detected light. Figure 6-3 shows the distribution of time delays induced by the scattering for a given distance to the emission point.

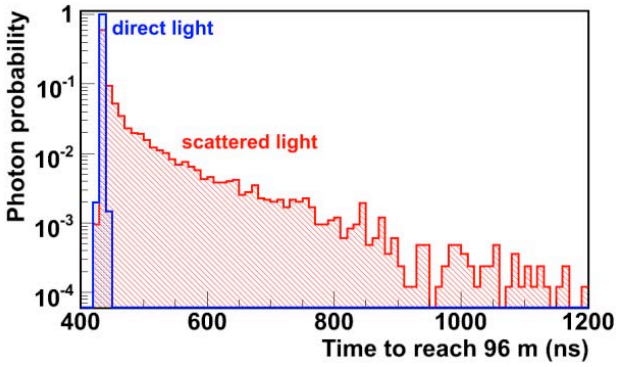

Figure 6-3: Time delay induced by the scattering of light at 96m from the muon segment.

6.3 Sensitivity Studies

The principal scientific objective of the KM3NeT neutrino telescope is neutrino astronomy, targeting the discovery of point-like neutrino sources. Therefore, the telescope optimisation was done with the main focus on such sources, assuming a power-law neutrino energy spectrum proportional to $E^{-\alpha}$ with $\alpha \approx 2$, implying that the main sensitivity must be in the energy range between a few TeV and about one PeV. All three neutrino flavours (ν_e, ν_μ, ν_τ) will be detected in the telescope; however, the best efficiency and angular resolution are achieved for muon neutrino reactions with a muon in the final state. All studies only consider neutrinos coming from below the horizon

For point source searches the MRF method described in Section 6.1.4 is used to evaluate sensitivities. The sensitivities have been obtained applying a "binned" method where the sky is divided in bins of declination and right ascension and the numbers of events detected per bin are analysed. The parameters that are optimised in order to minimise the MRF are the size of the search cone around the source, the cut on the reconstruction quality parameter and a cut on the number of neutrino hits that is related to the neutrino energy. The average number of events from a point-like source, at a given declination and with a spectral index α is estimated by means of Monte Carlo simulations, as well as the average number of background events inside the selected search cone centred on the source direction. The background is due to atmospheric neutrinos and atmospheric muons that are mis-reconstructed as up-going.

6.3.1 Detector Optimization and Performance

Three combinations of technical options as described in Chapter 3 have been investigated in simulation studies:

1. 127 bar-structure detection units arranged in a hexagonal grid (6 m lateral extent, 40 m between storeys, and 180 m between detection units). Each bar is equipped with 3 pairs of 8-inch PMTs.
2. 127 triangle-structure detection units arranged in a hexagonal grid (3 m lateral extent, 40 m between storeys, 150 m between detection units). Each storey is equipped with 3 pairs of 8-inch PMTs arranged in a triangular configuration.
3. 310 string detection units arranged in a rectangular grid (30 m between storeys, 130 m between detection units). Each storey is an optical module equipped with 31 3-inch PMTs.

All these homogeneous configurations are building blocks of the full detector. Detailed optimisation studies have been performed for all options and have led to the choice of dimensions given above. An example of such an optimisation is presented in the following for option 1.

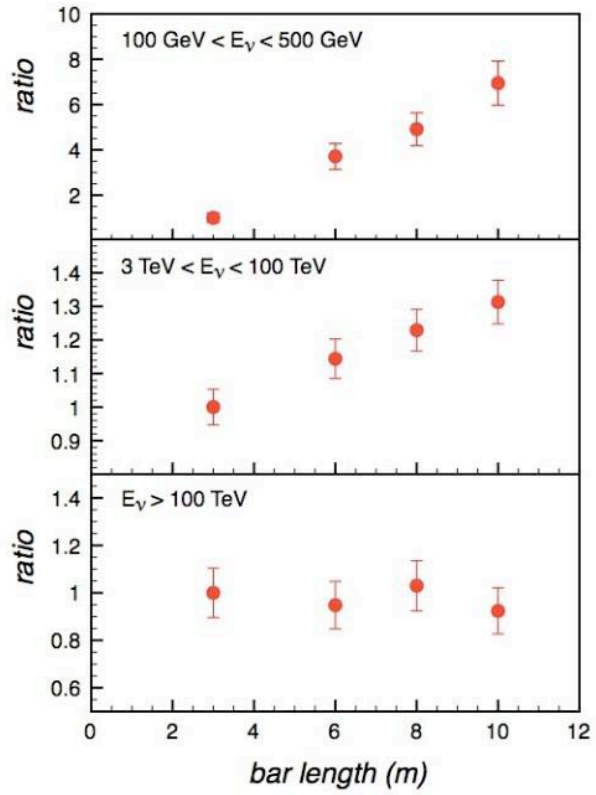

Figure 6-4: The change in neutrino effective area as a function of the bar length for the bar structure detection unit configuration. Shown is the ratio of the effective area relative to a bar length of 3m, for the three energy ranges indicated.

The bar structure offers the advantage that the three-dimensional arrangement of OMs within a single detection unit helps resolve ambiguities in the reconstruction of the azimuthal angle of a muon track. The effect of changing the lateral bar length between 3m and 10m is shown in Figure 6-4. It can be seen that at low and intermediate neutrino energies a significant gain can be obtained for larger lengths. .Taking into account simulation results and technical constraints (such as stability in currents, cost, logistics and safety), a bar length of 6 m is finally chosen as the optimum.

A further example of the optimization is given in Figure 6-5 which shows the point-like source sensitivity as a function of the detection unit separation, which was finally chosen at 180 m, where maximal sensitivity is found [75].

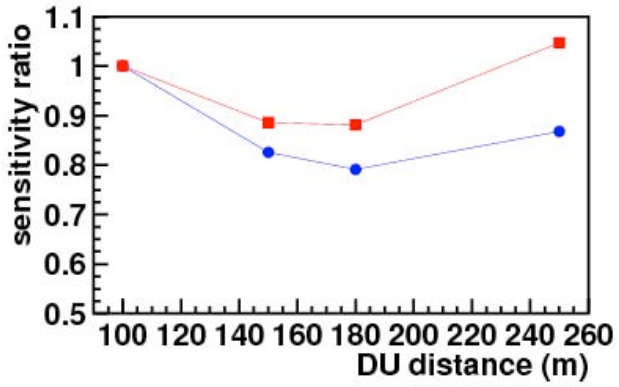

Figure 6-5: Change of the sensitivity of a point source search as a function of the detection unit separations for two different source spectra. The plot shows the ratio of the sensitivity relative to a separation of 100 m. The source spectra are proportional to $E^{-\alpha}$ with blue circles for $\alpha = 2.0$ and red squares for $\alpha = 2.2$.

Figure 6-6 shows the point-source search sensitivity for one year of observation time for one building block of each of the three options mentioned above, as a function of declination.

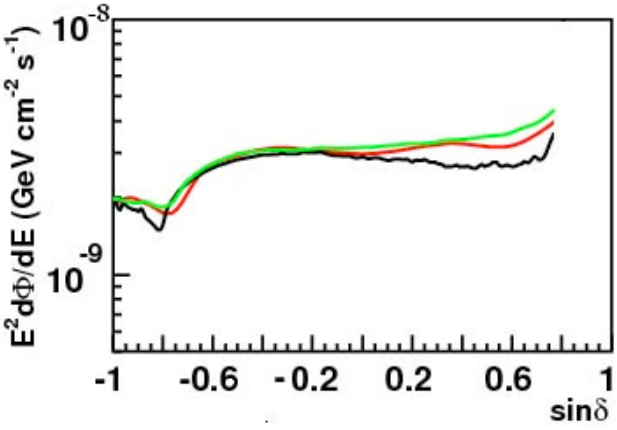

Figure 6-6: Sensitivity to point sources (E^{-2} flux) for one year of observation time, for the three detector configurations studied. The red line is for option 1, the green for option 2 and the black for option 3.

The performances of all building blocks are the same within about 20%. As will be described in Chapter 9 the estimated costs for the three options differ by less than 20%. In Chapter 9, Figure 9-1 shows the sensitivity for a full detector achievable for a capital investment of 220M€ in the three configurations. These final sensitivities are very similar and the best configuration is chosen for all the following results in this document.

The neutrino effective area for this full KM3NeT detector is shown in Figure 6-7 for loose cuts ensuring reasonable angular resolution and for quality cutswhich have been optimised for point-source searches for.

For searches for point-like neutrino sources, the angular resolution is a critical parameter. It is dominated by the intrinsic ν-μ angle at low energies, while at higher energy the telescope response dominates. For a deep-sea neutrino telescope the angular resolution profits from the strongly reduced scattering effects as compared to ice.
The left panel of Figure 6-8 shows the angular resolution, obtained with design option 1, in terms of the angle between the neutrino direction and the reconstructed muon track; in this figure the intrinsic angle between the neutrino and muon directions is also shown.

The cumulative point spread function, after quality cuts, is shown in the right panel of Figure 6-8. The telescope has a superb angular resolution; indeed about 70% of selected events lie within 0.2° of the neutrino direction.

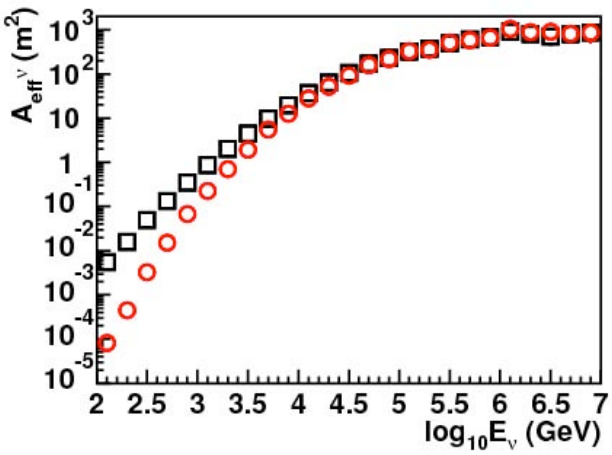

Figure 6-7: Neutrino effective areas for the full detector. The plot is for up-going neutrinos. The red dots are after quality cuts optimised for searches for point-like neutrino sources and the black squares are for looser quality cuts ensuring reasonable angular resolution.

6.3.2 Neutrino Point Sources

The observation of point-like sources of neutrinos would bring unique new insights on the nature of cosmic accelerators and resolve the enigma of the origin of cosmic rays which has been a mystery for the 100 years since their discovery. Observations by gamma ray telescopes have revealed many astrophysical objects, in which high-energy processes at and beyond the TeV level take place (see Figure 6-9); however, measurements with gamma rays alone cannot clearly distinguish whether the accelerated particles are leptons or hadrons. Only the observation of neutrinos from a source can unambiguously establish the hadronic nature of that source. Supernova remnants (SNR) of the shell type are the most probable sources of cosmic rays in the Galaxy. The material ejected during the explosion forms shock waves when it propagates into the interstellar matter. Particles are assumed to be accelerated in these shock waves, which can persist for several thousand years. The shell-type SNRs with the most intense gamma rays fluxes measured beyond 10 TeV are RX J0852.0-4622 (Vela Junior) and RX J1713.7-3946.

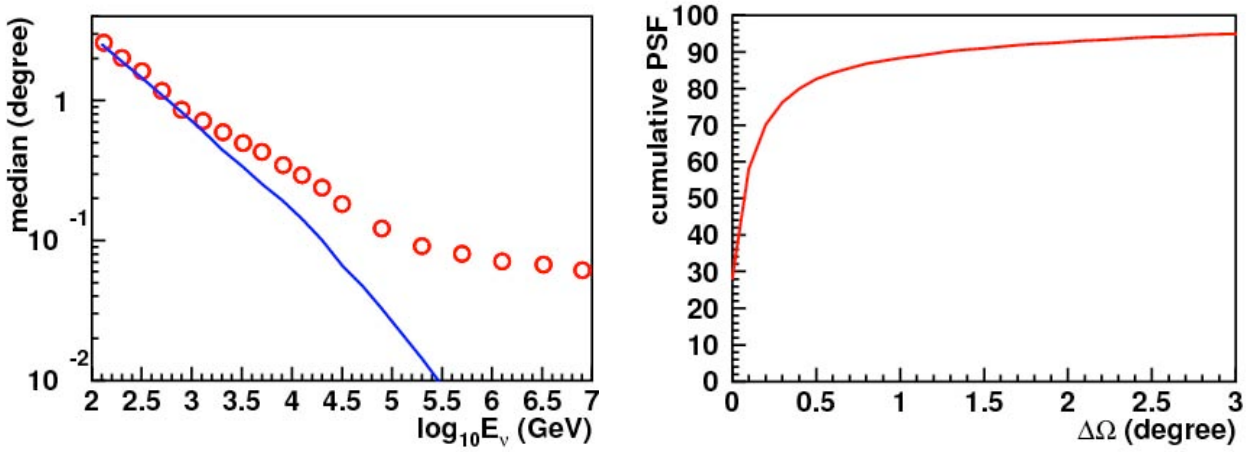

Figure 6-8: Left panel: Median of the distribution of the angle ΔΩ between the neutrino and the reconstructed muon track (red points). The blue line is the median of the intrinsic angle between neutrino and muon directions, driven by the dynamics of deep-inelastic neutrino-nucleon scattering and kinematics. Right panel: Cumulative point spread function for an energy spectrum according to E^{-2}, after quality cuts applied, i.e. the fraction of events with ΔΩ less than a given value.

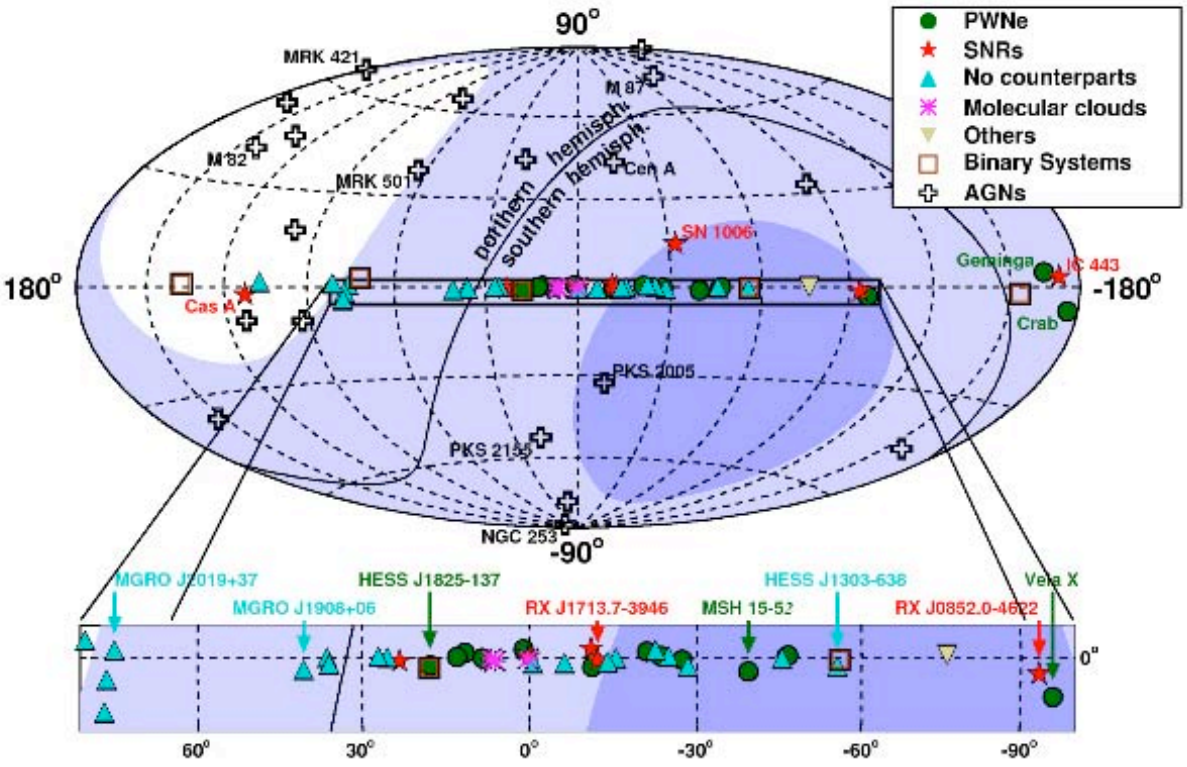

Figure 6-9: Sky coverage in Galactic coordinates for detectors located in the Mediterranean Sea and at the South Pole, where only the northern hemisphere can be observed. The shading indicates the visibility for a detector in the Mediterranean with 2π downward coverage; dark (light) blue areas are visible at least 75% (25%) of the time. The locations of observed sources of high-energy γ rays are also indicated.

Another class of intense gamma sources are the pulsar wind nebulae (PWNe) which differ from the shell-type SNRs in that the acceleration takes place in the region of the central pulsar emitting collimated, very fast-moving material into the surrounding matter. Radio, optical, X-ray and TeV gamma observations suggest a synchrotron origin for these emissions, indicating a leptonic acceleration process. However, for some intense sources such as Vela X, the possibility of a hadronic origin remains valid and they thus could be neutrino sources.

The Galactic Centre region contains many structures which could be neutrino sources, such as the TeV gamma source HESS J1745-290 coincident with the super massive black hole Sagittarius A*, as well as the SNR Sgr A East and the PWN G359.95-0.04. Other potential neutrino sources are microquasars, which are Galactic X-ray binary systems with relativistic jets observed in the radio regime. Among such sources are: GX339-4, SS 433, LS I +61 303 and LS 5039. A major advantage of KM3NeT relative to IceCube is the location in the Mediterranean Sea. Figure 6-9 shows the KM3NeT field of view compared to that of a neutrino telescope at the South Pole. This field of view allows for the observation of up-going neutrinos from a large fraction of the sky (about 3.5 π) including the Galactic Centre and most of the Galactic Plane. In this region many TeV gamma sources have been observed, among them several of those described above as well as further sources that have not yet been identified. It is also noteworthy that the closest extragalactic object in Figure 6-9, the AGN Centaurus A, is located in the southern hemisphere where it is always above the horizon for neutrino telescopes at the South Pole.

The sensitivity of the detector to neutrino point sources, based on one year of data, is shown in Figure 6-10 as a function of the declination. The detector performance is presented as the flux that can be excluded at 90% CL (flux sensitivity) and the flux that can be detected at 5σ with 50% probability (discovery flux). This calculation assumes a neutrino energy spectrum proportional to E^{-2}. For comparison, the plot also shows the flux sensitivity of IceCube [2] (using an unbinned method and a reconstruction algorithm that exploits energy-related information) and the IceCube discovery flux . The latter has been extrapolated from the flux sensitivity using a factor of 2.5 to 3.5 which is based on the corresponding ratio for the IceCube 40-string configuration[76]. The differences in shape of the sensitivity curves for KM3NeT and IceCube are caused by the different geographic location, the effect of neutrino absorption in the Earth and the different detector responses as a function of zenith angle. The use of an unbinned method is expected to give an improvement in the KM3NeT sensitivity of about 40%. From Figure 6-10 it can be seen that the KM3NeT sensitivity is better than that of IceCube over the full range of declinations, even those in the northern sky which is the central field of view from the South Pole. For the southern sky, which is best viewed from the Mediterranean Sea, KM3NeT will have a sensitivity nearly two orders of magnitude better than that of the current instruments, Baikal and ANTARES, whose sensitivity curves fall outside the limits of the figure. To illustrate the importance of this region of the sky, the positions in declination of the Galactic sources indicated in Figure 6-9 are shown.
The sensitivity as a function of the observation time is shown in Figure 6-11.
Many of the Galactic TeV gamma sources shown in Figure 6-9, and in particular the supernova remnants, have an angular size larger than the resolution of the neutrino telescope. For the search for such extended sources a study has been made of the impact of the source size on the sensitivity. Since these sources are in general expected to have a cut-off in their energy spectra at some TeV to some 10 TeV, a neutrino flux proportional to $E^{-2}\exp(-E/20\text{TeV})$ has been assumed. The result of this study, shown in Figure 6-12, indicates that the sensitivity is reduced by a factor of about 2 for typical source diameters of 1°.

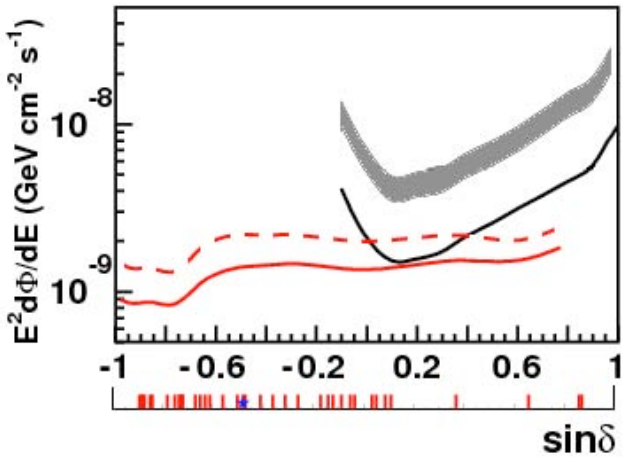

Figure 6-10: Sensitivity of the full KM3NeT detector to neutrino point sources with an E^{-2} spectrum for one year of observation, as a function of the source declination. The red lines indicate the flux sensitivity (90% CL;full line) and the discovery flux(5σ, 50% probability; dashed line). Both are estimated with the binned analysis method. The black line is the IceCube flux sensitivity for one year, estimated with the unbinned method [2] (full line). IceCube's discovery flux (5σ, 50% probability) is also indicated (shaded band, spanning a factor 2.5 to 3.5 above the flux sensitivity). The red ticks at the bottom of the horizontal axis show the positions of Galactic gamma ray sources [3]; the position of the Galactic Centre is indicated by a blue star.

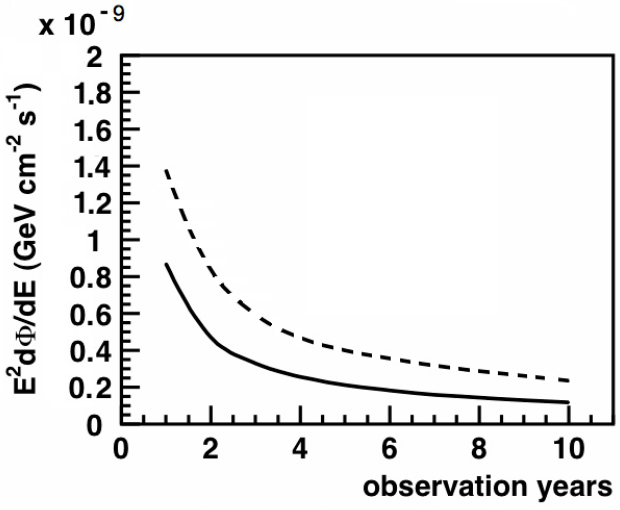

Figure 6-11: Flux sensitivity (90% CL; solid line) and discovery flux (5σ, 50% probability; dashed line) of the full KM3NeT detector as a function of observation time for declination δ =-60° (i.e. sin δ = -0.866) and α =-2.

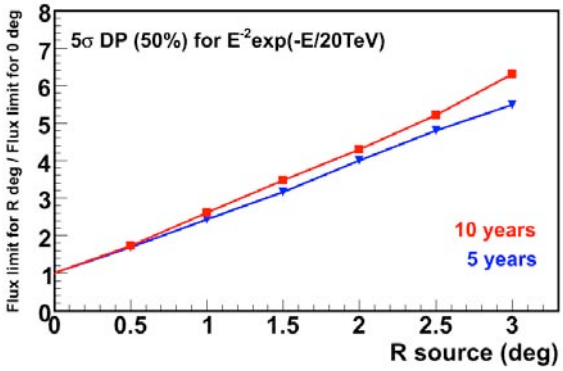

Figure 6-12: Dependence of the discovery flux (5σ, 50% probability) on the angular radius R of a neutrino source. The blue (red) lines and symbols indicate the sensitivities after 5 (10) years of observation, relative to point sources with R=0. For this study, homogeneous emission from the source region and a neutrino spectrum with a cut-off proportional to E^{-2} exp(-E/20TeV) were assumed.

The estimated sensitivity of the detector to neutrino fluxes from these point sources depends strongly on the extension of the spectrum to high energies. Figure 6-13 shows the dependence of flux sensitivity and discovery flux on the assumed cut-off energy. When the cut-off energy decreases from 1 PeV to 10 TeV the sensitivity worsens by an order of magnitude.

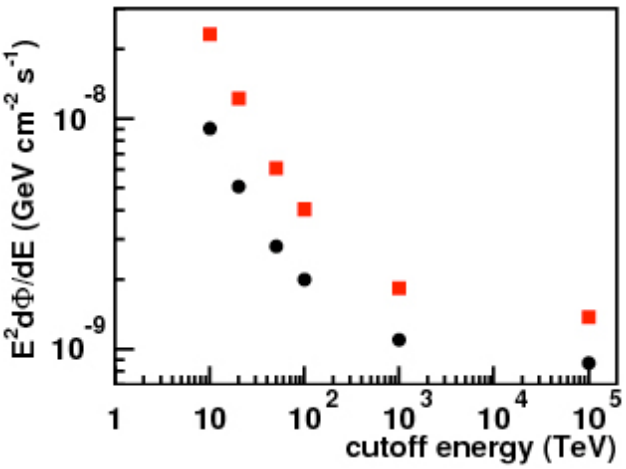

Figure 6-13: Evolution of the one year flux sensitivity (black dots) and discovery flux (5σ, 50% probability; red squares) for point sources at a declination of -60° as a function of the assumed cut-off of the energy spectrum.

The expected neutrino fluxes and the corresponding KM3NeT event rates from various Galactic high-energy gamma ray sources, observed by the HESS telescope, have previously been calculated assuming that the gamma emission is of purely hadronic origin, i.e. from π^0 decays [77]. This study has now been updated, using the most recent gamma flux measurements and the effective areas reported in this document. The results are presented in Table 6.1. Significant uncertainties arise from the fact that the gamma ray measurements do not precisely constrain the cut-off energy of the spectra, which are of central importance for the expected neutrino event numbers. For several sources, however, a significant detection after several years of observation time appears to be possible. This is confirmed by a dedicated study for RX J1713.7-3946 in which the source was simulated as an extended shell-type SNR. The study used a full Monte Carlo and analysis chain to determine the significance of the signal in the KM3NeT detector as a function of observation time (Figure 6-14).

Source Name	Source radius (°)	Visibility	Number of events for $E_\nu > 5$ TeV	
			Signal ν	Atm ν
RX J1713.7−3946	0.7	0.74	4 – 11	6.4
RX J0852.0−4622	1.0	0.84	2 – 6	17
Vela X	0.4	0.81	4 – 15	3.5
Crab Nebula	< 0.1	0.39	1 – 3	0.8

Table 6.1: Numbers of expected events in five years of observation time for a selection of possible Galactic sources of neutrinos. The numbers of signal events and of background events from atmospheric neutrinos inside the optimised cone cut is given. The source extension and the fraction of time the source is visible are also indicated.

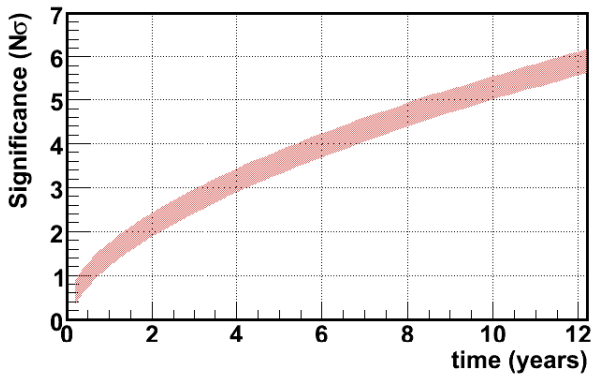

Figure 6 -14: Significance for discovery of supernova remnant RXJ1713 as a function of years of running time.

6.3.3 Transient Sources

For transient sources, it is possible to reduce the background dramatically by selecting a time window around the neutrino emission period. Different analysis techniques will be applied to objects like GRBs, AGN flares and microquasars, where information on the emission time is obtained from the observation of electromagnetic radiation, and to sources which have no emissions recorded by other instruments. To illustrate the performance of the KM3NeT detector, studies of GRBs and core-collapse supernovae are presented in the following. The two strategies used by ANTARES for the search of neutrinos coming from transient sources can also be applied for KM3NeT [78]. The first method is based on a search in conjunction with an accurate timing and positional information provided by external observations: the *Triggered Search*. For GRBs, the triggers are generated by a set of satellites sending signals to the Gamma Ray Burst Coordinates Network (GCN), which distributes the data of the GRBs detected by spacecraft. At the present time, GRB alerts are primarily provided by the Swift and FERMI satellites. For the future decade, several GRB missions have been proposed. One of the most advanced, with launch scheduled in 2012, is the

Space–based multi–band astronomical Variable Object Monitor (SVOM). The second search strategy exploits the very large field of view of a neutrino telescope and is based on multiplets of neutrino events coming from the same direction within a short time window: the *Rolling Search*. Gamma-ray bursts are the most energetic events in the Universe. Discovered in the late 1960s, their cosmological origin was unambiguously demonstrated only in 1997 when the first observation of a GRB afterglow provided a distance measurement. From the radiation flux on Earth, the typical gamma energy emitted by a GRB in a couple of minutes is estimated to be 10^{51}–10^{52} erg, depending on the collimation of the radiation flux. Observations suggest that the long-duration (>2 s) bursts originate probably from the collapse of a massive stellar progenitor into a black hole, whereas short-duration (<2 s) bursts progenitors, both lead to the formation of stellar black holes and collimated jet outflows. In the current canonical picture, the so-called *Fireball* model [79], "shells" of matter (plasma) are emitted from the vicinity of the new-born black hole into the interstellar medium with relativistic bulk Lorentz factors (typically >100). If shells with different velocities are emitted, a faster shell can reach a slower one and produce a shock which generates particle acceleration.
Using the Fireball model and measured gamma-ray spectra, it is possible to make predictions for the corresponding neutrino spectrum [80]. Figure 6-15 shows the neutrino energy spectrum calculated for a set of sample GRBs (see also [81]) detected by Swift and FERMI. Table 6.2 gives neutrino signals for the two most powerful bursts of Figure 6-15 plus the sum of 100 bursts according to a reference spectrum of Waxman and Bahcall [72]. It is clear that KM3NeT would be able to make a very significant discovery if these rates are correct. However, it has to be kept in mind that these predictions must be taken as order-of-magnitude estimates.
An example of the rolling strategy is the search for neutrino bursts from core-collapse supernovae. It has been suggested [83,48], that in some of these explosions the jet does not escape from the stellar environment and the gamma ray emission is "choked", so that the event cannot be observed by GRB satellites and only the neutrino emission is bright ("failed GRB").
In such models mildly relativistic jets ploughing through a star would be efficient in producing high energy neutrinos. The predicted neutrino spectrum follows a broken power law and for a supernova at a distance of 10 Mpc, about 60 events are

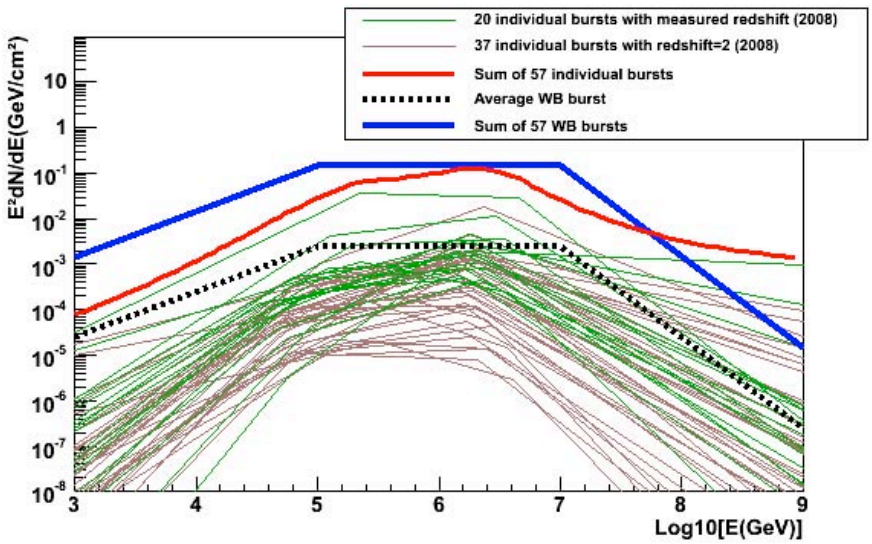

Figure 6-15: Neutrino spectra predicted for 57 GRBs detected in 2008 which could produce up-going events in the KM3NeT detector. The green lines indicate the expected neutrino fluxes for 20 GRBs with measured redshift, the brown lines the fluxes for 37 further GRBs without measured redshift, for which z=2 was assumed. The neutrino flux from an average GRB in the Waxmann Bahcall model [82] is indicated by the dashed black line. The sum of the individual GRB fluxes (green and brown lines) is shown as the red line, the sum of 57 average Waxman-Bahcall GRBs as the blue line.

neutrinos from the same celestial direction within a short time window. Within a distance of 10 Mpc, the rate of core-collapse supernovae is more than 1 yr^{-1} giving a high probability for the observation of such an event in the lifetime of the experiment. The basic idea of the rolling search method is that the detection of a small number of neutrinos in temporal and directional coincidence is statistically significant. For example, with KM3NeT, the probability of a random coincidence of three atmospheric neutrinos within a time window of Δ t=100 s and a solid angle of $\Delta\ \Omega = (2°)^2$ is $4x10^{-3}$/year. The method makes no assumption on the nature of the source and can be applied for any transient source of neutrinos.

At X-ray and lower gamma-ray energies, the sky is observed at any given time by modern space-based astronomical observatories like Swift and FERMI. Ground-based high-energy gamma-ray detectors like H.E.S.S. or MAGIC currently cover only a small fraction of the sky at any given moment. Multiwavelength astronomical observations can be used to associate neutrino point source detections with transient astronomical sources like AGN flares or jet-production events, thus significantly enhancing the discovery potential. Furthermore, it is possible to organise a follow-up programwith a small network of automated 0.3 - 1m telescopes, as originally proposed in [84]. Such optical telescopes already exist and many more are planned. For example, the TAROT network used by the ANTARES collaboration [85] and the ROTSE III network used by the IceCube collaboration[86], consist of several robotic telescopes, each with a 1.9° × 1.9° field of view.

GRB	Signal	Background
GRB080319B RX	2.6	5×10^{-4}
GRB080916C	2.7	5×10^{-4}
100 typical GRB	12	6×10^{-2}

Table 6.2: Number of expected signal and background events from the two most energetic GRBs detected by SWIFT (GRB080319B) and FERMI (GRB080916C) during 2008. Also shown is the sum of the signal expectations for 100 bursts (which roughly corresponds to the GRB detection rate per year with future satellite systems) according to the reference spectrum of Waxman and Bahcall [82].

6.3.4 Diffuse Fluxes

Beyond point-like sources, the following diffuse fluxes of neutrinos are expected:

- diffuse neutrino flux from unresolved extragalactic sources;
- cosmogenic neutrino flux produced during the propagation of ultra-high energy protons through the CMB radiation;
- a diffuse neutrino flux from the Galaxy.

Without the possibility of using a tight angular cut for reducing the background of atmospheric neutrinos, diffuse neutrino flux searches have to rely on a cut on the reconstructed energy. Such a cut is effective in separating cosmic neutrinos (with a spectrum expected to be roughly proportional to E^{-2}) from atmospheric neutrinos (spectrum proportional to about $E^{-3.7}$). In the case of a Galactic diffuse flux, directional information can be used for selecting events close to the Galactic Plane.

The energy reconstruction of neutrinos is based on the photon-counting capabilities of the detector. The energy loss of the final-state muon from charged current muon-neutrino events is, for muon energies above about 1 TeV, proportional to the muon energy. The number of detected photons is, in turn, proportional to the muon energy loss in the instrumented volume of detector. The neutrino energy is finally estimated from the muon energy, taking into account the kinematics of neutrino-nucleon interactions. For the present sensitivity studies, a simple energy estimator was used, based on hit counting for the reconstructed muon track. The neutrino energy resolution expected in KM3NeT for muon neutrino events is about $\Delta\log(E_\nu) = 0.5$.

A further difference between the atmospheric and cosmic neutrino fluxes which can be exploited in the analysis is the different composition in neutrino flavours. At high energies, the atmospheric neutrino flux mainly consists of ν_μ, while cosmic

flavours are distinct; for example, ν_e and most of ν_τ reactions induce shower-type events, the charged-current channel of muon neutrino interactions yields a muon-type event. For ultra-high neutrino energies, as expected e.g. for the cosmogenic neutrino flux, the Earth is opaque to neutrinos. In this case, neutrinos coming from the upper hemisphere have to be identified and separated from the atmospheric muon background. For such studies, shower events are important since they profit from a strongly reduced background induced by atmospheric muons. The sensitivity to diffuse neutrino fluxes presented here is based only on the ν_μ mode; a reconstruction of shower events is under study [87].

Diffuse Flux from Unresolved Extragalactic Sources

The cosmic rays above the "knee" of the spectrum at about 10^{15}eV are believed to have an extragalactic origin and are thought to originate from sources such as AGNs and GRBs. The neutrinos from a multitude of such objects are expected to form an isotropic, diffuse flux. Assuming that the proton energies in such cosmic ray sources is completely transferred to pions, which then produce neutrinos through their decays, one can derive an upper limit for the resulting extragalactic diffuse neutrino flux [88]. This is known as a "Waxman-Bahcall limit" and, for an E^{-2} spectrum, is equal to $E^{-2}\,dN/dE = 5 \times 10^{-8}$ GeV cm^{-2} s^{-1} sr^{-1}.

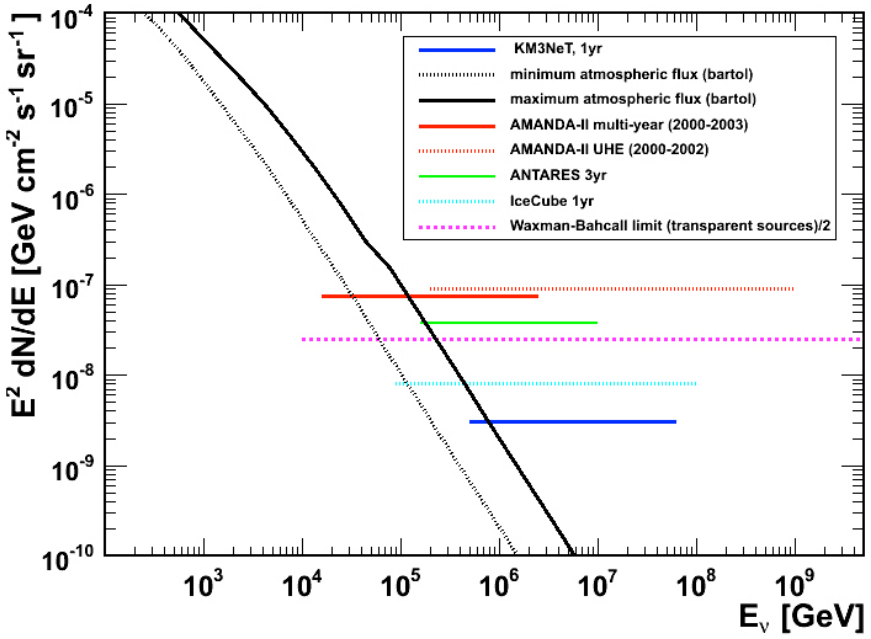

Figure 6-16: Diffuse flux sensitivity of the KM3NeT neutrino telescope for one year of observation time, together with Waxman-Bahcall limit [88] and sensitivity limits from AMANDA [89,90], ANTARES [91 and IceCube [92]: recent preliminary results from the 40 line IceCube detector show that these predicted limits have already been reached. For the experimental sensitivities, the horizontal extent of the limit lines indicates the energy range for which the study was performed.

The sensitivity to diffuse fluxes was optimised with the MRF method leading to an effective energy cut $E_\nu > 10^{5.6}$ GeV.
A neutrino flux with a spectrum proportional to E^{-2} was assumed. The minimal flux limit obtained is 3×10^{-9} GeV cm^{-2} s^{-1}sr^{-1} and is shown in Figure 6-16 together with results obtained for other neutrino telescopes.

Cosmogenic Neutrino Flux

A diffuse "cosmogenic" neutrino flux is generated during the propagation of cosmic rays through the cosmic microwave background radiation (CMB). Above about $10^{19.6}$ eV the cosmic ray protons produce pions through photo-production of Δ resonances: $p\gamma_{CMB} \rightarrow \Delta^{+} \rightarrow n\pi^{+}/p\pi^{0}$. The subsequent decay of the charged pions and neutrons results in a diffuse neutrino flux. For different cosmic ray compositions, the event rates per km^3 of water volume and per year are given in [93]. An estimate of the cosmogenic neutrino events rates in KM3NeT gives 2-3 events/year, assuming that all ultra-high energy cosmic rays are protons.

Galactic Neutrino Flux

The bulk of cosmic rays observed on Earth are produced in the Galaxy. The diffuse gamma and neutrino fluxes, which are produced in the interaction of cosmic ray protons and nuclei with the interstellar gas in the Galaxy, are expected to be roughly equal. The assumption that observed Galactic gamma emission comes from hadronic processes thus yields an estimate of the diffuse Galactic neutrino flux.

The Galactic plane occupies a relatively small area of sky, the inner part of which is visible from the Mediterranean Sea. This region has an extension of 0.097 steradians ($-40° < l < 40°$ and $-2° < b < 2°$, where l and b are Galactic longitude and latitude) and occupies less than 1% of the neutrino sky visible by KM3NeT.

The prediction used here for the neutrino flux was calculated from the multi-TeV gamma emission observed by MILAGRO [94]. The calculation assumes that the flux measured in the region $30°<l<65°$ is representative for the whole Galaxy (the inner part of the Galaxy was not visible to MILAGRO) and that the origin of this emission is entirely hadronic. The predicted event rates from the resulting Galactic diffuse neutrino flux in KM3NeT are given in Figure 6-17 for the three different cosmic ray spectra defined in reference [95]. Between 14 and 39 neutrino events are expected above 10 TeV in one year, depending on the cosmic ray spectra. The rate of atmospheric neutrinos under similar conditions corresponds to 80 events per year.

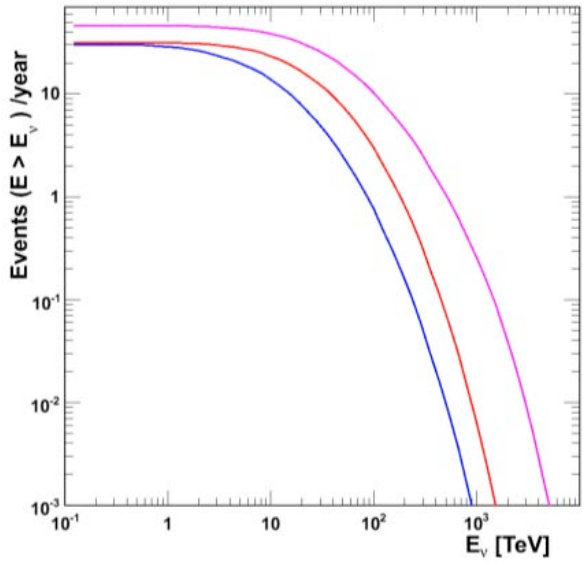

Figure 6-17: Integral neutrino event rates above a given energy in the KM3NeT neutrino telescope from the diffuse flux from the inner Galaxy; the three lines are the predictions for the different flux assumptions given [95]. About 80 atmospheric neutrino events are expected above 10 TeV.

6.3.5 Dark Matter

A deep-sea neutrino telescope allows for performing indirect search for Dark Matter, the existence of which is strongly indicated by astronomical observations and essential for the standard model of cosmology. Except in more exotic scenarios, Dark Matter is assumed to consist of neutral, weakly interacting massive particles (WIMPs) with masses of at least several GeV/c^2. Many theories, most notably Supersymmetry and Extra-Dimensions, feature a suitable candidate particle, which is stable due to conservation of a multiplicative quantum number that is different for Dark Matter and Standard Model particles. However, the annihilation of two Dark Matter particles into Standard Model particles is allowed. The Dark Matter is assumed to have frozen out of equilibrium with the lighter standard matter when the Universe cooled down. From measurements of the fluctuations of the Cosmic Microwave Background by the WMAP experiment, the current relic density of Dark Matter is derived, which poses strong constraints on the combination of mass and production/annihilation cross-section of the Dark Matter particles, independent of the specific theory [96].

Among the supersymmetric theories the minimal Supergravity model (mSugra) is especially well studied. In mSugra, the supersymmetry breaking occurs in the hidden sector and is communicated to the physical sector by gravity. Using the renormalisation group equation, the masses and couplings at the electroweak scale are calculated from four continuous parameters plus a sign defined at an energy scale of 10^{16} GeV. A valid candidate for Dark Matter could be the lightest of four neutralinos, which are the mass eigenstates of the four neutral higgsinos and gauginos.

The detection rate in KM3NeT of neutrinos originating from the annihilation of neutralinos captured in the Sun has been calculated for about four million distinct parameter combinations in the mSugra parameter space using DarkSUSY [97]. The scan was guided by comparison of the resulting relic density to the result from WMAP [96]. The ISASUGRA renormalisation group equation code [98] was used. For the Galactic halo profile, the Navarro-Frenk-White [99] parameterisation was chosen, and the mass of the top quark was set to 172.5 GeV/c^2.

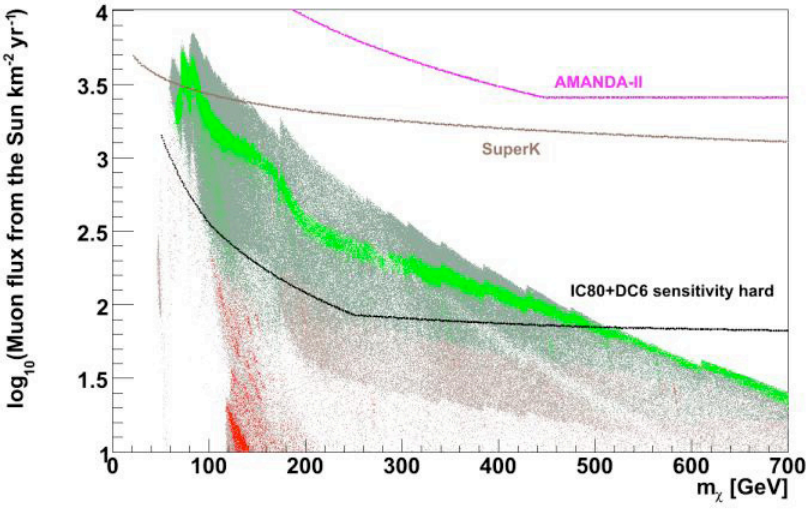

Figure 6-18: The muon flux above a threshold energy of one GeV induced in a neutrino telescope by neutrinos from annihilation of mSugra Dark Matter in the Sun, as a function of the neutralino mass The coloured points correspond to mSugra parameters consistent with the WMAP observations (see text). The models within (outside) the detection reach of KM3NeT are coloured green (red). The KM3NeT and IceCube sensitivities correspond to observation times of 10 years. Limits from selected experiments [100,103,102] are also indicated.

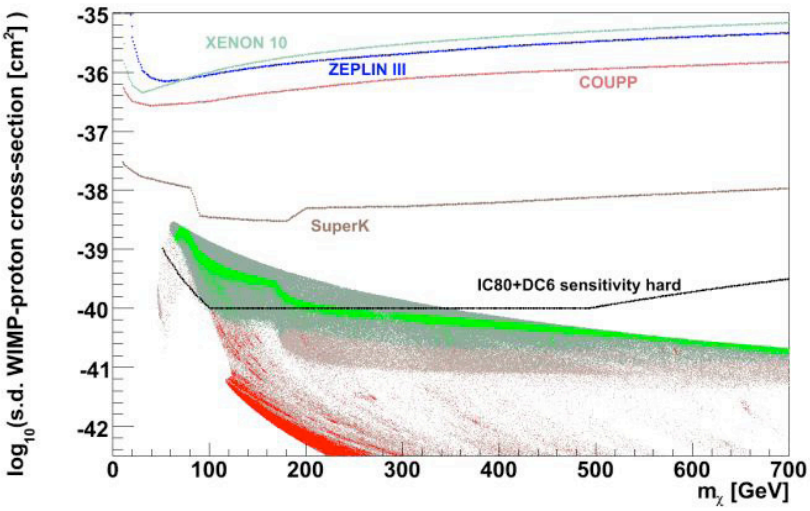

Figure 6-19: The spin-dependent WIMP-proton cross section plotted against the neutralino mass. The coloured points correspond to mSugra parameters consistent with the WMAP observations (see text). The models within (beyond) the discovery reach of KM3NeT are coloured green (red). Limits of selected experiments are also indicated.

From the detection rate for neutrinos originating from neutralino annihilation in the Sun, a 90% CL exclusion sensitivity for 10 years of data taking data was calculated. The analysis assumed a search cone of 3° radius around the Sun and the neutrino energy was restricted to be between 50 GeV and the mass of the neutralino. Detectable models are coloured green in Figure 6-18 and Figure 6-19, the others red. Bright colours indicate a relic density within the 2-sigma band of WMAP. The topmost branch of mSugra models corresponds to the Focus Point Region [104] of the parameter space. This region can be nearly completely assessed by KM3NeT. As seen from Figure 6-19, the sensitivity of KM3NeT on the spin-dependent WIMP-proton cross section is significantly higher than for current direct detection experiments [105,106,107], when measuring exclusively this quantity.

Comparing the IceCube experiment sensitivity [103], calculated under conservative assumptions, to the model-specific sensitivity of KM3NeT (Figure 6-18 and Figure 6-19), it can be concluded that IceCube's capabilities concerning Dark Matter detection will exceed those of KM3NeT. This is mostly due to the extra sensitivity added to IceCube by the "Deep Core" installation. Note that a similar set-up is also possible for KM3NeT and might be quickly installed in case findings from other experiments (IceCube, direct WIMP searches, LHC) suggest that this was appropriate.

7. Ecological Impact and Decommissioning

The environmental impact of the telescope infrastructure can be considered in the 4 time phases:
Phase 1: Construction and commissioning.
Phase 2: Operations and maintenance.
Phase 3: Decommissioning.
Phase 4: Legacy post-decommissioning.
Within each of these phases (to varying degrees) there are considerations regarding:
1. Shore-based infrastructure directly connected to the telescope.
2. Sub-sea infrastructure
3. The cable route.
4. Infrastructure and operations at the partner institutions.
5. Operations during manufacture at partner institutions and suppliers.

7.1 Construction and Commissioning

In general it is during this phase that the greatest environmental disturbance will occur associated with manufacture of the telescope components, their transport to the ultimate location and deployment in the sea. Once commissioned, the shore-based infrastructure connected to the telescope is modest in size comprising power supply systems and computers, which at the three main candidate sites can be accommodated in existing buildings. Therefore no major new construction works are anticipated on shore. The sea floor infrastructure implies assembly of a large weight and volume of material. For transportation it is expected that material will be containerised and total quantity will be of the order of 1000 Twenty-foot Equivalent Units (1000 TEU). This represents a small fraction of the annual traffic at regional ports Marseilles 0.8mTEU, Gioa-Tauro 3m TEU and Piraeus 1.6m TEU[108] and will be spread over several years of construction. Locations will be sought for final assembly and testing before loading onto the deployment vessels. Since distances in the Mediterranean Sea are short, such integration can be done at any convenient port location. Localised impact at the telescope site will be minimal.
During construction deployment vessels will occupy the water over the telescope site. Navigation by other shipping will be controlled by issuance of Notices to Mariners and display of appropriate shapes and lights under the IMO (International Maritime Organisation), Convention on the International Regulations for Preventing Collisions at Sea, 1972 (COLREGs). This will be carried out in consultation with local fishing and shipping interests and the guidance of relevant national coastguards. Deployment of the sub sea infrastructure itself is expected to have negligible impact.
Laying of the cable from the shore to the deep sea infrastructure raises issues of way- leaves for the cable through the littoral zone and possible need for trenching or cover to protect from anchoring and fishing until an appropriate depth is reached. Well-established best practice for cable and pipeline laying in the Mediterranean area will be followed

7.2 Operations and Maintenance

During normal operations of the telescope there will be no evidence of presence of the system on the surface. The top of the optical strings or towers will be more than 1500 m below the sea surface beyond the depths of concern for navigation by surface vessels, normal fishing gears or military submarines (maximum depths are classified but are specified as no more than 250 m). However fishing vessels in the Mediterranean Sea do deploy baited long lines or gill nets which may be more than 1500 m long and although intended to be deployed near the surface may sink deeper during shooting or recovery. Limitations on fishing activity over the array may be a prudent measure.
The system will occupy a volume of sea water of several cubic km and may form an obstruction to movements of large animals. There is life at all depths in the Mediterranean Sea but particularly the Eastern basin is considered oligotrophic (low productivity) and abundance of animal life is much lower than in e.g. the North Atlantic Ocean.

The maximum depth at which large sharks have been observed in the Eastern Mediterranean Sea is 2500 m[109] with only relatively smaller fishes and shrimps occurring at greater depths. The world record for the dive depth of whale was recorded in the Mediterranean Sea as 1900 m[110]. Depending on depth of location of the telescope infrastructure it is therefore possible that interactions may occur at the top of array with large animals such as whales and sharks. The array will emit sound and light from its test beacons which will be detectable by marine fauna. The acoustic frequencies used >10kHz are inaudible to fishes but will be detectable by marine mammals at close range. Most deep-sea animals can detect light in the blue part of the spectrum around 480 nm. There is the theoretical possibility that these animals may detect and reply to beacon signals. Sharks have electromagnetic sensors and may be able to detect switching of currents in the power supplies. The main biological effect of the array is that it will provide areas of hard substrate in an otherwise fluid environment upon which some species of organisms can settle and grow[111]. Whilst this provides opportunities for such organisms, this is considered to be undesirable fouling growth for operation of any underwater equipment. Fouling begins with a film of bacteria coating the equipment followed by colonisation by various sessile animals species such as sponges, corals and barnacles depending on the availability of source larvae. Trials so far indicate rates of fouling at the great depths proposed will be low but limited use of approved antifouling materials may be necessary on key components. From time to time the sub sea infrastructure may require maintenance interventions. Ships with remotely operated vehicles will then need to occupy the site.

7.3 Decommissioning

The intention is that buildings on shore will be reallocated for other uses. For the subsea components, KM3NeT will comply with UNCLOS1 – 1982 United Nations Convention on the Law of the Sea Article 60(3) which includes the following text *"Any installations or structures which are abandoned or disused shall be removed to ensure safety of navigation, taking into account any generally accepted international standards established in this regard by the competent international organisation. Such removal shall also have due regard to fishing, the protection of the marine environment and the rights and duties of other States. Appropriate publicity shall be given to the depth, position and dimensions of any installations or structures not entirely removed"*

Generally the KM3NeT infrastructure is too deep to be of concern for navigation or fishing. Decommission of offshore structures is generally governed by the United Nations Environment Programme (UNEP) and in the Mediterranean Sea KM3NeT should comply with the relevant UNEP regional seas agreement which is the Barcelona Convention, Convention for the Protection of the Marine Environment and the Coastal Region of the Mediterranean (Revised 1995)
All the sub-sea components above the sea floor will be cut off and removed to shore for disposal in accordance with the Barcelona Convention. In view of the great depth, inert ballast blocks and cables will be left in place; it is considered that the disturbance created by attempting to remove material which by this time will be encrusted with growth, covered in sediment and settled into the sea floor would be detrimental to the environment. Any cable exposed at less than 1500m depth will be cut off and removed to restore the sea floor to original condition for access by fishermen.
Cost of decommissioning will be included in the business plan for the infrastructure.

7.4 Legacy Post-Decommissioning

Following decommissioning there will be very little evidence of that the infrastructure was ever there. The precise locations of material, on the sea floor (bases of strings) will be lodged with international marine data centres and may form the basis for future investigations of marine processes on materials deployed at a known time in the past for comparison with the emerging field of deep sea archaeology in the Mediterranean Sea.

8. Quality Assurance and Reliability

The KM3NeT infrastructure must operate for at least 10 years, without significant degradation, at a depth of up to 5000 metres (50 MPa pressure) in the chemically-aggressive deep-sea environment. This imposes strict quality standards on each subsystem within the detector. To meet these standards a quality assurance system will be implemented covering each step of the detector production, transportation, deployment and operations.

During construction and operation, there is a need for:

1. Well defined actions for coordination, planning and control.

2. Identification of weak points in the design and operation of the detector and the subsequent corrective and mitigating actions through design improvements and operational procedures.

The quality assurance system requires the implementation of a management structure, the identification of responsibilities and resources, and the definition of procedures and activities.

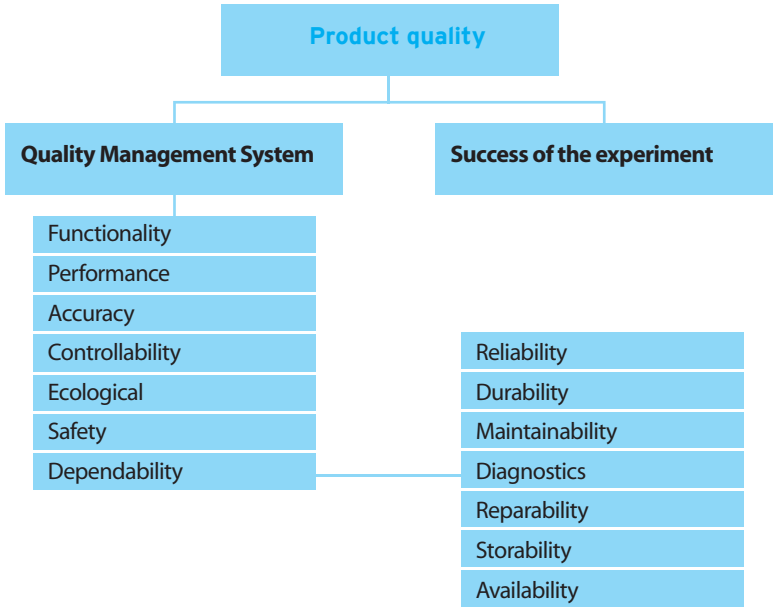

Figure 8-1: Schematic structure of product quality. [112]

A schematic structure of a generic product quality system is shown in Figure 8-1. It shows the link between quality and reliability of a product.

In the following the quality management system will be described based on an adopted methodology and risk and dependability analyses.

8.1 Methodology

Several different quality standards have been analysed. The choice has fallen on the ISO 9000 family of standards. It is widely adopted in industry and allows the freedom to customize the standard to the specific KM3NeT requirements.

The Quality Management System (QMS) must address the requirements of quality assurance (QA) and risk assessment (RA). It includes the quality control process through the Deming cycle, a design optimisation process, and allows for the risk analysis to proceed in parallel and interact with the design.

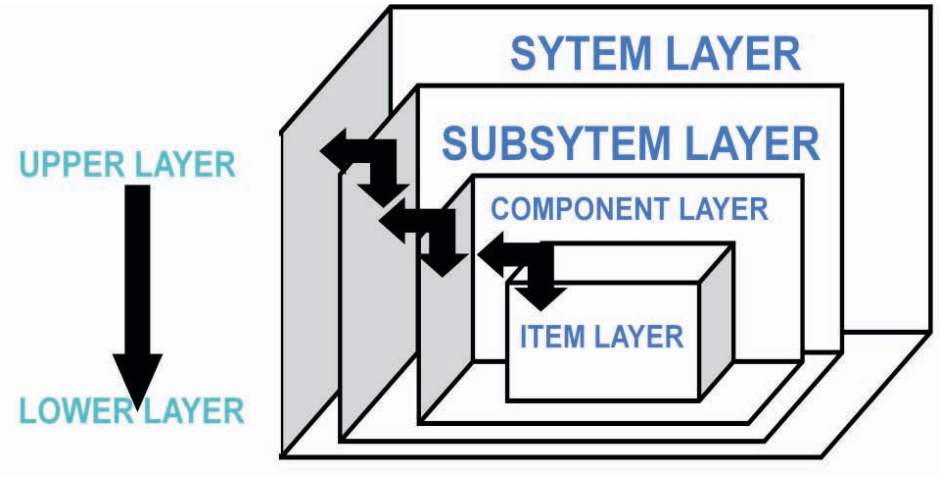

Figure 8-2: KM3NeT schematic logic scheme.

Following the ISO 9001 standard KM3NeT is described in terms of processes. The detector is represented by a logic scheme presented in Figure 8-2. Such a scheme enables the unique identification and traceability of components and describes their dependability. Within the framework of KM3NeT, the quality assurance and risk analysis are coupled to form an integrated system as shown in Figure 8-3.

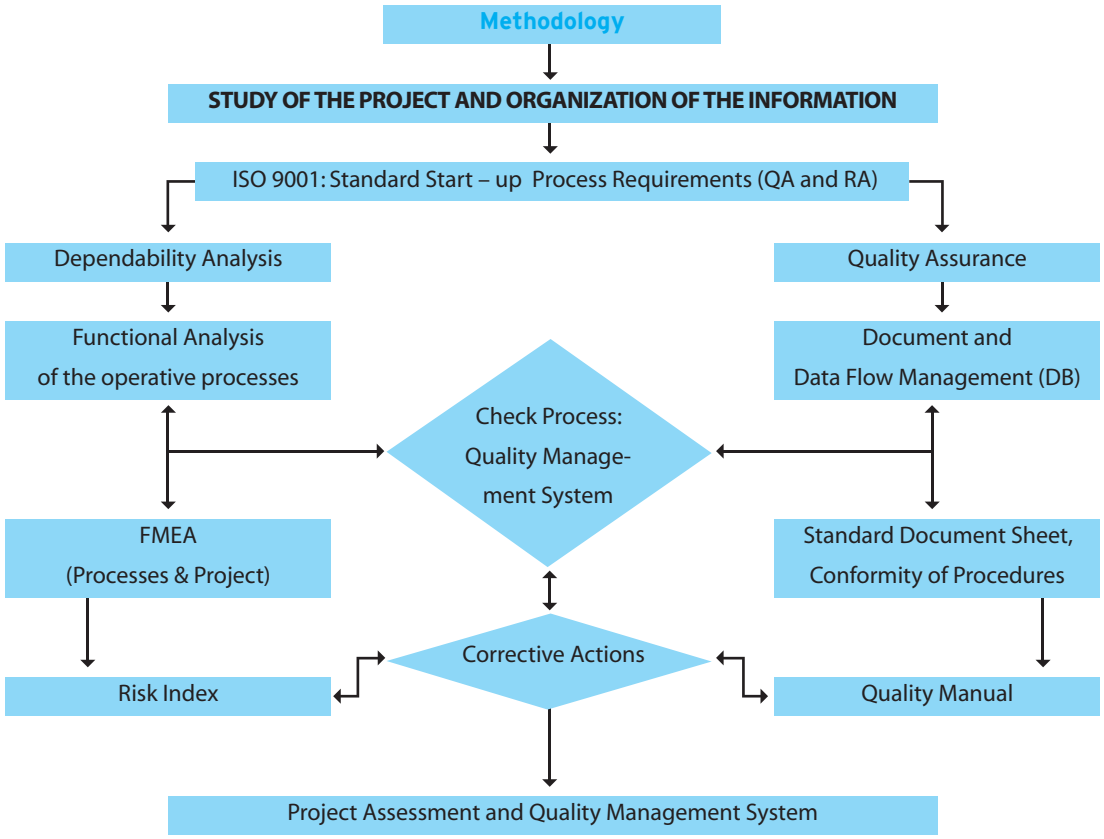

Figure 8-3: Schematic structure of the Deming cycle methodology Plan, Do, Check, Act.

In particular it has been translated into:

- An in depth study of the project, based on information from the pilot projects and the general requirements formulated in the KM3NeT design study.
- An organization of the collected information
- The analysis of QA and RA standards;
- The development of the QA and RA systems in parallel
- The monitoring of design activities;
- Identification of weak points and subsequent corrective actions.

The implementation has used questionnaires and audits for information gathering. The system functionality has been described in flow and block diagrams and a product breakdown structure has been defined.

8.2 Quality Management System

The QMS must take into account the complexity of KM3NeT not only in terms of number of components and systems but also in terms of the international nature of the consortium.

The QMS is modular and hierarchical as indicated in Figure 8-4. The quality assurance rules are passed down the structure and at each stage further restrictions and rules can easily be added. As far as possible the general structure of QMS should be respected.

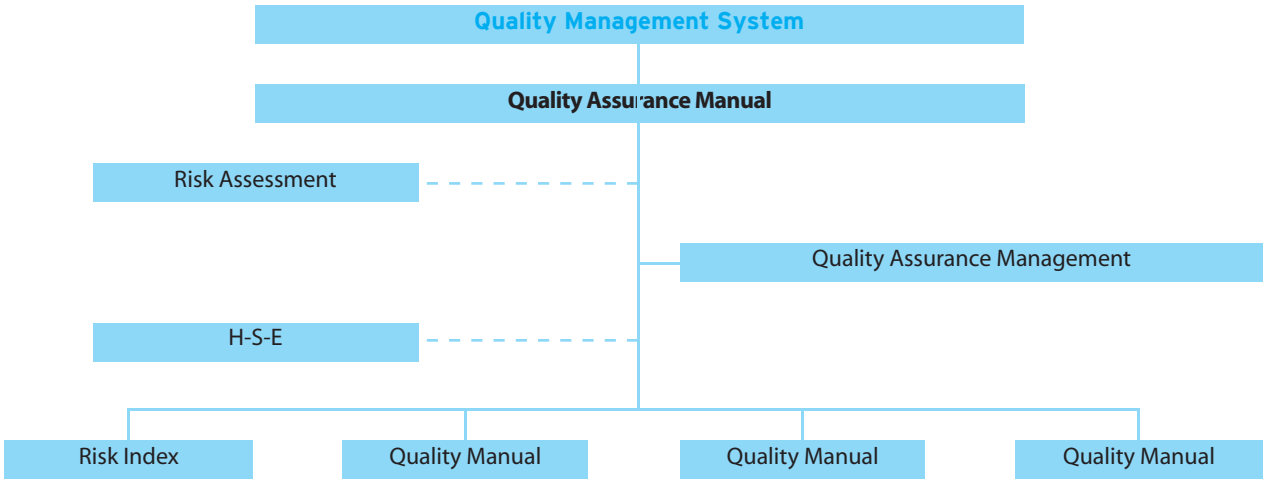

Figure 8-4: KM3NeT quality management system.

8.2.1 Quality Assurance Manual

The quality assurance manual describes the general structure of the QMS. It details the objectives of the project and the structure of the project management. It defines the quality policy and the quality documentation including reference documents, quality management documentation (QMD), procedures, quality plans and the quality management database.

The quality assurance is closely interwoven with risk assessment, both in terms of risk management and dependability analysis, and health, safety and environmental issues.

The risk assessment provides input to the design review process and the quality control actions to be taken to avoid and mitigate weak points. The analysis of health, safety and environmental issues provides input into the QMS procedures ensuring they comply with European and national laws. In each phase of the project, the quality assurance manual needs to be reviewed and updated where necessary.

Quality Assurance Management

The structure of the management is given in Figure 8-5. The overall management of the quality assurance is contained in the quality executive. It comprises a number of managers that are responsible for different aspects of quality control. The executive is in charge of:

- The management of the QMS;
- The definition of procedures and quality control actions in close cooperation with the experiment executive and technical experts;
- The internal and external quality auditing;
- The organisation of periodic quality assurance training courses.

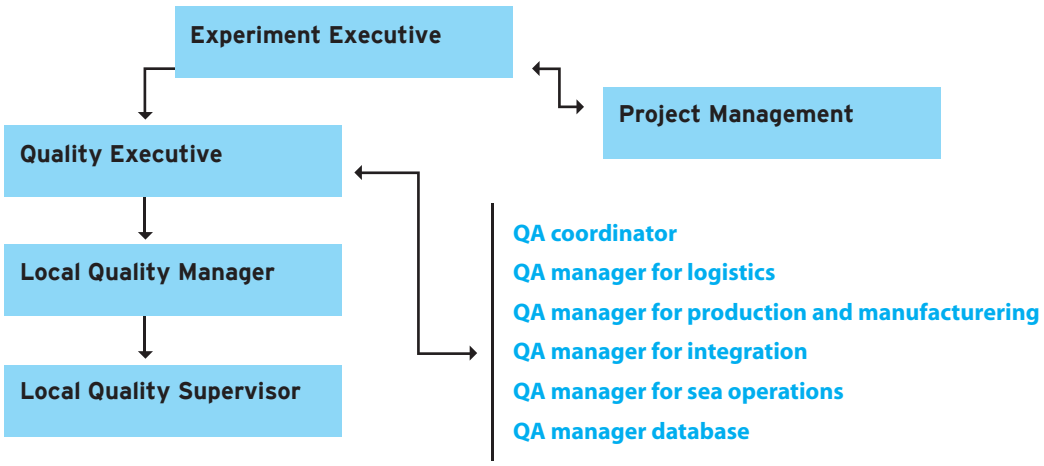

Figure 8-5: KM3NeT quality management.

The managers that comprise the executive are the following:

- The coordinator: the representative of the quality office in the steering committee;
- The logistics manager: oversees the packaging, storage and transportations;
- The production manager: oversees the communication of quality requirement to suppliers and defines and monitors acceptance tests;
- The integration manager: oversees the quality aspects of design integration and operation;
- The sea operations manager: oversees quality and health and safety during all sea operation activities;
- The quality assurance database manager: manages the QMS database.

The managers of the executive will define the quality assurance procedures in their individual areas of responsibility. Figure 8-6 shows some of these areas that will require procedure definition. This process is dynamic and the procedures will require continuous review and update.

Specific items such as optical modules, storeys, detection units and deployment operations will require customized quality plans. These are similar to those developed for and applied in the ANTARES and NEMO pilot projects. These will require the coordination of several quality managers.
At the local level the executive is represented by a local quality manager, responsible for all aspects of the QMS within his institute on a day to day basis, and a local quality supervisor, responsible for the quality control and application of the QMS in a specific area.

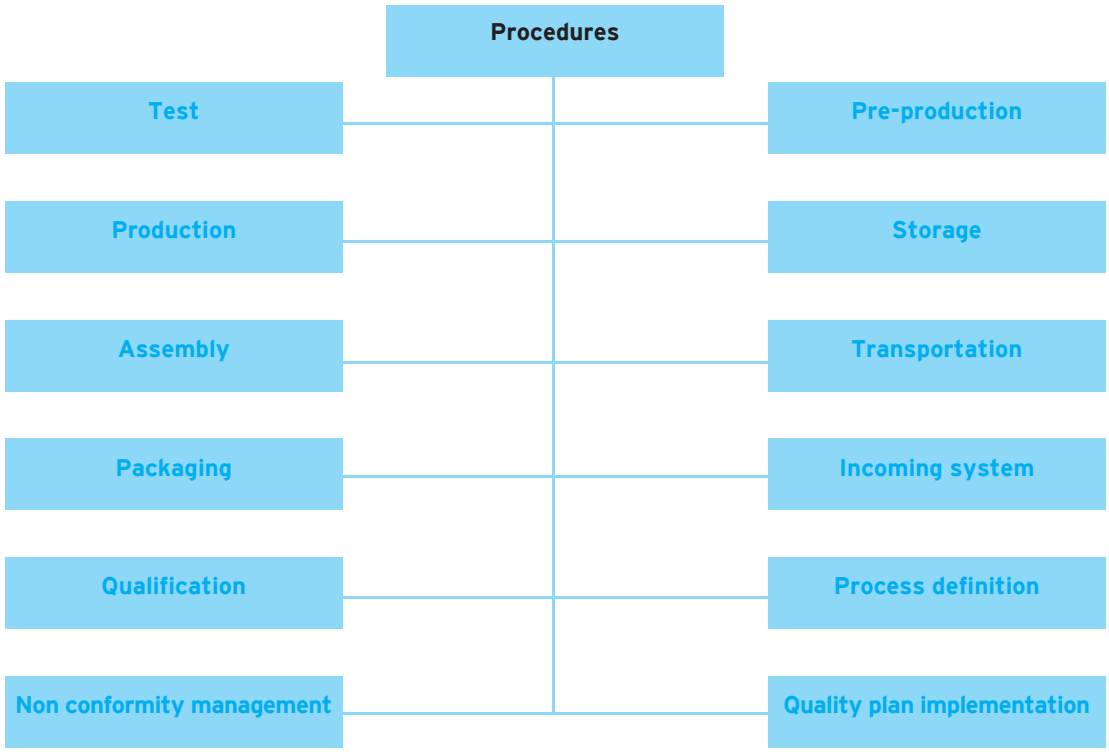

Figure 8-6: KM3NeT procedures.

Quality management documentation

Rules have been defined for the identification of documentation and components within the system.
For the documentation these include an identification number, categorization, validation by the appropriate quality assurance manager and an up to date history of the document.
For the components it comprises a product breakdown structure along the lines of the scheme presented in Figure 8-3.
Finally a naming convention has been developed.

Database

The documentation database design relies on the experience gained with such databases in the pilot projects. The requirements for the KM3NeT database have been defined and a prototype was developed. It includes on-line access to test records and the definition of the product breakdown structure.

It maintains document, component and system traceability during the qualification, construction and operation phases of KM3NeT.
It is modular and based on the product break down structure, as shown in Figure 8-7 and will contain the entire technical documentation.
The history and traceability of all the components and systems are contained in the storage module. Information on integration and deployment is stored in the respective modules and the current status of all deployed component is contained in the layout module. All modules are interlinked and are accessible through user interfaces.
The layout module is the interface in the control room. It provides all the technical information on the components deployed and running on the sea bed.

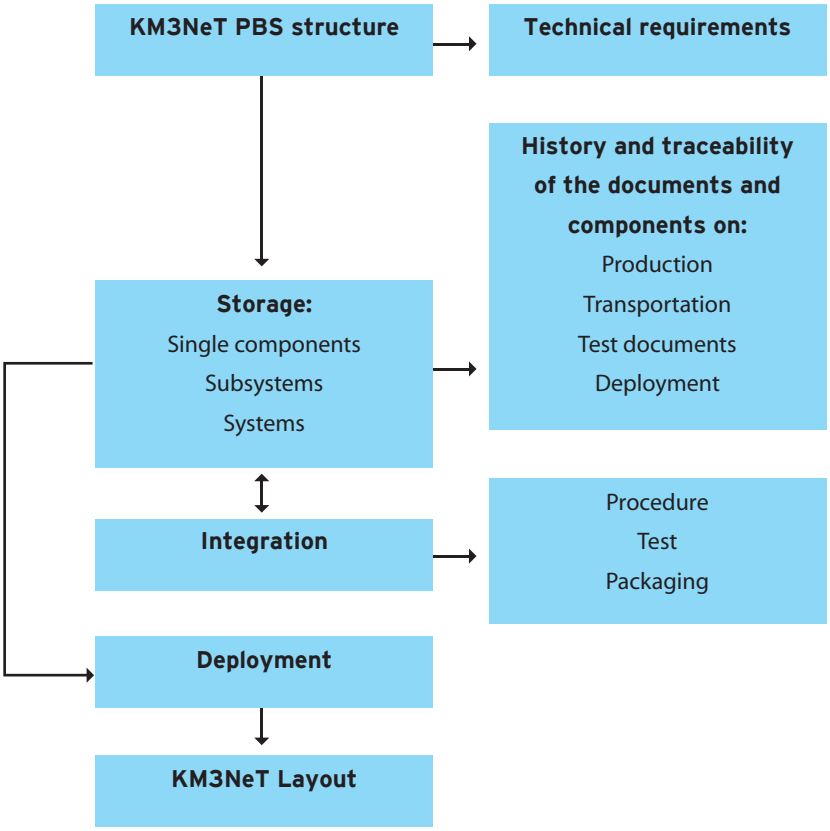

Figure 8-7: KM3NeT database structure.

8.3 Risk Assessment

In complex, expensive, unique or one-of-a-kind systems, like the neutrino telescope, assessment of the mechanisms of potential failures through analysis is a necessary ingredient of risk analysis because a statistical basis for the overall system performance is not available. Risk must therefore be synthesized from information about the performance of simpler subsystems or components of the system. This information comes either from past operational experience in other systems or through experimentation. The objectives of a risk analysis for KM3NeT are therefore

1. To define the mission of the neutrino telescope in quantifiable terms

2. Assess specific scenarios (sequences of events) that can lead to the inability of the system to perform its mission

3. Assess the probability of each and every scenario

In this sense a risk analysis results in a set of triplets $\{s_i,pi,ci\}$ providing specific scenarios (si) with their associated probability of occurrence (p_i) and consequence (c_i). Risk representation with the set of triplets provides more information and enables risk management decision making since it differentiates among different types of failures in terms of their severity and their relative probability. In reliability analyses it is customary to define only one type of consequence (e.g. mission failure) and then calculate only the probability of occurrence of the various paths that lead to it. This implies that all types of mission failure are equally important, which may not always be the case.

The risk analysis, described in the CDR [1], essentially entails the determination of the values for (s_i), (c_i) and (p_i). The first two can be obtained by a qualitative analysis of the full detector system, whereas the third is obtained from a quantitative analysis based on existing reliability figures obtained from pilot projects, results from accelerated testing of components or manufacturers data.

8.4 Dependability analysis

The dependability analysis is used in KM3NeT mainly as a "technological system". It assumes that the detector has been constructed and is operating. The analysis developed allows correlations between the reliability characteristics of the components and those of the total system to be made.

A first order approximation to the dependability analysis of the design of the neutrino telescope has been conducted. System availability criteria are generated from the existing functional and performance requirements, defined in the CDR. In terms of risk analysis a system, or component, is deemed available when it operates in excess of a predefined operational threshold.

For a complex system, availability of the system depends on the availability of the components. The first problem to be addressed in dependability analyses is the calculation of system availability as a function of component availabilities. The system performance can then be viewed from two different perspectives.

- Given the availabilities of all the components of the system, determine the availability of the system as a whole.
- Given a performance criterion or required function, expressed as a system availability level, determine the component availabilities that will satisfy this criterion.

Fundamental to the dependability analysis of any system, is the definition of its required function. The primary function of the neutrino telescope is to allow for the recording and analysis of tracks produced in the interaction of neutrino. The essential component in determining the telescope availability is the optical module. The optical module availability includes not only the optical module operability but also its ability to transport data back to shore. It is then reasonable to define the required function of the telescope to be a minimum number of available optical modules in the telescope. An additional requirement is that the telescope is available for a percentage of its useful life (10 years).

The large volume neutrino telescope consists of various components and subsystems that can be divided into three major subsystems:

- The detector network, from optical module to primary junction box;
- The deep-sea infrastructure, primary junction box to shore;
- The on-shore infrastructure.

All three subsystems must operate for the telescope to be available. Hence they are logically connected in series. The on-shore infrastructure subsystem was not included in this phase of the dependability analysis, since repairs of this system can be performed instantaneously.

The overall unavailability of the neutrino telescope is then a function of the unavailability of the detector network and the unavailability of the deep-sea infrastructure. The latter is easily evaluated as the combined unavailability of the primary junction box(es) and the main electro-optical cable(s) to shore.

The model developed for the calculation of the detector network unavailability was based on the method of successive decomposition. The detector network comprises the optical modules on the detection units, and the junction boxes for each detection unit, branch and sector. If a sector junction box or the associated cabling to the main junction box fails then all optical modules mounted in the detection units of the branches in this sector become unavailable. Similarly if the junction box of a branch or the cabling connecting it to the sector junction box fails then the optical modules of the detection units in this branch become unavailable. Finally if the junction box of a detection unit or the cabling connecting the detection unit to the branch junction box fails or the detection unit itself fails structurally then the optical modules of this detection unit become unavailable. Figure 8-8 gives the block diagrams at each decomposition level, illustrating the development of the unavailability model. It is a generic many level representation and allows for intermediate levels to be absent, if required by the design. On the basis of these observations and a detector function based on the minimum number of available optical modules, the detector network unavailability is calculated. Detailed information on the development of the unavailability model can be found in [113].

The developed unavailability model provides the combined unavailability of the detection network and the deep sea infrastructure based on component unavailability. As a first approximation the steady state dependability of the system was calculated. This means that the availability of each of its components is set equal to the mean availability over the life time of the system. The steady-state unavailability for all components was calculated. The assumptions made at this stage include:

a) parts of the detector are designed in such a way that they are retrievable, serviceable and replaceable;
b) failure of a component is immediately detectable;
c) repair starts immediately or only at predetermined intervals;

The different components were classified into two classes:

a) those that are retrievable and repairable
b) those that are not repairable

The risk analysis considered the two distinct approaches followed by the project. One being a design with extended storeys incorporating six optical modules with large PMTs (simulating the bar and triangle design) and the other being the string design with multi-PMT optical modules.

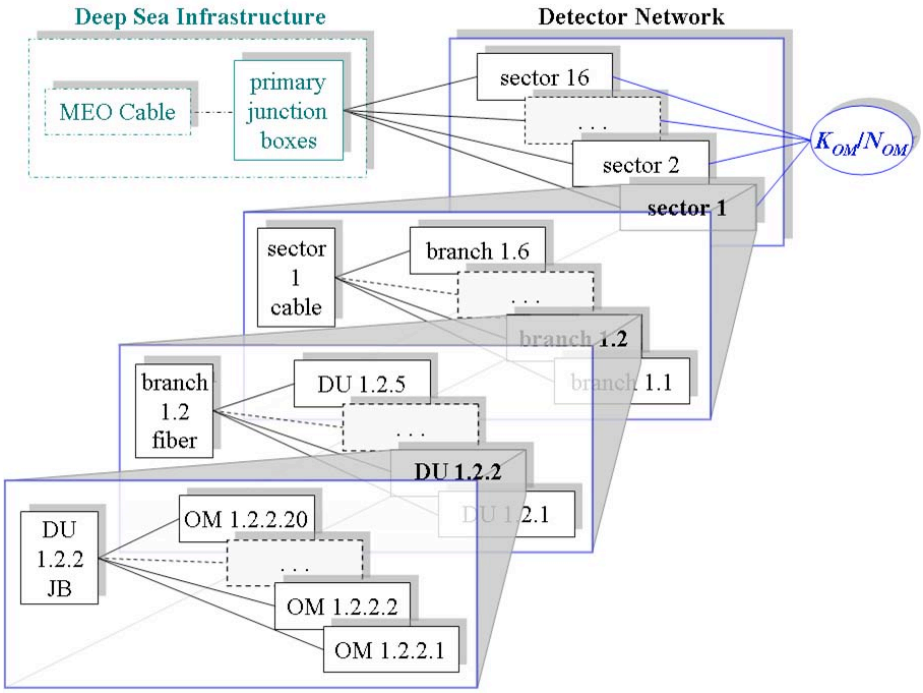

Figure 8-8: Generic detector network and deep sea infrastructure block diagrams.

For both case studies the cables connecting the detection units to the secondary junction boxes, those connecting secondary boxes to primary junction box and the cable running from primary junction box to shore are instantly repairable and the repair period is one month. The primary junction box is repairable. For the secondary junction boxes both instant reparability and non-reparability are investigated.

- For the extended storey design, the optical modules, the storeys and the detection units are either non-repairable or repairable with a repair period of one month and a maximum number of repairs per year of 12. The detector has a hexagonal layout and the design has 15240 optical modules and 2540 electronic modules.
- For the string design the optical modules and the detection units are non-repairable. The detector has a hexagonal layout and the design has 6200 optical modules.

A number of sensitivity analyses were performed on the two alternatives. A variety of detector network layouts were considered to investigate the tradeoffs in the total number of optical modules and their arrangement. The detailed results of the dependability analysis are reported elsewhere [113]. The results enable estimation of the trade-offs between the component mean time to failure (MTTF), the component reparability and the required availability over a 10 year period. The system availability criterion was set to 90% of optical modules available over a 10 year period. It should be noted that the actual effort of achieving a particular MTTF or performing the repair of a component within the same or different designs might vary significantly.

These practical issues are not addressed in the present work due to lack of data. Therefore the results can not be, as yet, used to compare the two alternative designs. This analysis, however, does allow for optimisation of the configuration of each of the two approaches considered..

8.4.1 Results of the dependability analysis

Since designs are under qualification and optimization process the results and the configurations of the case studies will be according modified. As present status the following reports the results related to the analysis applied to the extended storey design in the configuration as described in chapter 3. It provides the magnitude of the MTTF foreseen for the detector and its components.

Two different approaches to achieve the defined unavailability of the system are presented:

- The MTTF value can be reduced applying maintenance strategy,
- If this MTTF is not technically achievable or too expensive the required extra unavailability can be provided by extra redundancy in the number of detection units and hence the OMs.

Results of the dependability analysis: maintenance and reparability of components

The following describe the trade-offs between the various repair schemes, the unavailability targets and the component MTTF. For instance, consider that all the components of the Deep Sea Infrastructure (DSI) have a MTTF equal to 10 years and are immediately repairable with mean time to repair (MTTR) equal to one month. The MTTF, (assumed equal for all components) required to achieve a given system availability is calculated. Table 8-1 gives the results of the dependability analysis for the following cases, where c represents the system operability criterion and U_{max} the maximum telescope unavailability.

In the first case,the PJB-SJB cables, the SJBs, the detection units, the storeys and the optical modules are non-repairable:.

For c=10%, as the unavailability target increases from 5% to 20%, the required MTTFs for the non-repairable components decrease by 40%. For c=20% the observed decrease is at 35%. As c increases from 10% to 20%, the average reduction in MTTF

Case 1: C=10%, DSI: MTTF=10yrs, MTTR=1month

		SJB		DU		cable, STO, OM
U_{Max}	%	MTTF [yrs]	MTTF [yrs]	MDT [month]	MTTF [yrs]	MDT [month]
Case 1	5%	600	Non-rep	600	Non-rep	600
	10%	450	Non-rep	450	Non-rep	450
	20%	360	Non-rep	360	Non-rep	360
Case 2	5%	11	1,2	630	Non-rep	630
	10%	11	1,2	430	Non-rep	430
	20%	11	1,2	330	Non-rep	330
Case 3	5%	11	1,2	21	2,2	630
	10%	11	1,2	21	2,2	370
	20%	11	1,2	21	2,2	280

Case 2: C=20%, DSI: MTTF=10yrs, MTTR=1month

		SJB		DU		cable, STO, OM
U_{Max}	%	MTTF [yrs]	MDT [month]	MTTF [yrs]	MDT [month]	MTTF [yrs]
Case 1	5%	235	Non-rep	235	Non-rep	235
	10%	182	Non-rep	182	Non-rep	182
	20%	152	Non-rep	152	Non-rep	152
Case 2	5%	11	1,2	185	Non-rep	185
	10%	11	1,2	153	Non-rep	153
	20%	11	1,2	123	Non-rep	123
Case 3	5%	11	1,2	21	2,2	147
	10%	11	1,2	21	2,2	119
	20%	11	1,2	21	2,2	104

Table 8.1: Dependability analysis results for extend storey design.

In the second case, the PJB-SJB cables, the detection units, the storeys and the optical modules are non-repairable. The SJBs are repaired one at a time with MTTR one month. In this case, the mean downtime (MDT) of a SJB is higher than the specified MTTR, so a conservative estimate of the MDT may be derived using queuing theory. Taking the unavailability of the SBJs to be equal to that of the other repairable components, the estimated SJB MTTF is around 11 years with MDT 1.2 months. The observed trend in the required MTTS for non-repairable components is similar to case 1. The MTTF values are lower than those of case 1, unless they exceed the 600yrs, because then the unavailability of non-repairable components becomes higher that the unavailability of repairable components assumed here.

In the third case, the PJB-SJB cables, the storeys and the optical modules are non-repairable. The SJBs and the detection units are repaired one at a time with MTTR one month: The MTTFs and MDTs for the SJBs are the same as in case 2. Taking the unavailability of the detection units to be equal to that of the other repairable components, the MTTFs and MDTs are 21 years and 2.2 months. The observed trend in the required MTTS for non-repairable components is similar to the previous cases. Since the MDT and the frequency of failure decreases the unavailability drops down, so lower MTTFs of the non-repairable components can be used. This benefit becomes more evident at low c and U_{max} values.

For larger unavailability of the DSI, the reliability requirements for the Detector Network components become more severe. For example, if the main electro-optical cable MTTF decreases to 2 years, the required MTTFs of the non-repairable components case 3, with c=20% and Umax=5%, increase to 490 years.

Results of the dependability analysis: redundancy of detector components

Assuming all detector network components have the same MTTF, the required MTTF to meet the system availability criterion is 375 years. If this MTTF is not technically achievable or too expensive the required extra unavailability can be provided by extra redundancy in the number of detection units and hence the OMs. If the achievable MTTF of the components is equal to 150 years then an additional 12% of OMs (1828) are required. If the technically achievable MTTF is 75 years then an additional 30% of OMs (4572) are required.

8.5 Failure mode and effect analyses

Once a component reliability requirement has been assessed (either as a design target or as a requirement stemming from the system reliability) it is necessary to determine whether the existing or the proposed design for this component can meet this requirement. A component reliability requirement is usually expressed in terms of its MTTF MTTFs (or other reliability measures, e.g. *Failure In Time* (FIT) rate) can be determined from manufacturer specifications or from in-house testing. The failure rates of complex systems are functions of the failure rates of the individual components that constitute the system. To determine this function a Failure Mode Effect and Criticality Analysis (FMECA) is performed [114,115]. An FMECA is a procedure for identifying potential failure modes in a system and classifying them according to their determined severity values.

A FMECA is usually carried out progressively in two parts:

- The first part identifies failure modes and their effects (Failure Mode and Effect Analyses [FMEA]).
- The second part ranks failure modes according to the combination of severity and the probability of that failure mode occurring (Criticality Analysis).

The FMEA (FMECA) procedure may be summarised as completing the following steps:

1. Define the system to be analysed;
2. Construct a hierarchical block diagram (e.g. RBD-reliability block diagram);
3. Identify failure modes at all levels;
4. Assign effects to the failure modes;
5. Assign severity categories to effects;
6. Enter other failure mode data;
7. Rank failure modes in terms of severity (and criticality);
8. Produce reports highlighting critical failures;
9. Feed results back to designers or maintenance planners;
10. Estimate the final system failure rate;

If failure modes are assumed catastrophic, i.e. where subsystem failure leads to system failure, steps 4 to 8 become redundant. In this case the analysis can be considered conservative. All the information is collected into a table similar to those used in defence applications (MIL-STD-1629A) or in the space industry (ECSS-Q-30-02A). The result of the FMECA becomes the input to the dependability analysis. To achieve a reliable dependability analysis for the neutrino telescope full FMECA analyses of the subsystems must be performed. These subsystems are optical module, electronic module, master module, backbone cable, interlink cable, secondary junction box, branch cable, primary junction box, main cable and shore electronics and power delivery. These subsystems are described in the product breakdown structures in chapter 3. The failure modes must include the power delivery, the slow control and the data acquisition. This will yield an availability estimate for the full telescope.
A fault tree analysis can then be used to optimize the availability of the full system. For instance, such an analysis on the storey architecture in the NEMO1 pilot project yielded the result that reliability is enhanced by limiting the number of components connected in series, reducing the number of external connectors and providing redundancy of protective systems.
The basic structure for these analyses is in place. The full analysis will, however, only be possible when final figures for failure rates are known. Many of these await prototype tests that will allow for more solid design specifications. The risk analysis will then aid the optimisation of the design and also provide input to the detector maintenance strategy. The design optimisation and maintenance strategy must necessarily also include results from physics performance studies and is also impacted by financial considerations. The final requirement specification for components will be a trade-off between performance, cost and reliability. The quality management system is in place to ensure the compliance of all components with the design specifications deduced from the above analyses.

8.6 Quality Control

The results from the quality assurance and from the dependability analysis show the need for qualification and optimization processes: reliability demonstration programs should be defined once reliability has been allocated to various components (e.g. using accelerating testing) in order to examine (and guarantee) the performance of the required function by the overall system. Such activity is reported in Figure 8-9. The reliability program is developed through a qualification process that implies a design review, a FMEA and dependability analysis, the design of proper tests to check the functions and requirements of components / systems are satisfied, the execution of the tests and the check of the results obtained that includes the FMEA and the dependability analysis. Once such process is concluded for all the components and systems of KM3NeT the quality control can be defined for all the processes of the project (i.e. suppliers' qualification, in factory test, acceptance test, transportation and packaging test, integration test, delivering test, pre-installation test, etc.). The FMEA and FTA will support the definition of the quality control.

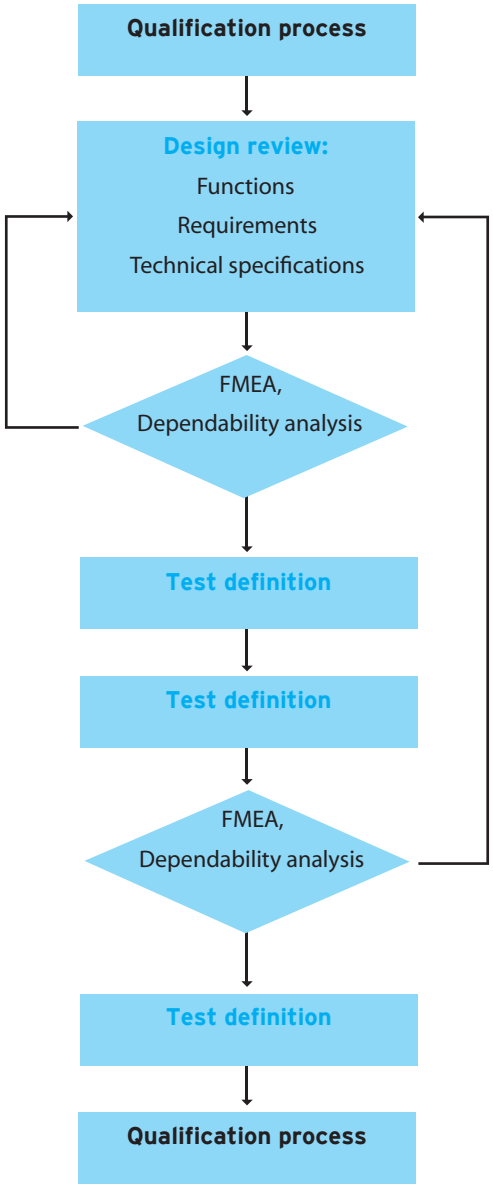

Figure 8-9: KM3NeT quality control process.

8.6.1 General rules for the quality control definition

A high level of reliability is required during the assembly processes, which can only be achieved by enforcing a rigorous quality control process at every stage of production.

For each type of item according to the ISO 9000 family, the QC activity will be adapted with respect to its specified level of dependability, its level of integration and its associated level of failure risk to the whole project. The QC would be done on a part or on entire item.

General rules

The general points for QC in assembly, transportation and test are the following one:

- **Resources**. To carry out this activity, at least, a dedicated and qualified quality supervisor will be identified for each production/assembly site. Operations shall be performed by trained and qualified personnel.
- **Documentation.** Dedicated documentation will be written, completed, recorded and archived following the Documentation Management Procedure.
- **Traceability.** Each product will be identified and stamped with a unique serial number, using an appropriate method such as bar codes. Using this serial number, each item will be traceable with respect to configuration, assembly and location details. These traceability records will be maintained and accessed via the QA database.
- **Non conformity.** The knowledge and traceability of defects is made through a Non Conformance Report (NCR). The NCR is initiated by people in assembly groups and then treated by the Local Quality Supervisor who releases it and follows the progress of the NCR.
- **Reviews.** Before each relevant phase, stage or operation, a review will take place to highlight all known risks.

Dedicated rules

The specific points in QA/QC for each type of activity are detailed below.

Assembly

The assembly process will be validated before starting production by a Production Readiness Review (PRR) and reviews with manufacturers. During production audits will be performed.

For each assembly activity (OM, container, DU…), a dedicated quality plan will be written. This document describes the process, the organization and the quality control to be applied.

As several sites will handle the same activities, a unique set of documentation for assembly and testing (procedures, test sheets…) will be defined and applied at all sites.

Each item or subsystem, delivered to an assembly site, will be accompanied by a conformity certificate of ensuring the item conforms to the defined specifications.

Logistics

The integrity of each item will be maintained and its location will be recorded during all logistical operations.

At each step, items will be accompanied by their "traveller" file (including its certificate of conformance and logbook).

Dedicated handling, storage, packaging and means of transport will be defined for each item, regarding its features/characteristics; operational conformity will be proved before transportation and checked after. Dedicated procedures will be written.

Test

For each test, a dedicated procedure will be written, identifying configuration, equipment, and protocols required. The results of each test will be recorded in the database. All equipment used during the testing procedure will itself have a file containing its maintenance and calibration schedules.

9. Cost and Feasibility of Construction

In this chapter, estimates of the capital investment required for the construction of the KM3NeT research infrastructure and of the running costs during its operation phase are described. In addition, a construction model is presented demonstrating that an installation time of below four years per building block is achievable with a reasonable deployment of human resources and assembly lines.

9.1 Capital Investment

The detection unit cost has been estimated using the following assumptions and procedures:

- With the exceptions quoted below, the costs of components were taken, in descending priority, from industrial quotations, corresponding costs as occurred in the pilot projects, public catalogues, and informal or confidential statements of providers.
- The costs of the photomultipliers are estimated according to informal and confidential statements of the corresponding companies.
- For the optical modules, the single-PMT option has been assumed for the flexible towers and the triangles, and the multi-PMT option for the slender strings.
- The costs for the junction boxes are based on the experience of the pilot projects.
- The on-shore installation is not included (except readout components).
- Contingency, cost for spares and inflation are not included. However, some of the prices include VAT of which an exemption can be expected in the governance framework of a European Research Infrastructure Consortium (ERIC).
- No costs of human resources for assembly are included; however, the sea operations needed for deployment are estimated based on the pilot project experience and include costs of crews, mobilisation and demobilisation of vessels.
- The design as described in this document has been assumed, i.e. no extra costs related to using fallback solutions have been included.
- A distance to shore of 100 km and a deep-sea network according to the "star option" of Section 3.4 has been assumed.

Based on the uncertainty of component prices, mostly caused by the fact that no binding quotations can be obtained at the current stage, the overall error margin on the total cost is estimated to be at least 20%.

The site dependence of the cost estimates is mostly related to the distance to shore (cable length and deployment) and to the water depth (even though the design is generally valid for all candidate sites, there are components and tools that need to be adapted to depths exceeding 4000m, such as connectors and ROVs). It is not expected that these issues will induce variations of more than 10% on the overall cost. The costs for the different design options are summarised in Table 9.1.

The goal of KM3NeT is to be the most sensitive neutrino telescope. Therefore it should surpass the performance of IceCube even at the declination where IceCube reaches its maximum sensitivity. Taking into account the above cost estimates, a detector with a total cost of about 220 M- is required to achieve this goal. In Figure 9-1 the sensitivities are shown that can be obtained for such a cost with the different design options. It clearly indicates that a decision between the design options on the basis of a figure of merit "sensitivity per Euro" is inappropriate and that instead further technical tests and risk analyses have to be considered.

Concept	Cost per Detection Unit (k€)				No. of Detection Units in Simulation	No. of detection units for 220 M€ giving sensitivity of Figure 9-1
	Structure	Seafloor Infrastructure	Deployment	Total		
Flexible towers	535	70	87	692	127	320
Slender strings	254	42	40	336	310	650
Triangles	657	70	55	782	127	280

Table 9.1: Costs for constructing and deploying a detection unit for the different design concepts. For comparison the construction cost for the ANTARES experiment was roughly 20 M€ for 12 detection units. The number of detection units, used in the simulations of Chapter 6, is indicated. The sensitivity indicated in Figure 9-1 can be achieved for a cost of about 220 M€ and requires the number of detection units given in the last column.

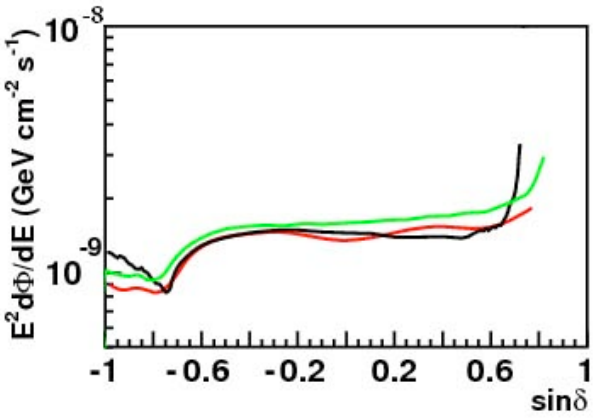

Figure 9-1 Sensitivity to point sources (E-2 flux) for one year of observation time, for a full detector of three configurations studied. See Section 6.3

9.2 Running costs

The running costs can be separated into three categories:

1. Maintenance of the detector

2. Power consumption of detector, shore station and data centre

3. Salary costs for shore station and data centre personnel

Category 2 and, for a given management structure (see below), category 3 are relatively straightforward to estimate but depend of course on the evolution of energy costs and salaries over the running period of the infrastructure. Category 1 depends on the maintenance plan of the detectors and therefore estimates require knowledge of the risks of failures inherent in the design and on the adherence to the quality assumed in the risk analysis. This implies that the error margins are larger in category 1 than they are in categories 2 and 3.

No running costs beyond the maintenance of the interface are currently taken into account for the earth and sea science installations.

9.3 Maintenance

The maintenance plan for the detection units will depend on their risk of failure. If the estimated failure rate of the detection units is at the level of 1% per year no maintenance will be necessary as the final 10-year failure rate is within requirements. A slightly increased detection unit failure rate of 2% per year, implying a 20% drop-out rate over 10 years, would require the manufacture of 10% spare detection units which can be immediately deployed. This is equivalent to a detector investment increase (or, at fixed budget, an average detector size decrease) of 10%. These options impact on the initial investment but do not contribute to long-term running costs. However, if the detection unit failure rate would be 10% or more per year, the full detector would have to be replaced in the running time of the experiment. This would clearly be unacceptable and would require a redesign. Therefore, a maximum detection unit failure rate of 5% is considered, and the maintenance costs estimated accordingly.

For the flexible tower structures, this would imply a repair rate of about 12 detection units per year, assumed to be performed in groups of 4. These costs are summarized in Table 9.2.

If a main electro-optical cable to shore fails, a separate operation for repair is necessary via MECMA. The experience with the repair of cables in pilot projects gives an estimate of 200 k€ for such an operation. Experience shows that there should be less than one repair every two years, providing a yearly maintenance cost of 100 k€. For junction box repairs that require ROV operations for connection and disconnection at most 500 k€ per year is assumed.

Action	**Cost in k€**
ROV operation for disconnection of 4 detection unit, together with reconnection of previous set of 4 detection units	150
Recovery sea operation	60
Redeployment	60
Replacement cost for failed equipment ~20% of unit cost	280
Total cost of repair of 4 detection units	550
Maximum total cost for repair per year (12 detection units)	1650

Table 9.2: Repair costs for one year assuming the repair of one detection unit per month.

Power consumption

The overall power consumption of the deep-sea detector will be 150 kW; for on-shore computers including cooling 350 kW are needed (assuming 1000 computers for shore station and data centre). This consumption adds up to 500 kW or about 4.5 GWh per year.
At the present price of 0.15€/kWh this gives a yearly power cost of 675 k€.

Human resources for shore station and data centre

Experience shows that a crew of 3 persons is adequate for local presence at a shore station. This crew will be required for computer, network and power maintenance. A presence at the shore station is also useful in terms of security. Including any overhead this corresponds to 100 k- per person per year. For the running of the data centre around the clock, 3 persons for 3 shifts, i.e. a crew of 9 persons is required, corresponding to 9 times 150 k- = 1650 k- per year including overhead.

Project management

A professional project management, comprising a chief manager and a project office with 4 further employees (see Chapter 10) will require 200 k€ plus 4 times 120 k€ = 680 k€ of salaries per year, including overheads. Maintenance of the project office, consumables and related travel are estimated to cost 50 k€ per year.

Travel and subsistence of the members of the governing bodies in the ERIC (see Chapter 10) are assumed to cost 100 k€ per year.

Miscellaneous

- MECMA membership: 75 k€.
- Replacement of the 1000 computers after 5 years: 2000 k€/5 = 400 k€/year.
- Outreach activities: 100 k€ per year.

Total

The yearly total (see Table 9.3) thus varies between 2% and 2.5% of the investment cost. Normally the running costs of an experiment of this complexity and magnitude lies between 5 and 15% of the investment cost. The preliminary estimate indicates that KM3NeT will certainly remain at or below the bottom end of this range.

Cost item	Cost in k€ with ≤ 2% detection unit failure rate	Cost in k€ with 5% detection unit failure rate
Cable repair	100	
Junction box repair	500	
Power	675	
Human resources for shore station and data centre	1650	
Project management	830	
Miscellaneous	575	
Detection unit maintenance	0	1650
Total	4330	5980

Table 9.3: Estimate of the total maintenance cost for two maintenance policies.

10. Implementation

This chapter describes the planned path from the publication of this report to the KM3NeT construction and sketches the project structure during construction and operation. It presents the projected strategy for implementing Quality Control and finally a time line for the project.

10.1 Decision Path and Development Plan

The implementation of KM3NeT requires a series of decisions, based on technological and scientific evidence and taking into account political and funding aspects. In addition, engineering development is needed that feeds into decisions or is initiated by decisions. The basic questions to be addressed in this section are which decisions are to be taken, when and how.

Decision/Milestone	Input required
Verification of the deployment concepts for the mechanical options	Field tests with prototypes of each of the structures Risk analysis
Verification of the vertical backbone cables	Successful deployment and operation over several months; Risk analysis
Verification of the readout scheme	Laboratory tests; Simulation; Risk analysis
Verification and final engineering of the capsule OM concept	Lab prototype tests including long-term pressure test; Risk analysis
Site decision	Simulation and risk analysis; Cost analysis; Political convergence
Decision on mechanical structures and OMs	Results of the viability studies described above; Simulation results; Risk analysis; Refined cost analysis; Availability of components
Verfication of and decision on design of deep-sea power and data network	Site and mechanical design decision; Knowledge of detector size; Engineering design of junction boxes; Market analysis on availability and cost of components Risk analysis

Table 10.1: Technical steps towards the implementation of the KM3NeT infrastructure.

10.1.1 Decisions and Resources

In Table 10.1, the major technical and strategic decisions up to the stage where preproduction detection units can be constructed and the input needed for them are summarised. Overall, a materials budget of the order of 5M€, beyond the KM3NeT-PP resources is needed to arrive at the bottom line of the decision path. Some national funding is available. Further funding through national or regional channels has to be acquired, possibly with the support of an ASPERA common call. This may require the drafting of a Memorandum of Understanding between the parties involved. Aligning and coordinating this process will be a major task of the KM3NeT-PP.

It is planned that the construction of the KM3NeT neutrino telescope starts out with the construction of the shore station and the deployment of the main cable, part of the deep-sea network and ca. 10 preproduction detection units that have special provision for easy recovery and will allow for performing a high-statistics, *in situ* test of the complete design over about a year. In case of malfunctions the corresponding detection units will be recovered and analysed.

Any design flaws found will be mitigated in the mass production. If the preproduction detection units work well, they become part of the neutrino telescope. The resources for construction and deployment of this setup will be part of the KM3NeT construction budget.

10.1.2 Consortium Organisation

A set of activities and decisions are required for reaching the construction phase of KM3NeT. With the end of the Design Study in October 2009, the mandate of the corresponding decision-taking bodies has come to an end. Therefore, the Preparatory Phase project (KM3NeT-PP), running until the end of February 2012, plays a central role in providing a framework for establishing the governance structure required. It is assumed that at the end of KM3NeT-PP this governance structure will be in place and functional.

Altogether, the following two phases will occur:

1) The time between the end of the Design Study and the end of the KM3NeT-PP project. During this phase, the KM3NeT-PP decision bodies will monitor the process and steer the ongoing development. For activities not funded inside KM3NeT-PP, a Memorandum of Understanding (MoU) should be set up to regulate the distribution of tasks and responsibilities.

2) Following the KM3NeT-PP project, the final governance structure of the KM3NeT project will be in place in time to conclude contracts, issue tenders and generally allow KM3NeT to act as a legal entity.

10.1.3 Time lines

The decisions listed in Table 10.1 require the exact definition of the criteria along which they are taken. It is planned that these criteria are defined, agreed (see below) and documented by May 2010. All the following time scales have as a starting point this date.

For the viability decisions, extensive engineering work, repeated sea operations as well as the construction, deployment, operation and recovery of several engineering prototypes are necessary. It is expected that these activities will take 18 months. The site decision should, from a scientific and technical point of view, be taken as soon as possible in order to finalise design details. Also, the attractiveness for other countries and institutes to join the project will strongly increase once a site decision has been taken. However, this decision is also dependent on the process of political convergence towards project endorsement. The corresponding process is coordinated through the Preparatory Phase project. A decision must be taken after 18 months at the latest, to allow for a timely continuation of the project.

The final design will be presented in a detailed technical proposal, encompassing simulation and risk studies, using the site properties, as well as a refined cost estimate. The presentation of this document will coincide with the end of the KM3NeT-PP. At this stage it will be possible to launch KM3NeT construction. A period of 12-18 months is required to set up the assembly lines, to prepare tenders, to finalise the funding agreements. Thus, a start of production and installation is envisaged after 36-42 months, i.e. in 2013. This will start with the preproduction units mentioned above.

10.2 Future Project Structure

The KM3NeT Research Infrastructure will require an international governance structure allowing the stakeholders to establish a suitable legal entity, oversee the project, take financial and strategic decisions and execute the project management. The latter will be controlled by a body composed of representatives of the participating scientific institutions.

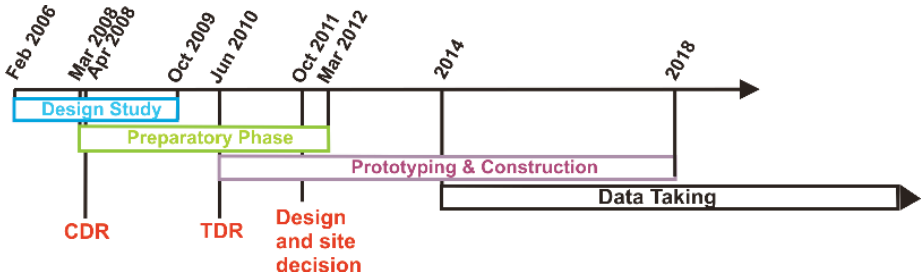

Figure 10-1: Overall time schedule of the KM3NeT project.

10.2.1 Governance

The exact definition of the legal and governance structure is a future task addressed by the Preparatory Phase project. The recently established *European Research Infrastructure Consortium (ERIC)*[7] is a candidate structure that is appropriate and has attractive and unique advantages: All requirements relating to the nature of the Research Infrastructure are fully satisfied by KM3NeT by virtue of the presence of KM3NeT on the ESFRI Roadmap;

The membership regulations of an ERIC are fully satisfied by KM3NeT;

The ERIC regulation also allows for the envisaged participation by countries outside the member states and associated countries. Furthermore, intergovernmental organisations can become ERIC members. This would allow, for example, for a future involvement of CERN.

For setting up an ERIC for KM3NeT, funding commitments and the site choice do not have to be fully established. It will, however, be necessary to endow the ERIC with an initial budget until the major funding commitments are decided. The initial statutory seat of the KM3NeT ERIC does not have to coincide with the country or one of the countries hosting the KM3NeT Infrastructure and may subsequently be changed. The establishment of a KM3NeT ERIC has some consequences and advantages. Subject to the member states' declaration recognising the KM3NeT ERIC as an international body the KM3NeT construction expenditure will not be subject to value added tax. In addition the KM3NeT ERIC could qualify for funding under title VI of the EC Financial Regulation as well for funding under the Cohesion Policy in conformity with the relevant Community legislation. The ERIC legal framework thus provides a sound basis for the future project structure. The prospects of setting up the KM3NeT ERIC will be explored in the KM3NeT-PP project.

10.2.2 Project Management

In the following, a management scenario is described that reflects the current plans of the KM3NeT Consortium. The precise management structure will be defined in the KM3NeT-PP project.

The core component will be a professional management team working on a full-time basis for the project. It will be led by the project manager, who directs a management team with competence in system engineering, quality control and risk management, legal and administrative issues, logistics and procurement. The management team will administer the construction and operation budgets. The project will be divided into subtasks addressed by appropriate working groups of experts. Examples for such subtasks are marine operations, assembly and construction, deep-sea technology, readout and electronics, physics and simulation, software. The convenors of the working groups will form the project coordination group which takes responsibility for the execution of the project and reports to the decision-making instance(s) established under the ERIC.

A data centre is planned for collection, mass storage, primary reconstruction and distribution of the neutrino telescope data and for providing the scientific community access to appropriate analysis tools. The administrative responsibility for the data centre is with the project manager.

[7] *Council Regulation (EC) 723/2009 (25 June 2009)*

11. Conclusions

A technical design has been presented for the KM3NeT Deep-Sea Research Infrastructure. The infrastructure will host a neutrino telescope with an instrumented volume of several cubic kilometres and provide the connectivity for an extensive multi-disciplinary earth and sea science observatory.

The neutrino telescope will detect neutrinos of cosmic origin by measuring the Cherenkov light induced by charged particles produced in neutrino interactions in the sea water or in the rock beneath the detector structure. This light is recorded in a three-dimensional array of light sensors located on structures with height of almost one kilometre and distributed over a base area of around six square kilometres. The installation will be located in the Mediterranean Sea at a depth of a few thousand metres and be permanently connected to shore for data collection.

The light sensors will be photomultiplier tubes housed in glass containers; the present design concept presents alternatives both for using large and small photomultipliers. These sensors are attached to vertical structures which are anchored to the seabed by a deadweight and held upright by a submerged buoy at the top. The deployment and behaviour of these "detection units" is a critical issue of the design and extensive field tests are required. As a consequence, alternatives are pursued, which yield the similar performance for the same cost. Final decisions will be made after the completion of prototype studies.

A readout technology has been developed that is suitable for all options considered. A sea-floor network of cables linking detection units to nodes of junction boxes will be installed for data transport and power provision. This network will also serve the earth and sea science observatory. On shore an installation for filtering and recording the incoming data is planned.

For the definition of the sensor layout in the sea, a detailed optimization has been performed based on the primary science objectives of the project. The resulting sensitivity for the detection of cosmic point-like neutrino-sources exceeds by a substantial factor that of the largest existing neutrino telescope, IceCube at the South Pole. For Galactic sources the sensitivity of KM3NeT surpasses that of the existing neutrinos telescopes, ANTARES in the Mediterranean Sea and Baikal in Siberia, by nearly two orders of magnitude.

Further essential considerations in the system optimization have been reliability and cost. The design study has shown that the major physics objectives can be met within a budget of 220 to 250 M€. The design is modular and so allows for staged implementation with continuously increasing science capabilities.

Final technical and site decisions will be made at the end of 2011 and a technical proposal will be presented in early 2012. Thereafter, the transition from ongoing prototyping activities to the construction phase will occur. Data taking will already start during the construction period with first science data becoming available around 2014.

Glossary

ADC	Analogue-to-digital converter
ADCP	Acoustic Doppler current profiler
AGN	Active galactic nucleus
AMANDA	Antarctic muon and neutrino detector array (neutrino telescope at the South Pole)
ANTARES	Astronomy with a neutrino telescope and abyss environmental research (neutrino telescope in the Mediterranean Sea)
ApPEC	Astroparticle physics European coordination
ASIC	Application specific integrated circuits
AUV	Autonomous underwater vehicle
CDM	Cold dark matter
CERN	Centre européenne pour la recherche nucléaire (particle physics laboratory)
CPU	Central processing unit
CTD	Conductivity-temperature-depth probe
CU	Crab unit (unit of flux for photons)
DEOS	Dynamics of Earth and ocean systems (deep-sea observatory network)
DAQ	Data acquisition
DB	Delta-Berenike
DMAS	Data management and archiving system
DMS	Data management system
DUMAND	Deep underwater muon and neutrino detector (neutrino telescope near Hawaii)
EBL	Extra-galactic background light
EDFA	Erbium doped fibre amplifier
EGRET	Energetic gamma-ray experiment telescope (satellite-borne)
EMSO	European multidisciplinary seafloor observatories (deep-sea observatory network)
ERDF	European regional development funds
ESFRI	European strategy forum on research infrastructures
ESONET	European seafloor observatory network of excellence
ESONIM	ESONET implementation model
EU	European Union
eV	Electron Volt
FPGA	Field-programmable gate array
FWHM	Full width at half maximum
GCN	Gamma-ray burst coordination network
GMES	Global monitoring for environment and security (monitoring network)
GOOS	Global ocean observing system
GPS	Global positioning system
GRB	Gamma-ray burst
GUI	Graphical user interface
GUT	Grand unified theories
GZK G	Greisen-Zatsepin-Kuzmin cut-off
H.E.S.S.	High energy stereoscopic system (TeV gamma-ray telescope)
ICG/NEAM	Intergovernmental Coordination Group for the Tsunami Early Warning and Mitigation System in the North East Atlantic, the Mediterranean and connected seas, part of IOC-UNESCO IOC – Intergovernmental Oceanographic Commission of UNESCO

IR	Infrared
LAERTIS	Laboratory in the abyss of Europe with real time data transfer to shore for interdisciplinary studies
LBNS	Long baseline acoustic navigation system
LED	Light-emitting diode
LIMS	Light intensity measuring system
MACRO	Monopole, astrophysics and cosmic ray observatory
MARS	Monterey accelerated research system (cabled observatory project)
MECMA	Mediterranean cable maintenance agreement
NEMO	Neutrino Mediterranean observatory (neutrino telescope in the Mediterranean Sea)
NEPTUNE	North east pacific time-integrated undersea networked experiments
NESTOR	Neutrino extended submarine telescope
OM	Optical module
ORFEUS	Observatories and research facilities for European seismology
pc	Parsec (astronomical unit of length)
PC	Personal computer
pe	photo-electron
PWN	Pulsar wind nebulae
QMS	Quality management system
RAM	Random access memory
RMS	Root mean square (deviation)
ROV	Remotely operated vehicle
RTV	Room temperature vulcanisation
SN	Supernova
SNR	Supernova remnant
spe	Single photon equivalent signal in a photomultiplier
SUSY	Supersymmetry
TDC	Time-to-digital converter
TDR	Technical design report
VHE	Very high energy
WIMP	Weakly interacting massive particle
X-HPD	Crystal scintillator hybrid photon detectors

Bibliography

[1] P.Kooijman *et al.* (ed.), *Conceptual design report for KM3NeT.* 2008, ISBN.9789064880315.

[2] R. Abbasi *et al.* (Ice-Cube collaboration), *Astrophys. J., 701(2009)L47.*

[3] F. Aharonian *et al., Rep. Prog. Phys.*, 71(2008)096901.

[4] F. Halzen, *Phys. Rept.*, 333(2000)349.

[5] P. Sapienza and G. Riccobene, *Riv. Nuovo Cim.*, 032(2010)591.

[6] T. Chiarusi and M. Spurio, *Eur. Phys. J.*, C65(2010)591.

[7] C. Spiering, *AIP Conf. Proc.*, 1085(2009)18.

[8] Dalhousie University. Ocean Tracking Network. http://oceantrackingnetwork.org/

[9] F. Briand, in *CIESM Workshop Monographs 34*, 2008.

[10] The Mediteranean Science Commission. http://www.ciesm.org/index.htm

[11] "EU Blue Paper on an Integrated Marine Policy," European Commission -- Marine Affairs COM(2007) 575, 2007.

[12] G. Bourlis *et al., Nucl. Instrum. and Meth.*, A602(2009)129.

[13] G. Bourlis *et al., Nucl. Instrum. and Meth.*, A626-627(2011)S163.

[14] A. Belias and A. Fotiou, *Nucl. Instrum. and Meth.*, A626-627(2011)S176.

[15] B. Howe *et al., IEEE J. Oceans Eng*, 27(2002)267, http://www.neptune.washington.edu.

[16] M. Anghinolfi *et al., Nucl. Instr. Meth.*, A567(2006)527.

[17] Universal Joint Consortium. http://www.ujcosortium.com

[18] M. Ardid *et al., Nucl.Instr. and Meth.*, A602(2009)174.

[19] E. Migneco *et al., Nucl. Instr. and Meth.*, A508(2008)111.

[20] D. Boersma, L. Gladstone, and A. Karle, in *Proc. of 31st Int. Cosmic Ray Conference*, Łódź, Poland,2009, contribution 1173; also arXiv:1002.4900 .

[21] A.G. Tsirigotis *et al., Nucl. Instrum. Meth.*, A595(2008)80.

[22] A. Leisos *et al., Nucl. Instrum. and Meth.*, A626-627(2011)S231.

[23] E. Anassontzis *et al., Nucl. Instrum. and Meth.*, A626-627(2011)S226.

[24] Ifremer. FP5 Assem project. http://ifremer.fr/assem

[25] T. Niedzielski, I.G. Priede, and A. Holford, *Marine Geophysical Researches*, 30(2009)217.

[26] KM3NeT, "Report on evaluation of existing water, oceanographic, biological and geological data from candidate sites," KM3NeT-WP5 summary http//www.roma1.infn.it/exp/nemo/KM3NeT/WP5_Deliverable5_1_090407.pdf , 2007.

[27] P. Amram *et al.* (ANTARES Collaboration), *Astroparticle Physics*, 19(2003)253.

[28] NEMO collaboration. (2002) nemoweb.lns.infn.it/sites/SiteReport/NEMO-Site-Report.pdf

[29] E. Trimonis and M. Rudenko, "Geomorphology and bottom sediments of the Pilos area," in Proc. of 2nd NESTOR International Workshop, Pylos, 1992, also at http://www.nestor.noa.gr/2nd/files/321_339_trimonis.pdf .

[30] E.G. Anassontzis *et al.*, (NESTOR collaboration), NESTOR NOTE.160.2007, 2007.

[31] E. A. Widder, I. M. Latz, and J. F. Case, *Biol. Bull.*, 165(1983)791.

[32] P. J. Henning (ed.), *Bioluminescence in action*. London, U.K.: Academic Press, 1978.

[33] I. G. Priede *et al., Deep Sea Reseach, Part I* 55(2008)1474.

[34] J. Craig *et al., Nucl. Instrum. and Meth.*, A602(2009)224.

[35] J.A. Aguilar *et al.* (ANTARES collaboration), *Astroparticle Physics*, 23(2005)131.

[36] R. Riccobene *et al., Astroparticle Physics*, 27(2007)1.

[37] A. Capone *et al., Nucl. Instr. Meth.*, A487(2002)423.

[38] R. C. Baker and K. S. Smith, *Appl. Opt.*, 20(1981)177.

[39] E.G. Anassontzis *et al., Astroparticle Physics*, 34(2010)187.

[40] E.G. Anassontzis *et al.* (NESTOR collaboration), *Nucl. Instrum. and Meth.*, A349(1994)242.
[41] P. Amram *et al.* (ANTARES Collaboration), *Astroparticle Physics*, 13(2000)127.
[42] J.A. Aguilar *et al.* (ANTARES Collaboration), *Astroparticle Physics*, 26(2006)314.
[43] M. Naumann-Godó, *Nucl. Phys.*, B (Proc. Suppl.) 172(2007)36.
[44] A. G. Tsirigotis, Ph.D.Thesis, Hellenic Open University, Patras, Greece, 2004.
[45] G. Aggouras *et al., Nucl.Phys.*, B(Proc. Suppl.)151(2006)279.
[46] T. Sjöstrand, *Comput. Phys. Commun.*, 82(1994)74.
[47] R. Engel *et al., Phys. Rev.*, D80(2009)094003.
[48] S. Ando and J. Beacom, *Phys. Rev. Lett.*, 95(2005)061103.
[49] V. Agrawal *et al., Phys. Rev.*, D53(1996)1314.
[50] E.V. Bugaev *et al., Phys. Rev.*, D58(1998)054001.
[51] A. Heijboer, Ph.D. Thesis, University of Amsterdam, Amsterdam, the Netherlands, 2004.
[52] D. Pandel, Diplom Thesis, HU Berlin, 1996.
[53] N. van Eijndhoven *et al., Astropararticle Physics*, 28(2007)456.
[54] J. Ahrens *et al., Nucl. Instr. Meth.*, A524(2004)169.
[55] G.C. Hill *et al.*, "Statistical problems in particle physics, astrophysics and cosmology," in *World Scientific eProceedings*, 108.
[56] G. J. Feldman and R. Cousins, *Phys. Rev.*, D57(1998)3873.
[57] G.Ingelman *et al..*, Comput. *Phys. Commun.*, 101(1997)108134.
[58] P. Antonioli *et al., Astroparticle Physics*, (1997)357.
[59] G. Carminati *et al., Comput. Phys. Commun.*, 179(2008)915.
[60] C. Forti *et al., Phys. Rev.*, D42(1990)3668.
[61] Geant3. http://wwwinfo.cern.ch/asdoc/geant_html3/geantall.html
[62] C. Kopper, *Nucl. Instrum. Meth.*, A602(2009)107.
[63] A. Gazizov and M. Kowalski, *Comput. Phys. Commun.*, 172(2005)203.
[64] H. L. Lai *et al., Eur. Phys. J.*, C12(2000)375.
[65] D Heck *et al.*, Forschungszentrum Karlsruhe FZKA 6019, 1998.
[66] D. Chirkin and W. Rhode. http://icecube.wisc.edu/~dima/work/MUONPR/
[67] C. Kopper, Ph.D. Thesis, Univ. Erlangen, Erlangen, 2010.
[68] Geant4 consortium. http://wwwasd.web.cern.ch/wwwasd/geant4/geant4.html
[69] J. Carr *et al., in Proc. 30th Int. Cosmic Ray Conference*, Mérida, Mexico 5(2008)1413, and 5(2008)1417
[70] A. G. Tsirigotis, A. Leisos, and S. E. Tzamarias, *Nucl. Instrum. and Meth.*, A626-627(2011)S185.
[71] A. G. Tsirigotis, A. Leisos, and S. E. Tzamarias, *Nucl. Instrum. and Meth.*, A626-627(2011)S188.
[72] A. G. Tsirigotis and S. E. Tzamarias, *Nucl. Instrum. Meth.*, A602(2009)91.
[73] C. D. Mobley, *Light and Water; Radiative Transfer in Natural Waters*. San Diego, U.S.A.: Academic Press, 1994.
[74] A. Ivanoff, *Introduction à l'océanographie*. Paris, 1972, vol. 2.
[75] R. Coniglione *et al.*, in *Proc. of 31st Int. Cosmic Ray Conference*, Łódź, Poland, 2009, contribution 1358.
[76] A. Karle for the IceCube Collaboration, in *Proc. of 31st Int. Cosmic Ray Conference*, Łódź, 2009, Highlight Talk; also arX A.
[77] Kappes *et al., Astrophys. J.*, 665(2007)870.
[78] S. Basa *et al., Nucl. Instrum. Meth.*, A602(2009)275.
[79] P. Meszaros and M. J. Rees, *Astrophys. J.*, 405(1993)278.
[80] D. Guetta *et al., Astroparticle Physics*, 20(2004)429.

[81] R. U. Abbasi *et al.*, *Astrophys. J.*, 710(2010)346.
[82] E. Waxman and J. N. Bahcall, *Phys. Rev. Lett.*, 78(1997)2292.
[83] S. Razzaque *et al.*, *Phys. Rev.*, D69(2004)023001.
[84] M. Kowalski and A. Mohr, *Astroparticle Physics*, 27(2007)533.
[85] D. Dornic *et al.*, in *Proc. of 31st Int. Cosmic Ray Conference*, Łódź, Poland, 2009, contribution 55.
[86] A. Franckowiak *et al.*, in *Proc. of 31st Int. Cosmic Ray Conference*, Łódź, Poland, 2009, contribution 1173; also arXiv:0909.0631.
[87] R. Auer, *Nucl. Instrum. Meth.*, A602(2009)84.
[88] E. Waxman and J. N. Bahcall, *Phys. Rev.*, D59(1999)023002.
[89] A. Achterberg *et al.* (IceCube coll.), *Phys. Rev.*, D76(2007)042008, *erratum*, D77(2008),089904.
[90] M. Ackermann *et al.* (IceCube Coll.), *Astrophys. J*, 675(2008)1014.
[91] J. De Dios Zornoza, PhD. Thesis, Universitat de Valéncia, Valéncia, Spain, 2005.
[92] J. Ahrens *et al.* (IceCube collaboration), *Astroparticle Physics*, 20(2004)507.
[93] L. A. Anchordoqui *et al.*, *Astroparticle Physics*, 29(2008)1.
[94] A.A. Abdo, *Astrophys. J. Letters*, 664(2007)L91.
[95] A.M. Taylor *et al.*, *Nucl. Instrum. Meth.*, A602(2009)113.
[96] D. N. Spergel *et al.*, *Astrophys. J. Suppl.*, 148(2003)175.
[97] P. Gondolo *et al.*, *Journ. of Cosmology and Astroparticle Physics*, 0407(2004)8.
[98] F. E. Paige *et al.*,, *arXiv:hep-ph*, 0312045(2003).
[99] J. F. Navarro, C. S. Frenk, and S. D. M. White, *Astrophys. J.*, 490(1997)493508.
[100] S. Desai, *et al.*, *Phys. Rev.*, D70(2004)083523.
[101] G. Wikström, "A search for solar dark matter with the IceCube neutrino telescope," Ph.D. Thesis, Stockholm University, Stockholm, Sweden, 2009.
[102} R. Abbasi *et al.*, *Phys. Rev. Lett.*, 102(2009)201302.
[103] J. Braun, and D. Hubert (for the IceCube Collaboration), *in Proc. of 31st Int. Cosmic Ray Conference*, Łódź, Poland, 2009, contribution 834.
[104] J. L. Feng, K. T. Matchev, and T. Moroi, *Phys. Rev.*, D61(2000)075005.
[105] V. N. Lebedenko *et al.*, *Phys. Rev. Lett.*, 103(2009)151302.
[106] J. Angle *et al.*, *Phys. Rev. Lett.*, 101(2008)091301.
[107] O. Behnke *et al.*, *Science*, 319(2008)933.
[108] D. Coronado, M. Acosta, and M. del Mar Cerb, *Economic Impact of the Container Traffic at the Port of Algeciras Bay*. Berlin: Springer, 2006.
[109] E. G. Jones *et al.*, *Marine Ecology Progress Series*, 251(2003)75.
[110] P. L. Tyack *et al.*, *The Journal of Experimental Biology*, 209(2006)4238.
[111] R. S. Lampitt, *Nature*, 345(1990)805.
[112] M. BĩIŷ, "Dependability of mechanical systems ," in *Studies in mechanical engineering 8*. Elsevier, 1989.
[113] I. A. Papazoglou and E. C. Marcoulaki, ""Dependability analisis of the conceptual design of a VLVNT in the Mediterranean Sea"," KM3NeT WD-KM3NeT-DS-T-RA-DA-09-001-REV0 1, 2009.
[114] "Procedures for performing a failure mode, effect and criticality analysis," AMSC N3074 (MIL-STD-1629), 1980.
[115] "Failure modes, effect and criticality analysis (FMECA)," ESA-ESTEC Requirements & Standards Division ECSS-Q-30-02A, 2001.
[116] E. Bernardini *et al.* (IceCube collaboration), *Nucl. Instrum. Meth.*, A567(2006)418.

Graphic design: ori ginale